Characterization and Modelling of 3rd Generation Advanced High Strength Steel Automotive B-Pillars from Forming to Crash

by

Jon Edward Gutierrez

A thesis
presented to the University of Waterloo
in fulfillment of the
thesis requirement for the degree of
Master of Applied Science
in
Mechanical and Mechatronics Engineering

Waterloo, Ontario, Canada, 2022

Author's Declaration

I hereby declare that I am the sole author of this thesis. This is a true copy of the thesis, including any required final revisions, as accepted by my examiners.

I understand that my thesis may be made electronically available to the public.

Abstract

This thesis investigates the application of 3rd Generation Advanced High-Strength Steels (3rd Gen AHSS) with ultimate tensile strengths of 980 and 1180 MPa to the forming and crash performance of an automotive B-pillar. The two primary steels considered were a 3rd Gen 980 and 3rd Gen 1180 V1. A third steel, 3rd Gen 1180 V2, was made available later in the project to enable select comparisons with the other two steels. The steel sheets were formed into a full-sized automotive B-pillar with the assistance of Bowman Precision Tooling and then subjected to dynamic impact testing.

The B-pillar tool was designed was by Bowman Precision Tooling using preliminary material data generated early on in the project using AutoForm R7 software. As improved plasticity and formability data became available, the correlation of the AutoForm predictions with the stamping trials could be revisited to investigate formability and springback prediction. Forming simulations were also performed using LS-DYNA to support mapping of the forming predictions to the secondary impact simulations. The 3rd Gen 980 B-pillar was successfully formed in the stamping trials as predicted by both LS-DYNA and AutoForm. The 3rd Gen 1180 V1 simulations predicted multiple false-positives for fracture in regions of bending while occasional splitting in the forming trials only occurred at one location near in-plane uniaxial tension.

Springback prediction was investigated by varying the constitutive models and element settings and evaluated with white-light scanned B-pillars. Overall, springback predictions were deemed successful by the industry partners since deviation of the final shape over the B-pillar was on the order of the sheet thickness. Springback predictions were found to be sensitive to the kinematic hardening parameters and is a direction for future work to consider more advanced models.

Impact testing of the B-pillars involved laser cutting of the formed B-pillars and spot welding of 590R steel backing plates. A modified three-point bend test fixture was designed to approximate the boundary conditions for a side impact scenario. Deformation and force evolutions from impact tests were compared and correlated under different friction conditions with LS-DYNA simulations. It was shown that different friction conditions had a marked effect on the forces and the deformation of the side wall, in particular for the 3rd Gen 980. No fractures occurred in the crash testing of the 3rd Gen 980 while minimal cracking was observed in the 3rd Gen 1180 V1, highlighting the potential of this emerging class of steels for automotive lightweighting.

Acknowledgements

The work carried out in this thesis would not have materialized without the help from all the contributing members throughout this project. Firstly, the amount of help provided by Prof. Cliff Butcher, my supervisor, has been immeasurable. His knowledge, support, and guidance have helped me hone my analysis skills, improved my technical writing, and has shown me the significance of accurately describing constitutive behaviour of sheet steels. His support during the emergence of this pandemic has helped me get through the difficulties of finishing a graduate degree in the midst of a time of uncertainty. Thank you for your support, Cliff. I am immensely grateful. I would like to acknowledge the help of Prof. Mike Worswick and Dr. José Imbert-Boyd for their support and technical expertise during crash testing. Crash testing would not have happened without your support, patience, and knowledge during the impact testing phase of the project.

The American Iron and Steel Institute (AISI) Automotive Program, Honda Development and Manufacturing America (HDMA), and Bowman Precision Tooling provided substantial technical support. The leadership, support (and patience) of Dr. Ezzat of AISI was instrumental to the success of the project. Neil Parker of Bowman Precision Tooling was always available for questions, and I sincerely appreciate his patience and time spent on the project to share his expertise in tool design and simulation. The expertise of those in AutoForm Engineering who kindly provided the use of their product to assist in the forming simulations of the B-pillar. Gratitude is extended in particular to Kanaan Kidambi who provided training and assisted in the many questions that I had about AutoForm. Last but certainly not least, I particularly wish to thank Jim Dykeman and Cameron O'Keeffe of HDMA for their support of the project, technical advice on formability and crash, and providing the computational resources to run detailed forming models in hours compared to weeks per run locally at Waterloo.

Support in the lab has been vital in the completion of experiments and I would like to thank Eckhard Budziarek, Tom Gawel, Andy Barber, E3 and E5 Engineering Machine Shop Personnel. Assistance. The kind assistance of the Welding and Joining group of Prof. Elliot Biro in spotwelding the B-pillars was an unexpected and invaluable service. The help of Abdelbaset Midawi in arranging the spotwelding service is greatly acknowledged. Many thanks to Nicholas Aydemir for being a reliable lab buddy, classmate, and someone to influence me to go on a Tim

Hortons or bakery run when I am not even feeling hungry. Thank you to Kaab Omer, Steven Lee, Stan Lu, Alirezah Mohamadizadeh, Sante DiCecco, and Chris Kohar for the knowledge and advice you have imparted after entertaining many tedious questions of mine.

To Jacqueline Noder who has supported and mentored me throughout the beginning of the Master’s degree. I am perpetually grateful for guiding me through the ups and downs of grad school, assisting me in my experiments, correcting my shortcomings as an engineer, and for being a loyal friend. I will remember the kindness you have given.

To my missionary team in Belize. Your support during mission has been a great pillar for me to lean on as I was writing and teaching. The time I have had there has been fruitful and formative. It truly was an unforgettable time.

Similarly, to my friends in Waterloo who have supported me throughout my stay in grad school has kept me strong. A particular mention to my Exodus brothers who were a source of strength at that time.

To my family whose undying support has kept me fed, uplifted, and always striving to achieve my goals. Their support pre-pandemic, during the pandemic, and post-pandemic will always be there. To my mom and dad, who inspired me to become an engineer, know that I will not be here without your prayers and support.

Lastly, to my youngest sister, Lea. I dedicate this thesis for you. I dedicate the rest of my work and my life to honor your memory. I will carry your cross for the rest of my days.

To Lea, my baby sister

Contents

List of Figures x

List of Tables xix

1. Introduction 1

  - 1.1 Microstructure & Mechanical Properties of 3rd Generation AHSS 6
    - 1.1.1 Forming Challenges with Lightweighting 8
  - 1.2 Formability 9
    - 1.2.1 Global Formability 9
    - 1.2.2 Experimental Forming Limits 12
    - 1.2.3 Analytical Forming Limits 14
    - 1.2.4 The Forming Limit Curve and its Dynamic Considerations 14
  - 1.3 Springback 18
    - 1.3.1 The Bauschinger Effect and Elastic Modulus Degradation 18
    - 1.3.2 Numerical Analysis of Springback Operations 23
  - 1.4 Fracture Characterization 25
    - 1.4.1 Crashworthiness and the Role of Forming Strain 27
  - 1.5 Current Work 32

2 Constitutive Characterization and Modelling of 3rd Gen AHSS 34

  - 2.1 Anisotropy Characterization 35
  - 2.2 Calibration of Isotropic Hardening Response 37
  - 2.3 Hardening Response at Elevated Strain Rates 38
  - 2.4 Yld2000 Anisotropic Yield Function 41
  - 2.5 Chord Modulus Evolution 43
  - 2.6 Tension-Compression Tests 44
  - 2.7 Fracture Characterization and Fracture Locus Calibration 46

3 Experimental and Analytical Formability Characterization 47

  - 3.1 Characterization of In-Plane Formability using Marciniak and Nakazima Tests 47
  - 3.2 DIC Settings and Limit Strain Detection 51
  - 3.3 Fracture Modes 53
  - 3.4 Process corrections of Nakazima and Marciniak limit strains 55
  - 3.5 Analytical models to predict the FLC 59
    - 3.5.1 MK Model 60

3.5.2 MMFC Model 61
3.5.3 Bressan-William-Hill Model 62
3.6 Discussion of Predicted FLCs using the MK, MMFC, and BW models 65
3.6.1 MK Model Forming Limits 65
3.6.2 MMFC Forming Limits 66
3.6.3 BWH and BWx Model Forming Limits 66
3.6.4 MMFC and BWX comparisons between 3rd Gen 1180 V1 and V2 67
3.7 Discussion and Recommendations on Formability Characterization 68
4 B-pillar Design, Stamping Trials and Correlation 69
4.1 AutoForm R8 Model Development, Tool Design, and Springback Compensation 69
4.2 Forming Simulation Methodology and Results 73
4.3 Correlation of AutoForm R8 Simulations with Forming Trials 78
4.4 Discussion, Conclusions, and Recommendations on AutoForm Forming Simulations . 80
5 B-pillar Forming Simulations and Correlation using LS-DYNA 81
5.1 Simulation Stages for B-pillar Forming 81
5.1.1 Simulation Stage – Gravity Loading 81
5.1.2 Simulation Stage – Forming 82
5.2 Simulation Parameters 83
5.3 Simulated Results – Forming 84
5.3.1 Influence of the Strain Rate Sensitivity and Number of Integration Points 85
5.3.2 Study on 3rd Gen 1180 V2 90
5.4 Discussion, Conclusions and Recommendations on LS-DYNA Forming Simulations . 91
6 B-pillar Springback Prediction and Correlation 92
6.1 Simulation Stages 92
6.1.1 Trimming 92
6.1.2 Springback 94
6.1.3 Best-fitting 94
6.2 LS-DYNA Springback and Best-fitting Correlations 95
6.2.1 Springback Predictions 95
6.2.2 Springback Correlation 98
6.3 AutoForm Springback Predictions and Evaluation of Separation Distance 101
6.4 Discussion and Recommendations on Springback Methodology 106

7 B-pillar Impact Tests and Simulation 107
  7.1 Experimental Setup 107
    7.1.1 B-pillar Fixture 107
    7.1.2 B-pillar Attachment (U-channel, Backing Plate, M10 Bolts) 110
    7.1.3 Crash Sled and Impactor Friction 114
    7.1.4 Lighting and camera placements 116
  7.2 Impact Testing 120
    7.2.1 DIC Strain Measurement 122
  7.3 FE Model Development of the B-Pillar Impact Tests 123
    7.3.1 Modelling of Boundary Conditions 123
    7.3.2 B-pillar Attachments 125
    7.3.3 Modelling of the crash event 128
  7.4 Impact Test Correlations 130
    7.4.1 Force and Energy Comparisons 130
    7.4.2 Deformation modes – low COF 139
    7.4.3 Deformation modes – high COF 140
    7.4.4 Surface strain measurement 142
  7.5 Discussion of Force Correlations 143
  7.6 Discussion, Conclusions, and Recommendations of Impact Tests and Simulations 144
8 Summary 145
  8.1 Conclusions 145
    8.1.1 Forming 145
    8.1.2 Springback 145
    8.1.3 Crashworthiness 146
  8.2 Recommendations 146
    8.2.1 Forming 146
    8.2.2 Springback 147
    8.2.3 Crashworthiness 147
References 148
Appendices 158
  Appendix A: Mesh Regularization 158
  Appendix B: Double Impactor 168

List of Figures

Figure 1: Composition of materials used in BIW (Hovuron *et al.*, 2017)....................................1

Figure 2: Body-in-white of the 2016 Honda Pilot and the various compositions of steel used in the BIW (American Honda Motor Co., 2016) 2

Figure 3: Engineering stress-strain curves of 1st Gen AHSS (Billur and Altan, 2013) 3

Figure 4: Engineering stress-strain curve comparing 2nd Gen AHSS with 1st Gen AHSS (Billur, Dykeman, and Altan, 2014)..3

Figure 5: Comparison of tensile strength and total elongation of varying grades of steel (Billur and Altan, 2014)..4

Figure 6: Comparison of 3rd Gen AHSS with strengths of 590 MPa, 980 MPa, and 1180 MPa (Noder *et al.*, 2021)..5

Figure 7: Body-in-white model of a passenger vehicle highlighting the B-pillar (Carbrain, 2021)6

Figure 8: Thermal cycle for quenching and partitioning (World Auto Steel, 2020) 7

Figure 9: Forming limit curves of DP980 and Q&P980 (Chen *et al.*, 2017) 8

Figure 10: Comparison of tonnage and energy requirements between DP and HSLA (Keeler and Ulnitz, 2019)...9

Figure 11: Comparison of springback for DP steel and HSLA (World Auto Steel, 2019).............9

Figure 12: Visualization of diffuse necking in a tensile test with formation of a localization band of height *h* and its collapse to a plane during acute localization (Noder, 2021) 10

Figure 13: The (a) hardening curves for TRIP (T600), DP, and HSLA steels along with its (b) instantaneous n-values as a function of engineering strain and their (c) corresponding analytical FLCs for each steel (Konieczny, 2003)..11

Figure 14: Hill-Swift criterion with varying n-values demonstrating the effect of changing n-value to the FLC (Paul, 2021)...12

Figure 15: Schematic of the a) Nakazima test and b) Marciniak test (Noder, 2021) 13

Figure 16: Radius fracture that occurred in the Marciniak test for 3rd Gen 1180 V1 13

Figure 17: Strain paths and corresponding limiting strains for (a) Nakazima and (b) Marciniak tests for AA5182 highlighting nonlinearity (Noder and Butcher, 2019) 15

Figure 18: Uncorrected limiting strains (a) of Marciniak tests, and dome tests with 101.4 mm (Nakazima-4) punch diameter and 50.8 mm diamater (Nakazima-2) along with the (b) corrected limiting strains (Min *et al.*, 2016)..15

Figure 19: Evolution of FLCs after prestraining in equibiaxial tension. Four different prestrain levels are shown along with the FLC of the virgin material (Graf and Hosford, 1993) 16

Figure 20: Evolution of FLC during prestraining indicating original draw stages and modified draw stage to exploit the dynamic behavior of nonlinear strain paths (Stoughton and Yoon, 2012) 17

Figure 21: Conversion of a FLC in a) strain space to b) stress space indicating independence of load history (Stoughton and Yoon, 2012) 18

Figure 22: Illustration of the experimental apparatus for a) cylindrical bending b) U-bending and c) V-bending (Burchitz, 2005)...19

Figure 23: Illustration of a stress-strain curve under reverse loading highlighting its effects (Yoshida and Uemori, 2002) 19

Figure 24: Directions of tensile and compressive stresses occurring in a bending operation.......20

Figure 25: Stress-strain evolution of sidewall curl occurring at the tension and compression side of the sheet (WorldAutoSteel, 2019) 20
Figure 26: Visualization of isotropic hardening in 3D stress space (left) and its plastic strain response (right) for a tension compression cycle (Chaboche, 2008) 21
Figure 27: Visualization of kinematic hardening in 3D stress space (left) and its plastic strain response (right) for a tension compression cycle (Chaboche, 2008) 22
Figure 28: Loading and unloading cycles of DP600 steel a) under different prestrains and b) a zoomed in image of one cycle highlighting the chord modulus (Lajarin *et al.*, 2020) 22
Figure 29: Comparison of stress-strain curve of cyclic tension-compression tests using the QPE model vs. the stress-strain curve obtained experimentally (Sun and Wagoner, 2011) 23
Figure 30: Comparison of shapes of U-bending tests between experiments and numerical predictions using varying yield functions and hardening models (Seo *et al.*, 2018) 24
Figure 31: Stress-strain curve of cyclically loaded simple shear experiments obtained from experiments superimposed with simulation results using the HAH model (Barlat *et al.*, 2011) ..25
Figure 32: Example of a plane stress fracture locus for a structural steel from Kõrgesaar, (2019). 27
Figure 33: Reaction forces of the front side member by Huh *et al.* (2003) highlighting peak forces when considering forming effects...28
Figure 34: Reaction forces of s-rail tubes by Oliveira *et al.* (2006) highlighting peak forces when considering forming effects 28
Figure 35: Images of undeformed and deformed axial crush tests of Ductibor® 500-AS (Peister, 2018) 29
Figure 36: Alignment of deformable barrier with stationary vehicle from the SICE 60 30
Figure 37: IIHS safety ratings by model year from 2003 to 2017 (Teoh and Lund, 2011) 31
Figure 38: B-pillar structures highlighting push on the pelvis area (Hall, 2020) 32
Figure 39: Geometries used to perform a) tensile tests, b) simple shear tests (Peirs *et al.*, 2012), and c) high-rate tests (Smerd *et al.*, 2005). All dimensions are in mm where darkened regions are areas that are clamped (Noder *et al.*, 2021a) 34
Figure 40: Engineering stress-strain responses of 3rd Gen AHSS tested in the transverse direction (TD) (Noder, 2021a) 35
Figure 41: Hardening response of the calibrated MHS model superimposed with the tensile and converted shear data for both steels tested in TD (Noder, 2021a). 37
Figure 42: Dynamic hardening response and strain rate comparisons for a) 3rd Gen 980 and b) 3rd Gen 1180 V1 superimposed with the modified Johnson-Cook model and the c) 3rd Gen 1180 V2 superimposed with the Cowper-Symonds model 40
Figure 43: Superimposed von Mises and Yld2000 (a) yield functions, (b) experimental tensile and shear stress ratios superimposed with predicted values, and (c) experimental r-values superimposed with predicted values for 3rd Gen 980, 3rd Gen 1180 V1, and 3rd Gen 1180 V2 (Noder *et al.*, 2021) 42
Figure 44: Interrupted tensile tests with (a) 8 unloading cycles for 3rd Gen 980 and (b) a zoomed in view of the non-linear behavior during unloading of the 7th unloading cycle........................43
Figure 45: Experimental and numerical chord modulus using the Yoshida model.....................44

Figure 46: Stress-strain response of cyclic tension-compression tests for a) 3rd Gen 980 and b) 3rd Gen 1180 V1....45
Figure 47: The Generalized Drucker-Prager fracture model of Rahmaan *et al.* (2018) for the 3rd Gen 980 and 3rd Gen 1180 V1 & V2 (Noder *et al.*, 2021)....46
Figure 48: Strain paths showing uniaxial tension, plane strain tension, and equibiaxial tension under proportional loading a) and the dogbone specimen used to obtain limiting strains b)....48
Figure 49: Nakazima (left) and Marciniak (right) tool sets where the dimensions are in mm and in accordance with the ISO12004-2 standard....49
Figure 50: MTS dome tester layout at the University of Waterloo High Pressure Lab....50
Figure 51: Orientation of DIC cameras overlooking the dome tester to capture images of deformation of specimens....50
Figure 52: Strain paths superimposed with ISO12004-2 standard limit strains for a) Nakazima and b) Marciniak tests for 3rd Gen 980....52
Figure 53: Strain paths superimposed with ISO12004-2 standard limit strains for a) Nakazima and b) Marciniak tests for 3rd Gen 1180 V1....52
Figure 54: Strain paths superimposed with ISO12004-2 standard limit strains for Marciniak tests for 3rd Gen 1180 V2....52
Figure 55: Major strain distributions of 3rd Gen 1180 V1 Marciniak tests for sample widths that are subjected to a) uniaxial tension to c) plane strain tension....54
Figure 56: Cross-sections of fractured Marciniak specimens for 3rd Gen 980 (left) and 3rd Gen 1180 V1 (right) undergoing a) uniaxial stretch, b) plane strain tension and c) equi-biaxial stretch....55
Figure 57: Marciniak limit strains pre- and post-correction for NLSP for a) 3rd Gen 980 and b) 3rd Gen 1180 V1....58
Figure 58: Uncorrected limiting strains of a) 3rd Gen 980 and b) 3rd Gen 1180 V1 superimposed with the limit strains corrected for NLSP....58
Figure 59: Corrected (NLSP + P) limiting strains superimposed with the NLSP-corrected limit strains of a) 3rd Gen 980 and b) 3rd Gen 1180 V1 for Nakazima tests....59
Figure 60: Corrected limiting strains for Nakazima (NLSP + Pressure corrected) and Marciniak (NLSP corrected) tests for a) 3rd Gen 980 and b) 3rd Gen 1180 V1....59
Figure 61: Illustration of the imperfection band under biaxial stretch deforming in plane stress conditions....61
Figure 62: Forming limits in stress-space a) of an isotropic material using power law hardening highlighting the horizontal FLC of Hance and Huang (2018) and b) the converted FLC in strain space of the BWx model....64
Figure 63: Analytical forming limit strains generated from the MK model with varying imperfection factors for a) 3rd Gen 980 and b) 3rd Gen 1180 V1 superimposed with its process-corrected limiting strains....65
Figure 64: Analytical forming limit strains from the MMFC model using the method of Hora *et al.* (2013) and its linearized form for a) 3rd Gen 980 and b) 3rd Gen 1180 V1 superimposed with its process-corrected limiting strains....66
Figure 65: Analytical forming limit strains from the BWH and BWx model for a) 3rd Gen 980 and b) 3rd Gen 1180 V1 superimposed with its process-corrected limiting strains....67

Figure 66: Analytical forming limit strains from the a) BWx and b) MMFC model for the 3rd Gen 1180 steels superimposed with experimental limit strains..67
Figure 67: Analytical FLC variants with the best agreement superimposed with the limit strains that have undergone process corrections for a) 3rd Gen 980 and b) 3rd Gen 1180 V1................68
Figure 68: B-pillar CAD geometry a) before trimming used in tooling design, b) a formed 3rd Gen 980 B-pillar before trimming indicating the locations of the side sill, fold initiators, and roof rail and c) a formed 3rd Gen 980 B-pillar after trimming...70
Figure 69: Preliminary simulations used to drive the modifications of the B-pillar tooling where the forming contours of the a) 3rd Gen 980 are visualized and the b) 3rd Gen 1180 V1 forming simulations are visualized..72
Figure 70: Tooling of the B-pillar geometry designed and machined by Bowman Precision Tooling 73
Figure 71: General dimensions and initial mesh of the blank before the B-pillar is formed........74
Figure 72: Refined mesh size of the blank at the drawbeads after B-pillar forming....................74
Figure 73: Press motion during forming where the last 100 mm of the press stroke forms the B-pillar 75
Figure 74: Binder pressure response of 16 gas cylinders using nitrogen as its pressure medium, 100 SPM, and a binder stroke of 100 mm (Kaller, 2021) 75
Figure 75: Formability contours of a) 3rd Gen 980, b) 3rd Gen 1180 V1, and c) 3rd Gen 1180 V2 along withs its FLC showing linear and non-linear strain paths 77
Figure 76: A successful forming trial of the 3rd Gen 980 B-pillar...78
Figure 77: Split on located at the forming trial of the 3rd Gen 1180 V1 B-pillar.......................78
Figure 78: Formability contour a) of 3rd Gen 1180 V1 B-pillar using AutoForm R8 with the activation on the NLSP option b) using the BWx model as the FLC 79
Figure 79: The strain paths of the splitting elements located at bending regions on the 3rd Gen 1180 V1 B-pillar after being formed. The alternate picture shows a zoomed in strain path highlighting non-linearity where the BWx model is used as the FLC..79
Figure 80: Major strain of 3rd Gen AHSS grades undergoing v-bending, Nakazima testing, and Marciniak testing. Note that no Nakazima tests were performed for 3rd Gen 1180 V2..............80
Figure 81: Side view of the binder and blank with and without gravity loading 82
Figure 82: Tool set arrangement of the B-pillar tooling emulating the forming trials 82
Figure 83: Strain distribution of a) 3rd Gen 980 and b) 3rd Gen 1180 V1 using 11 integration points and GISSMO disabled. 85
Figure 84: Legends from the forming simulations where each data point represents an element in the B-pillar simulation...86
Figure 85: Strain contour of 3rd Gen 980 with 7 NIPs without strain rate effects. Strain paths extracted in Figure 86 is extracted from Tumblehome – bottom 87
Figure 86: Strain contour of 3rd Gen 980 with 7 NIPs coupled with strain rate effects. Strain paths extracted in Figure 86 is extracted from Tumblehome – bottom 87
Figure 87: Formability strain cloud indicating risk of cracking, wrinkling, and the BWx model for 3rd Gen 980 using a) 3 NIPs, b) 7 NIPs, and c) 11 NIPs. The strain path from the crack location is extracted located at the tumblehome and at the bend area. Refer to Figure 83 for legend. 88

Figure 88: Strain contour of 3rd Gen 1180 V1 with 7 NIPs without strain rate effects highlighting the bend area and tumblehome. The strain path in Figure 89 is extracted from Tumblehome – bottom........89
Figure 89: Strain contour of 3rd Gen 1180 V1 with 7 NIPs coupled with strain rate effects highlighting the bend area and tumblehome. The strain path in Figure 89 is extracted from Tumblehome – bottom........89
Figure 90: Formability strain cloud indicating risk of cracking, wrinkling, and the BWx model for 3rd Gen 1180 V1 using a) 3 NIPs, b) 7 NIPs, and c) 11 NIPs. The strain path from the crack location is extracted located at the tumblehome and at the bend area........90
Figure 91: Formability strain cloud indicating risk of cracking, wrinkling, and the BWx model for 3rd Gen 1180 V2 using 7 NIPs. The strain path from the crack location is extracted located at the tumblehome and at the bend area........91
Figure 92: Visualization of a) the trimming outline used on the B-pillar and b) the trimmed B-pillar........93
Figure 93: Effect of element tolerance on elements post-trimming........93
Figure 94: Constraints applied to formed and trimmed geometry of the B-pillar for its springback simulation........94
Figure 95: Location of node pairs selected for best-fitting........95
Figure 96: Contour plot of the *x*-displacement of the 3rd Gen 980 B-pillar post-springback with no rate effects with 3 NIPs........96
Figure 97: Contour plot of the *y*-displacement of the 3rd Gen 980 B-pillar post-springback with no rate effects with 3 NIPs........97
Figure 98: Selected locations for extracting nodal displacements. Each node is labelled indicating which direction the displacement is directed........97
Figure 99: *Y*- and *x*-displacements extracted from the 3rd Gen 980 springback simulations. *Y*-displacements are extracted from Locations 1 and 2 while *x*-displacements are extracted from Locations 3 and 4........98
Figure 100: *Y*- and *x*-displacements extracted from the 3rd Gen 1180 V1 springback simulations. *Y*-displacements are extracted from Locations 1 and 2 while *x*-displacements are extracted from Locations 3 and 4........98
Figure 101: Contour plot of the separation distances of the 3rd Gen 980 B-pillar using 3 NIPs and no rate effects........99
Figure 102: Contour plot of the separation distances of the 3rd Gen 1180 V1 B-pillar using 3 NIPs and no rate effects........99
Figure 103: Separation distances between the scanned part and simulation model from the springback model of the 3rd Gen 980 B-pillar at Locations 1 to 4 using LS-DYNA........100
Figure 104: Separation distances between the scanned part and simulation model from the springback model of the 3rd Gen 1180 V1 B-pillar at Locations 1 to 4 using LS-DYNA........100
Figure 105: Cyclic tension compression tests of a) 3rd Gen 980 and b) 3rd Gen 1180 V1........101
Figure 106: Best-fitting of 3rd Gen 980 springback simulations exported from AutoForm R8 showcasing results using a) isotropic hardening, b) kinematic hardening (KH) obtained from experimental cyclic tests and c) kinematic hardening parameters obtained from literature data (Aryanpour, 2011 and Seo *et al.*, 2017)........103

Figure 107: Best-fitting of 3rd Gen 1180 V1 springback simulations exported from AutoForm R8 showcasing results using a) isotropic hardening, b) kinematic hardening (KH) obtained from experimental cyclic tests and c) kinematic hardening parameters obtained from literature data (Aryanpour, 2011 and Seo *et al.*, 2017) 104
Figure 108: Separation distances between the scanned part and simulation model from the springback model of the 3rd Gen 980 B-pillar at Locations 1 to 4 using AutoForm R8 105
Figure 109: Separation distances between the scanned part and simulation model from the springback model of the 3rd Gen 1180 V1 B-pillar at Locations 1 to 4 using AutoForm R8 105
Figure 110: Assembly of the B-pillar Fixture generated using CAD software 108
Figure 111: Roof rail fixture used for impact testing of the B-pillar 109
Figure 112: Side sill fixture that suspends the B-pillar used in impact testing 109
Figure 113: Placement of the U-channel on the slotted inserts. The U-channel is secured in the slotted inserts with the insert caps using M14 bolts. Underneath the U-channel, M10 nuts were welded where the B-pillar is bolted on top of the U-channel. 110
Figure 114: Fully assembled fixture with the B-pillar attached for impact testing 110
Figure 115: Dimensions of the U-channel. All dimensions are in mm. 111
Figure 116: Power law approximations for the hardening response of a) Class 10.9, M10 bolts and b) ASTM 36 U-channels obtained from FEMA (2002) and Noury (2014), respectively 111
Figure 117: Locations of spotwelds on the B-pillar outlined by the yellow dashed line 112
Figure 118: Cross-tension test specimen of 3rd Gen 1180 V1 spotwelded with 590R 113
Figure 119 : Hardening response for JAC590R which uses the MHS model 113
Figure 120: Force-displacement graph for 3rd Gen 980 and 3rd Gen 1180 V1 extracted from cross-tension tests. The abrupt drop in loads indicate the end of the test. 114
Figure 121: Crash sled experimental setup for B-pillar impact testing 115
Figure 122: Setup of piezoelectric load cells attached to the sled face and impactor plate. Impactor surface conditions are varied with the use of a) Teflon ® and b) 120 grit sandpaper 116
Figure 123: Camera and lighting configurations used on the B-pillar impact tests 118
Figure 124: Top a) and isometric b) view of the B-pillar crash test using the Photron SA-5 and SA-Z respectively 119
Figure 125: Back a) and side b) view of the B-pillar crash test using the Photron SA-4 and SA-5 respectively 119
Figure 126: Speckle images captured by the Photron AX-100 cameras used for DIC analysis . 120
Figure 127: Honeycomb showcasing its a) full-length and its b) crushed form post-test 120
Figure 128: Synchronized frames of the B-pillar crash test and simulation highlighting the modes of deformation for the low friction condition for 3rd Gen 980 121
Figure 129: Synchronized frames of the B-pillar crash test and simulation highlighting the modes of deformation for the low friction condition for 3rd Gen 1180 V1 121
Figure 130: Folding caused by low friction conditions on the B-pillar crash tests for a) 3rd Gen 980 and b) 3rd Gen 1180 V1 122
Figure 131: Typical area of interest for DIC analysis for impact tests 122
Figure 132: Major principal strain contour of 3rd Gen 980 under high friction case 123
Figure 133: Boundary conditions prescribed on the B-pillar. The side sill is secured by bolting the U-channel underneath the B-pillar. The side sill lays above the rigid posts that act as rollers. .. 124

Figure 134: Locations of SPCs and the degrees of freedom constrained for the a) loose configuration and the b) secured configuration. 124
Figure 135: Physical modelling of the inserts in the crash simulation where the inserts and caps are modelled as a) rigid material and all degrees of freedom are constrained. Elastic inserts are modelled in b) where the caps are secured to the inserts with M14 bolts. The nodes of the bottom face of the inserts are constrained in all degrees of freedom to secure the assembly. 125
Figure 136: Spider mesh applied on the U-channel and B-pillar modelling nuts and bolts 126
Figure 137: Location of spotwelds on the backing plate 127
Figure 138: Hex weld configurations from 1-hex to 16-hex configurations.............................127
Figure 139: A 8-hex weld configuration indicating the directions of the forces and moments experienced by the weld (Malcolm and Nutwell, 2007) 128
Figure 140: Crash sled modelling method 129
Figure 141: Force response of 3rd Gen 980 and 3rd Gen 1180 V1 showing a) unfiltered and b) filtered results 131
Figure 142: Impact test of 3rd Gen 980 under high COF at 40 mm crush distance showing that the side walls from the simulation model collapses much earlier than the experiment...................132
Figure 143: Force response of the crash simulation overlaid with the experimental results showing all modelling methods and friction conditions for the a) 3rd Gen 980 and b) 3rd Gen 1180 V1. Note that the black solid lines represent the experiments with high COF and the black dashed lines represent the experiments with low COF. 134
Figure 144: Force response of the B-pillar crash simulation with virgin steel and strain mapping for a) 3rd Gen 980 and b) 3rd Gen 1180 V1 135
Figure 145: Energy reported by the experiments overlaid with the energy of the simulations for both a) 3rd Gen 980 and b) 3rd Gen 1180 V1. 136
Figure 146: Force readings of all 3rd Gen AHSS impact simulations......................................137
Figure 147: Energy response of all 3rd Gen AHSS integrated from the force response 137
Figure 148: Contour plot of the D-parameter for the middle integration point using biaxial regularization factors for a) 3rd Gen 980 B-pillar a) and b) the crash tested 3rd Gen 980 B-pillar where no splits occur in the simulation using plane strain or biaxial regularization. 138
Figure 149: Contour plot of the D-parameter parameter for the middle integration point using biaxial regularization factors for a) 3rd Gen 1180 V1 B-pillar b) and the crash tested 3rd Gen 1180 V1 B-pillar showing splitting. It should be noted that splitting in the impact test occurred past free crush. 138
Figure 150: Synchronized frames of the B-pillar crash test and simulation highlighting the modes of deformation for the low friction condition for 3rd Gen 980 139
Figure 151: Synchronized frames of the B-pillar crash test and simulation highlighting the modes of deformation for the low friction condition for 3rd Gen 1180 V1..139
Figure 152: Synchronized frames of the B-pillar crash test and simulation highlighting the modes of deformation for the high friction condition for 3rd Gen 980 140
Figure 153: Synchronized frames of the B-pillar crash test and simulation highlighting the modes of deformation for the high friction condition for 3rd Gen 1180 V1.......................................140

Figure 154: Crash simulations of 3rd Gen 980 showcasing the bending and wrapping mode utilizing a) low and b) high friction, respectively. The bottom images highlight the deformation at 100 mm crush distance below where its perspective is shown by the lateral eye symbol. 141
Figure 155: Crash simulations of 3rd Gen 1180 V1 showcasing the bending mode utilizing a) low and b) high friction, respectively. The bottom images highlight the deformation at 100 mm crush distance below where its perspective is shown by the lateral eye symbol. 141
Figure 156: Comparison of crash experiments with DIC analysis and crash simulations showing its strain contour plot at 50 mm and 100 mm for 3rd Gen 980 low COF highlighting the a) DIC strain analysis synchronized with b) the crash simulations...142
Figure 157: Bending caused by the impactor on the 3rd Gen 980 B-pillar with low COF where the dashed lines highlight the bending..143
Figure 158: Average mesh size used in mesh regularization for a) equi-biaxial and b) plane strain Nakazima dome test simulations 159
Figure 159: Experimental damage curve for a) 3rd Gen 980, b) 3rd Gen 1180 V1, and c) 3rd Gen 1180 V2. No plane strain dome simulations were performed. Unscaled fracture loci provided by Dr. Jacqueline Noder...160
Figure 160: Force-displacement curves of the Nakazima dome tests for 3rd Gen 980 undergoing a) equi-biaxial stretch and b) plane strain tension and overlaying the experimental results against the simulations ran with 0.6 mm mesh size. No experimental Nakazima dome tests were performed for 3rd Gen 1180 V2. 161
Figure 161: Force-displacement curves of the Nakazima dome tests for 3rd Gen 1180 V1 undergoing a) equi-biaxial stretch and b) plane strain tension and overlaying the experimental results against the simulations ran with all mesh sizes. No experimental Nakazima dome tests were performed for 3rd Gen 1180 V2. 161
Figure 162: B-pillar forming simulations of a) 3rd Gen 980 and b) 3rd Gen 1180 V1 with 3 NIPs using equi-biaxial regularization factors showing the D-parameter for the upper integration point 163
Figure 163: B-pillar forming simulations of a) 3rd Gen 980 and b) 3rd Gen 1180 V1 with 11 NIPs using equi-biaxial regularization factors showing the D-parameter for the upper integration point 164
Figure 164: B-pillar forming simulations of a) 3rd Gen 980 and b) 3rd Gen 1180 V1 with 3 NIPs using plane strain regularization showing the D-parameter for the upper integration point.......166
Figure 165: B-pillar forming simulations of a) 3rd Gen 980 and b) 3rd Gen 1180 V1 with 11 NIPs using plane strain regularization showing the D-parameter for the upper integration point.......167
Figure 166: Model of the IIHS test cart highlighting the moving deformable barrier (MDB) (IIHS, 2020) 168
Figure 167: Crash simulation of the 3rd Gen 980 B-pillar where the impactor is centered at the fold initiators at approximately 150 mm crush distance 169
Figure 168: Crash simulation of the 3rd Gen 980 B-pillar where double impactors are used at approximately 150 mm crush distance...169
Figure 169: Top view schematic of the crash sled assembly with the B-pillar showing a) single and b) double impactor configurations indicating the direction of reaction forces. Not to scale. 171
Figure 170: Indicator of left and right offsets locations relative to the fold initiator 172

Figure 171: Deformation of the 3rd Gen 980 B-pillar using the a) left offset configuration and b) right offset configuration..173

List of Tables

Table 1: Mechanical properties of the 3rd Gen AHSS in TD obtained from JIS uniaxial tensile tests........36

Table 2: Parameters for plastic anisotropy and normalized stress in tension and shear with respect to uniaxial tension in RD........36

Table 3: Coefficients for the MHS model for the 3rd Gen 980 and 3rd Gen 1180 V1 and V2 38

Table 4: Calibration parameters for the rate-dependent hardening response using a reference strain rate of 0.001 s^{-1} 39

Table 5: Coefficients for the Yld2000 yield function where RD is the reference direction (Noder, 2021a)........41

Table 6: Coefficients for the calibrated Yoshida model to describe the chord modulus as a function of pre-strain (Noder, 2021a). 44

Table 7: Summary of friction coefficients of 3rd Gen 980 and 3rd Gen 1180 V1 under tension and compression 45

Table 8: Sample width and carrier blank (CB) material used for both Marciniak and Nakazima tests. (MS denotes mild steel, SS denotes stainless steel) 48

Table 9: Mechanical properties of steel used in the rigid tooling........84

Table 10: Weld parameters used for cross-tension tests specimens 112

Table 11: Test matrix for B-pillar crash testing........116

Table 12: Coefficients used to define the contact between metal interfaces used in the crash simulation 129

Table 13: Regularization factors for 3rd Gen 980 and 3rd Gen 1180 V1 utilizing plane strain (PS) and equibiaxial (EB) dome tests. Only equi-biaxial dome experiments for 3rd Gen 1180 V2…161

Hope does not disappoint for the love of God is poured into our hearts through the Holy Spirit who has been given to us

Romans 5:5

1. Introduction

Vehicle weight reduction is one of the primary strategies of automakers to meet the Corporate Average Fuel Economy (CAFE) requirements (CAFE, 2017). According to Tisaza and Czinge (2018) and as shown in Figure 1, the body-in-white (BIW) which is the frame of the car body, accounts for 55% of the total mass of the vehicle which is composed of approximately 55% steel. Among the steel grades shown in Figure 2, tensile strengths range from 270 MPa for mild steels used on body panels to structural steels for anti-intrusion such as 1500 MPa Ultra High Strength Steel (UHSS). The CAFE legislation in 2012 required passenger vehicles to increase in fuel economy from 39.6 – 40.1 to 55.3 – 56.2 mpg. These requirements were recently updated with a new ruling by the Environmental Protection Agency (EPA) and National Highway Traffic Safety Administration (NHSTA). The Safer Affordable Fuel-Efficient (SAFE) Vehicle Rules replaced the fuel economy for vehicles made in the years 2021 to 2026. Upon its amendment, cars must have a fuel economy of 46.3 mpg and 32.6 mpg for light trucks by 2022 and gradually improve its fuel efficiency to 47.8 mpg and 33.3 mpg, respectively, by 2026 (NHSTA, 2020). This demand on fuel economy has pushed the automotive industry to continue lightweighting of vehicles using three generations of advanced high-strength steels (AHSS) to form thinner gage parts while retaining or improving crash performance. Lightweighting is now being extended into electric vehicles (EV). The demand for EVs is projected only to increase such that more than half of new vehicles in the US will be electric within the next decade (World Auto Steel, 2021). AHSS can be integrated into cross members, rails, and pillars which can greatly enhance protection of the passenger and vital components of the EV such as the battery.

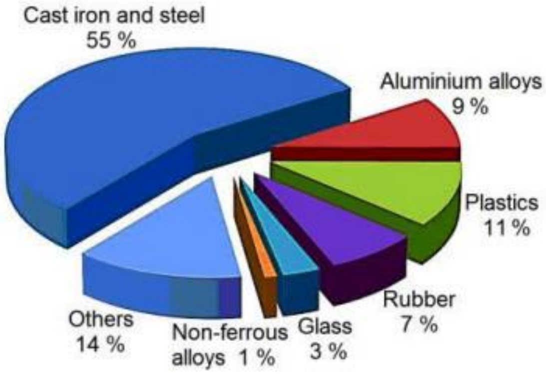

Figure 1: Composition of materials used in BIW (Hovuron *et al.*, 2017)

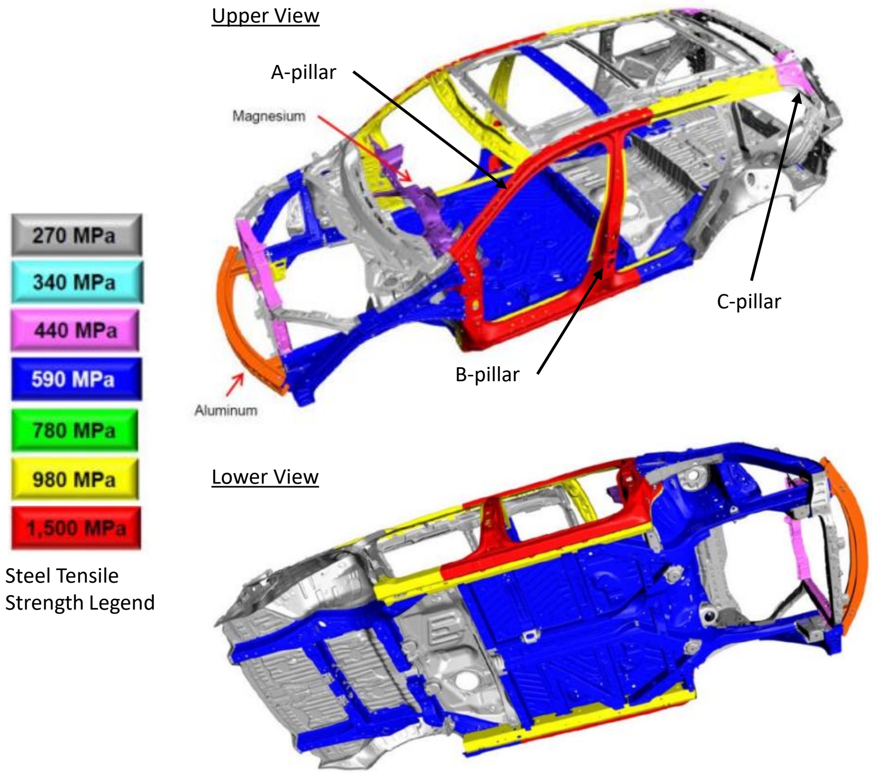

Figure 2: Body-in-white of the 2016 Honda Pilot and the various compositions of steel used in the BIW (American Honda Motor Co., 2016)

Mild steels were the common BIW material used until the 1990s but were largely replaced by high strength steels (HSS) and the first generation of AHSS, particularly dual-phase (DP) steels, during the 2000s. The microstructure of the 1st Gen AHSS utilized a ferrite matrix with a combination of microstructures such as martensite and bainite which provided strength and ductility or retained austenite to trigger transformation-induced plasticity (TRIP effect). The hardening response of the aforementioned steels can be seen in Figure 3. The trade-off is evident between formability and tensile strength which limited the applications of 1st Gen AHSS and led to the development of 2nd Gen AHSS (Billur and Altan, 2013).

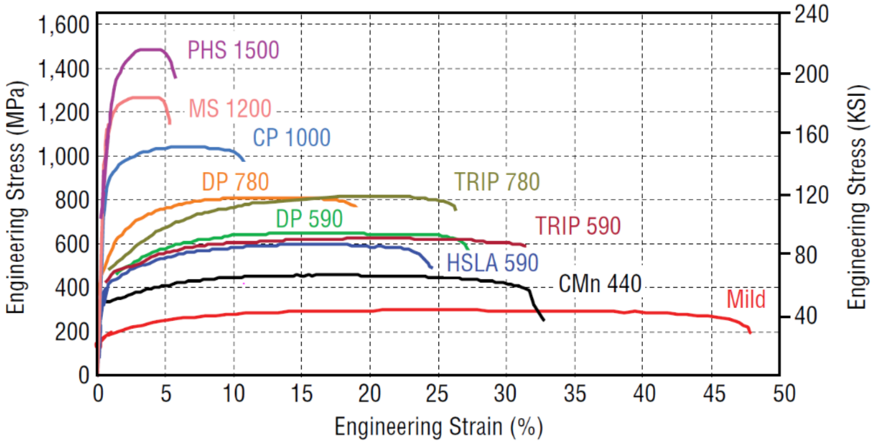

Figure 3: Engineering stress-strain curves of 1st Gen AHSS (Billur and Altan, 2013)

The main difference between the 1st and 2nd Gen AHSS is the replacement of a ferritic microstructure with an austenitic one. The 2nd Gen AHSS steels are typically alloyed with 12% to 30% manganese along with other elements such as silicon, aluminum, chromium, copper, nitrogen, niobium, titanium, and vanadium (De Cooman *et al*., 2018). The combination of the high alloying elements produces twinning-induced plasticity (TWIP) steels with significantly higher strength and ductility than the 1st Gen AHSS. For example, the formability is effectively doubled for the 2nd Gen TWIP980 steel compared to its 1st Gen AHSS counterpart of TRIP980 as seen in Figure 4. Despite the superior mechanical properties of the 2nd Gen AHSS, the significant alloy content increased cost and caused challenges with weldability and delayed cracking. To date, only a select few vehicles have integrated 2nd Gen AHSS into the BIW (Billur *et al*., 2014) where industry has slowly veered off from its usage.

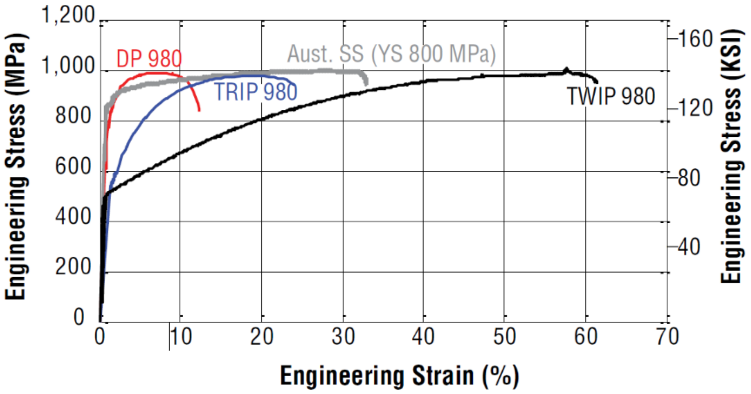

Figure 4: Engineering stress-strain curve comparing 2nd Gen AHSS with 1st Gen AHSS (Billur, Dykeman, and Altan, 2014)

The 3rd Gen AHSS represent a trade-off between the 1st and 2nd Gen AHSS which obtain their properties by deformation-induced phase transformations of retained austenite without the high alloy content of the 2nd Gen AHSS. The differences in strength and ductility between all three generations are seen in Figure 5. The ductility of a 3rd Gen AHSS that has a nominal strength of 980 MPa is comparable to a 590 MPa visualized in Figure 6. Formability and ductility of 3rd Gen AHSS is sufficiently improved to compete with hot stamping for some structural applications. There is increasing interest by automakers to expand their capabilities to produce 3rd Gen AHSS B-pillars with comparable strengths to hot stamping using existing infrastructure for conventional “cold stamping”. However, the design of the 3rd Gen AHSS tooling is complicated as the high strength leads to increased springback that must be accurately predicted in the virtual design phase. Springback is the elastic recovery of the sheet steel after forming. There is also uncertainty in the consumption of ductility in the forming operation as it may affect crash performance. Although not a focus of the present study, the press tonnages required for forming 3rd Gen AHSS can be prohibitively large for stamping on current production lines. The spot welding of 3rd Gen AHSS is also an active area of research due to the potential for liquid-metal-embrittlement (LME).

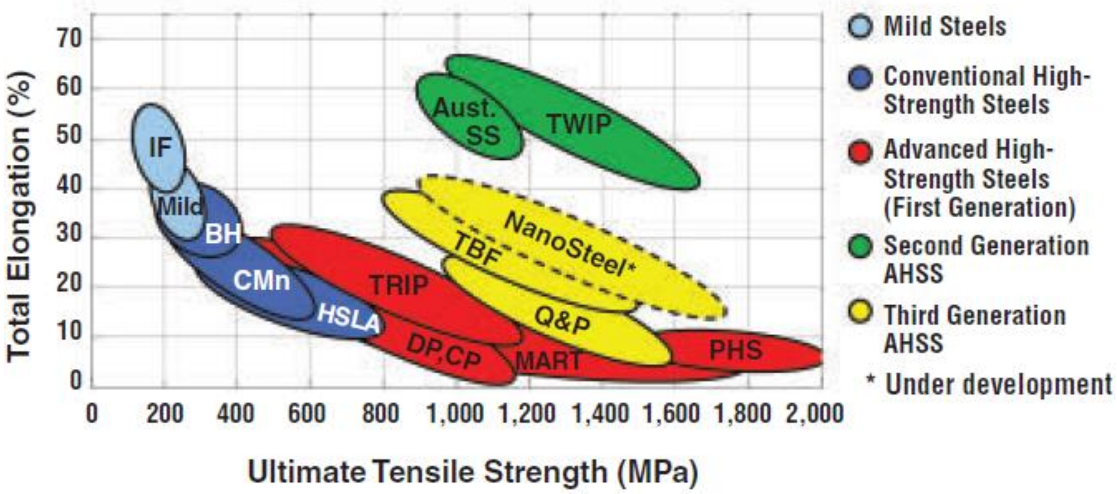

Figure 5: Comparison of tensile strength and total elongation of varying grades of steel (Billur and Altan, 2014)

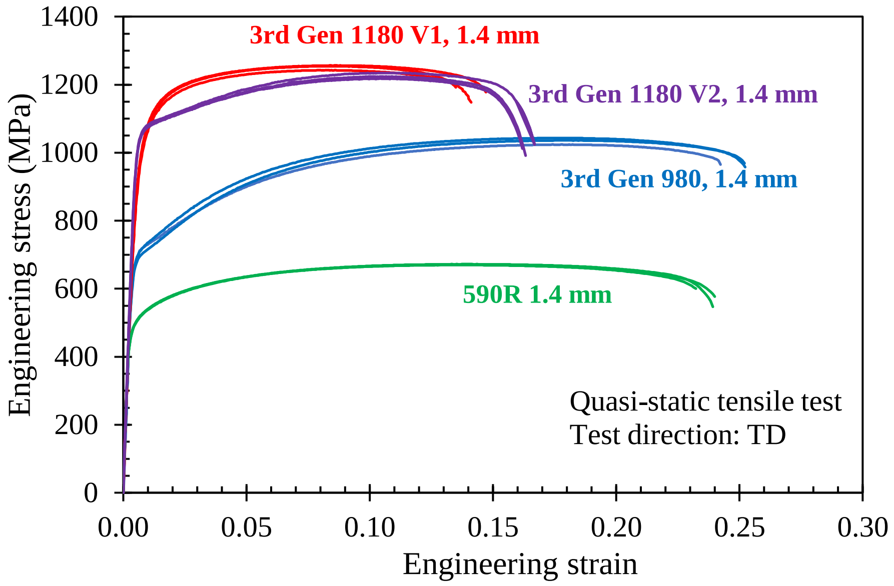

Figure 6: Comparison of 3rd Gen AHSS with strengths of 590 MPa, 980 MPa, and 1180 MPa (Noder *et al.*, 2021)

The focus of this thesis is on the forming and crashworthiness of industrially representative B-pillars using two 3rd Gen AHSS with nominal ultimate tensile strengths of 980 MPa and 1180 MPa. Springback is also investigated which is the geometry change in the part caused by the elastic recovery after forming. Over the past decade, B-pillars, visualized in Figure 7, have migrated from 1st Gen AHSS to ultra-high strength hot stamped steels. The hot stamping process enables the forming of complex B-pillar shapes with strengths up to 1500 MPa with minimal springback. Hot stamping of structural components has many advantages for lightweighting but is also relatively expensive in terms of the infrastructure and tooling required along with constraints upon the cycle time due to the solutionizing and quenching process. Secondary forming operations can also be challenging due to the high strength where laser trimming is required. The high carbon footprint and energy costs associated with hot stamping is also driving interest in pursuing cold stamped alternatives.

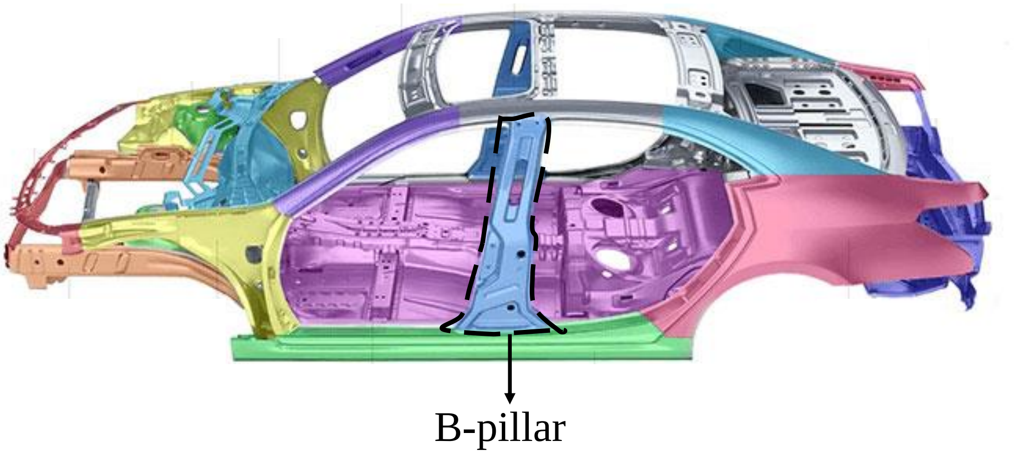

Figure 7: Body-in-white model of a passenger vehicle highlighting the B-pillar (Carbrain, 2021)

The development of the 3rd Gen AHSS and its potential for structural lightweighting is reviewed in the present chapter.

1.1 Microstructure & Mechanical Properties of 3rd Generation AHSS

The 3rd Gen AHSS are multi-phase steels that depend on the retained austenite to trigger the TRIP effect in a martensite or bainite matrix (World Auto Steel, 2020). Steel manufacturers may have their own specification on the chemistry of 3rd Gen AHSS achieving maximum strength and ductility levels though globally defined standards do not yet exist. Nominally, a 3rd Gen AHSS steel could have 1180 MPa as its ultimate tensile strength but have a vastly different chemistry and microstructure between suppliers. Among the commonly known 3rd Gen AHSS steels, the types of steel to be discussed are TRIP-assisted Bainitic Ferrite (TBF) grade and the Quenched and Partition (QP) grade. There is a strong reliance on the TRIP effect to achieve the required strength for these steels.

The microstructure of TRIP steel consists of a ferrite matrix with a combination of retained austenite, martensite, and bainite in various amounts. The retained austenite within TRIP steels transforms into martensite during forming that increases the hardening rate and delays the onset of necking. Refined methods of heat treatment and improved chemistry have led to the creation of a finer bainitic matrix along with secondary phases of ferrite retained austenite and martensite. In comparison to the conventional bainite matrix in 1st Gen TRIP steels, local formability has been improved due to the finer grain size and greater dislocation density of ferrite and the promotion of the TRIP effect from the retained austenite. The combination of the finer microstructure in a primarily bainite matrix has resulted in the name of TRIP Assisted Bainitic-Ferrite (TBF) steels (World Auto Steel, 2020).

TBF steels have already been implemented on some vehicle models. A TBF1180 was first used in the 2015 Nissan Murano where its A-pillars and reinforcements were downgauged from 1.6 mm to 1.2 mm in comparison to its previous model (Oakley, 2015). Similarly, 980 MPa steel in the A- and B-pillars of the 2016 Nissan Maxima were replaced by 1180TBF.

Quench and partitioned steel (Q&P) refers to the heat treatment process that generates microstructures with retained austenite stabilized by carbon partitioning originating from martensite (Speer *et al.*, 2015). The thermal cycle for the Q&P process is illustrated in Figure 8. After austenitization, the steel is quenched just below the temperature where martensite starts to form (1 → 2). It is then raised to a temperature just above the martensite transformation (2 → 3). The steel is then held at this temperature for an appropriate amount of time to achieve the desired microstructure phases (3 → 4) until it is quenched (4 → 5) to a temperature below martensite formation. The Q&P microstructure consists of martensite and austenite. The initial quench, around 200 to 350°C, creates a controlled amount of martensite. After increasing the temperature to the partitioning temperature of 300 to 500°C, the isothermal hold lets carbon diffuse from the carbon-supersaturated martensite into the austenite which enriches the austenite while consuming the martensite. Tempered martensite is also formed because the partitioning temperature is slightly above the required temperature for martensite formation.

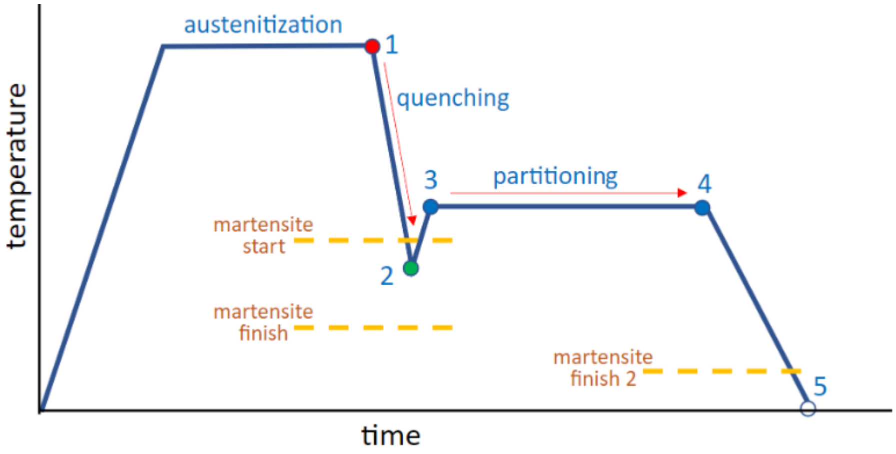

Figure 8: Thermal cycle for quenching and partitioning (World Auto Steel, 2020)

Currently, the two primary strength levels of 3rd Gen AHSS that are commercially available have strength levels of 980 MPa and 1180 MPa. Mechanical properties of QP steels show similarities with steels that are of approximately the same strength although with different microstructures. The superior formability of the Q&P980 compared to a DP980 is evident in Figure 9 that shows the forming limit strains corresponding to acute neck formation.

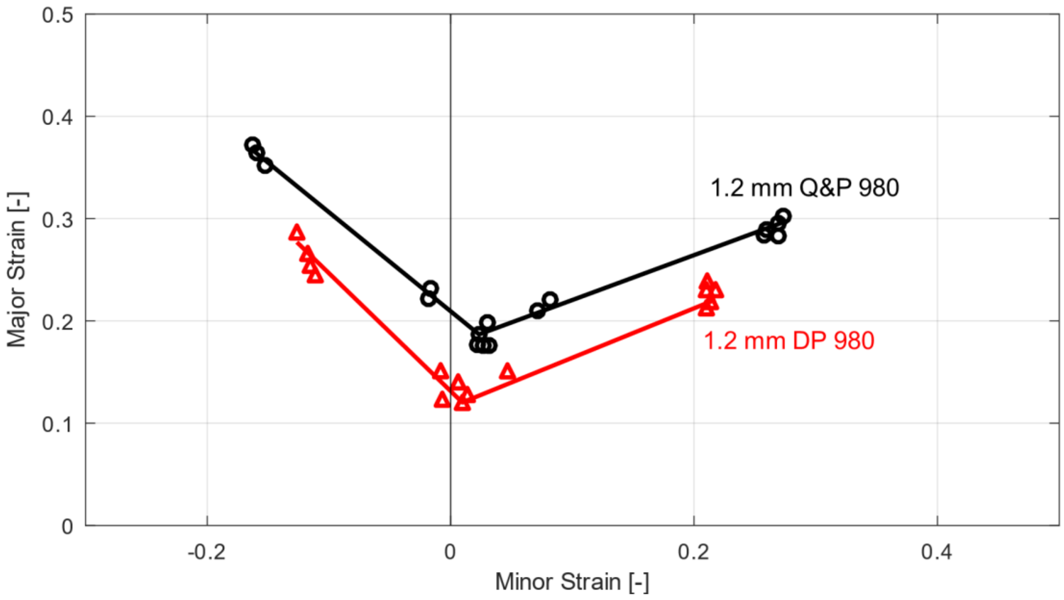

Figure 9: Forming limit curves of DP980 and Q&P980 (Chen *et al.*, 2017)

1.1.1 Forming Challenges with Lightweighting

The mass market production of vehicles is centered around conventional stamping lines using mechanical and hydraulic presses with low cycle times. Unlike in hot stamping where the quenching process dictates the strength, material substitution to a higher strength material of the same thickness still introduces challenges. Putting aside differences in formability, which typically decreases as strength increases, part distortion or springback will be markedly different and can require a significant redesign of the tooling. Mitigation of springback can be difficult and costly since springback compensation involves remodeling and re-machining the tooling. Studying the formability and springback of 3rd Gen AHSS is paramount to justify its feasibility within the assembly of the BIW. The press loads and energy requirements also increase which change the contact pressure consequently affecting metal flow and friction. An example of the change in press tonnage and springback associated with a change of an HSLA350 with a DP600 is shown in Figure 10 and Figure 11. The press tonnages required for 3rd Gen AHSS with 980 MPa and higher are a present concern for automakers and Tier 1 suppliers to be able to form these parts on existing stamping lines along with the higher wear on the presses.

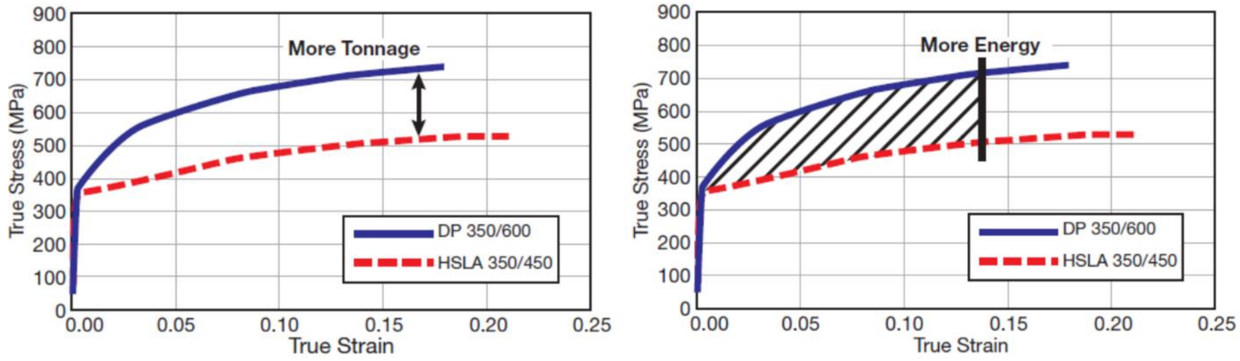

Figure 10: Comparison of tonnage and energy requirements between DP and HSLA (Keeler and Ulnitz, 2019)

DP 350 / 600 HSLA 350 / 450

Figure 11: Comparison of springback for DP steel and HSLA (World Auto Steel, 2019)

1.2 Formability

1.2.1 Global Formability

Formability of sheet steels has been traditionally described with the forming limit curve (FLC). The FLC is measure of the formability of sheet steel undergoing stress states from uniaxial tension to equi-biaxial stretching assuming in-plane stress. Significant advancements in the experimental characterization of the FLC have been made in the past 15 years due to optical strain measurement since its introduction by Keeler and Backofen (1963) and Goodwin (1968) in the 1960’s. The simplicity of the FLC has made it an attractive tool for industry to estimate the forming limits of a material undergoing stress states from uniaxial tension to equi-biaxial tension. These forming limits are obtained through Nakazima (Nakazima *et al.*, 1963) or Marciniak (Marciniak and Kuczynski, 1967) tests where a steel sheet is clamped then stretched by a hemispherical or cylindrical punch, respectively. These limiting dome height (LDH) tests, as they are generally called, are performed to measure the major and minor strains of the steel sheet as it is being stretched by the tool.

Global formability is quantified by the limit strains which indicate the onset of strain localization. As observed in tensile tests seen in Figure 12, the transition from diffuse to acute necking determines the limiting strains in a FLC as the instability in the material. Global formability is governed by the hardening rate of the material. In its simplest form, work hardening is represented by the Holloman power law

$$\sigma = K\varepsilon^{n} \tag{1}$$

where σ is the flow stress, K is the strength coefficient, ε is the equivalent plastic strain, and n is the hardening exponent.

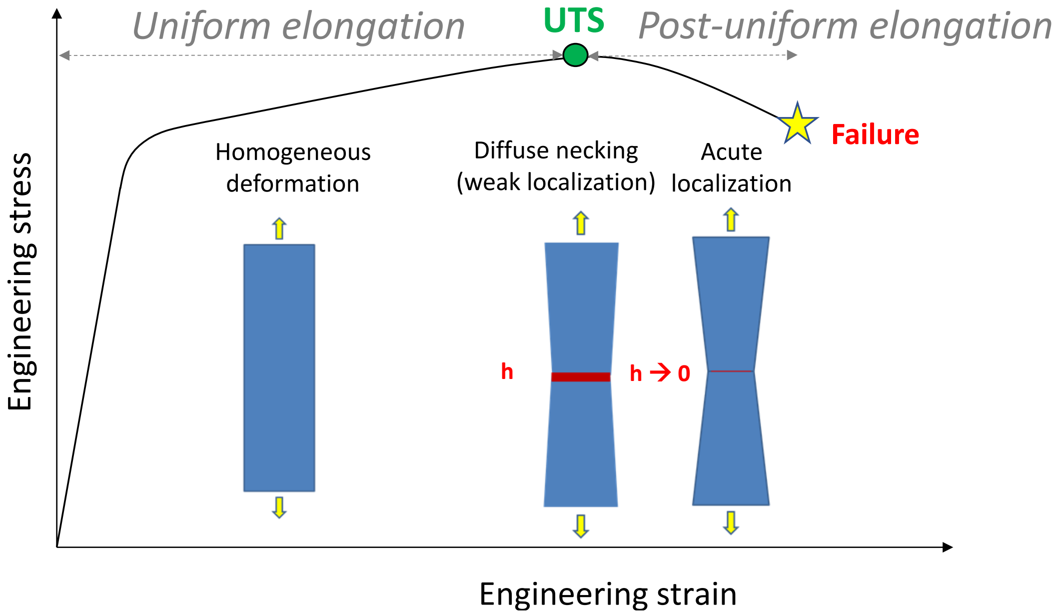

Figure 12: Visualization of diffuse necking in a tensile test with formation of a localization band of height *h* and its collapse to a plane during acute localization (Noder, 2021)

Mathematically, the hardening exponent is the key parameter in describing the instantaneous hardening rate of the material. The hardening rates of DP steels and HSLA typically stagnate at moderate to high strains whereas a gradually increasing n-value may be exhibited by TRIP steels seen in Figure 13. The higher the hardening exponent, the higher the forming limits as illustrated in Figure 13c for a comparison of TRIP, DP and HSLA steels from Konieczny (2003).

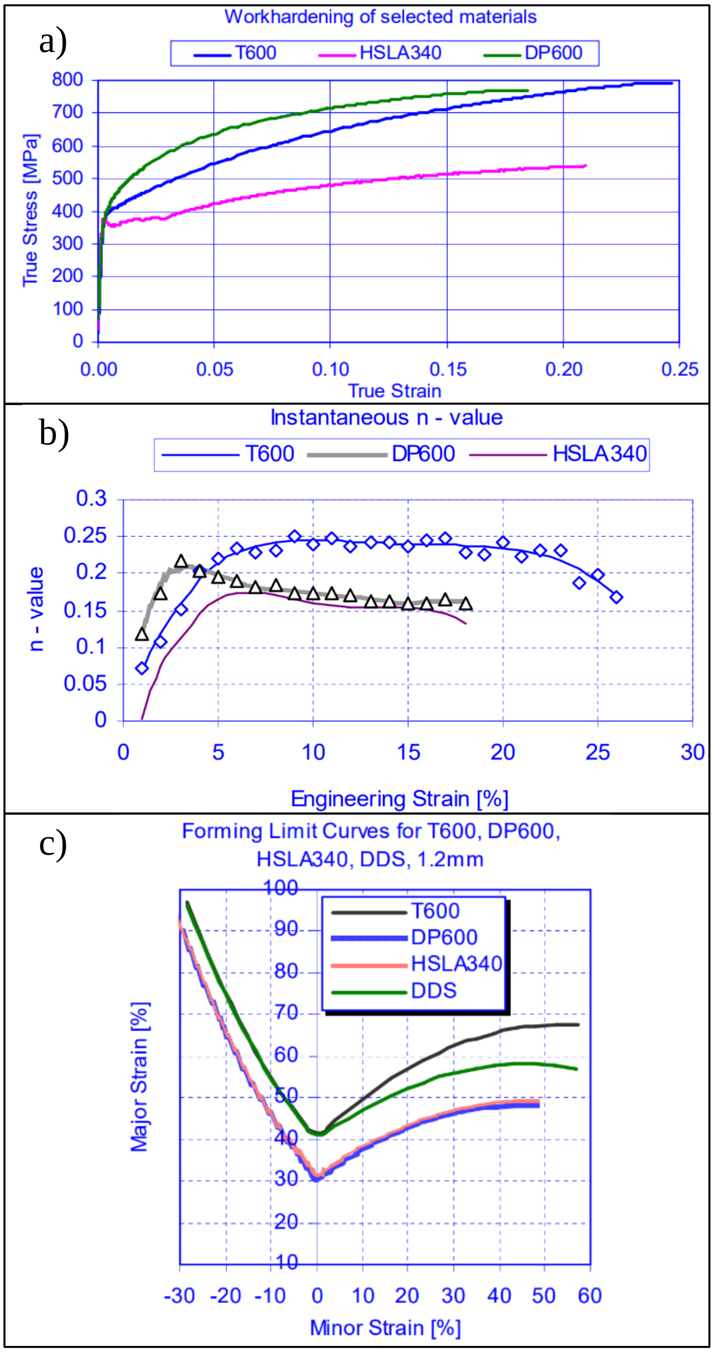

Figure 13: The (a) hardening curves for TRIP (T600), DP, and HSLA steels along with its (b) instantaneous n-values as a function of engineering strain and their (c) corresponding analytical FLCs for each steel (Konieczny, 2003)

The strong influence of the n-value is more noticeable in mathematical instability models such as Hill-Swift criterion as used by Paul (2021) and seen in Figure 14. According to Hill (1952), the plane strain point of the FLC, corresponding to $\varepsilon_2 = 0$, for a rate-independent material is equivalent to the n-value.

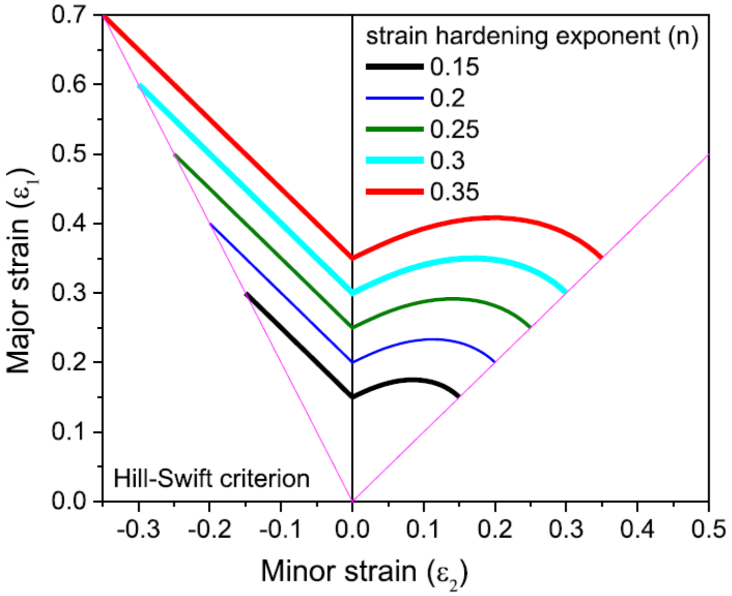

Figure 14: Hill-Swift criterion with varying n-values demonstrating the effect of changing n-value to the FLC (Paul, 2021)

1.2.2 Experimental Forming Limits

Nakazima limiting dome height and Marciniak tests, seen in Figure 15, are the two accepted methods for limit strain identification in ISO16330. The Marciniak test requires a carrier blank with a central hole that is placed between the punch and steel blank to promote in-plane stretching. Although the Marciniak test provides the ideal in-plane deformation without surface friction and contact pressure due to the carrier blank placement, it also introduces complexities. Selection of carrier blank material, thickness and central hole diameter often require experimental iteration to ensure that the failure location is within the expanded central hole and prevent fracture occurring at the edge of the punch as seen in Figure 16. Nakazima proposed the alternative hemispherical punch of 100 mm diameter which does not use a carrier blank but introduces non-linear strain paths, mild bending friction and contact pressure effects which all serve to increase the forming limits. Nonetheless, the FLC generated by either the Nakazima or Marciniak test is a powerful tool that is heavily utilized in industry that can accurately predict failure when used correctly.

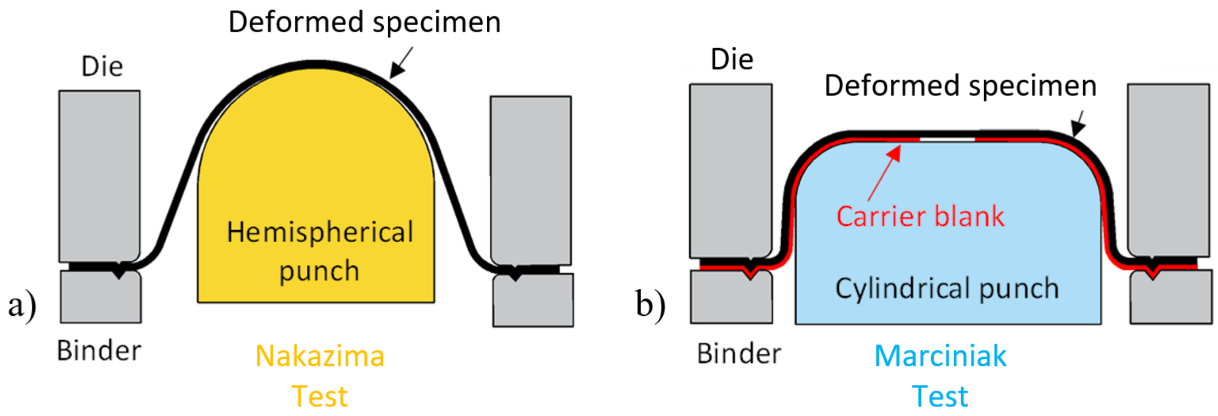

Figure 15: Schematic of the a) Nakazima test and b) Marciniak test (Noder, 2021)

Figure 16: Radius fracture that occurred in the Marciniak test for 3rd Gen 1180 V1

Since the 1960s, circle grid analysis (CGA) was used to measure the forming strains post-mortem but is now obsolete for FLC characterization. Utilization of digital image correlation (DIC) enables full-field strain measurement of the entire test at higher resolutions than CGA to track the strain history at the necking location. The use of DIC has allowed for the development of the ISO12004-2 standard of measuring limit strains and enabled the modelling of physically-motivated limit strain detection techniques such as methods by Volk and Hora (2011) and Min *et al.* (2016).

1.2.3 Analytical Forming Limits

Various instability models have been postulated to analytically predict the limiting strains. Among the instability models that have been proposed is the well-known MK model of Marciniak and Kucyznski (1967) and the modified maximum force criterion (MMFC) by Hora *et al.* (2013). Simpler models are also used such as Hill's (1952) zero-extension model which is equivalent to the maximum force criterion of Swift (1952) in plane strain tension. Coupling of different instability models have also been utilized to accommodate for the different behavior of steels in either the biaxial or uniaxial tension side of the FLC. Coupling of the Hill model for draw states and Swift's for biaxial stretching produced the so-called Hill-Swift criterion used by Paul (2021) and Alsos *et al.* (2008). Gutierrez *et al.* (2020) expanded upon the instability criterion based on the theory of Bressan and Williams (1982) of through thickness shear localization and the maximum normal stress criterion of Hance and Huang (2018). The so-called BWx model will be discussed in Chapter 3.

Although DIC and limit strain detection methods have experienced substantial growth in recent years, analytical formability models have arguably lagged behind and remain calibrated to test data inconsistent with the mechanics of the models. The MK-model and the MMFC model are commonly calibrated or evaluated with forming limits obtained from Nakazima FLCs. An inconsistency arises in this methodology of calibration since the analytical FLCs are based on the assumption of proportional in-plane stretching. Nakazima tests, due to the hemispherical shape of the tooling, induce out-of-plane deformation, tool contact pressure, and nonlinearity in the strain paths. The detailed analysis of Min *et al.* (2016) clearly showed that the Nakazima process effects have a non-trivial influence on the limit strains with a systemic bias towards increasing the FLC limit strains.

1.2.4 The Forming Limit Curve and its Dynamic Considerations

Prior to DIC, it was a common assumption that the strain paths in Nakazima tests were sufficiently linear with bending and contact pressure effects being marginal. Due to the limitations of CGA, a linear strain path assumption is required and the inherent variation in strain measurements of fracture specimens with a circle grid resolution of 1 to 2.5 mm was unable to sufficiently resolve differences in a Nakazima FLC compared to a Marciniak FLC. Nonlinearity in FLCs is now identifiable through DIC which is evident in the strain paths generated by Noder and Butcher (2019) in Figure 17.

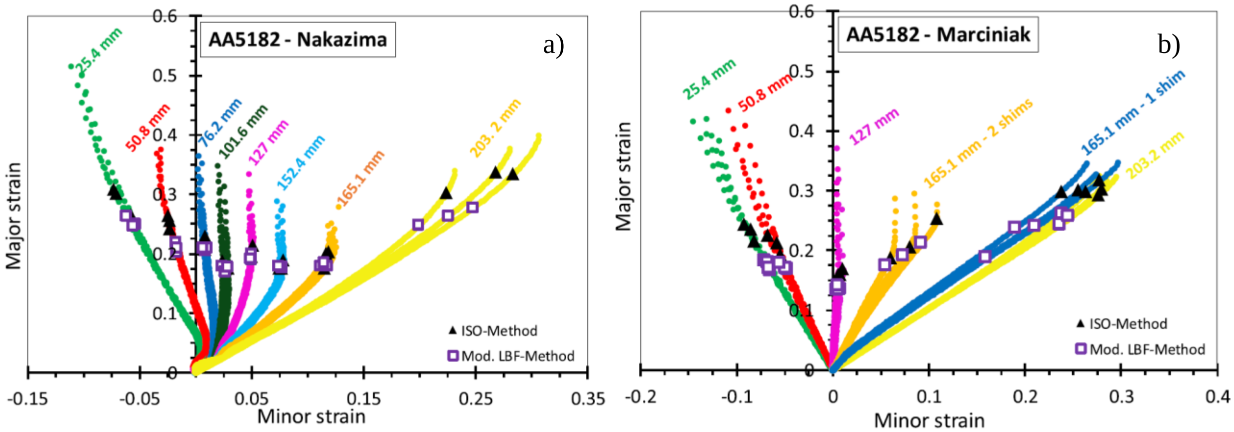

Figure 17: Strain paths and corresponding limiting strains for (a) Nakazima and (b) Marciniak tests for AA5182 highlighting nonlinearity (Noder and Butcher, 2019)

The assumption of in-plane proportional loading in Nakazima tests is inconsistent with the FLC framework as work done by Ghosh and Hecker (1974, 1975) confirmed that out-of-plane loading caused by hemispherical punch increases the forming limits. The correction methods of Min *et al.* (2016), highlighted in Figure 18, were able to revise the Nakazima limit strains for an MP980 steel to become similar to the Marciniak values. Noder and Butcher (2019) and Butcher *et al.* (2020) also reported that Min's corrections were successful for DP980 and DP1180 steels respectively. The influence of process corrections for 3rd Gen AHSS will be investigated in Chapter 3.

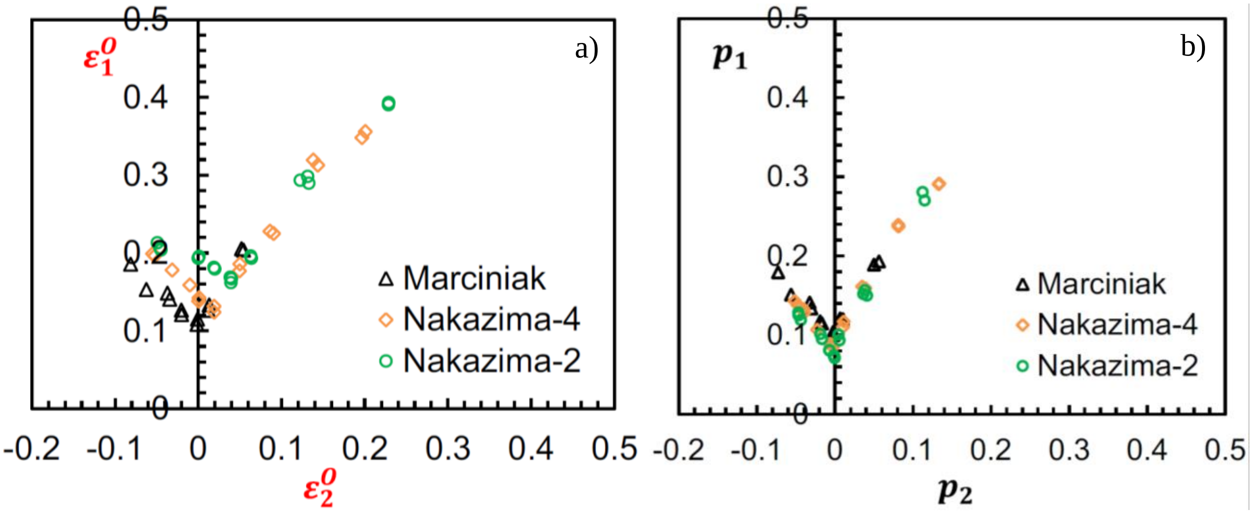

Figure 18: Uncorrected limiting strains (a) of Marciniak tests, and dome tests with 101.4 mm (Nakazima-4) punch diameter and 50.8 mm diamater (Nakazima-2) along with the (b) corrected limiting strains (Min *et al.*, 2016)

In addition to the process effects, another deformation mode that occurs in stamping operations that is not accounted by the conventional in-plane FLC is stretch-bending. Experimental studies done by Tharrett and Stoughton (2003) observed an increase in plane strain forming limits with a significant degree of bending. As will be shown in Chapter 4, limitations of the traditional FLC when correlations between simulations and forming trials of a 1180 MPa steel B-pillar were inconsistent at locations of approximate plane strain stretch-bending.

Although process effects can affect plasticity altering the FLC, some researchers have shown that nonlinearity can be exploited to improve formability. Graf and Hosford (1993) showed that pre-straining the sheet invariably affects the forming limit as seen in Figure 19. Similar work done by Ishigaki (1977) at Toyota Motors sought to exploit the dynamic nature of the forming limit via pre-straining. An improvement of formability was attained by reaching thinning strains up to 60% for a quarter panel that was formed in multiple stages that yielded a net minor strain of zero. Toyota engineers pre-strained the virgin metal sheet in uniaxial tension to take advantage of the evolved FLC, seen in Figure 20, to ensure a successful subsequent draw. This dynamic behavior of the FLC indicates that it is strain path dependent where the forming limits can change if the stamping process induces process effects on the part, which is the case for most automotive applications.

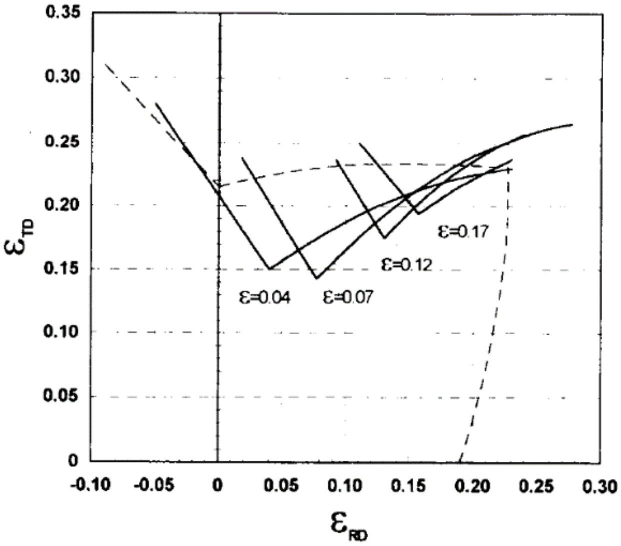

Figure 19: Evolution of FLCs after prestraining in equibiaxial tension. Four different prestrain levels are shown along with the FLC of the virgin material (Graf and Hosford, 1993)

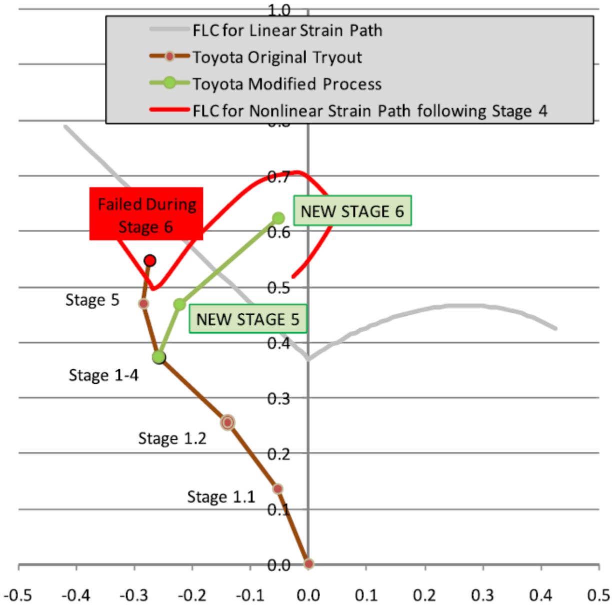

Figure 20: Evolution of FLC during prestraining indicating original draw stages and modified draw stage to exploit the dynamic behavior of nonlinear strain paths (Stoughton and Yoon, 2012)

Alternative methods have been proposed by numerous studies to remove path dependence on the FLC. Muschenborn and Sonne (1975) postulated a solution to account for nonlinearity by using plastic-work balance. Arrieux *et al.* (1982) proposed using a forming limit stress diagram (FLSD) where it was shown that the FLSD is path-independent for materials with isotropic hardening. Subsequent research by Stoughton and Yoon (2012) showed that the FLSD reported path independence by showing the transformed FLCs for a material pre-strained under proportional loading. The converted FLC to stress space from strain space showed that the FLCs were effectively superimposed on each other indicating a minimized dependence on the strain path as seen in Figure 21. A limitation of stress-based forming limit curves is their low resolution as the hardening rate of many automotive alloys is relatively low at the deformation levels related to the forming limits. As the hardening behavior is seldom known to high accuracy at large strains, subtle changes in the hardening model can produce significant changes in the forming limits. To take advantage of the reduced path dependence in a stress-based representation, the equivalent strain can be used as in the polar-EPS method later proposed by Stoughton and Yoon (2012).

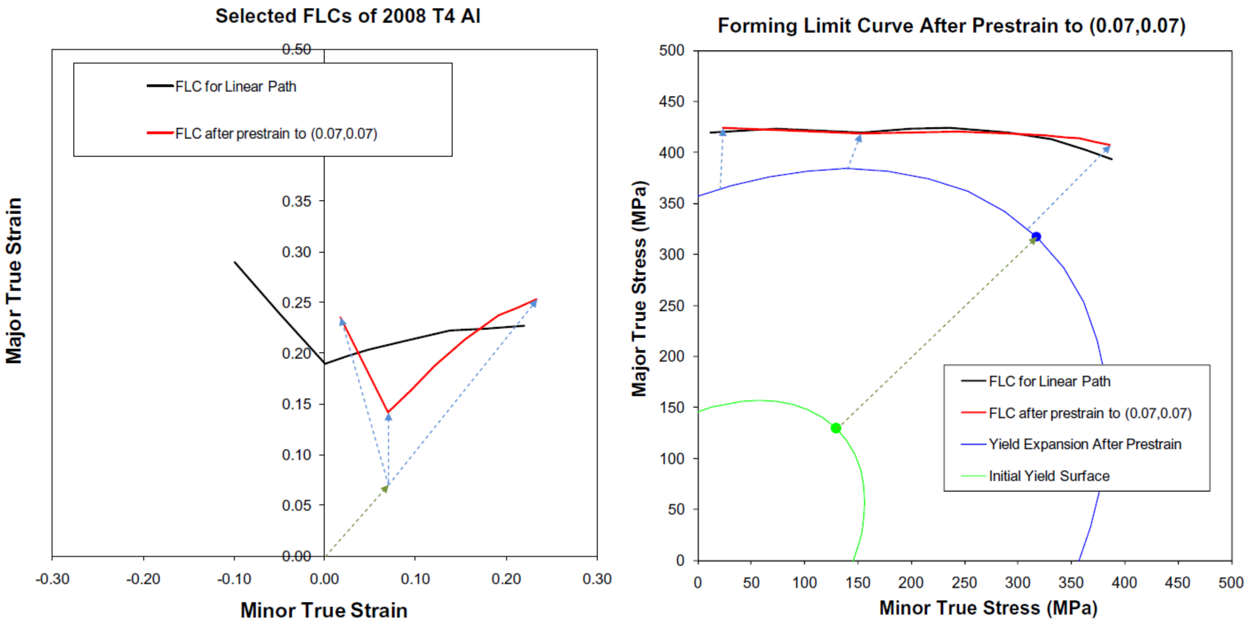

Figure 21: Conversion of a FLC in a) strain space to b) stress space indicating independence of load history (Stoughton and Yoon, 2012)

Although numerous tools and metrics have been developed for the FLC, experimentally and numerically, the dynamic nature of the forming limits due to bending, contact pressure and varying deformation modes remains an open challenge and often are not considered in tool design. The limitations of FLCs are well known within the automotive industry but the static interpretation remains prevalent. The experience of the tool designer is relied upon (for better or worse) to interpret the FLC and adjust safety margins.

1.3 Springback

1.3.1 The Bauschinger Effect and Elastic Modulus Degradation

Various characterization tests have been proposed to study springback to predict the final shape of stamped parts. Cylindrical bending (Meinders *et al.*, 2006), U-bending (Meinders *et al.*, 2006 & Chou and Hung, 1999), and V-bending (Han and Park, 1999, Tekiner, 2004 & Zhang *et al.*, 1997) are two common tests and are shown in Figure 22. These tests are attractive because springback can be readily measured by the angle change after forming. A disadvantage of these tests is that they are generally not representative of the forming conditions in stamping a practical part geometry.

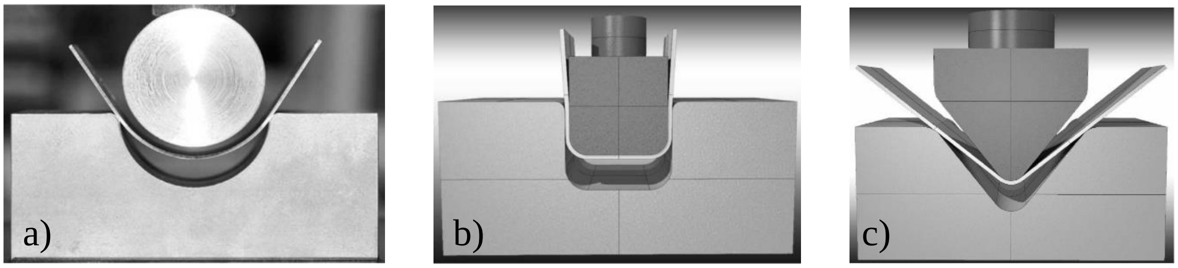

Figure 22: Illustration of the experimental apparatus for a) cylindrical bending b) U-bending and c) V-bending (Burchitz, 2005).

A stamped automotive part often experiences a gradient of stresses through the thickness caused by the geometry of the part, particularly at bending locations. Material flow into the die over radii and through drawbeads represents bending-unbending, activating complex hardening effects such as softening due to Bauschinger effects seen in Figure 23. From this bending and unbending, compressive stresses are induced on the inner layer of the sheet while tensile stresses occur on the outer layer which is visualized in Figure 24. The curvature created by the bending and unbending is referred to as the sidewall curl.

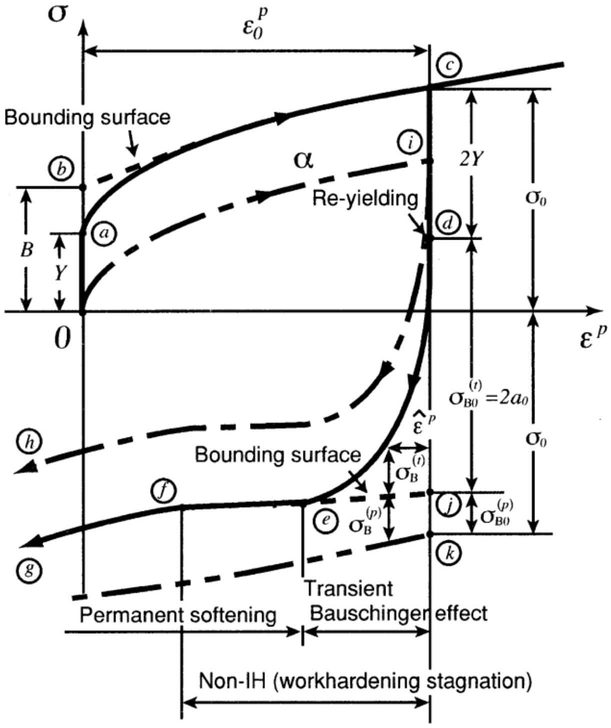

Figure 23: Illustration of a stress-strain curve under reverse loading highlighting its effects (Yoshida and Uemori, 2002)

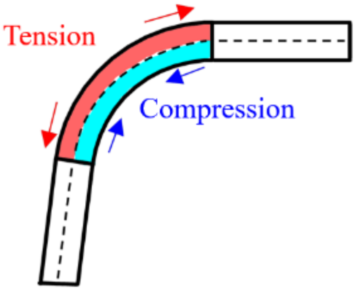

Figure 24: Directions of tensile and compressive stresses occurring in a bending operation

The sidewall curl is caused by the uneven stress distribution through the thickness of the sheet (World Auto Steel, 2019). Figure 25 describes the evolution of the stress and strain of the sheet for both the compression and tension side. Side *A* is initially under tensile loads (*A1*) during bending and undergoes compression (*A2*) in the unbending phase. Side *B* starts with compression loads (*B1*) then experiences tensile loads during unbending (*B2*). Upon removal of the punch, side *A* will be stretched and side *B* will be compressed. The gradient of stress through the thickness will cause springback due to elastic recovery. The level of elastic recovery is directly proportional to material strength so springback will always be higher for a 3rd Gen AHSS than a 1st Gen AHSS of the same strength because it will work harden to a higher strength during forming.

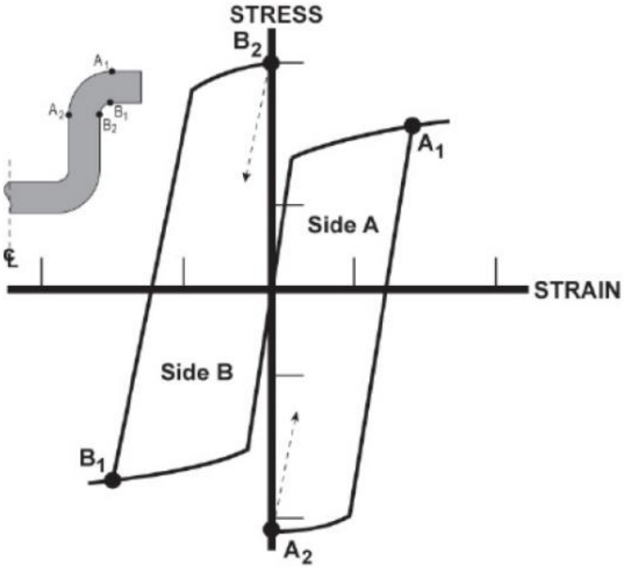

Figure 25: Stress-strain evolution of sidewall curl occurring at the tension and compression side of the sheet (WorldAutoSteel, 2019)

Ductile metals experience a well-known tendency to effectively soften during a load reversal whether it be compression to tension or vice versa. This mechanism in materials is called the Bauschinger effect, named after Johann Bauschinger, who first observed this mechanism in 1886 (Bauschinger, 1886). Baushinger effects include early re-yielding, cross-hardening, work-hardening stagnation and permanent softening and deeply tied to the microstructure and dislocation dynamics.

To describe the Bauschinger effect, it is paramount that the evolution of the yield surface is properly captured. It is commonly assumed in sheet metal forming that the yield surface evolves under isotropic hardening as shown in Figure 26. Isotropic hardening is a sound assumption if the deformation is undergoing proportional loading but fails to capture the decrease in strength in reversed loading. A kinematic hardening model, illustrated in Figure 27, where the yield surface can translate is able to describe the Baushinger effects with cyclic tension-compression tests performed to calibrate the hardening model.

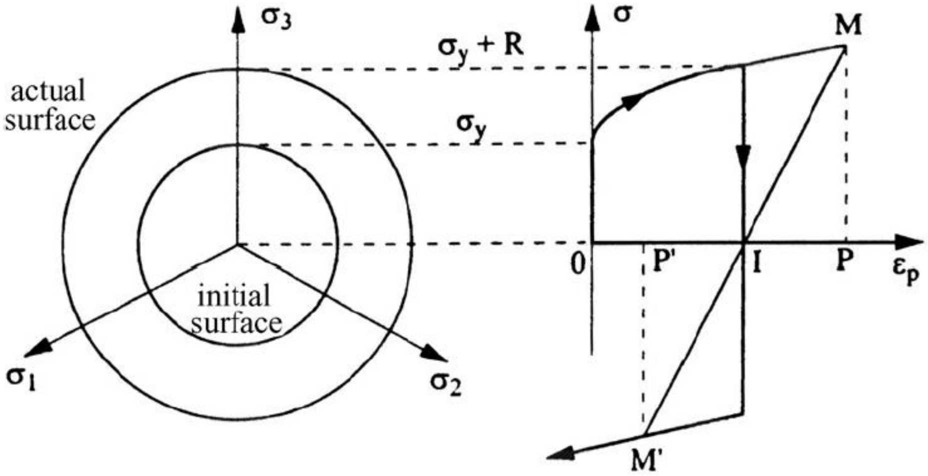

Figure 26: Visualization of isotropic hardening in 3D stress space (left) and its plastic strain response (right) for a tension compression cycle (Chaboche, 2008)

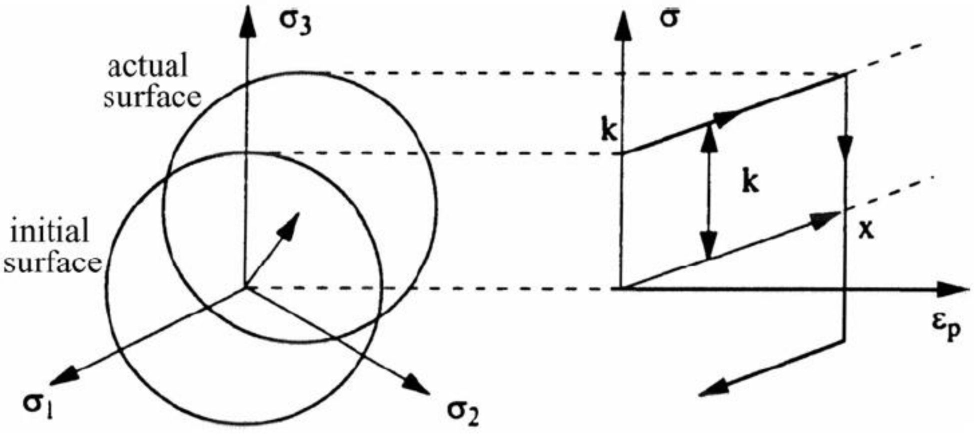

Figure 27: Visualization of kinematic hardening in 3D stress space (left) and its plastic strain response (right) for a tension compression cycle (Chaboche, 2008)

Degradation of the elastic moduli is a significant factor in springback prediction. Work done by Lems (1963) and Morestin and Boivin (1996) showed a decrease in elastic modulus with increasing plastic strain. It was later confirmed by Yoshida *et al.* (2002) and Eggersten and Mattiasson (2010) that during unloading and reverse loading that their paths are not linear. The so-called chord modulus represents the unloading modulus and its exponential degradation to a constant value with plastic strain is calibrated to cyclic data. This is visualized in the works of Lajarin *et al.* (2020) in Figure 28 showing the change in modulus after a certain amount of pre-strain during the unloading phase.

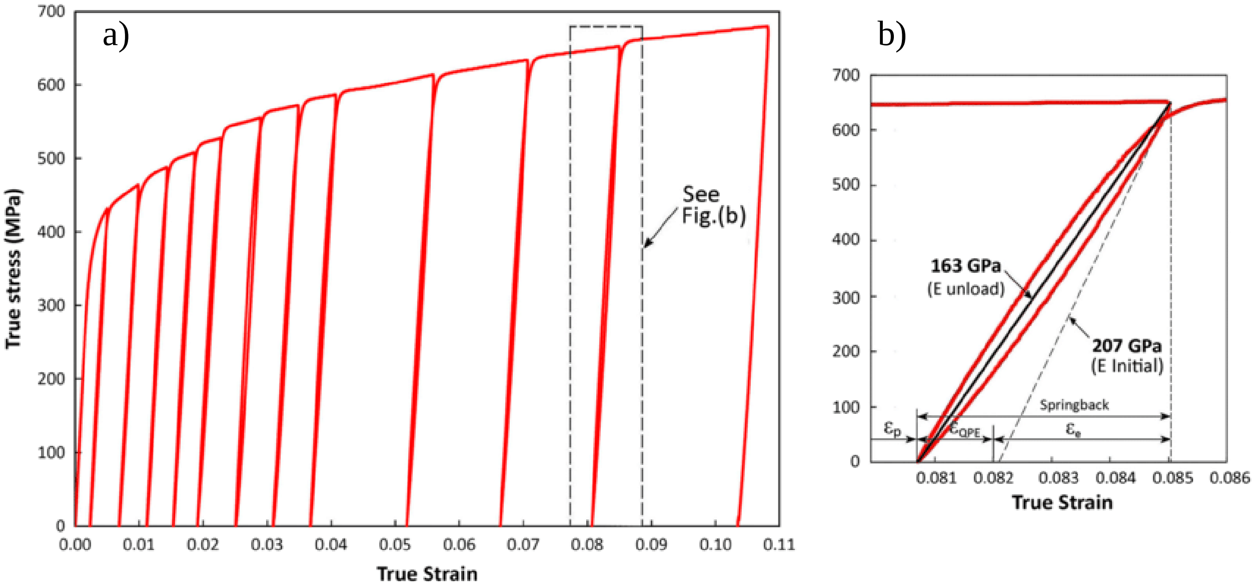

Figure 28: Loading and unloading cycles of DP600 steel a) under different prestrains and b) a zoomed in image of one cycle highlighting the chord modulus (Lajarin *et al.*, 2020)

To capture the behavior of nonlinear unloading in cyclic tests, Sun and Wagoner (2011) developed a two-surface model yield function that captures the quasi-elastic-plastic (QPE) characteristics of a DP980 steel. This QPE model can capture the recovery in elastic strain and energy dissipation exhibited in plastic strain. This QPE model was integrated in cyclic tension-compression tests in ABAQUS via user-generated material cards and accurately captured the stress-strain evolution illustrated in Figure 29. Academically, there are promising kinematic hardening models in the literature but their complexity, sensitivity to calibration parameters and their requirement of specialized test data remains a significant barrier for practical application.

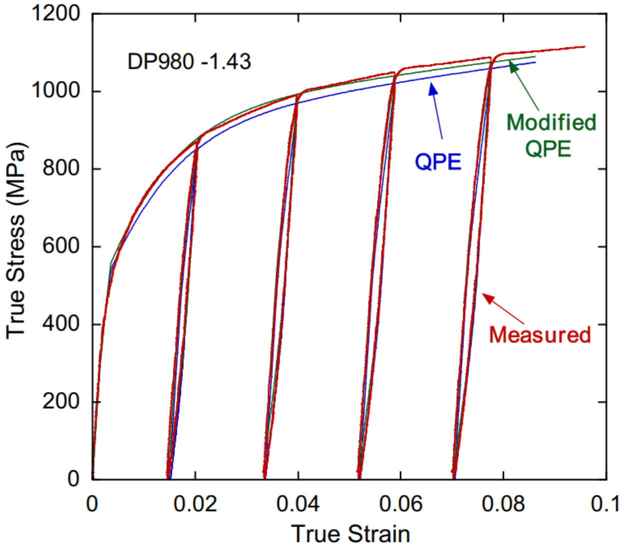

Figure 29: Comparison of stress-strain curve of cyclic tension-compression tests using the QPE model vs. the stress-strain curve obtained experimentally (Sun and Wagoner, 2011)

1.3.2 Numerical Analysis of Springback Operations

Prager (1956) proposed one of the first kinematic hardening models to describe softening during cyclic loading. Mroz (1967) investigated hysteresis loops and proposed a multi-surface plasticity model. The model of Armstrong and Frederick model (1966), later extended by Chaboche (1986), became widely used due to their relatively simple expressions for translation of the yield surface.

The modelling of complex hardening and springback prediction of AHSS is an active field of research with the multi-surface kinematic hardening model of Yoshida-Uemori (YU) (2001) gaining traction in the literature. Aryanpour (2011) simulated sidewall curl using the YU model with less than 8% error in modelling sidewall curl for channels of TRIP780 and DP980 steels. A similar study was conducted by Seo *et al.* (2018) where a similar implementation of the YU model was used to evaluate the springback of U-bending experiments of TRIP1180. It was found that with the use of the Barlat Yld2000 yield function combined with the Yoshida-Uemori model predicted the most representative shape when compared with the experiment. The use of isotropic hardening underpredicted springback for the U-channel as seen in Figure 30. The studies mentioned emphasize the proper characterization of a springback model. From the validation of these tests with the implementation of an appropriate hardening model, the experiments are accurately captured through the springback simulations.

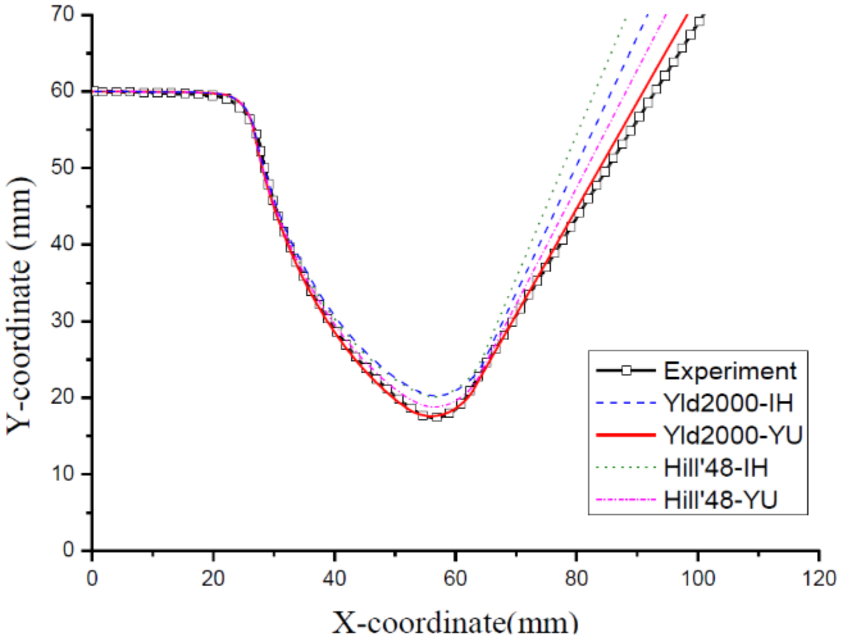

Figure 30: Comparison of shapes of U-bending tests between experiments and numerical predictions using varying yield functions and hardening models (Seo *et al.*, 2018)

A unique method to capturing kinematic hardening was proposed by Barlat *et al.* (2011) with the proposal of the homogenous anisotropic hardening (HAH). As opposed to the translation and expansion of the yield surface, the yield surface itself is distorted to capture the kinematic hardening of the material. The HAH model proved effective as simulations accurately captured the stress-strain history obtained from cyclically loaded simple shear experiments shown in Figure 31.

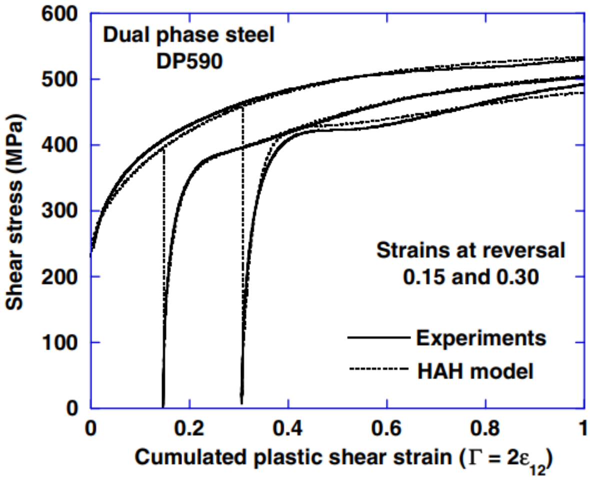

Figure 31: Stress-strain curve of cyclically loaded simple shear experiments obtained from experiments superimposed with simulation results using the HAH model (Barlat *et al.*, 2011)

1.4 Fracture Characterization

An appropriate fracture criterion is critical to predict the performance of AHSS structural components during a crash event. Before a material model can be accepted for use in full-vehicle simulations, component-level impact tests and simulations are used to correlate the force and energy responses. Modelling of parameters such as residual stresses and strains becomes imperative as the ductility of the AHSS has been consumed during the forming process. The further a material is work-hardened, its ductility is equivalently consumed consequently affecting its crashworthiness.

Mechanical damage models can be broadly categorized to either a micromechanical damage model or a continuum damage model. Micromechanical damage models attempt to mimic the ductile fracture process of void nucleation, growth, and coalescence and thus employ numerous sub-models to calibrate with microstructure information. Industrial crashworthiness simulations employ continuum damage models for computational efficiency and ease of calibration. Detailed microstructural analysis is not required to estimate damage parameters as the failure model is calibrated directly from coupon tests in different stress states. The so-called Generalized Incremental Stress-Strain Model (GISSMO) fracture criterion available in LS-DYNA software represents the current industrial standard for crash simulations. This failure criterion is stress-dependent that incrementally computes the damage parameter (*D*) denoted by the formula

$$dD = \frac{n}{\varepsilon_f(\eta, \xi)} D^{\frac{n-1}{n}} d\varepsilon_p \tag{2}$$

where ε_f denotes failure strain as a function of triaxiality, η, and lode parameter, ξ. The damage exponent is represented by *n* and $d\varepsilon_p$ is the change in plastic strain. The damage parameter begins at zero and accumulates according to Eq. 2. When the damage parameter reaches a value of unity, the corresponding element is deleted.

Calibration of GISSMO models in forming and crash simulations require a minimum of four tests to calibrate a proportional fracture locus in pure shear, uniaxial tension, plane strain tension, and equi-biaxial tension. From these tests, their equivalent plastic strains are plotted against their corresponding triaxiality seen in Figure 32. These points are then used to calibrate the fracture loci according to the selected model. A commonly used fracture locus that accounts for both lode angle and triaxiality is the Bai-Wierzbicki (2008) model

$$\hat{\varepsilon}_f(\eta, \xi) = \left[\frac{1}{2}\left(C_1 e^{-C_2\eta} + C_5 e^{-C_6\eta}\right) - C_5 e^{-C_4\eta}\right]\xi^2 + \frac{1}{2}\left(C_1 e^{-C_2\eta} + C_5 e^{-C_6\eta}\right) + C_3 e^{-C_4\eta} \tag{3}$$

where $C_{1\text{-}6}$ are calibration parameters identified from coupon tests that provide a range of unique stress states such as shear, uniaxial tension, plane strain tension and equal-biaxial stretching.

Fracture loci are typically calibrated using the fracture stress and strain data from simulations using a fine mesh of 0.5 mm and then regularized (scaled) to industrially relevant element sizes for crash of 3-7 mm. The failure strains decrease with element size as the larger element cannot as accurately resolve the deformation field (Eller *et al.* 2014). Mesh regularization consists of performing the coupon simulations with increasingly coarse elements to scale the failure loci as a function of element size. Although the process appears straightforward in theory, the regularization factors significantly depend upon not only the stress state but the deformation mode. A plane strain tension test (in-plane) that has necking will have a different regularization factor than a plane strain bending test. At present, there is no consensus for the regularization strategy which depends upon the intended application. The uniaxial tension and biaxial tension tests are common choices for scaling of the fracture locus.

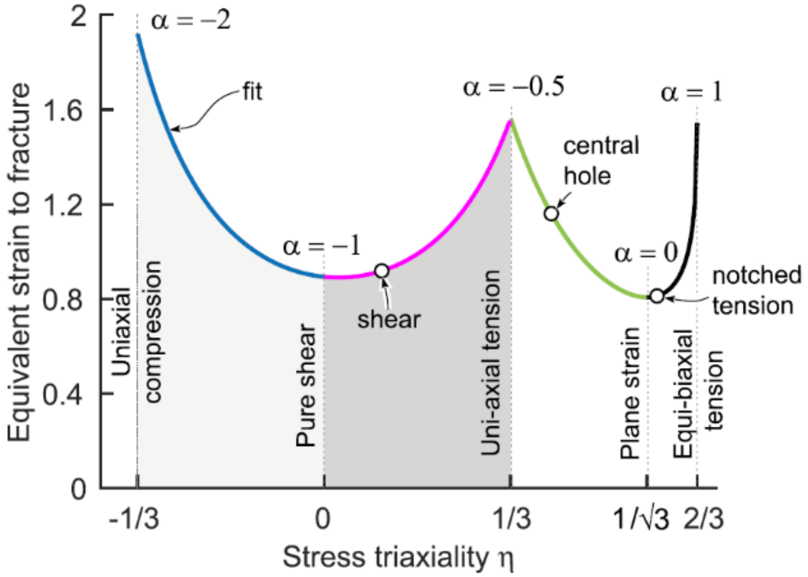

Figure 32: Example of a plane stress fracture locus for a structural steel from Kõrgesaar, (2019).

1.4.1 Crashworthiness and the Role of Forming Strain

Industrial crash simulations are commonly performed using the nominal sheet thickness and ideal geometry without accounting for residual strains, thinning or springback. The residual strains, thinning and accumulated damage from the forming operation may significantly alter the crash predictions but in many cases, the data is not available. The OEM crash engineer simulating a vehicle sub-assembly may not have the data from its suppliers, or they may have used different simulation software that is not readily compatible, or the forming simulations diverged from the as-formed tooling during tooling try-outs so that it is not current.

Huh *et al.* (2003) studied the effect of forming histories on crashworthiness of a front side member. It was observed that the peak force in the idealized model was 135 kN while accounting for the forming strains and thinning yielded a peak force of 165 kN as shown in Figure 33.

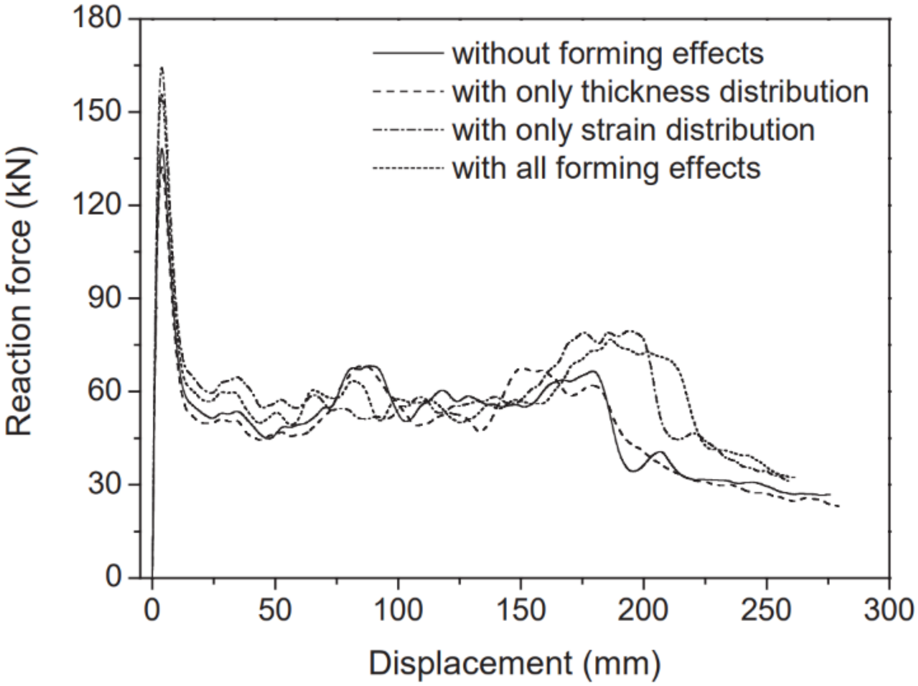

Figure 33: Reaction forces of the front side member by Huh *et al.* (2003) highlighting peak forces when considering forming effects

A similar study was conducted by Oliveira *et al.* (2006) on hydroformed aluminum s-rail components. The impact response of the 3.5 mm thick tubes with no forming history reported a peak force of 58 kN whereas 83 kN was the peak force with the forming history included. A similar trend was observed for 2.0 mm thick tubes as shown in Figure 34.

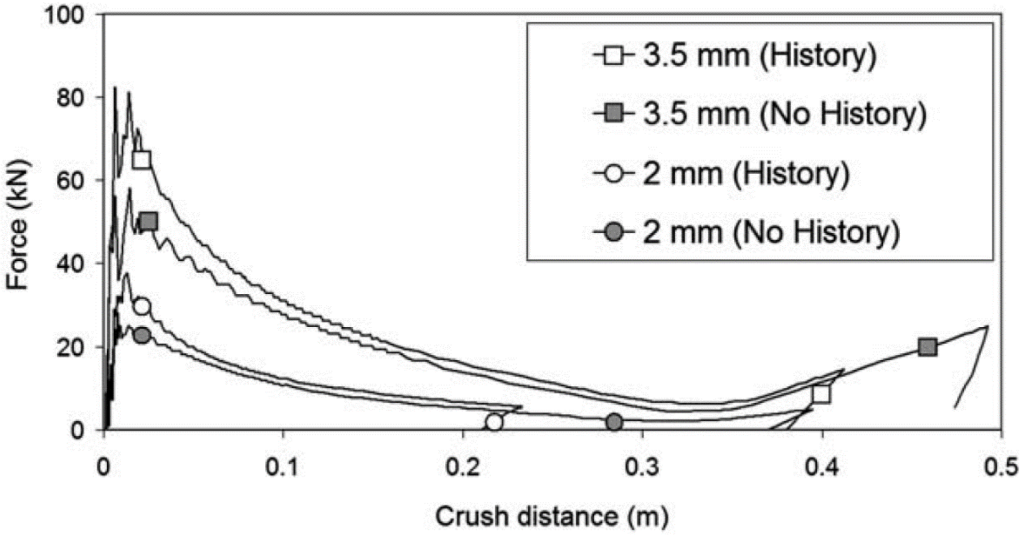

Figure 34: Reaction forces of s-rail tubes by Oliveira *et al.* (2006) highlighting peak forces when considering forming effects

Full BIW impact tests are ideal in that they mimic the true boundary conditions in a crash event but are also complex and expensive to undertake. Intermediate component-level impact tests are required to evaluate the plasticity and fracture models used in crash simulations. Representative geometries are used to mimic the parts used in vehicles to develop lab-scale “technology demonstrators” to evaluate characterization and modelling strategies. Component-level testing such as the three-point bend test, axial crush tests, and dynamic impact tests of the B-pillar provide a relatively inexpensive method of determining the crashworthiness of the structure and the material.

Axial crush tests used in frontal and rear impact tests are designed with a formable material to initiate folding in the structure to maximize energy absorption with a portion of the structure possessing a stiff, high strength end to prevent intrusion. An example of an axial crush test demonstrating folding can be seen from where Peister (2018) performed axial crush tests on Ductibor® 500-AS seen in Figure 35.

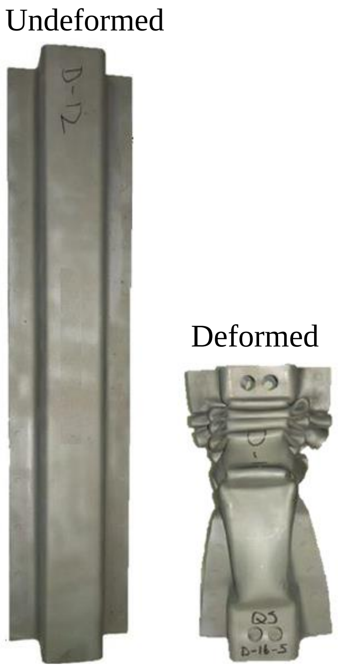

Figure 35: Images of undeformed and deformed axial crush tests of Ductibor® 500-AS (Peister, 2018)

Side impact tests evaluate the performance of the B-pillar in limiting intrusion into the cabin. The Insurance Institute for Highway Safety (IIHS) has established the Side Impact Crashworthiness Evaluation (SICE). It consists of a stationary vehicle being struck by a wheeled deformable barrier (also known as a buck) on the driver side at 90° with an impact velocity of 60 km/h (IIHS, 2020) as seen in Figure 36. Among the metrics recorded in the side impact test are dummy kinematics and contact locations, vehicle crush profile and compartment intrusion. The data recorded from these tests are used to evaluate the structural performance of the vehicle and the potential injury a passenger may receive from accidents due to side impacts.

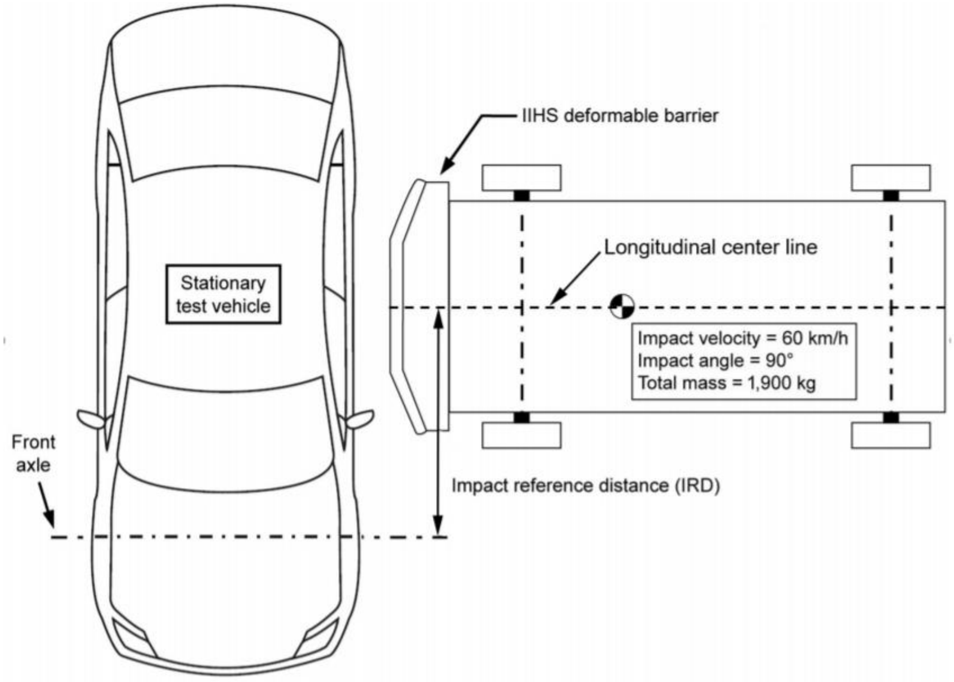

Figure 36: Alignment of deformable barrier with stationary vehicle from the SICE 60

Historically, fatality rates were found to be much higher before the implementation of crashworthiness evaluations such as the SICE. From Figure 37, the number of vehicles attaining "Good" IIHS side impact ratings have substantially increased throughout the decade. Such an example according to Teoh and Lund (2011) found that when a vehicle is struck at the driver side, drivers with vehicles that have a "Good" IIHS rating were 70% less likely to die in comparison to drivers who drove a vehicle with a "Poor" rating. Among the structures that are scrutinized to assess the rating of a vehicle are the A- and B-pillars of the vehicle as these are the primary structures that protect the passengers from side impacts.

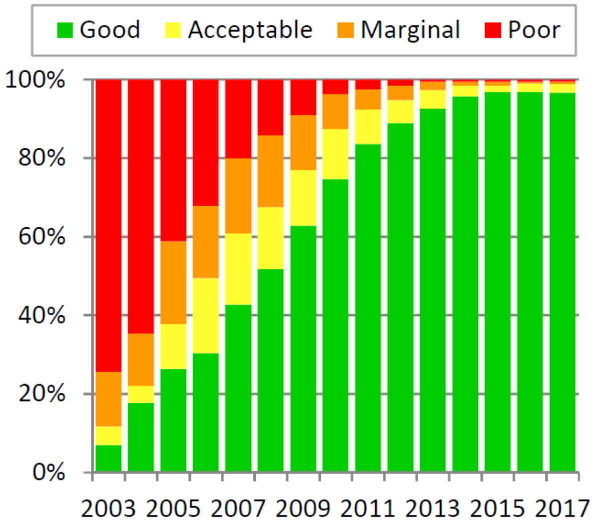

Figure 37: IIHS safety ratings by model year from 2003 to 2017 (Teoh and Lund, 2011)

The vehicle crush profile is quantified by comparing spatial coordinates of the B-pillar pre- and post-crush (IIHS, 2020). From the post-crush profile, the amount of passenger intrusion from the crash can be determined whether it is within acceptable ratings. Along with the crush profile, energy is generally measured along with the peak reaction force during the crash. High energy absorption by the structure leads to a safer design however an exorbitant amount of peak reaction force can result in a rejected design due to the forces from the deceleration being transferred to the passengers (Ibrahim, 2009).

Energy absorption varies considerably upon comparing frontal crash tests and side impact tests. In a frontal crash there is a relatively large amount of physical space along with the engine, between the occupants and the front bumper of the vehicle. Axial crush rails are designed to exploit folding mechanisms to absorb energy. In contrast to the axial crush rails, every millimeter of space is critical between the passenger and vehicle interior for side impact testing. The B-pillar is designed to channel vehicle intrusion towards the pelvic region. This design also serves to minimize injury since the pelvis area can receive more force than the abdominal region. Tested B-pillars from different vehicles are shown in Figure 38 (Hall, 2020).

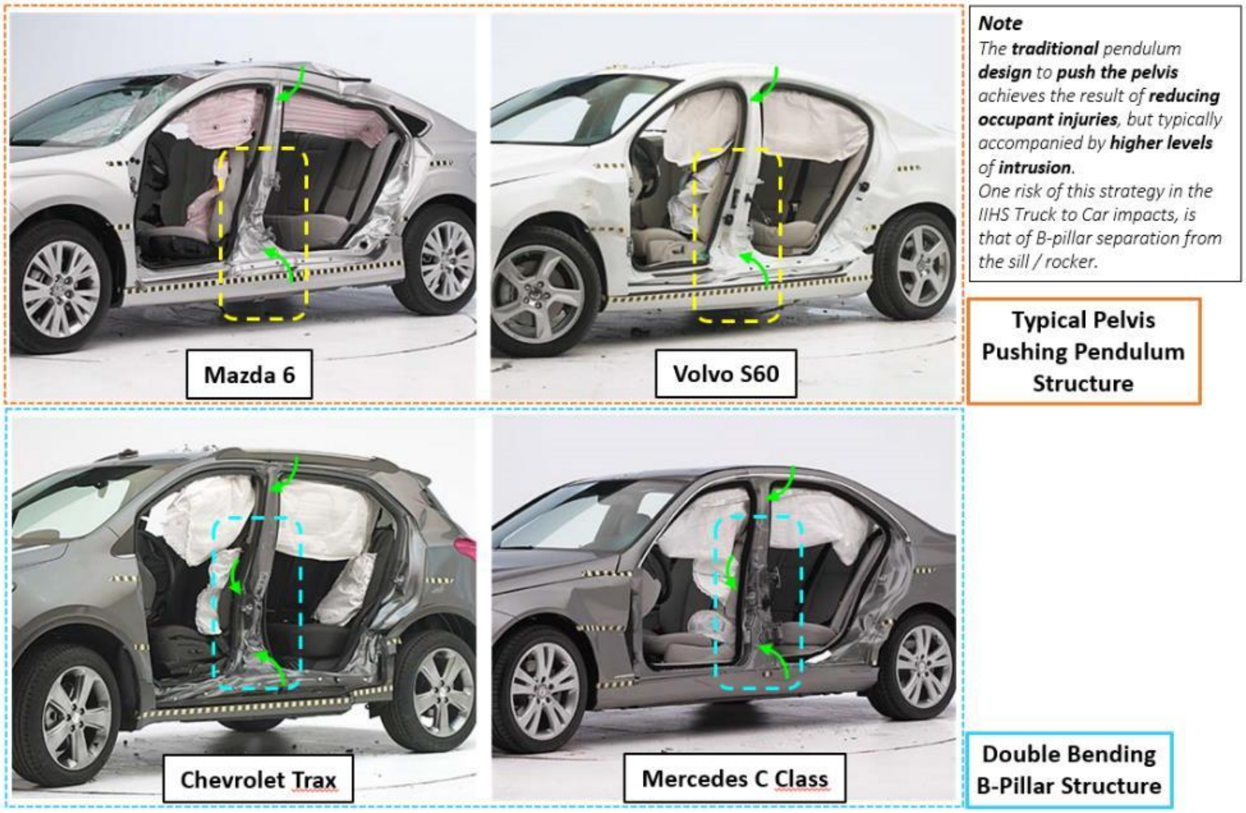

Note
*The **traditional** pendulum **design** to **push the pelvis** achieves the result of **reducing occupant injuries**, but typically accompanied by **higher levels** of **intrusion**.*
One risk of this strategy in the IIHS Truck to Car impacts, is that of B-pillar separation from the sill / rocker.

Figure 38: B-pillar structures highlighting push on the pelvis area (Hall, 2020)

1.5 Current Work

The state of the current literature has shown that the mechanical properties of 3rd Gen AHSS have significant potential for structural lightweighting. The primary theme of this thesis is to assess the formability and crashworthiness of two 3rd Gen AHSS of with a nominal tensile strength of 980 MPa and 1180 MPa. The structure formed is a full-sized B-pillar for a midsize SUV with the initial geometry provided by the project partner, HDMA. The steels, designated as 3rd Gen 980, 3rd Gen 1180 V1 and V2 with a nominal 1.4 mm thickness, were provided by steel member companies of the Automotive Program of the American Iron and Steel Institute (AISI) where the identity of the suppliers was kept blind to all parties involved in the project.

An additional 3rd Gen AHSS with a nominal strength of 1180 MPa is also considered which was provided later in the project to be compared with the first 3rd Gen 1180. To distinguish between them, the first lot will be called 3rd Gen 1180 V1 and the second lot is designated as 3rd Gen 1180 V2. The primary focus of the thesis is the study of the 3rd Gen 980 and 3rd Gen 1180 V1 where 3rd Gen 1180 V2 will be discussed as a comparison.

At present, there is a scarcity within the academic literature that correlates full-sized stamped components of 3rd Gen AHSS with finite-element simulations from forming-to-crash. The benefit of this study provides an extensive learning opportunity to evaluate and correlate experimental characterization techniques for constitutive, formability and fracture with a stamped and crashed B-pillar demonstrator. The constitutive model generated via tensile tests, cyclic tests, and high-rate tests, discussed in Chapter 2, are all utilized in the forming simulation and are then compared with the forming trials. Experimental FLC generation is performed with ISO12004-2 standard and is compared with analytical forming limits using a shear instability criterion all of which are discussed in Chapter 3.

The B-pillar tooling was designed and fabricated in collaboration with Bowman Precision Tooling based in Brantford, Ontario. The geometry of the B-pillar was altered from an initially hot stamped B-pillar design where production-related features were removed. This was done to allow the full-sized B-pillar to be used as a technology demonstrator suitable for public dissemination. The modified geometry was utilized for forming simulations performed with LS-DYNA and AutoForm R8. These simulations, discussed in Chapters 4 & 5, were then evaluated with the forming trials conducted at Bowman Precision Tooling to identify areas of splitting and excessive wrinkling. A similar investigation was conducted for springback, discussed in Chapter 6, validation to compare the predictive accuracy of the models with the stamped B-pillars. Ease of use and implementation of kinematic hardening within AutoForm R8 is made available and will be also assessed in the thesis to validate springback methodology.

Dynamic crash testing of the B-pillars on a custom test frame at Honda Development and Manufacturing America (HDMA) to accurately mimic the loading during a side impact was not feasible due to the impact of COVID-19 and a scaled-down version was developed for testing using the crash sled at the University of Waterloo. The results of the impact tests were then evaluated with the predictions using LS-DYNA that considered the influence of mapping the forming strain and damage. Impact testing is thoroughly discussed in Chapter 7.

2 Constitutive Characterization and Modelling of 3rd Gen AHSS

This chapter entails the constitutive characterization of the steels that will be used in the finite element modelling of forming, springback, and impact simulations in Chapters 4 to 7. The isotropic hardening behaviour of each material was determined using uniaxial simple shear tests using the methodology of Noder and Butcher (2019). High-rate tensile tests were also performed to include the forming simulations to account for the nonlinear motion of the press as well as the dynamic impact tests. The geometries used for tensile tests, simple shear, and high-rate tests are illustrated in Figure 39 and are discussed in greater detail in their respective sections. To describe the anisotropy of the material, calibration of the Yld2000 yield surface of Barlat *et al.* (2003) was used for LS-DYNA simulations. The most representative yield function within AutoForm R8 that best describes the anisotropy of the steel uses the Vegter yield function (Vegter and van den Boogaard, 2006). Lastly, to account for springback behavior, cyclic tension compression tests and interrupted tensile tests were used to quantify the Bauschinger effect and the chord moduli, respectively. The tensile and shear tests, yield surface calibration, and cyclic tension-compression tests were carried out by Dr. Jacqueline Noder, PhD. The high-rate testing was performed by Amir Zhumagulov, Research Associate. The formability characterization and modelling were performed by myself with collaboration from Dr. Noder for providing the MMFC analysis code.

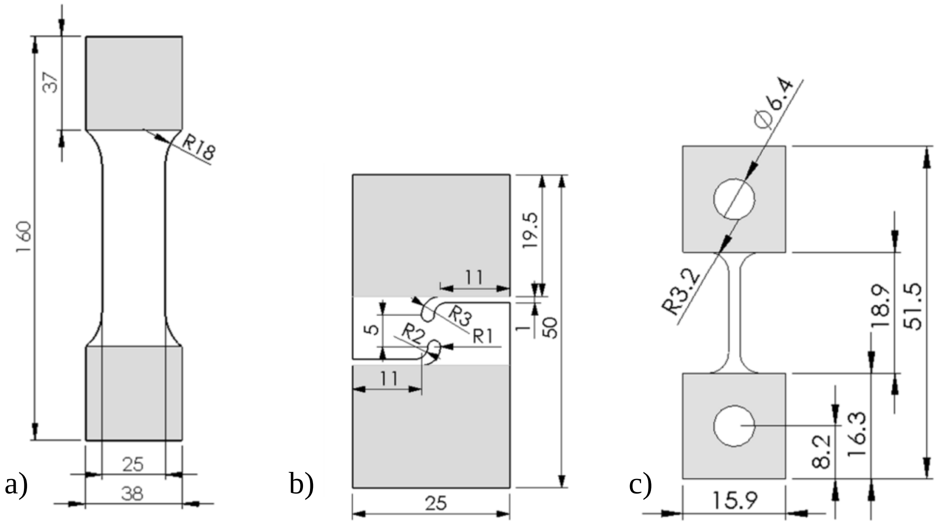

Figure 39: Geometries used to perform a) tensile tests, b) simple shear tests (Peirs *et al.*, 2012), and c) high-rate tests (Smerd *et al.*, 2005). All dimensions are in mm where darkened regions are areas that are clamped (Noder *et al.*, 2021a)

2.1 Anisotropy Characterization

Due to the AISI requirement for the steel suppliers of the specific grades on the project to be unknown to all members of the team, microstructure analysis of the steels was prohibited. A minimum of three samples were tested for each steel. The stark difference in the engineering stress-strain response between the 980 MPa and 1180 MPa grades is illustrated in Figure 40 where the uniform elongation of the 3rd Gen 980 is more than double than 3rd Gen 1180 V1. A moderate improvement is seen for 3rd Gen 1180 V2, which had a higher hardening rate translating to a slightly higher uniform and total elongation than the V1.

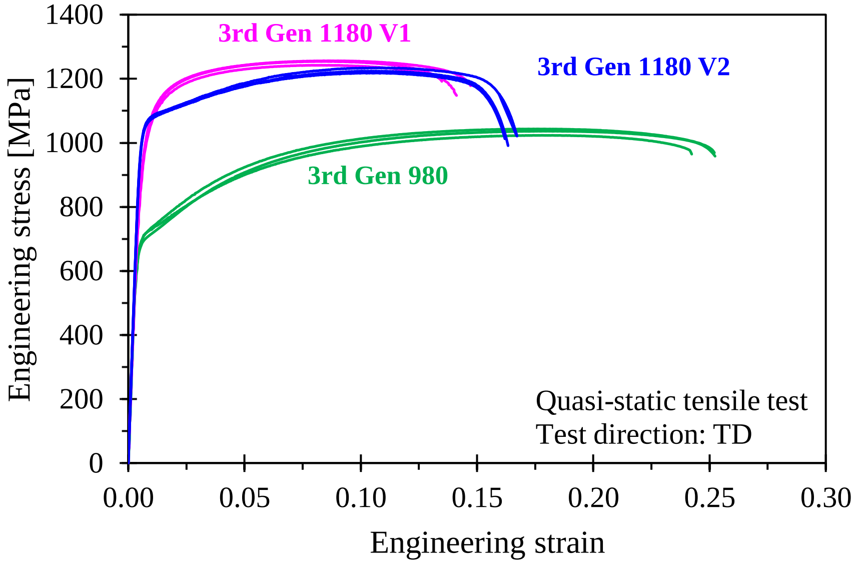

Figure 40: Engineering stress-strain responses of 3rd Gen AHSS tested in the transverse direction (TD) (Noder, 2021a)

All formability and fracture tests were performed with the major principal strain aligned with the transverse direction (TD). The TD is the limiting direction for all steels where the limit and fracture strains were lowest. The tensile mechanical properties were conducted in 22.5° increments with respect to the rolling direction (RD) obtained using the JIS No. 5 specimen geometry shown in Figure 39a are summarized in Table 1. The simple shear geometry of Peirs *et al.* (2012) in Figure 39b was employed with the samples extracted such that the principal stress directions were oriented in the RD and TD. Strain measurements were performed via DIC using Vic-3D® 7 software. The virtual strain gage length (VSGL) is used as a metric where the product of strain filter (pixels), image resolution (mm/pixel), and step size is calculated into an effective gage length where the strains are averaged. The VSGL of the shear tests was calculated to be 0.3 mm. Details on the methodology for DIC and validation for the shear experiments can be found in Rahmaan *et al.* (2017). The R-values and stress ratios are summarized in Table 2.

$$VSGL = strain\ filter\ \times step\ size\ \times resolution \tag{3}$$

Table 1: Mechanical properties of the 3rd Gen AHSS in TD obtained from JIS uniaxial tensile tests

Grade	**Nominal thickness [mm]**	**Yield Strength [MPa]**	**Ultimate Tensile Strength [MPa]**	**Uniform Elongation [%]**	**Total Elongation [%]**
3rd Gen 980	1.4	681(±8)	1034(±10)	18.0(±0.5)	24.9(±0.6)
3rd Gen 1180 V1	1.4	950(±12)	1251(±8)	8.4(±0.2)	14.1(±0.6)
3rd Gen 1180 V2	1.4	1043(±4)	1225(±8)	10.7(±0.4)	16.4(±0.3)

Table 2: Parameters for plastic anisotropy and normalized stress in tension and shear with respect to uniaxial tension in RD

3rd Gen 980	σ_0/σ_0	$\sigma_{22.5}/\sigma_0$	σ_{45}/σ_0	$\sigma_{67.5}/\sigma_0$	σ_{90}/σ_0	τ_0/σ_0
	1.000 (±0.013)	0.981 (±0.001)	0.971 (±0.006)	0.979 (±0.003)	0.998 (±0.008)	0.585
	R_0	$R_{22.5}$	R_{45}	$R_{67.5}$	R_{90}	R_B
	0.86 (±0.01)	0.86 (±0.01)	0.93 (±0.01)	0.91 (±0.01)	0.90 (±0.00)	1.00 (±0.05)
3rd Gen 1180 V1	σ_0/σ_0	$\sigma_{22.5}/\sigma_0$	σ_{45}/σ_0	$\sigma_{67.5}/\sigma_0$	σ_{90}/σ_0	τ_0/σ_0
	1.000 (±0.015)	0.996 (±0.010)	1.001 (±0.004)	1.010 (±0.007)	1.022 (±0.006)	0.618
	R_0	$R_{22.5}$	R_{45}	$R_{67.5}$	R_{90}	R_B
	0.76 (±0.01)	0.83 (±0.00)	0.93 (±0.00)	0.90 (±0.02)	0.90 (±0.01)	0.92 (±0.03)
3rd Gen 1180 V2	σ_0/σ_0	$\sigma_{22.5}/\sigma_0$	σ_{45}/σ_0	$\sigma_{67.5}/\sigma_0$	σ_{90}/σ_0	τ_0/σ_0
	1.000 (±0.015)	0.996 (±0.010)	1.001 (±0.004)	1.010 (±0.007)	1.022 (±0.006)	0.618
	R_0	$R_{22.5}$	R_{45}	$R_{67.5}$	R_{90}	R_B
	0.89 (±0.00)	0.91 (±0.00)	0.94 (±0.01)	0.93 (±0.00)	0.87 (±0.00)	0.92 (±0.00)

2.2 Calibration of Isotropic Hardening Response

The formability predictions of analytical models are strongly influenced by the selection and calibration of the hardening law, particularly in biaxial stretching where the necking strains can far exceed those of uniaxial tension. If data from tensile tests is solely relied on, the predictions on the limit strains depend on the unverified hardening response post-uniform elongation (Mohammadi *et al.*, 2014). Hydraulic bulge tests can achieve higher strains post-uniform elongation though require specialized equipment and meticulous DIC analysis specified by Min *et al.* (2016). Alternatively, simple shear tests provide a simple solution to obtaining the hardening response higher strain levels due to its compatibility to a universal test frame.

The coupling of tensile and simple shear data is used in this study to obtain the isotropic hardening both steels as outlined by Rahmaan *et al.* (2017) (see Figure 39a and b). This method uses the stress responses from the uniaxial and simple shear stresses and converts them into plastic work. The hardening response from the tensile test is used up until the initiation of diffuse necking while the shear stress ratio at the corresponding work level is used to convert the shear stress into an equivalent tensile stress. The equivalent plastic strain is then calculated from the plastic work. The hardening response of the coupled tensile and shear test is visualized in Figure 41. For clarity, the hardening response of 3rd Gen 1180 V2 is not plotted in Figure 41 as its behavior follows a very similar trend as 3rd Gen 1180 V1. The methodology of the tensile and shear test coupling was verified in a study performed in Gutierrez *et al.* (2020) where the model predictions of the global stress-strain response performed via simulation closely matched the tensile experiments.

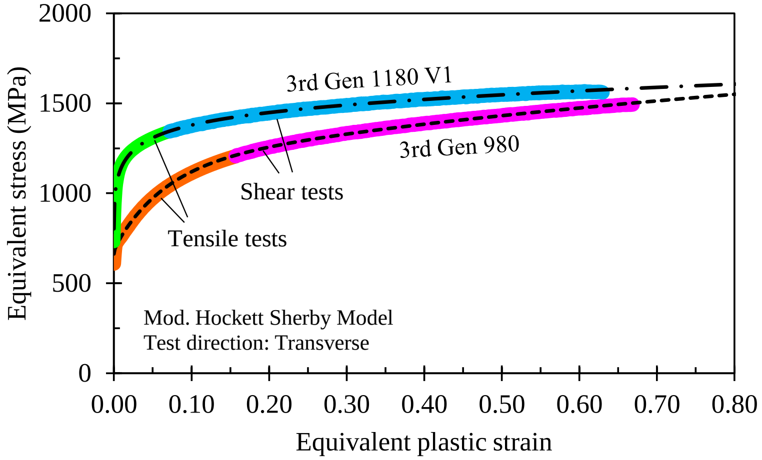

Figure 41: Hardening response of the calibrated MHS model superimposed with the tensile and converted shear data for both steels tested in TD (Noder, 2021a).

The study of Noder and Butcher (2019) emphasized the significance of imposing the Considère criterion upon the hardening model with respect to formability prediction. The hardening model must be constrained using the Considère criterion at the onset of diffuse necking for uniaxial tension where the hardening rate equals to the major principal stress such that

$$\frac{d\sigma_1}{d\varepsilon_1} = \sigma_1 \tag{4}$$

The hardening model is enforced with Eq. 4 at the experimentally measured plastic strain for uniform elongation.

The modified Hockett-Sherby model (MHS) of Noder and Butcher (2019) was selected and calibrated to the hardening data as shown in Figure 41. The MHS model is defined as

$$\bar{\sigma}^{MHS} = C_1 - (C_1 - C_2)\exp(-C_3\bar{\varepsilon}^{C_4}) + C_5\sqrt{\bar{\varepsilon}} \tag{5}$$

where $\bar{\sigma}$ represents the flow stress, $\bar{\varepsilon}$ is the equivalent plastic strain, and C_{1-5} are the parameters for calibration. These parameters were calibrated using a least squares method in MATLAB® utilizing its *fmincon* function. These values are tabulated in Table 3.

Table 3: Coefficients for the MHS model for the 3rd Gen 980 and 3rd Gen 1180 V1 and V2

	Modified Hockett-Sherby Model Parameters					
Grade	**C_1 [MPa]**	**C_2 [MPa]**	**C_3**	**C_4**	**C_5 [MPa]**	**Plastic Strain at Uniform Elongation**
3rd Gen 980	985.73	664.79	20.34	1.103	634.69	0.158
3rd Gen 1180 V1	1323.56	785.18	5.29	0.395	281.46	0.075
3rd Gen 1180 V2	1288.99	1063.62	28.40	1.260	355.90	0.093

2.3 Hardening Response at Elevated Strain Rates

The hardening response for the high-rate tests utilized the miniature dogbone specimen of Smerd *et al.* (2005) (see Figure 39c) with a gage length of 12.5 mm. The hydraulic intermediate strain rate (HISR) test frame was used to obtain nominal strain rates of 1 s^{-1} and 100 s^{-1} with test velocities of 125 mm/s and 1250 mm/s, respectively. A strain rate of approximately 1000 s^{-1} was obtained using the tensile split Hopkinson bar (TSHB). The strain-rate dependent hardening response of all steels are visualized in Figure 42. The quadratic Johnson-Cook model is used to describe the rate sensitivity of the 3rd Gen 980 and 3rd Gen 1180 V1 which is defined as

$$\sigma_f(\dot{\varepsilon}) = \sigma_f(\dot{\varepsilon}_{ref}) \left[1 + X \ln\left(\frac{\dot{\varepsilon}}{\dot{\varepsilon}_{ref}} \right) + Y \left(\ln\left(\frac{\dot{\varepsilon}}{\dot{\varepsilon}_{ref}} \right) \right)^2 \right] \tag{6}$$

where σ_f denotes the flow stress at the reference strain rate, $\dot{\varepsilon}_{ref}$, and X and Y are calibration parameters recorded in Table 4. The 3rd Gen 1180 V2 exhibited markedly reduced strain rate sensitivity as seen in Figure 42c. It was found that the Cowper-Symonds model provided a better fit to the test data than the Johnson-Cook for 3rd Gen 1180 V2. The Cowper-Symonds model is defined as

$$\bar{\sigma}(\dot{\varepsilon}) = \bar{\sigma}(\dot{\varepsilon}_{ref}) \left(1 + \left[\frac{1}{C} \ln\left(\frac{\dot{\varepsilon}}{\dot{\varepsilon}_{ref}} \right) \right]^{\frac{1}{p}} \right) \tag{7}$$

where C and p are calibration parameters. A summary of all calibration parameters is tabulated in Table 4.

Table 4: Calibration parameters for the rate-dependent hardening response using a reference strain rate of 0.001 s^{-1}

Model Parameters: Modified Johnson-Cook or Modified Cowper-Symonds				
Grade	***X***	***Y***	***C***	***p***
3rd Gen 980	3.38E-03	4.55E-04	-	-
3rd Gen 1180 V1	-5.00E-04	9.27E-04	-	-
3rd Gen 1180 V2	-	-	55.92	0.485

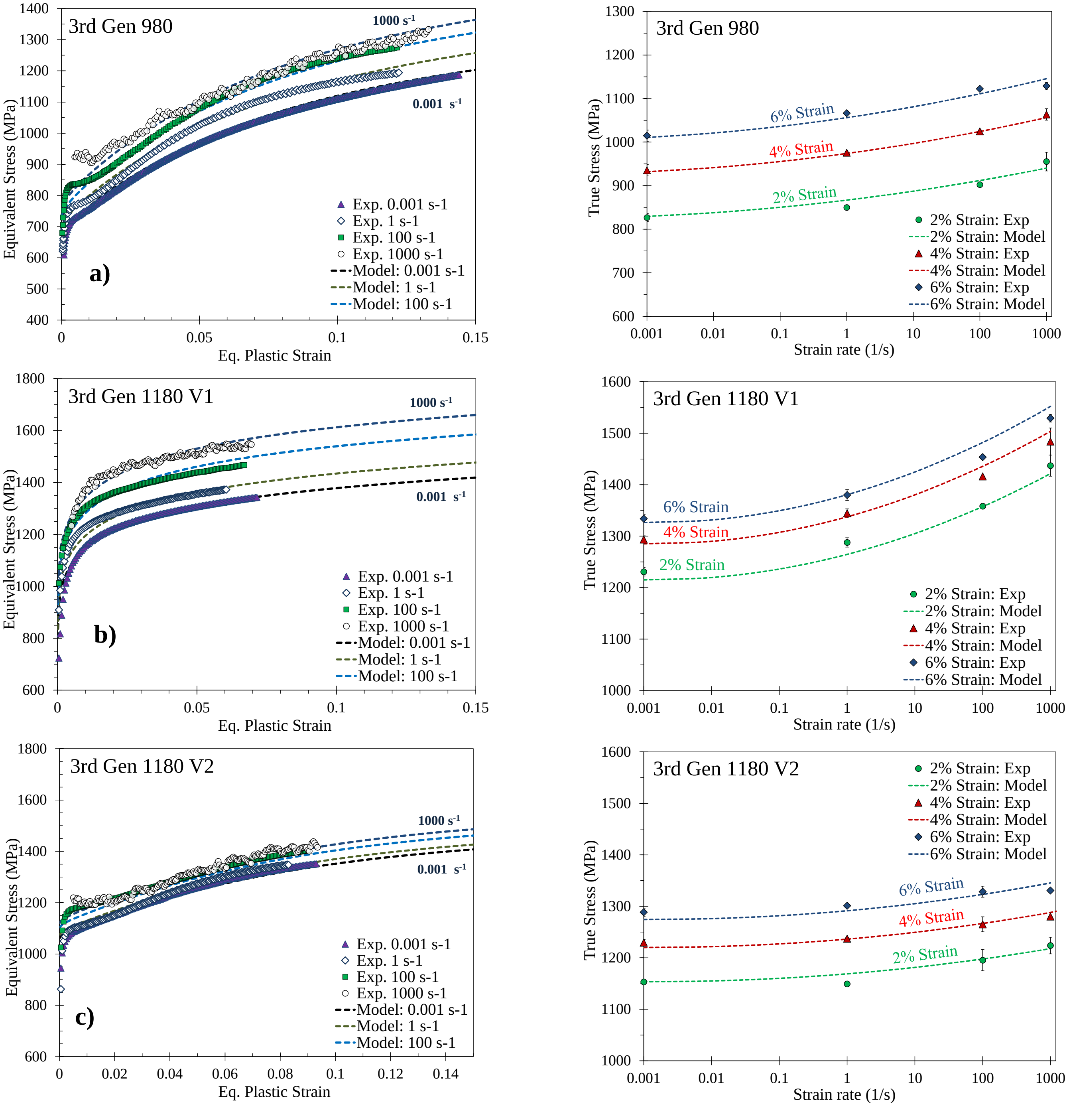

Figure 42: Dynamic hardening response and strain rate comparisons for a) 3rd Gen 980 and b) 3rd Gen 1180 V1 superimposed with the modified Johnson-Cook model and the c) 3rd Gen 1180 V2 superimposed with the Cowper-Symonds model

2.4 Yld2000 Anisotropic Yield Function

The Yld2000 anisotropic plane stress yield function of Barlat *et al*. (2003) was selected which contains eight calibration coefficients, $\boldsymbol{a_{1\text{-}8}}$, and a yield function exponent, m. An estimate for steels with a Body Centered Cubic (BCC) crystal structure for its yield exponent is 6. The equivalent stress given by the Yld2000 model is written as

$$\sigma_{eq}^{YLD2000} = \left(\frac{\left|X_1' - X_2'\right|^m + \left|2X_2'' + X_1''\right|^m + \left|2X_1'' + X_2''\right|^m}{2} \right)^{1/m} \tag{8}$$

where and are the principal deviatoric stresses from two linear transformations by $\boldsymbol{X}' = \mathbf{L}' : \boldsymbol{\sigma}$ and $\boldsymbol{X}'' = \mathbf{L}'' : \boldsymbol{\sigma}$. The coefficients are implemented within the fourth-order transformation tensors. The coefficients for the 3rd Gen steels are recorded in Table 5. For brevity of the full details on the derivation of the Yld2000 model, the reader is referred to Barlat *et al.* (2003).

Table 5: Coefficients for the Yld2000 yield function where RD is the reference direction (Noder, 2021a)

	Barlat Yld2000 Calibration Coefficients								
Grade	a_1	a_2	a_3	a_4	a_5	a_6	a_7	a_8	m
3rd Gen 980	0.970	1.005	1.000	1.007	1.011	0.992	1.015	1.077	6
3rd Gen 1180 V1	0.969	0.946	0.978	0.998	1.016	0.964	0.993	1.066	4.7
3rd Gen 1180 V2	0.995	0.987	0.976	1.004	1.009	1.015	1.004	1.037	5.6

The Yld2000 yield surface is compared with the isotropic von Mises yield surface in Figure 43a along with the tensile stress ratios and R-values illustrated in Figure 43b and c. For 3rd Gen 1180 V1, a better correlation was achieved with a lower yield exponent of 4.7 as it was shown by Kuwabara and Nakajima (2011) that a range of 4 – 6 for yield exponents provided results that are in better agreement for a DP980 steel. It is evident that while the Yld2000 model is over-constrained with more experiment data than parameters, it can accurately predict the anisotropy for both steels.

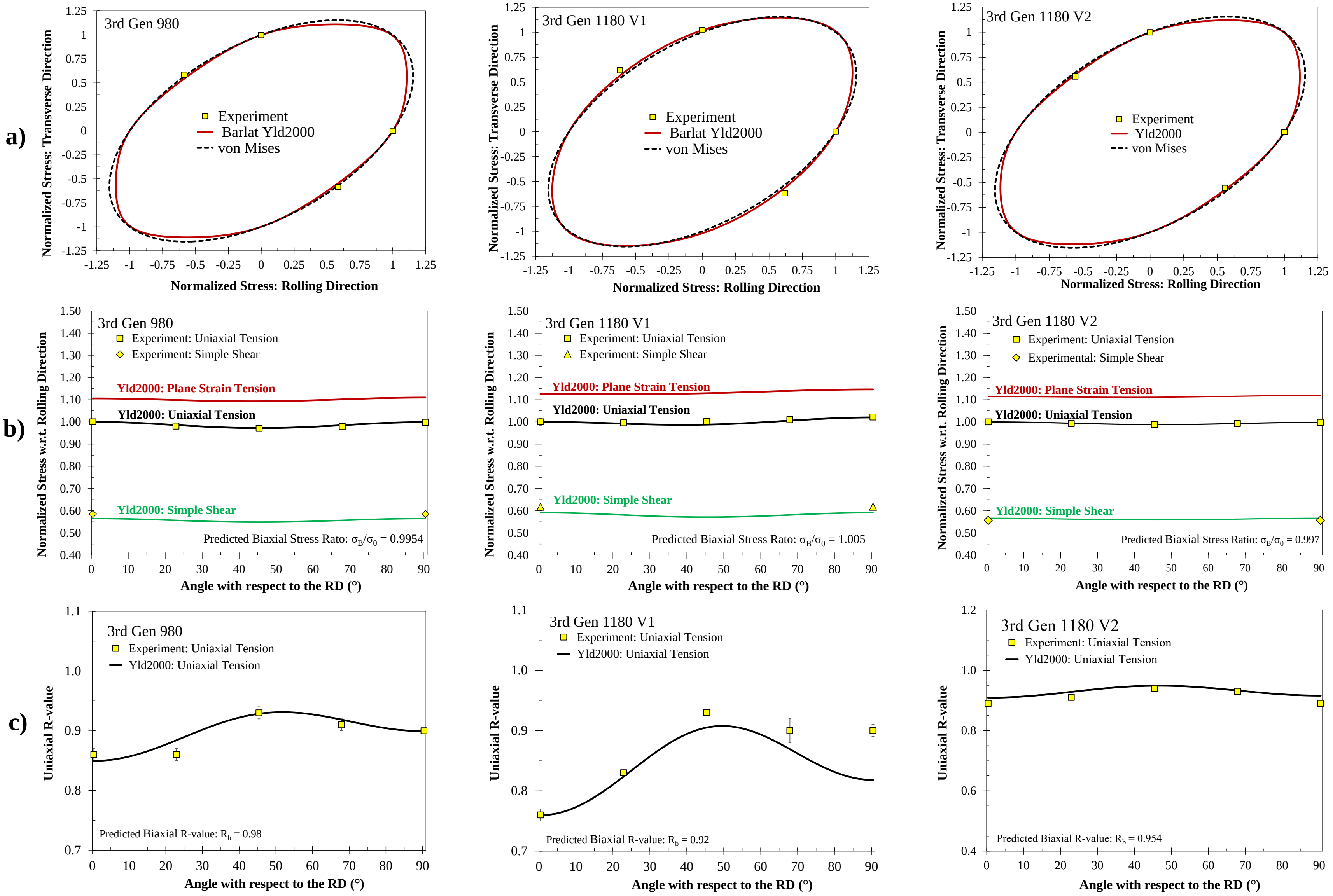

Figure 43: Superimposed von Mises and Yld2000 (a) yield functions, (b) experimental tensile and shear stress ratios superimposed with predicted values, and (c) experimental r-values superimposed with predicted values for 3rd Gen 980, 3rd Gen 1180 V1, and 3rd Gen 1180 V2 (Noder *et al.*, 2021)

2.5 Chord Modulus Evolution

The chord modulus is an important parameter for springback modelling and is defined as the slope of the unloading curve in a tensile test (Kupke, 2017). JIS No. 5 tensile tests in the TD were loaded and unloaded to measure the chord modulus. The tensile specimen was loaded under displacement control at a speed of 0.05 mm/s and then unloaded at 800 N/s on an AGX Shimadzu universal test frame to maintain quasi-static loading conditions. The tensile specimen cycled through 5 – 9 cycles of loading and unloading to create the stress-strain evolution visualized in Figure 44.

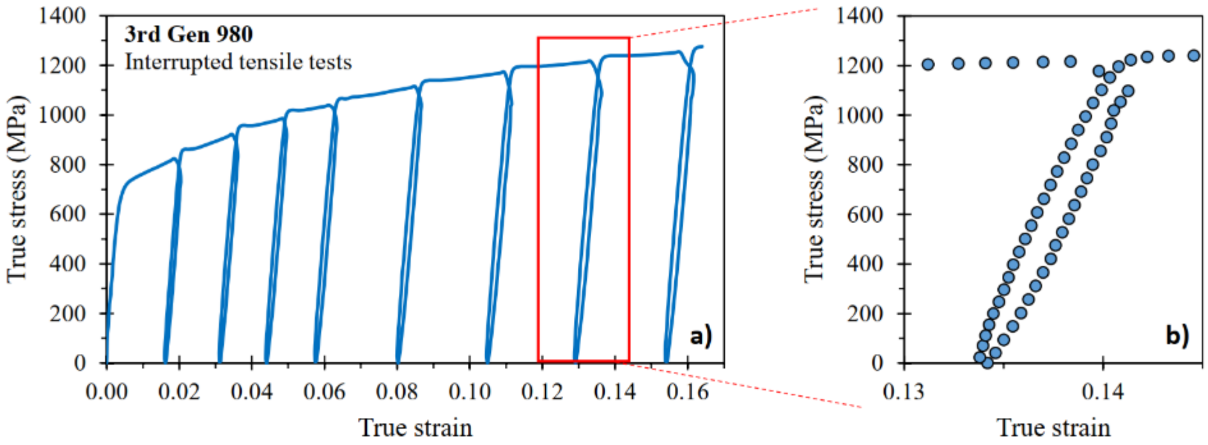

Figure 44: Interrupted tensile tests with (a) 8 unloading cycles for 3rd Gen 980 and (b) a zoomed in view of the non-linear behavior during unloading of the 7th unloading cycle

The chord modulus illustrated in Figure 44b and previously shown in Figure 30b highlights the non-linear behavior of the steels during unloading. It is believed that this is caused by micro-plastic strain (Cleveland and Ghost, 2002). This micro-plastic strain is caused by (i) residual stresses from stress-strain partitioning and (ii) dislocation motion caused by repulsion and pile-ups (Mompiou, *et al.*, 2012 & Kupke, 2017). Various methodologies have been generated to describe the chord modulus (Cleveland and Ghosh, 2002, Govik *et al.*, 2017, Sun and Wagoner, 2013). The methodology carried out in this study adheres to the methodology of Yoshida *et al.* (2002) where the chord modulus was averaged over a range of stresses. The chord modulus was computed using a line of best fit that passes through the stress-strain curve from 0 to 95% of the stress before unloading. The equation formulated by Yoshida *et al.* (2002) is expressed as

$$E_{chord} = E_0 - \left(E_0 - E_S\right)\left(1 - \exp\left(-\xi\varepsilon_{eq}\right)\right) \tag{9}$$

where E_0 is the Young's modulus of the virgin steel, E_S represents the modulus of saturation, and lastly ξ is denoted as a calibration parameter. The coefficients of for each material after calibration is recorded in Table 6. The chord modulus for all 3rd Gen AHSS variants, seen in Figure 45, shows similar results averaging a saturation modulus of 172 (±6.8) GPa without a clear dependence upon the strength level.

Table 6: Coefficients for the calibrated Yoshida model to describe the chord modulus as a function of pre-strain (Noder, 2021a).

	E_0 (GPa)	**E_S (GPa)**	**ξ**
3rd Gen 980	208.3	167.3	31.3
3rd Gen 1180 V1	205.2	169.7	131.0
3rd Gen 1180 V2	209.0	176.1	145.9

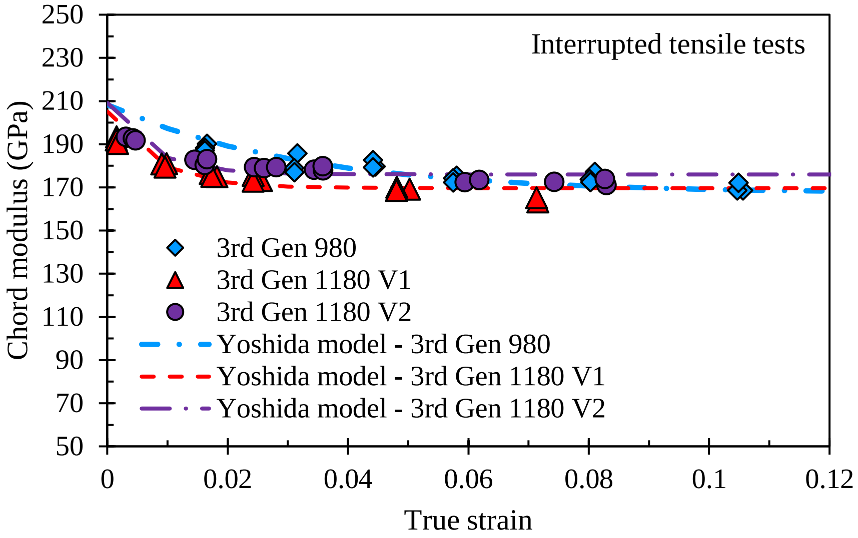

Figure 45: Experimental and numerical chord modulus using the Yoshida model

2.6 Tension-Compression Tests

The experiments for the tension-compression tests were performed by Dr. Jacqueline Noder which utilizes an anti-buckling test fixture based upon the design of Kupke (2017). Polycarbonate inserts in the anti-buckling device were used to enable viewing of the sample with DIC strain measurement through a viewing region in one of the plates. The influence of friction due to the clamping must be considered. Tensile tests with and without clamping were used to estimate the coefficient of friction with the values summarized in Table 7. The tension-compression test results with and without friction correction responses are presented in Figure 46.

Table 7: Summary of friction coefficients of 3rd Gen 980 and 3rd Gen 1180 V1 under tension and compression

COF	***Tension***	***Compression***
3rd Gen 980	0.065 ± 0.006	0.155 ± 0.020
3rd Gen 1180 V1	0.067 ± 0.024	0.082 ± 0.032

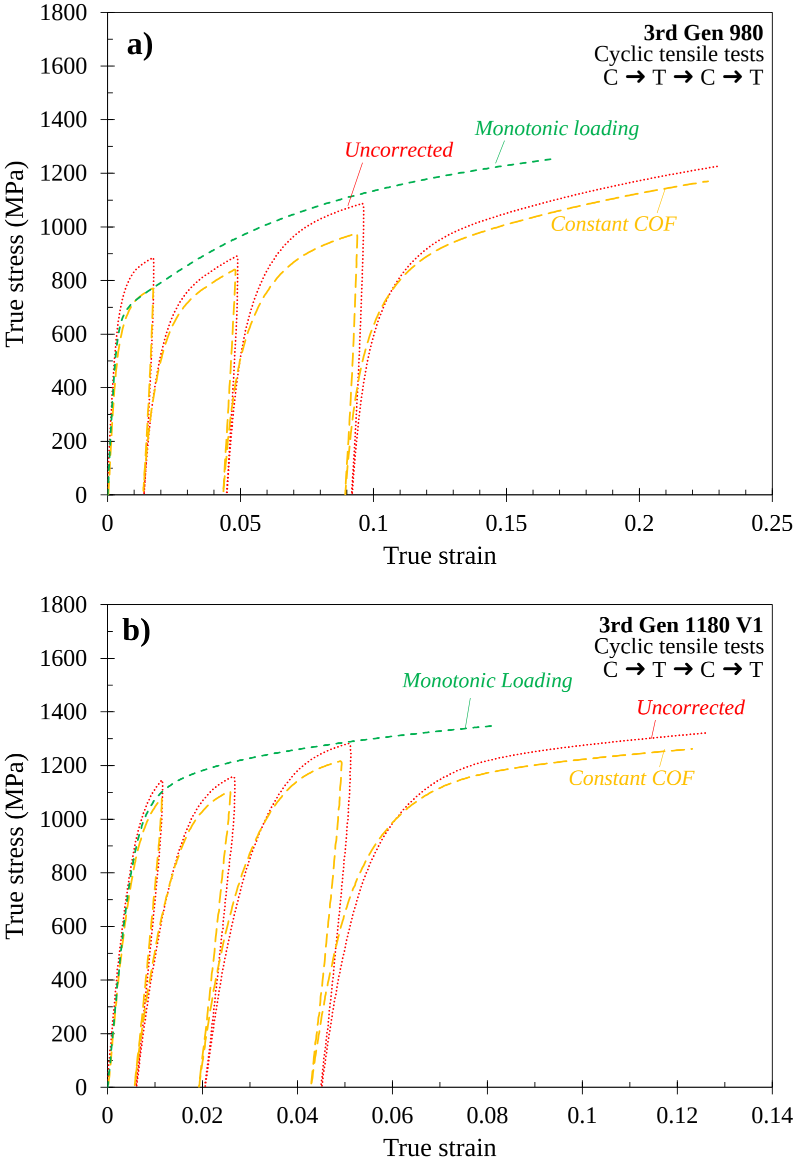

Figure 46: Stress-strain response of cyclic tension-compression tests for a) 3rd Gen 980 and b) 3rd Gen 1180 V1

2.7 Fracture Characterization and Fracture Locus Calibration

The fracture behavior often governs the response of the component during a crash event. The methodology outlined by Noder *et al*. (2021) is used to characterize the fracture behavior and to calibrate an experimental fracture locus for each steel. This methodology exploits tool contact and bending mechanics to impede necking by inducing a compressive through-thickness stress. Fracture then occurs at the surface of the sheet on the convex side undergoing tension instead of the mid-plane, enabling the use of DIC strain measurement. The equivalent failure strains were calculated by strain path integration and the use of the Barlat Yld2000 yield surface. The fracture locus uses four different experiments to generate data points for calibration namely, the simple shear test, the conical hole expansion test, the v-bend test, and the miniature dome test. The fracture model used for the description of the fracture model uses the Generalized Drucker-Prager (GDP) fracture model proposed by Rahmaan *et al.* (2022). The fracture loci for 3rd Gen 980 and both lots of 3rd Gen 1180 is illustrated in Figure 47. For brevity, the reader is referred to Noder *et al.* (2021) where the test details and results are presented in detail.

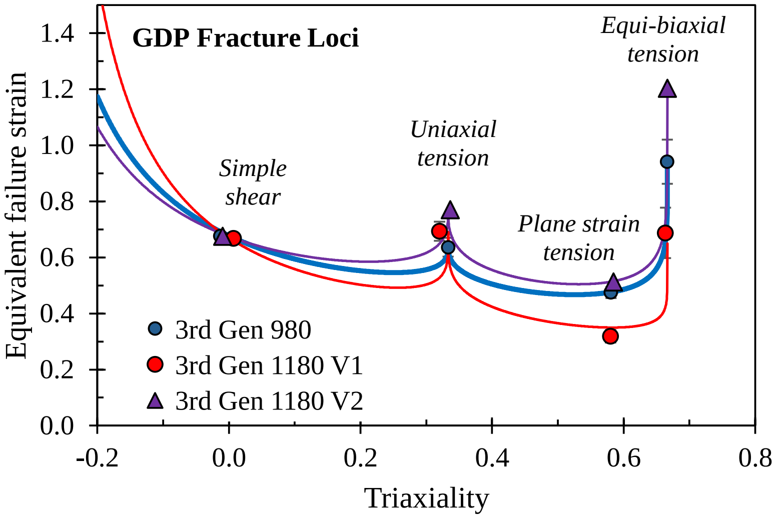

Figure 47: The Generalized Drucker-Prager fracture model of Rahmaan *et al.* (2018) for the 3rd Gen 980 and 3rd Gen 1180 V1 & V2 (Noder *et al.*, 2021)

3 Experimental and Analytical Formability Characterization

This chapter entails the experimental methodology to obtain the forming limit strains of 3rd Gen 980 and 3rd Gen 1180 V1 using both Nakazima and Marciniak tests. The forming limits of 3rd Gen 1180 V2 were later added into the project with only Marciniak tests. Microscope imaging of the 3rd Gen 980 and 3rd Gen 1180 V1 were investigated to study the fracture modes of the steels. The objective of this chapter is to assess the formability of 3rd Gen 980 and 3rd Gen 1180 V1 using the in-plane FLC. The analytical FLCs generated in this chapter are later used in Chapters 4 and 5 to predict locations of splitting in the forming simulations.

Upon identification of the experimental limiting strains, process corrections were carried out to account for tool contact pressure, and non-linear strain paths. Multiple instability models were then evaluated and modified to identify the methodology to use for 3rd Gen AHSS. A deterministic approach was taken to predict the forming limit strains by only using mechanical property data to objectively predict the FLC without any calibration parameters. Although commonly used in academia, formability models such as Marciniak and Kuczynski (1967) MK model require FLC data to calibrate the imperfection factor. Consequently, the models are of limited practical value to industry who seeks to minimize time-intensive testing such as FLC characterization. The code to perform the process corrections and the MMFC and MK formability models were provided by Dr. Jacqueline Noder and Prof. Cliff Butcher.

3.1 Characterization of In-Plane Formability using Marciniak and Nakazima Tests

The Marciniak and Nakazima tests were performed according to the ISO12004-2 standard to characterize the forming limits under approximately in-plane stretching from uniaxial tension to equi-biaxial stretching. Specimen widths were varied from 25.4 mm to 203.2 mm shown in Figure 48 and recorded in Table 8. All samples were extracted with the principal strain direction aligned in the TD.

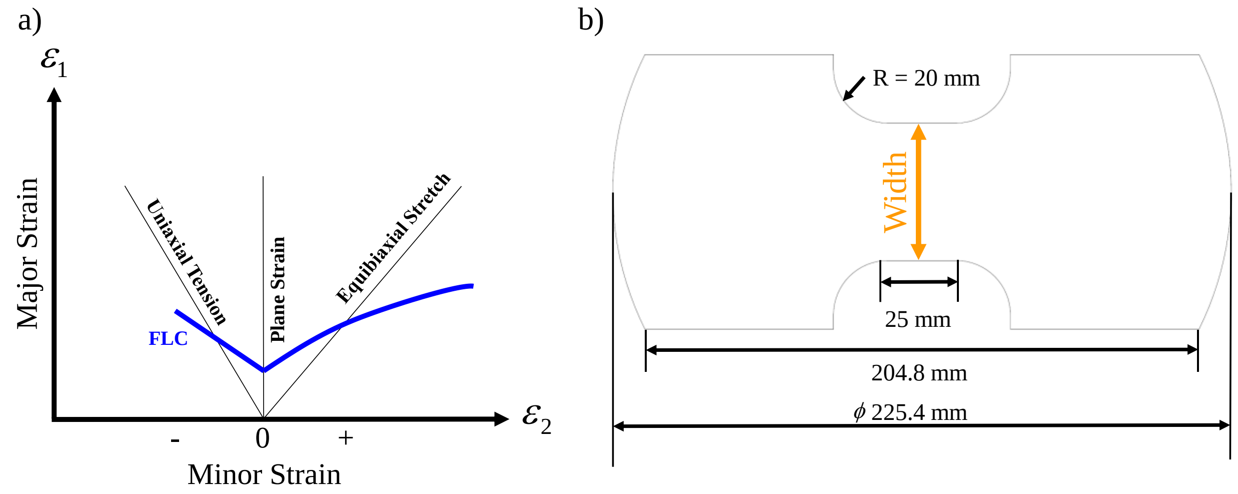

Figure 48: Strain paths showing uniaxial tension, plane strain tension, and equibiaxial tension under proportional loading a) and the dogbone specimen used to obtain limiting strains b).

Table 8: Sample width and carrier blank (CB) material used for both Marciniak and Nakazima tests. (MS denotes mild steel, SS denotes stainless steel)

	Sample Width [mm]								
Nakazima	25.4	50.8	-	101.6 (*FLC_0*)	-	139.7	152.4	-	203.2
Marciniak	25.4	50.8	76.2	-	127 (*FLC_0*)	-	152.4	165.1	203.2
CB Material for 3rd Gen 980	MS	MS	MS	X	MS	X	SS	X	SS
CB Material for 3rd Gen 1180 V1/V2	MS	MS	MS	X	MS	X	X	SS	SS

The dimensions for the tool sets for Marciniak and Nakazima tests correspond with the ISO 12004-2 standard and are illustrated in Figure 49. A hemispherical punch with a 101.6 mm diameter is used for the Nakazima test whereas a cylindrical punch is utilized for Marciniak tests of the same diameter where a 12 mm radius at the edge of the punch. The Nakazima tooling has an inner diameter of 106 mm with a 6.35 mm entry radius. The Marciniak die set, it has a 119 mm inner diameter and a 16 mm entry radius. Both toolsets have a lockbead height of 4.7 mm with a clamping load of 640 kN. An alternate punch was used for both 3rd Gen 1180 steels for biaxial Marciniak tests with a 25 mm profile. Initial biaxial Marciniak tests for 3rd Gen 1180 V1 resulted in radius fracture previously shown in Figure 18. A punch velocity of 0.25 mm/s was used. In the

Nakazima tests with along with Teflon® sheet lubricated with petrolatum placed between the punch and the sample. In the Marciniak tests, the Teflon® sheets were placed in between the punch and carrier blank.

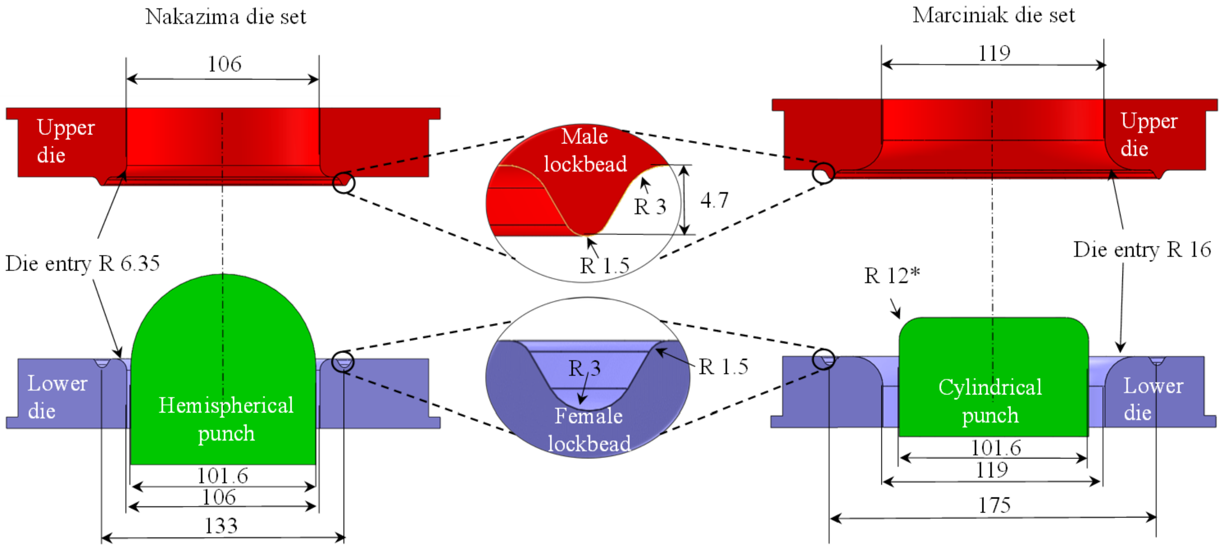

*Alternate punch has an edge profile of 25 mm

Figure 49: Nakazima (left) and Marciniak (right) tool sets where the dimensions are in mm and in accordance with the ISO12004-2 standard.

A sand-blasted 0.9 mm thick 1004 cold-rolled mild steel (MS) carrier blank was used initially for both steels. Due to the high ductility of the 3rd Gen 980, a more ductile carrier material was required therefore stainless steel (SS) carrier blanks with a thickness of 1.2 mm was used for biaxial strain paths. The square MS carrier blanks with a length of 203.2 mm and a 32 mm diameter central hole whereas the SS carrier blank had a 27 mm hole diameter. The carrier blank material for both materials used for each test is listed in Table 8.

The hydraulic MTS formability tester at the University of Waterloo is shown in Figure 50. Two MTS 407 controllers are installed in this setup where the binder holding force is controlled by one of the 407 controllers while the other controls punch displacement. The punch force and displacement measurements are synchronized with the DIC images with the overall set-up shown in Figure 51.

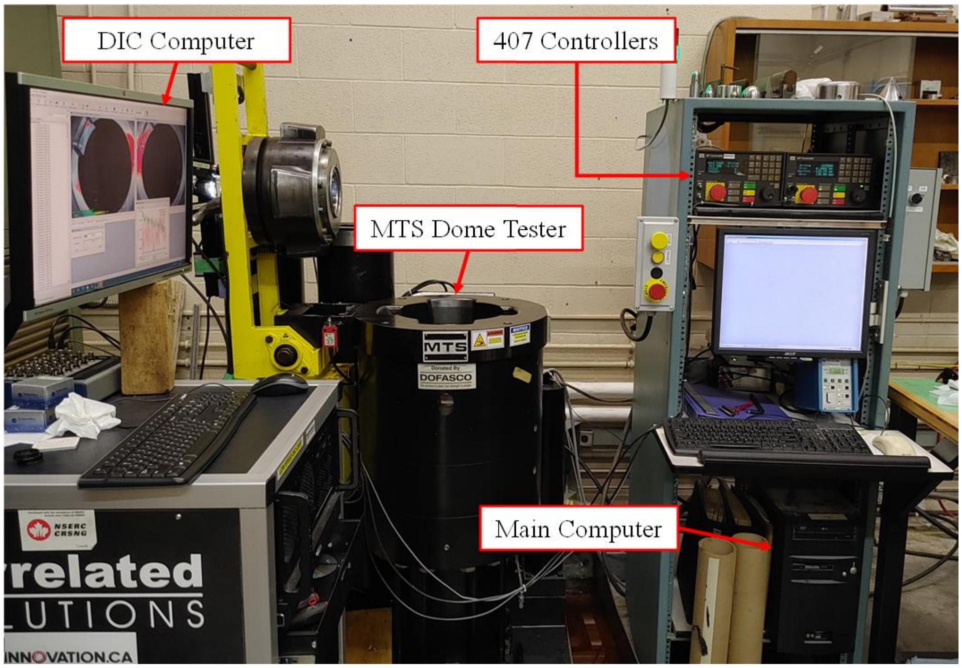

Figure 50: MTS dome tester layout at the University of Waterloo High Pressure Lab

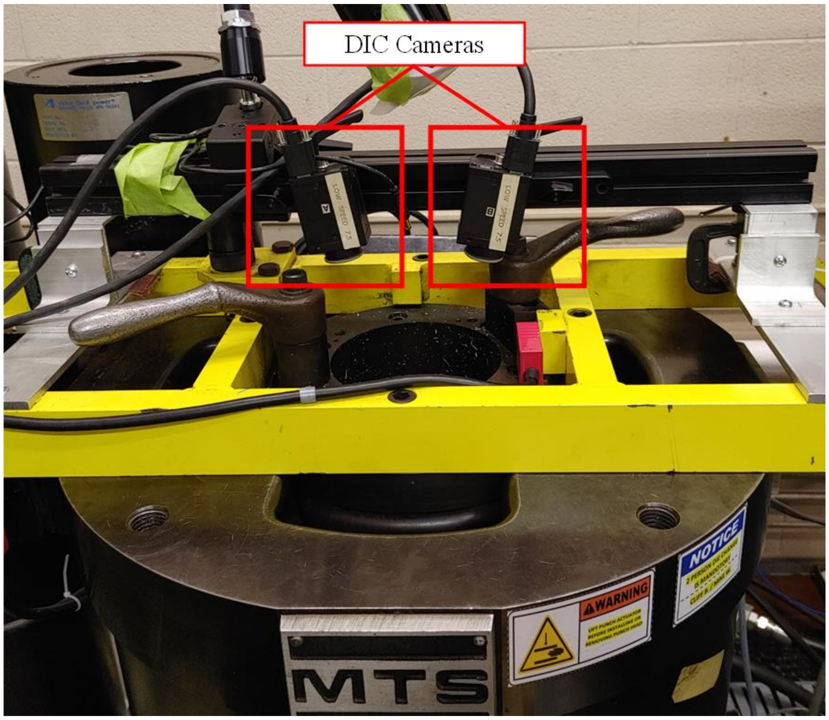

Figure 51: Orientation of DIC cameras overlooking the dome tester to capture images of deformation of specimens

3.2 DIC Settings and Limit Strain Detection

The software Vic-3D7® from Correlated Solutions Inc. was used which utilizes stereoscopic full-field DIC. A strain filter of 9 pixels, step size of 2, a resolution of 0.057 mm/pixel, subset of 35 pixels corresponding to an approximate VSGL of 1.0 mm was adopted for strain analysis. A minimum of 300 images per test for both steels using a frame rate of 5 – 6 images per second was implemented.

All limit strains were obtained based on the methodology of the ISO12004-2 standard. Five DIC line slices were aligned perpendicular to the crack location. As specified in ISO12004-2, parabolas were fit to the major and thickness strain distributions with plastic volume conservation used to calculate the minor strain. In the ISO methodology the minor strain may not be coincident to the strain path at the necking location. This is corrected by the procedure by Noder and Butcher (2019) where the minor strain was selected from the measured DIC strain path according to its corresponding major strain. The process is repeated for each line slice and the average major and minor limit strains reported for the sample. Figure 52 and Figure 53 show the strain paths spanning uniaxial tension to equi-biaxial stretch acquired from Marciniak and Nakazima tests superimposed with the limit strains for 3rd Gen 980 and 3rd Gen 1180 V1. The Marciniak tests results for 3rd Gen 1180 V2 are in Figure 54. Nonlinearity is evident from Nakazima tests as seen in Figure 52a and Figure 53a where the hemispherical punch initially stretches the specimen biaxially then transitions to its target strain path. This is apparent for samples that predominantly experience uniaxial stretch (25.4 mm and 50.8 mm specimens).

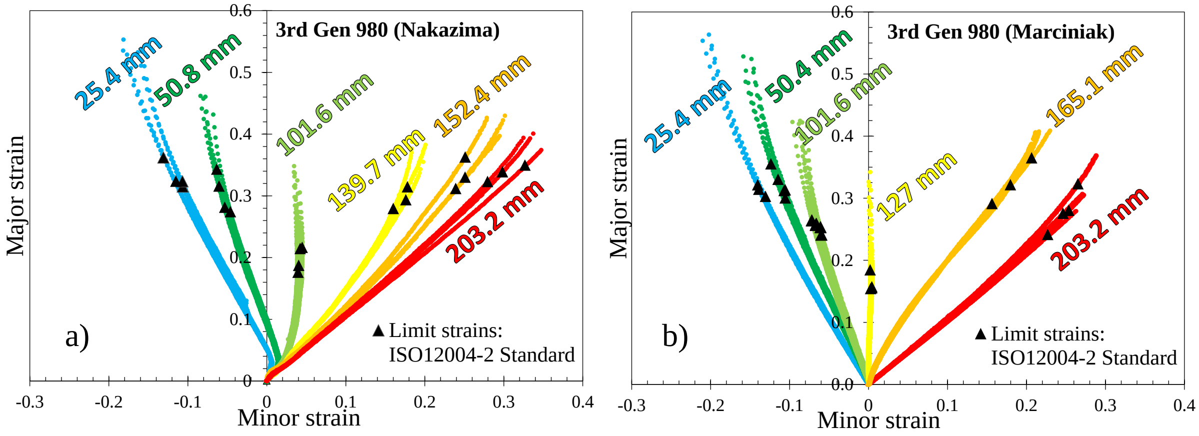

Figure 52: Strain paths superimposed with ISO12004-2 standard limit strains for a) Nakazima and b) Marciniak tests for 3rd Gen 980

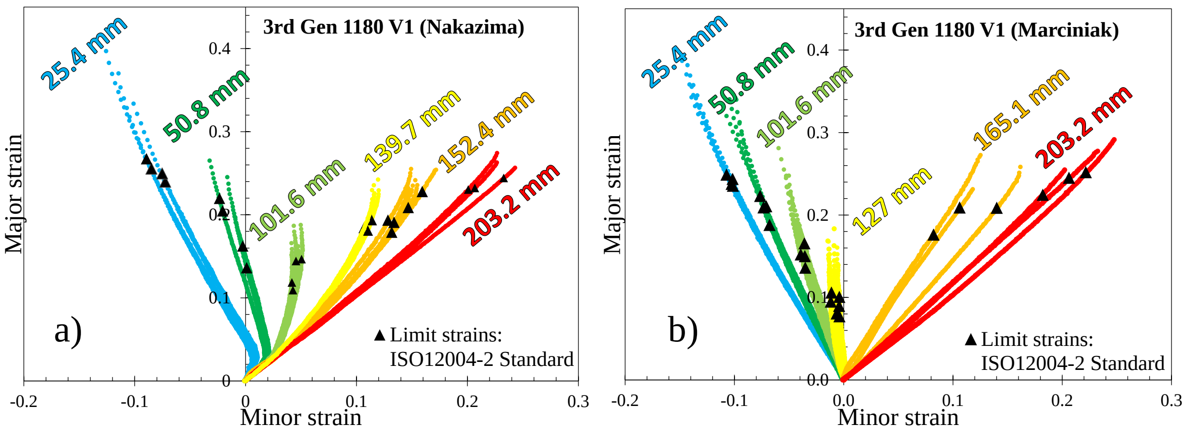

Figure 53: Strain paths superimposed with ISO12004-2 standard limit strains for a) Nakazima and b) Marciniak tests for 3rd Gen 1180 V1

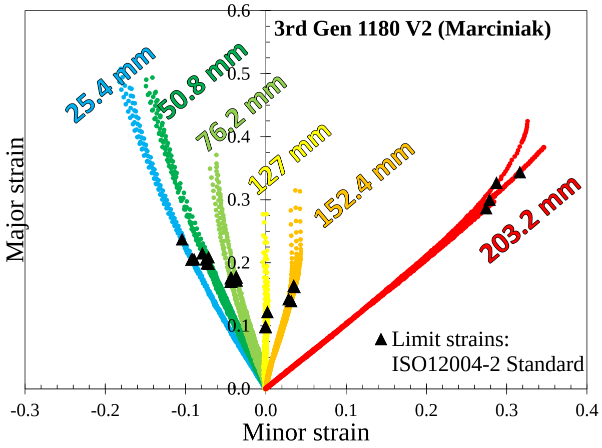

Figure 54: Strain paths superimposed with ISO12004-2 standard limit strains for Marciniak tests for 3rd Gen 1180 V2

3.3 Fracture Modes

Localization occurred transverse to the principal stretching direction for all steels as shown in Figure 55. Note that in biaxial stretching the neck is aligned with the RD which corresponds to fracture in the TD. Marcinak test specimens were sectioned to observe the fracture that occurred using an optical microscope. The sectioned specimens experienced a strain path of uniaxial stretching, plane strain tension, and equi-biaxial stretching and are shown in Figure 56. Thinning at the fracture location for the more ductile 3rd Gen 980 shows evident necking as seen by the cup-cone fracture exhibited by specimens that experienced uniaxial tension and plane strain tension. In contrast to 3rd Gen 980, the higher strength 3rd Gen 1180 V1 experiences less necking and failed via through-thickness shear fracture. Fracture analysis was not performed for the 3rd Gen 1180 V2.

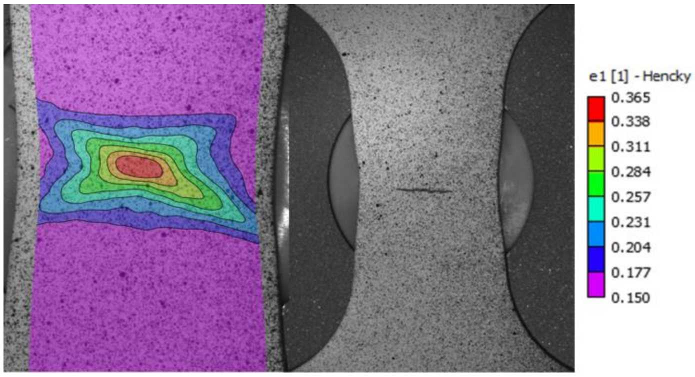

a) 25.4 sample

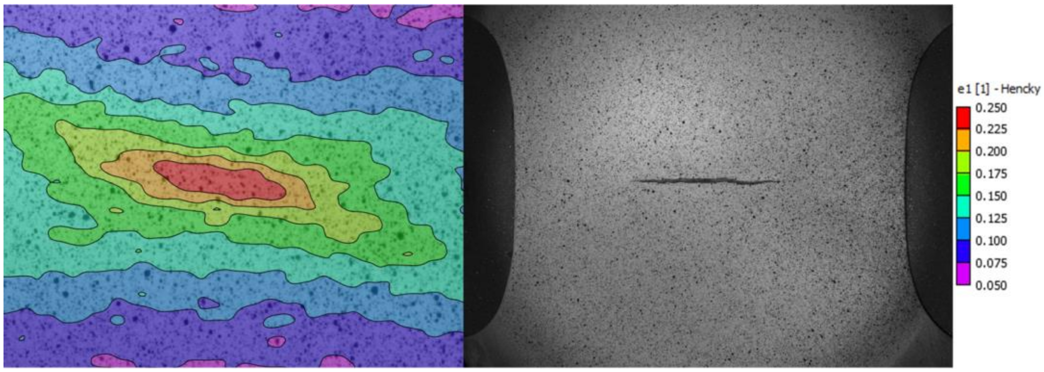

b) 76.2 mm sample

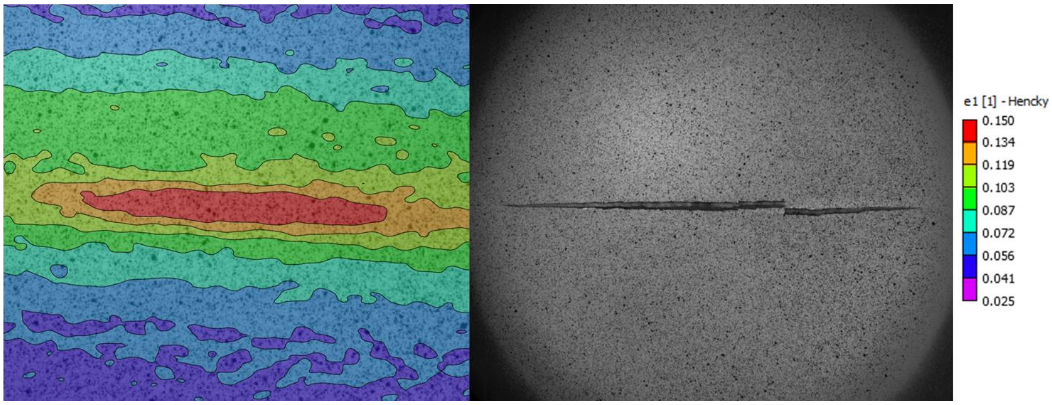

c) 127 mm sample

Figure 55: Major strain distributions of 3rd Gen 1180 V1 Marciniak tests for sample widths that are subjected to a) uniaxial tension to c) plane strain tension

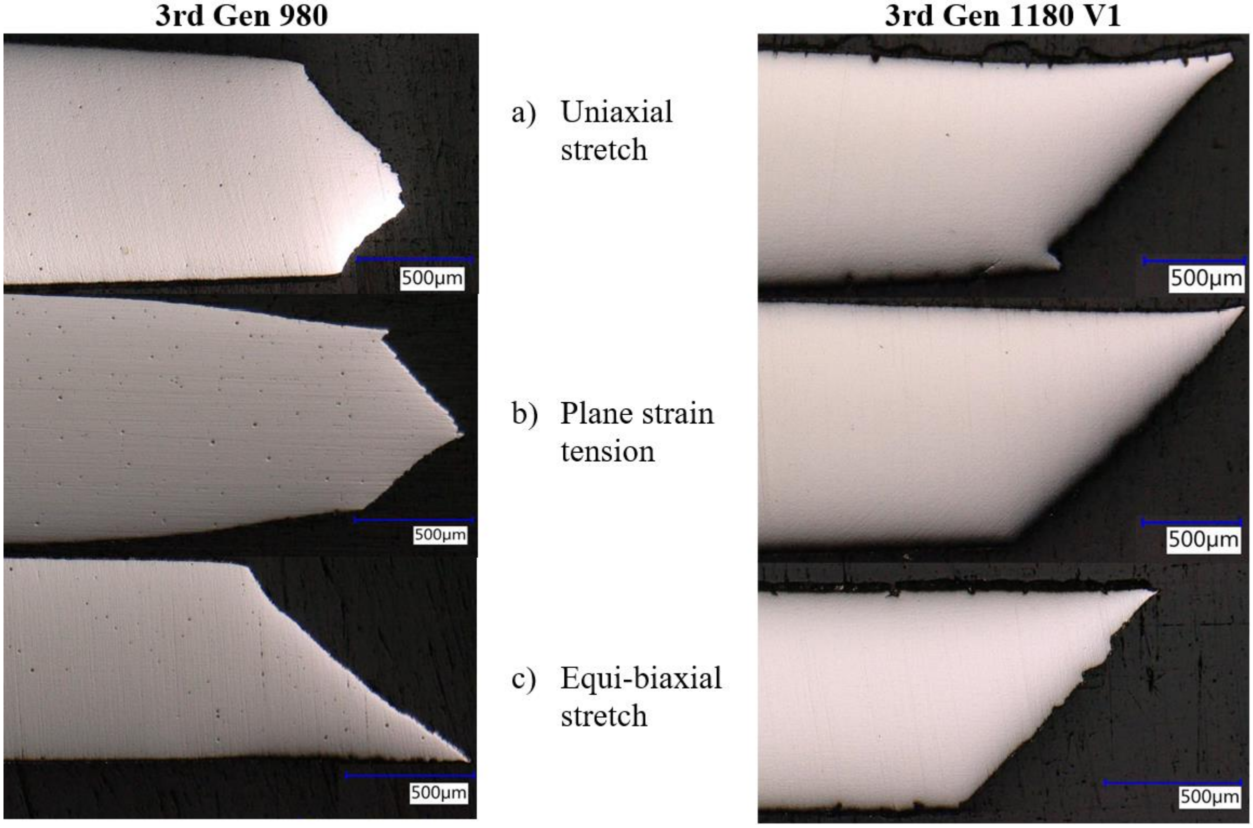

Figure 56: Cross-sections of fractured Marciniak specimens for 3rd Gen 980 (left) and 3rd Gen 1180 V1 (right) undergoing a) uniaxial stretch, b) plane strain tension and c) equi-biaxial stretch

3.4 Process corrections of Nakazima and Marciniak limit strains

In this section, the process effects in the Nakazima tests are corrected to compare with Marciniak tests. The material is idealized as rigid-plastic such that the measured DIC strains are assumed to be plastic strain and neglect elasticity. The critical layer of material that governs necking was selected as the inner layer of the blank in contact with the punch. The inner layer of the blank in the Nakazima test experiences compressive stresses due to bending and tool contact pressure which delays localization and creates a three-dimensional stress state. The use of DIC has enabled the calculation of the instantaneous principal strain ratio, ρ^{exp}, along with its associated flow rule yields the in-plane stress ratio in the principal directions, α:

$$\rho^{\exp} = \frac{\partial \varepsilon_2}{\partial \varepsilon_1} = \frac{N_2}{N_1} = \frac{\partial \sigma_{eq} / \partial \sigma_2}{\partial \sigma_{eq} / \partial \sigma_1} \tag{10}$$

$$\alpha = \frac{\sigma_2}{\sigma_1} \tag{11}$$

The through-thickness stress ratio, χ, due to punch contact is represented by the equation given by Min *et al.* (2016)

$$\chi = \frac{\sigma_3}{\sigma_1} = -\frac{t}{R_1}\left(1+\frac{t}{2R_2}\right) - \frac{t}{R_2}\left(1+\frac{t}{2R_1}\right)\alpha \tag{12}$$

$$t = t_o \exp\left[-(1+\rho^{\exp})\varepsilon_1\right] \tag{13}$$

where R_1 and R_2 denote the major and minor principal radii of curvatures on the outer surface. The localization for 3rd Gen 980 and 3rd Gen 1180 V1 occurred close to the dome apex, therefore the 50.8 mm Nakazima punch radius was chosen for the curvature for major and minor directions. Thinning of the specimen thickness was estimated using Equation 13 where t_0 and t refer to the initial and instantaneous thickness of the sheet, respectively.

Computation of the equivalent plastic strain, $\bar{\varepsilon}$, was performed by incremental integration of the equivalent strain using plastic work balance, where $\bar{\sigma}$ denotes the flow stress and k is the ratio of the major stress and the equivalent stress, σ_{eq}, where the equivalent stress is related to the yield function where

$$\bar{\varepsilon}(\alpha,\chi) = \int \frac{\boldsymbol{\sigma} : d\boldsymbol{\varepsilon}^p}{\bar{\sigma}} = \int k(\alpha,\chi)\left[1+\alpha\rho^{\exp} - (1+\rho^{\exp})\chi\right] d\varepsilon_1 \tag{14}$$

$$k(\alpha,\chi) = \frac{\sigma_1}{\sigma_{eq}(\alpha,\chi)} \tag{15}$$

The corrected major and minor principal strains, ε_1^{linear} and ε_2^{linear}, are calculated by linearizing the equivalent plastic strain by the strain and stress state when the limit strain was reached as

$$\varepsilon_1^{linear} = \frac{\bar{\varepsilon}}{k(\alpha,\chi)\left[1+\alpha\rho^{\exp}-(1+\rho^{\exp})\chi\right]} \tag{16}$$

$$\varepsilon_2^{linear} = \rho^{\exp}\varepsilon_1^{linear} \tag{17}$$

To correct for the though-thickness stress gradient caused by the tool contact, Min *et al.* (2016) incorporated a phenomenological mapping method from the actual 3D state to an equivalent 2D plane stress state with the same in-plane stress ratio. The in-plane stress ratio of the 3D stress state is used to compute the in-plane equivalent stress, σ_{eq}^{PS}, seen in Equation 18. The calculation of the in-plane strain ratio, ρ^{PS}, is calculated through the flow rule using the in-plane stress ratio expressed as

$$\sigma_{eq}^{PS}\left(\alpha\right) = \bar{\sigma}^{PS}(\bar{\varepsilon}^{PS},\alpha) = \frac{\sigma_1}{k(\alpha)} = \frac{k(\alpha,\chi)\bar{\sigma}(\bar{\varepsilon})}{k(\alpha)} \tag{18}$$

$$\rho^{PS}(\alpha) = \frac{\partial\varepsilon_2}{\partial\varepsilon_1} = \frac{\partial\sigma_{eq}^{PS} / \partial\sigma_2}{\partial\sigma_{eq}^{PS} / \partial\sigma_1} \tag{19}$$

The plane stress principal limit strains are obtainable from the equivalent plastic strain and stress ratios denoted as

$$\varepsilon_1^{PS} = \frac{\bar{\varepsilon}^{PS}}{k(\alpha)\left[1+\alpha\rho^{PS}\right]} \tag{20}$$

$$\varepsilon_2^{PS} = \rho^{PS}\left(\alpha\right)\varepsilon_1^{PS} \tag{21}$$

The contact pressure correction was shown by Noder and Butcher (2019) to be directly coupled to the hardening rate. Extreme over-corrections can occur as the hardening rate decreases with it being an infinite correction if the material becomes perfectly plastic. Nevertheless, good results have been obtained by Min *et al.* (2016), Noder and Butcher (2019) and Butcher *et al.* (2020) for AHSS.

The non-linear strain path (NLSP) effects are first corrected then followed by contact pressure. The effects of NLSP being removed from Marciniak tests are seen in Figure 57.

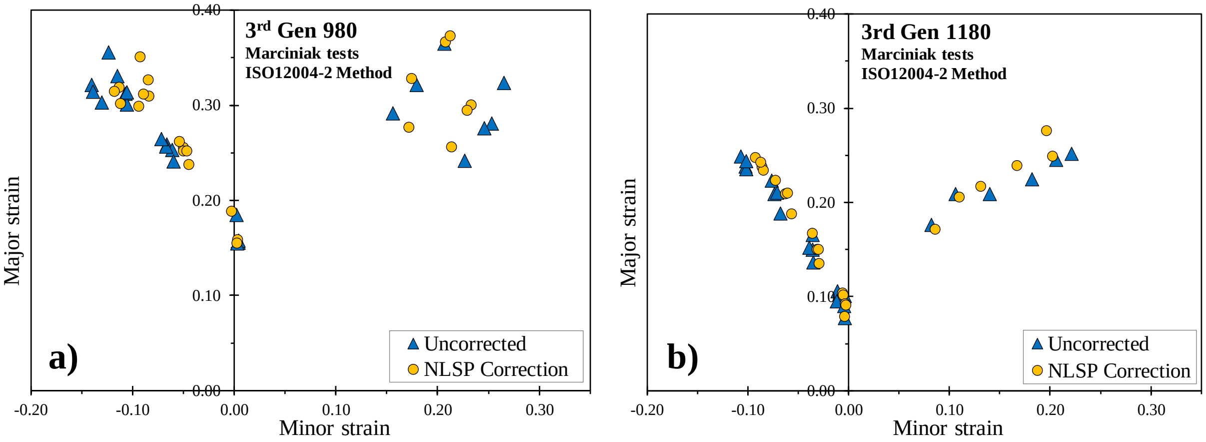

Figure 57: Marciniak limit strains pre- and post-correction for NLSP for a) 3rd Gen 980 and b) 3rd Gen 1180 V1

Corrections for Nakazima tests are more pronounced due to the hemispherical punch such that the FLC_0 does not have a zero minor strain. Removal of the biaxial non-linear strain path shift increases the limit strains and shifts them to the left (draw-side) such that the FLC_0 now occurs at approximately zero minor strain as seen in Figure 58.

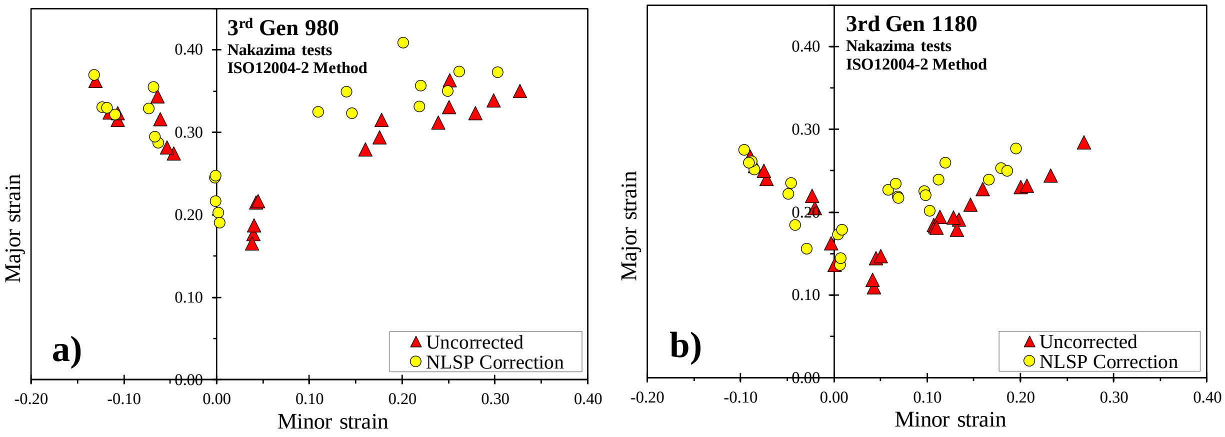

Figure 58: Uncorrected limiting strains of a) 3rd Gen 980 and b) 3rd Gen 1180 V1 superimposed with the limit strains corrected for NLSP

The contact pressure correction is applied to the NSLP corrected limit strains shown in Figure 59. The contact pressure correction is most pronounced for the 3rd Gen 980 in contrast to the 3rd

Gen 1180 V1 steel because of its higher hardening rate. In the methodology of Min et al. (2016), the higher the hardening rate, the larger the contact pressure correction.

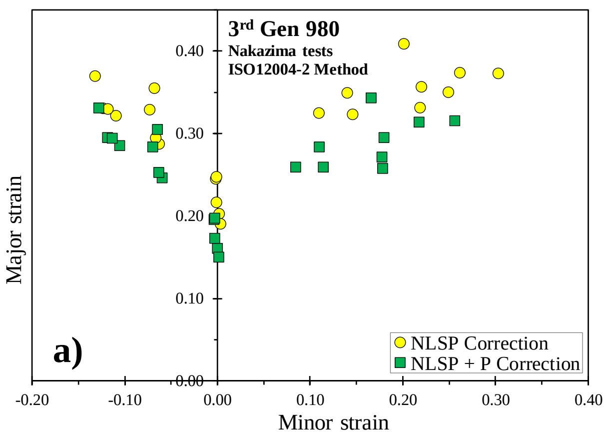

Figure 59: Corrected (NLSP + P) limiting strains superimposed with the NLSP-corrected limit strains of a) 3rd Gen 980 and b) 3rd Gen 1180 V1 for Nakazima tests

The process corrected limit strains from Nakazima and Marciniak tests are directly compared in Figure 60. Overall, there is reasonable correlation between the two test methods especially at around plane strain and on the draw side (left-hand side) of the FLC.

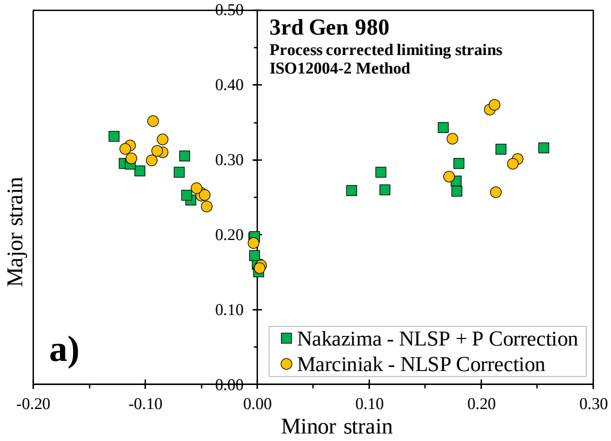

Figure 60: Corrected limiting strains for Nakazima (NLSP + Pressure corrected) and Marciniak (NLSP corrected) tests for a) 3rd Gen 980 and b) 3rd Gen 1180 V1

3.5 Analytical models to predict the FLC

Four analytical models were selected to compare their predictions of formability with the experimental in-plane limit strain data. The models were: (i) the MK model of Marciniak and Kuczynski (1967), (ii) a version of the modified maximum force criterion postulated by Hora *et al.* (2013), and (iii) a through-thickness instability model by Bressan and Williams (BW) (1983) for biaxial stretching coupled with Hill's (1952) in-plane localization model for uniaxial stretching. A fourth model is then proposed (iv) to couple the BW model with the maximum shear stress model of Hance and Huang (2018).

3.5.1 MK Model

The MK model is based on the assumption of a thickness imperfection in the form of a band or a groove inclined at an angle, θ, illustrated in Figure 61. The forces experienced within the band is proportional in the homogeneous region where '*a*' denotes the homogenuous region and the imperfection band is represented by '*b*'. Deformation within the band is controlled by equilibrium and compatibility equations where the equilibrium and compatibility equations are expressed as

$$\sigma_{nn}^{b} = \frac{\sigma_{nn}^{a}}{f}, \tag{22}$$

$$\sigma_{nt}^{b} = \frac{\sigma_{nt}^{a}}{f}, \tag{23}$$

$$d\varepsilon_{tt}^{a} = d\varepsilon_{tt}^{b} \tag{24}$$

where the subscripts, *nn* and *tt*, on the stress and strain components denote the normal and tangential components to the band, respectively, and *nt* denotes the shear direction. The thickness imperfection factor, f, changes with deformation which is expressed as

$$f = f_0 \exp(\varepsilon_3^b - \varepsilon_3^a) \tag{25}$$

Acute localization is defined as occuring when the equivalent plastic strain rate in the band was 10 times higher than outside the band. Numerical integration of the MK model was performed using the Newton-Raphson method of Butuc (2004). The limit strains were calculated in 2 degree increments for band angles and the lowest limit strain value of all angles reported at the forming limit.

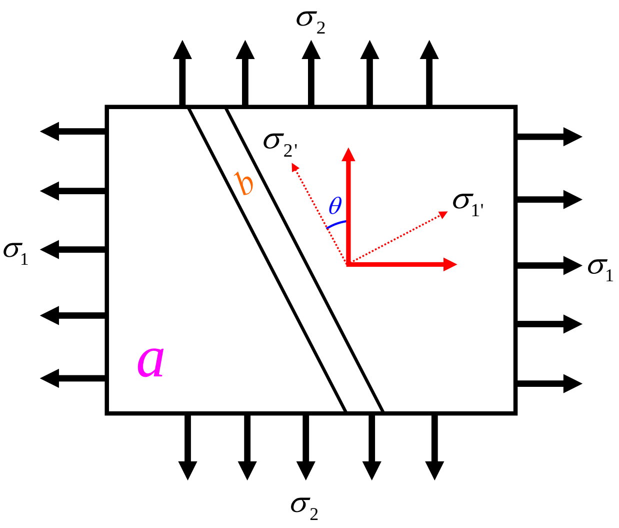

Figure 61: Illustration of the imperfection band under biaxial stretch deforming in plane stress conditions

The MK model predictions are extremely sensitive to the value of the thickness imperfection factor with it often being used as a calibration parameter as discussed by Ratchev *et al.* (1994) and Butcher *et al.* (2021). Although this procedure can provide good results, it is effectively a closed-loop calibration procedure. Forming limit data is required to predict it. In the present study, for the MK model to be considered predictive, an imperfection factor of 0.996 was selected from the work of Barlat and Jalinier (1985) from an analysis of microstructural imperfections in commercial sheet metals that would produce the initial thickness inhomogeneity

3.5.2 MMFC Model

Hora *et al.* (2013) postulated the modified maximum force criterion (MMFC) based upon an extension of the maximum force criterion of Dorn model (1947) to predict diffuse necking. The Dorn model is less rigorous than that of the derivation of Swift (1952) as it only considers the major principal stress and is problematic in that it predicts localization in shear under a positive hardening rate. However, the models are identical in uniaxial, plane strain and biaxial tension which is the range of loading considered in the forming limit tests of the present study. Hora *et al.* (2013) introduced a second term that is activated at the onset of diffuse necking to account for the effective hardening related to the transition of the stress state towards plane strain as

$$\frac{\partial\sigma_1}{\partial\varepsilon_1}+\frac{\partial\sigma_1}{\partial\rho}\geq\sigma_1 \tag{26}$$

where the derivative of the principal major stress is expressed as

$$\frac{\partial \sigma_1}{\partial \rho} = \frac{\partial \sigma_1}{\partial \alpha}\frac{\partial \alpha}{\partial \rho} = \bar{\sigma}\frac{\partial k}{\partial \alpha} / \left(\frac{\partial \rho}{\partial \alpha}\right) \tag{27}$$

such that

$$\frac{\partial \rho}{\partial \alpha} = \frac{1}{N_1}\left(\frac{\partial N_2}{\partial \alpha} - \rho \frac{\partial N_1}{\partial \alpha}\right) \tag{28}$$

$$N_i = \frac{\partial \sigma_{eq}}{\partial \sigma_i} \tag{29}$$

In the MMFC model, an acute neck is assumed to have developed when incremental strain path reaches plane strain, $\rho = 0$. Since the predicted strain path in the MMFC model is inherently non-linear and inconsistent with the corrected experimental limit strains for proportional loading, linearization is proposed using the average strain path

$$\bar{\rho} = \frac{1}{\bar{\varepsilon}}\int \rho d\bar{\varepsilon} \tag{30}$$

where the average stress ratio, $\bar{\alpha}$, can be calculated from the flow rule using $\bar{\rho}$. The linearized major and minor strains are computed using strain and stress ratios defined by equations 10 and 11, respectively.

3.5.3 Bressan-William-Hill Model

Bressan and Williams (1983) extended the zero-extension model of Hill (1952) biaxial stress states. There is no angle of zero-extension, ϕ, in the plane of the sheet during biaxial stretching since both in-plane strains are non-zero. However, one angle does exist in the through-thickness direction. Through-thickness shear failure with minimal necking is consistent with the micrograph images of the fracture surfaces of the 3rd Gen 1180 V1 shown previously in Figure 56. The angle of zero-extension corresponds to the angle where plane strain tension occurs and is obtained from a strain transformation as

$$\cos 2\phi = -\frac{\rho}{2+\rho}, \qquad \rho \geq 0 \tag{31}$$

The BW model makes the assumption of localization through the thickness that occurs at a critical shear stress when

$$\tau_{cr} = \frac{\sigma_1}{2}\sin 2\phi = k(\alpha)\bar{\sigma}(\bar{\varepsilon})\frac{\sqrt{1+\rho}}{2+\rho}, \qquad \rho \geq 0 \tag{32}$$

The critical shear stress is considered as a material constant. For the present work, the critical shear stress is identified in plane strain tension from Swift's (1952) MMFC where it is also analogous to the method of Hill (1952) for plane strain tension. In this approach, the critical shear stress is removed as a calibration parameter such that the FLC is predicted from the yield function and hardening model. A localized neck is formed model of Hill (1952) occurs when

$$k(\alpha)\frac{\partial\bar{\sigma}}{\partial\bar{\varepsilon}} = \bar{\sigma}\left(\frac{1+\rho}{1+\alpha\rho}\right), \qquad \rho \leq 0 \tag{33}$$

The critical shear stress for the BW model in Eq. 32 is determined from Eq. 33 in plane strain when α obtained from the yield function coressponds to $\rho = 0$. The BW model is limited to biaxial stress states such that the solution of Hill (1952) is used for uniaxial stretching forming the so-called BWH model initially proposed by Alsos *et al*. (2008). The zero-extension angle can be seen in Figure 61 where the development of localization occurs in the plane of the sheet and is deonoted by

$$\theta = \tan^{-1}\left(\sqrt{-\rho}\right), \ \rho \leq 0 \tag{34}$$

3.5.3.1 The Extended Bressan-Williams (BWx) Model

The BWH model is consistent in how it employs the concept of zero-extension but inconsistent in application. The biaxial limit strains are governed by a critical shear stress but are not on the draw side using the Hill solution. In this thesis, a simple but effective extension of the BW model is proposed, denoted as the BWx model and was published in Gutierrez *et al.* (2020), where the in-plane critical shear stress is used to determine the limit strains for the draw side of the FLC. The formulation of Hill (1952) is replaced such that the in-plane critical shear stress is used to identify acute localization and defined as

$$\tau_{cr}^{BWx} = \begin{cases} \dfrac{\sigma_1}{2} = \dfrac{k(\alpha)\bar{\sigma}(\bar{\varepsilon})}{2}, & \rho \le 0 \\ \dfrac{\sigma_1}{2}\sin 2\phi = k(\alpha)\bar{\sigma}(\bar{\varepsilon})\dfrac{\sqrt{1+\rho}}{2+\rho}, & \rho \ge 0 \end{cases} \tag{35}$$

No additional variables are added into the framework of the BWx model. The BWx model could alternatively be interpreted as a modification of the model by Hance and Huang (2018) where a maximum normal stress is assumed as the criterion for instability but replacing the biaxial limit strains with the BW criterion. The model of Hance and Huang can be viewed as a flat line in a stress-based FLC that is not a function of the minor stress which can be seen in Figure 62. A power law hardening material with n = 0.15 and von Mises yield function were arbitrarily implemented to illustrate the representation of the FLC in stress space to generate Figure 62b. It should be noted that for stress states spanning uniaxial to biaxial tension, only a factor of two is the difference between the maximum shear stress and maximum normal stress so model of Hance and Huang could alternatively be described as a maximum shear stress criterion.

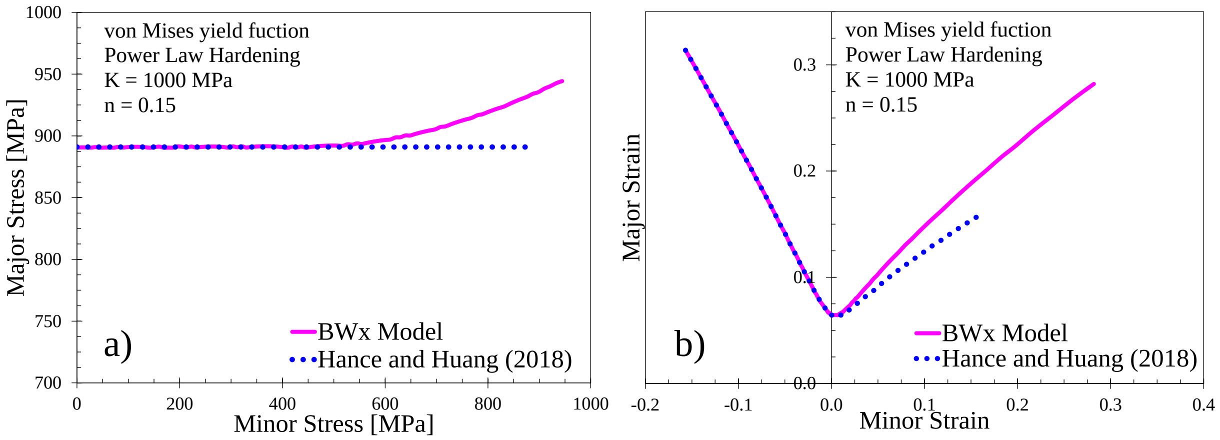

Figure 62: Forming limits in stress-space a) of an isotropic material using power law hardening highlighting the horizontal FLC of Hance and Huang (2018) and b) the converted FLC in strain space of the BWx model

3.6 Discussion of Predicted FLCs using the MK, MMFC, and BW models

3.6.1 MK Model Forming Limits

The MK imperfection factor of 0.996 from Barlat and Jalinier (1985) can reasonably predict the limit strains in biaxial stretching but underestimates the limit strains in uniaxial tension as shown in Figure 63. Alternate imperfection factors were obtained based on the surface roughness of the steel with values of 0.9992 and 0.9993 for 3rd Gen 980 and 3rd Gen 1180 V1, respectively. Unfortunately, the imperfection factor based on the surface roughness did not yield better predictions. The predicted FLC was shifted upwards which further overpredicts the limit strains in the biaxial region with only a marginal increase in the draw side limit strains.

A similar result was observed by Chan *et al.* (1994) and Ratchev *et al.* (1985) who reported that the MK biaxial limit strains were heavily influenced by the imperfection factor. According to Hutchinson (1978), the strain rate sensitivity of the material has a more pronounced effect on the draw side than the biaxial side in the MK model formulation. A significant increase was reported by Zhang *et al.* (2009) where limit strains for uniaxial tension increased by 73% and the biaxial side increased by 12% upon changing the strain rate exponent from 0.01 to 0.04. To maintain consistency, all instability criteria are generated undergoing quasi-static conditions. Strain-rate sensitivity was not included in the MK model to provide a comparison with the MMFC and BW models that used quasi-static hardening data.

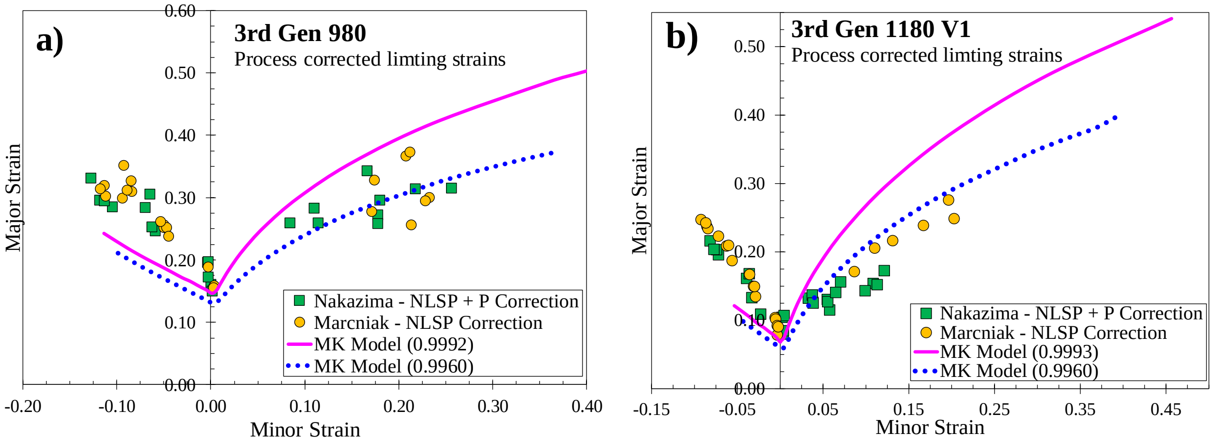

Figure 63: Analytical forming limit strains generated from the MK model with varying imperfection factors for a) 3rd Gen 980 and b) 3rd Gen 1180 V1 superimposed with its process-corrected limiting strains

3.6.2 MMFC Forming Limits

The FLC predicted by the MMFC model is shown in Figure 64 along with its linearized version. The predicted FLC$_0$ are in excellent correlation with the Marciniak and corrected Nakazima limit strains for both steels. The original MMFC model of Hora *et al*. (2013) acts as the upper bound of the experimental forming limits while the linearized form correlates better with the FLC across all conditions.

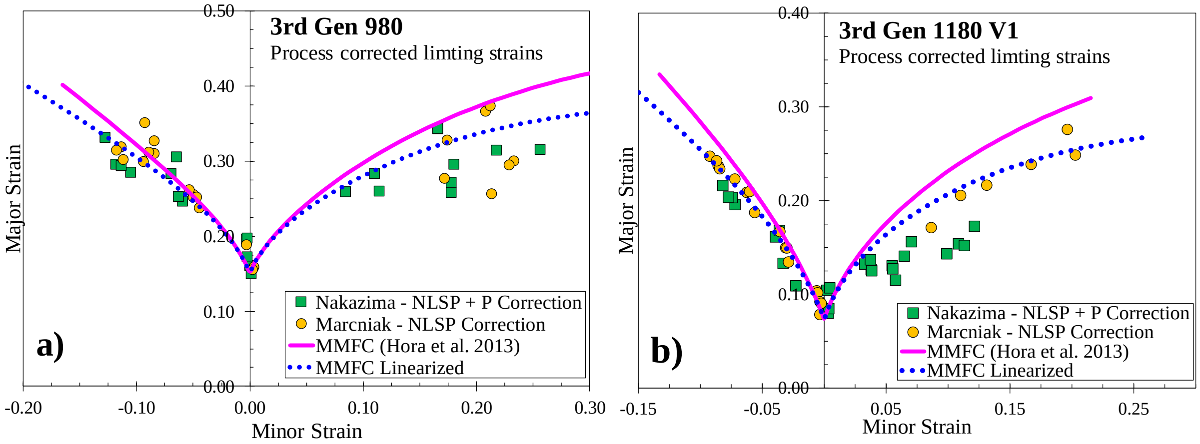

Figure 64: Analytical forming limit strains from the MMFC model using the method of Hora *et al.* (2013) and its linearized form for a) 3rd Gen 980 and b) 3rd Gen 1180 V1 superimposed with its process-corrected limiting strains

3.6.3 BWH and BWx Model Forming Limits

The predicted FLCs of the BWH and BWx models for both steels are presented in Figure 65. For biaxial stretching, the analytical limit strains are the same for both models as they both use the BW model. The predicted limit strains for 3rd Gen 980 are conservative while they are in close agreement for the 3rd Gen 1180 V1 which exhibited through-thickness localization.

The FLC predictions on the draw side using the model of Hill (1952) severely underpredicted the limit strains of both steels while the BWx model was a close estimate. The BWx model provides good overall agreement in comparison to the more complex MK model despite its simple formulation.

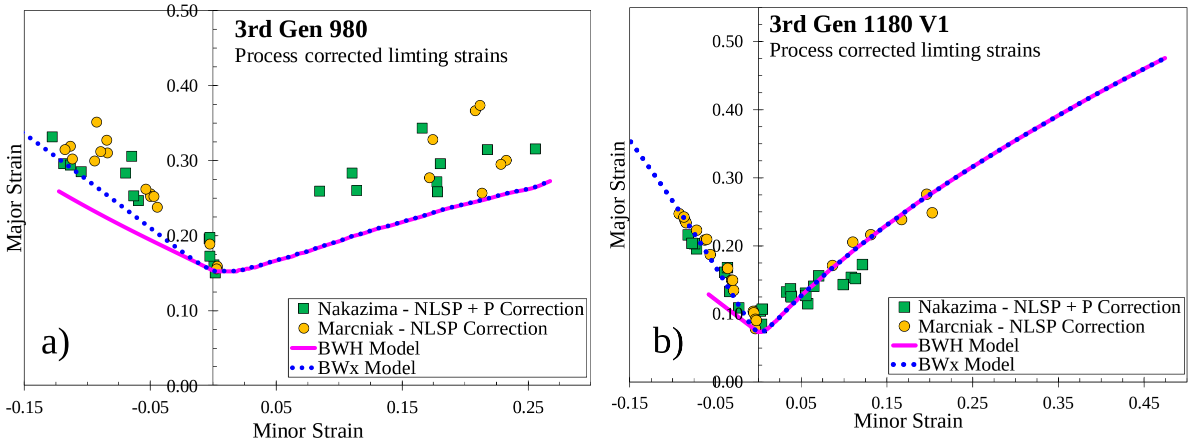

Figure 65: Analytical forming limit strains from the BWH and BWx model for a) 3rd Gen 980 and b) 3rd Gen 1180 V1 superimposed with its process-corrected limiting strains

3.6.4 MMFC and BWX comparisons between 3rd Gen 1180 V1 and V2

Comparisons between 3rd Gen 1180 V1 and V2 were performed to see the differences in formability from different lots. Only the BWx model and linearized MMFC model are generated for comparison of forming limits in Figure 66. The BWx model shows good correlation and suggests that the 3rd Gen 1180 V2 may also be exhibiting through-thickness shear localization such as the 3rd Gen 11180 V1. Excellent correlation is seen in uniaxial tension for both 3rd Gen 1180 steels and for both BWx and MMFC models. The biaxial side of the 3rd Gen 1180 V2 upon comparing with the MMFC model underestimates the experimental limit strains.

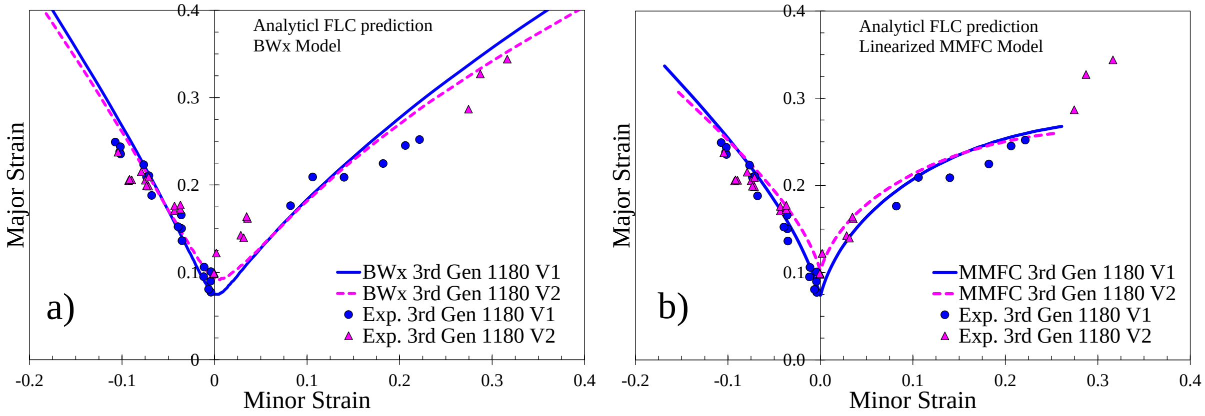

Figure 66: Analytical forming limit strains from the a) BWx and b) MMFC model for the 3rd Gen 1180 steels superimposed with experimental limit strains

Overall, the simple BWx model was effective at predicting the FLCs for the 1180 MPa strength steels and reasonable for the 3rd Gen 980 which exhibited more of a necking-based mode than through-thickness shear. The MMFC model and its linearized form performed well for all materials and also does not require any calibration. The complex MK model and its imperfection factor provided reasonable predictions on the biaxial side but underestimated the draw-side limit strains, likely due to excluding rate sensitivity. For the steels considered in the present work, the predictive accuracy of the MK model, when weighed against its complexity and requirement of calibration, is difficult to justify. The simpler BWx and MMFC models can be used without the appearance of calibration bias.

3.7 Discussion and Recommendations on Formability Characterization

Three analytical models are compared with the process corrected limit strains presented in Figure 67. The FLC models were selected due to their superior overall agreement with the process corrected limit strains compared to their other model variants. For both steels, the MK model predictions are conservative, particularly on the draw side. The simpler MMFC and BWx models show good correlation where the MMFC model has the best overall agreement.

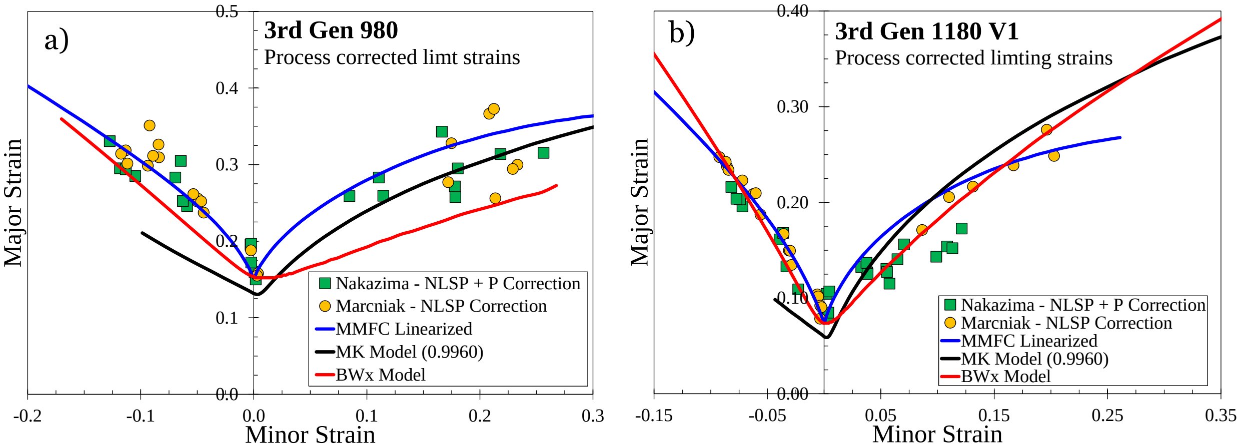

Figure 67: Analytical FLC variants with the best agreement superimposed with the limit strains that have undergone process corrections for a) 3rd Gen 980 and b) 3rd Gen 1180 V1

From this study, an objective and deterministic methodology to generate analytical limit strains was made. The methods presented are free of calibration bias where only mechanical test data is required to generate the FLC. Process corrections are also an essential step to enable direct comparisons with analytical FLCs. To objectively conduct an analysis of limit strains from an experimental perspective, it is recommended that a similar methodology is implemented.

4 B-pillar Design, Stamping Trials and Correlation

This chapter discusses the methodology employed in the design phase of the B-pillar technology demonstrator using AutoForm R8 finite element software followed by correlation of the models with the stamping trials. Bowman Precision Tooling led the design of the B-pillar demonstrator in collaboration with HDMA, AISI and the University of Waterloo project team. The constitutive and formability models described in Chapters 2 and 3 were provided to Bowman in AutoForm for the design phase. Using AutoForm R8 with the constitutive and formability models from Chapters 2 and 3 to generate the material model, the formability of the 3rd Gen 980 and 3rd Gen 1180 V1 B-pillars will be assessed. The objective of this chapter is to determine splitting locations on the B-pillar and observe how predictions correlate with the forming trials. Kinematic hardening data of the 3rd Gen AHSS was not available at the time of the B-pillar design so literature data was employed to aid in the springback compensation of the tooling. Bowman Precision Tooling fabricated the tooling and performed the forming trials in the first year of the project to enable an assessment using conventional modelling practices. My role in the B-pillar design was to work with Bowman in developing the AutoForm material cards and aid with the forming simulations to revise the models and correlation in the project as more data became available such as the kinematic hardening data for springback. In parallel, I was developing the detailed forming model of the B-pillar process in LS-DYNA with fracture for correlation with the stamping trials and for transferring the model into the LS-DYNA impact simulation that are discussed in Chapters 5 and 7, respectively.

4.1 AutoForm R8 Model Development, Tool Design, and Springback Compensation

HDMA provided the B-pillar geometry for a hot stamped TWB B-pillar for a mid-size SUV to adapt to the 3rd Gen AHSS as a demonstrator while removing production-related features as seen in Figure 68a. The primary features of the untrimmed B-pillar are the side sill, roof rail, and the fold initiators seen in Figure 68b and the trimmed B-pillar seen in Figure 68c. The B-pillar technology demonstrator was designed by Neil Parker of Bowman Precision Tooling using AutoForm R7 software in consultation with the CAE team at HDMA. The beginning of the project utilized AutoForm R7 but switched to R8 later in the project when the software was released.

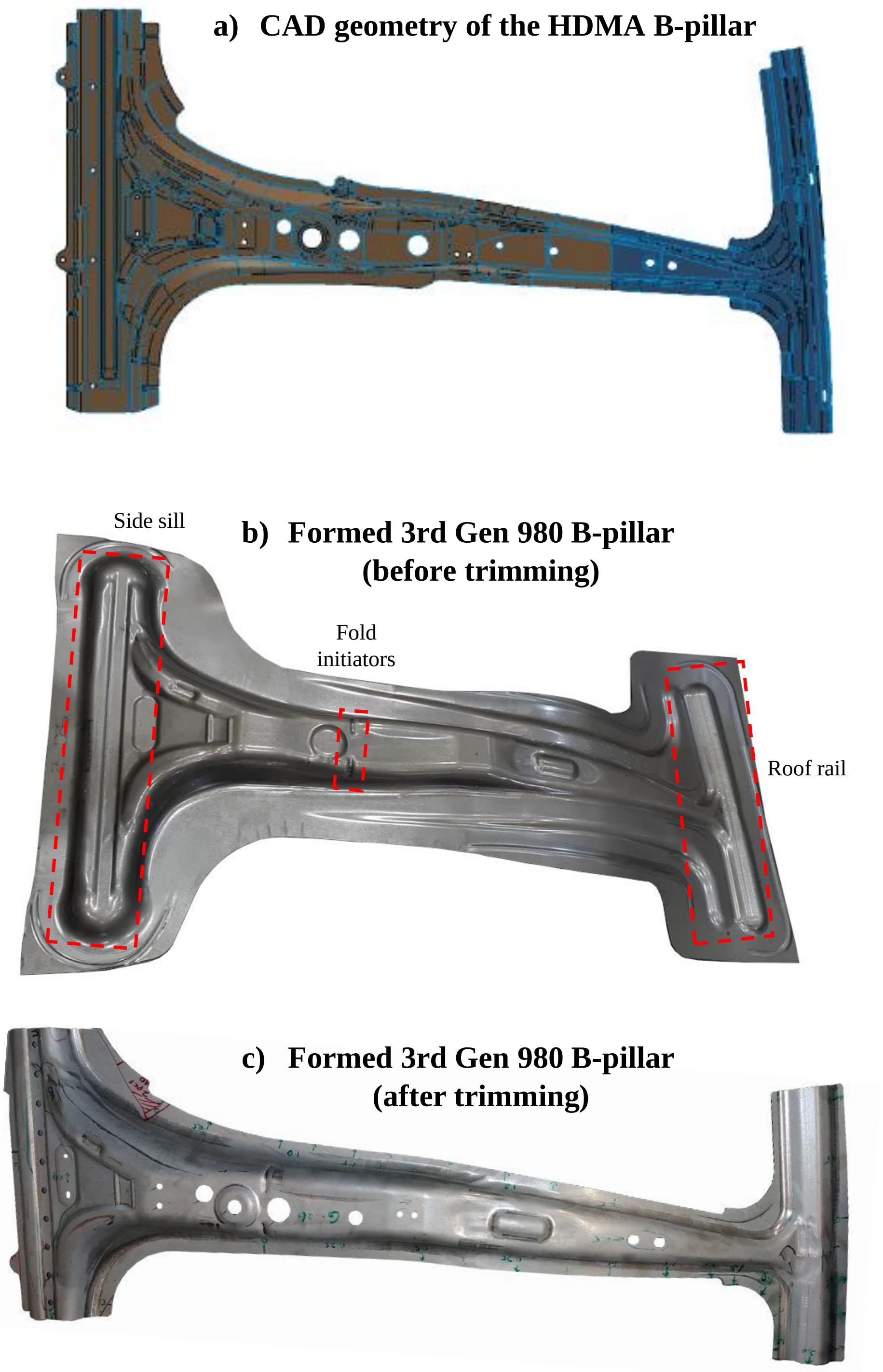

a) CAD geometry of the HDMA B-pillar

b) Formed 3rd Gen 980 B-pillar (before trimming)

c) Formed 3rd Gen 980 B-pillar (after trimming)

Figure 68: B-pillar CAD geometry a) before trimming used in tooling design, b) a formed 3rd Gen 980 B-pillar before trimming indicating the locations of the side sill, fold initiators, and roof rail and c) a formed 3rd Gen 980 B-pillar after trimming

The initial AutoForm simulations used in designing the tool and the corresponding forming limit curves are shown in Figure 69. The tooling was designed for the 3rd Gen 980 with no indications of splitting predicted which was later confirmed in the forming trials. The AutoForm simulations of the 3rd Gen 1180 V1 predicted severe splitting particularly at the bending regions. It will be shown later in the chapter that splitting in the forming trials of the 3rd Gen 1180 V1 B-pillars only occurred in one location instead of several. The initial tool design was performed using von Mises isotropic plasticity, isotropic hardening determined from the tensile and shear tests, and a preliminary FLC obtained using the Marciniak test data.

With the B-pillar geometry identified, the tooling must then be modified to compensate for springback of the blank to its desired final shape. A total of five iterations of tool compensation were performed which included the forming and trimming to predict the final part shape. The as-fabricated tooling is shown in Figure 70. Chapter 6 will focus upon the methodology and material data used in the springback modelling.

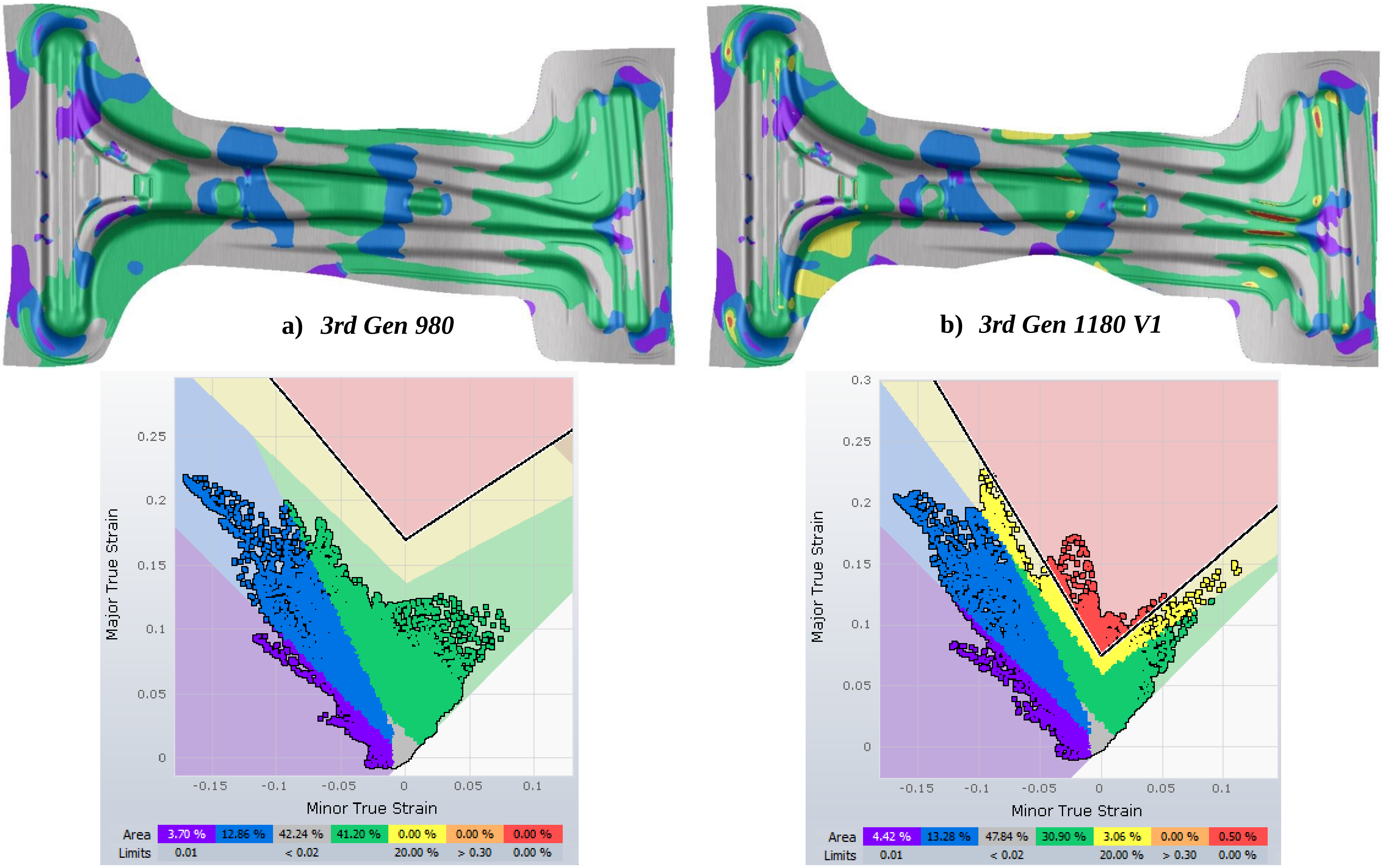

Figure 69: Preliminary simulations used to drive the modifications of the B-pillar tooling where the forming contours of the a) 3rd Gen 980 are visualized and the b) 3rd Gen 1180 V1 forming simulations are visualized

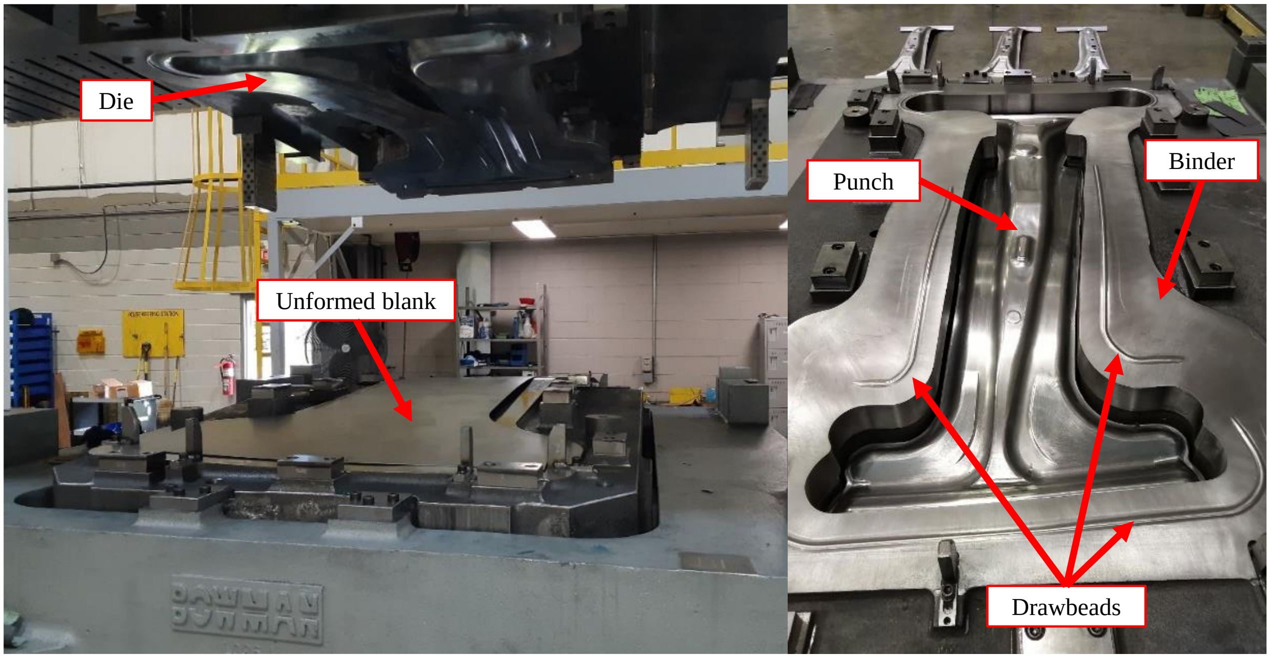

Figure 70: Tooling of the B-pillar geometry designed and machined by Bowman Precision Tooling

4.2 Forming Simulation Methodology and Results

The final shape and general dimensions of the initial blank was generated iteratively to minimize the likelihood of the splitting using AutoForm R8. The initial shape of the blank and its general dimensions are seen in Figure 71. The mesh is automatically generated in AutoForm R8 which exclusively uses triangular elements utilizing elasto-plastic shell theory with mesh refinement focused on areas of high deformation where the finest mesh refinement occurs at the drawbeads visualized in Figure 72. A setting of 11 through-thickness integration points and a maximum number of 6 mesh refinements were selected to improve predictions at high strain areas such as the drawbeads and at locations with high deformation. The profile of the blank was assumed to be water or laser cut and not sheared to minimize the risk of splitting which is common in the initial design of tooling.

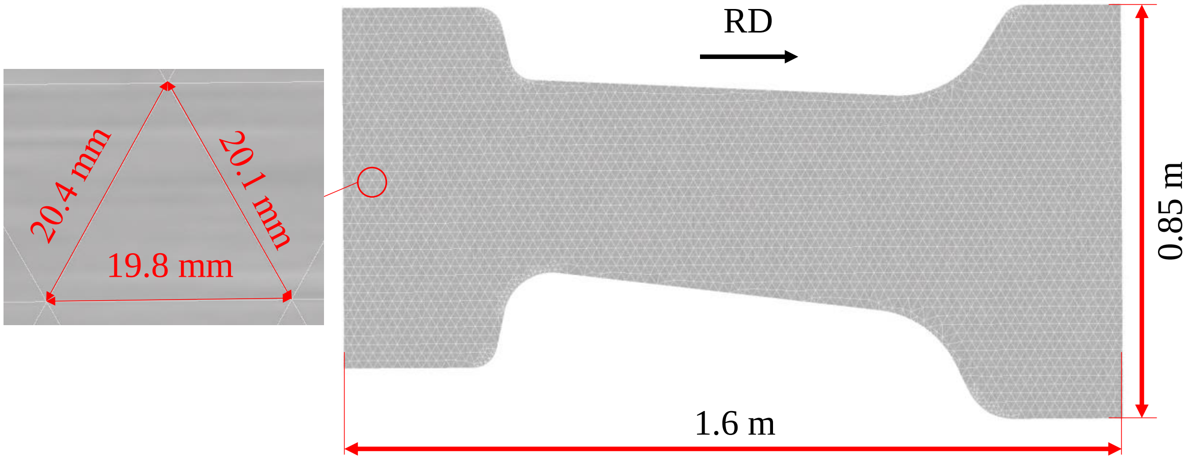

Figure 71: General dimensions and initial mesh of the blank before the B-pillar is formed

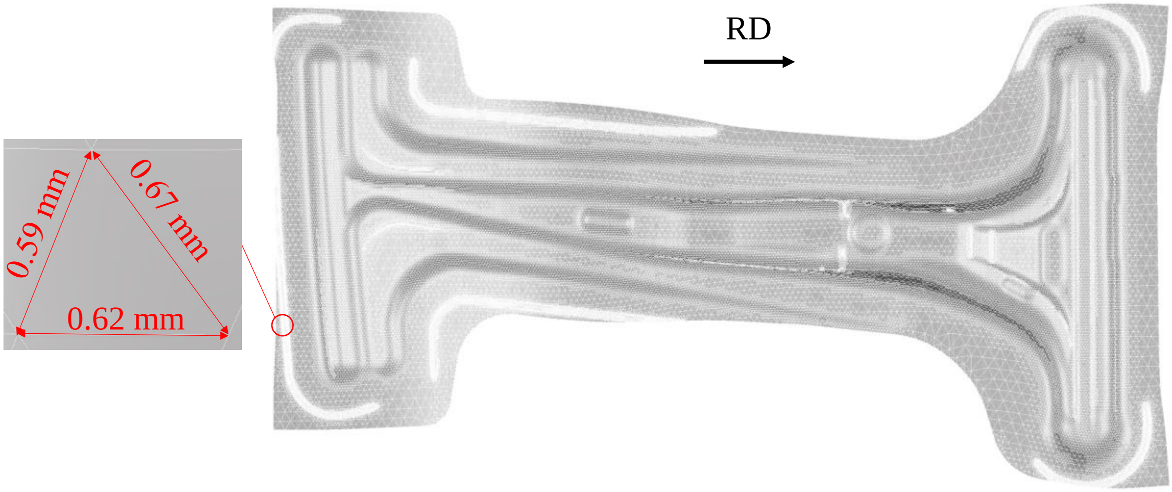

Figure 72: Refined mesh size of the blank at the drawbeads after B-pillar forming

The forming process parameters were selected based upon the 1600-ton mechanical forming press at Bowman. The speed of the press was run at 10 SPM which uses a 900 mm press stroke with forming occurring during the last 100 mm. The motion of the press was emulated by the sinusoidal motion curve in Figure 73 where the movement follows the behavior of an idealized crank-slider. A binder pressure of 1600 kN using 16 Kaller® X20000-125 nitrogen cylinders were employed and modelled by using the pressure vs. displacement curve for a charging pressure of 1500 psi. Kaller® provides a force calculator that accounts for the X-series, its model, stroke length, number of cylinders used, stroke distance, and stroke rate. The binder pressure response is seen in Figure 74.

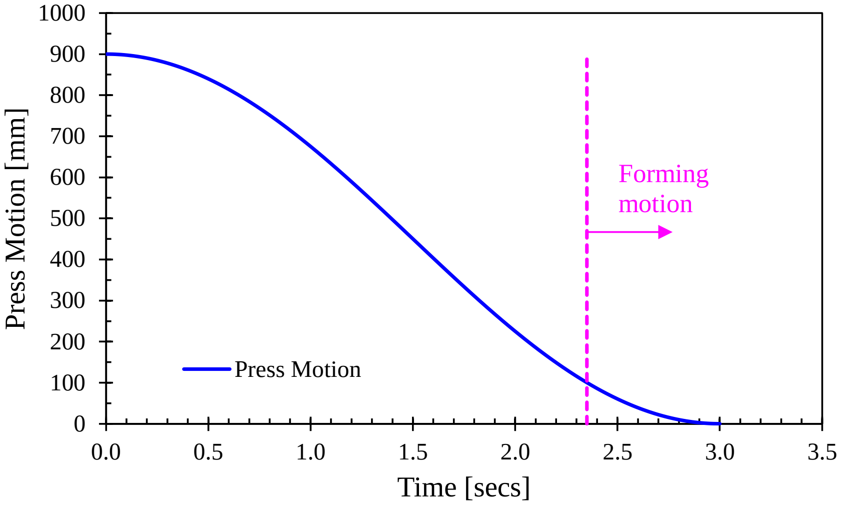

Figure 73: Press motion during forming where the last 100 mm of the press stroke forms the B-pillar

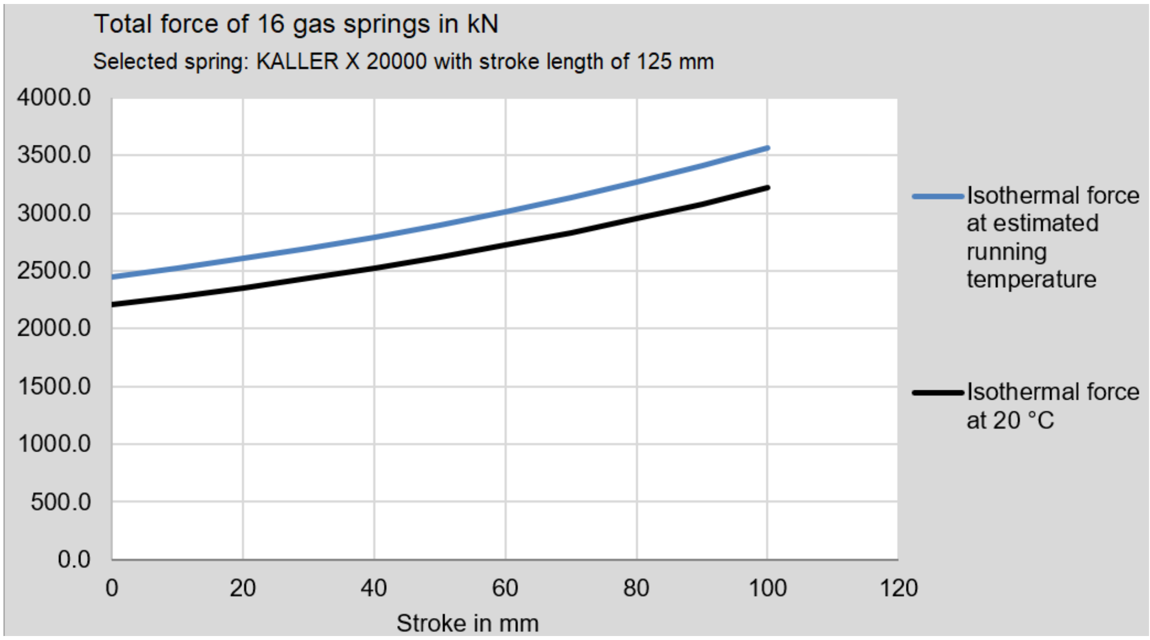

Figure 74: Binder pressure response of 16 gas cylinders using nitrogen as its pressure medium, 100 SPM, and a binder stroke of 100 mm (Kaller, 2021)

The lubricant for the forming trials was CommDraw™ 220, a water-soluble lubricant used in high-tonnage stamping processes. Twist compression tests (TCT) of the lubricant on the steels were performed by Dr. Jacqueline Noder with an approximate friction coefficient of 0.15. The drawbeads in the tool were modelled analytically to minimize run time. The tooling was machined with 5-axis machining that used a DMU 340 Gantry with a positional accuracy of 15 μm.

The hardening behavior is described using the modified Hockett-Sherby model with strain rates represented in Figure 41. The yield function selected was the Vegter yield function (Vegter and van den Boogaard, 2006) where a second-order Bezier curve creates a piecewise convex yield surface. The methodology of Abspoel *et al*. (2017) is used in AutoForm R8 to create the Vegter yield function where it generates the biaxial, plane strain, and shear points by only using tensile data. The tensile data that is used by the Vegter yield surface are the uniform elongation, tensile strength, and r-values oriented at 0°, 45°, and 90° with respect to the rolling direction. Lastly, the FLC predicted by the BWx model was input into AutoForm R8 to predict necking and splitting.

The predicted B-pillar strain distributions for the three 3rd Gen AHSS steels are visualized in Figure 75, along with its corresponding FLCs showcasing the linear and non-linear strain path options. Both linear and non-linear strain path settings were considered to determine their effects on the forming predictions. This comparison of the linear and non-linear strain path options can help with the assessment of potential splits as most industrial forming operations involve nonlinear paths. A larger safety margin is evident in the 3rd Gen 980 B-pillar when using the non-linear FLC option in comparison to the linear FLC where a similar trend was also observed for 3rd Gen 1180 V2 with mild splitting occurring in some areas. The predictions from 3rd Gen 980 and 3rd Gen 1180 V2 are contrasted by the predictions of 3rd Gen 1180 V1 where the opposite trend is observed. Upon activation of the NLSP setting, the likelihood of splitting increased as the strain data points approached closer to the FLC.

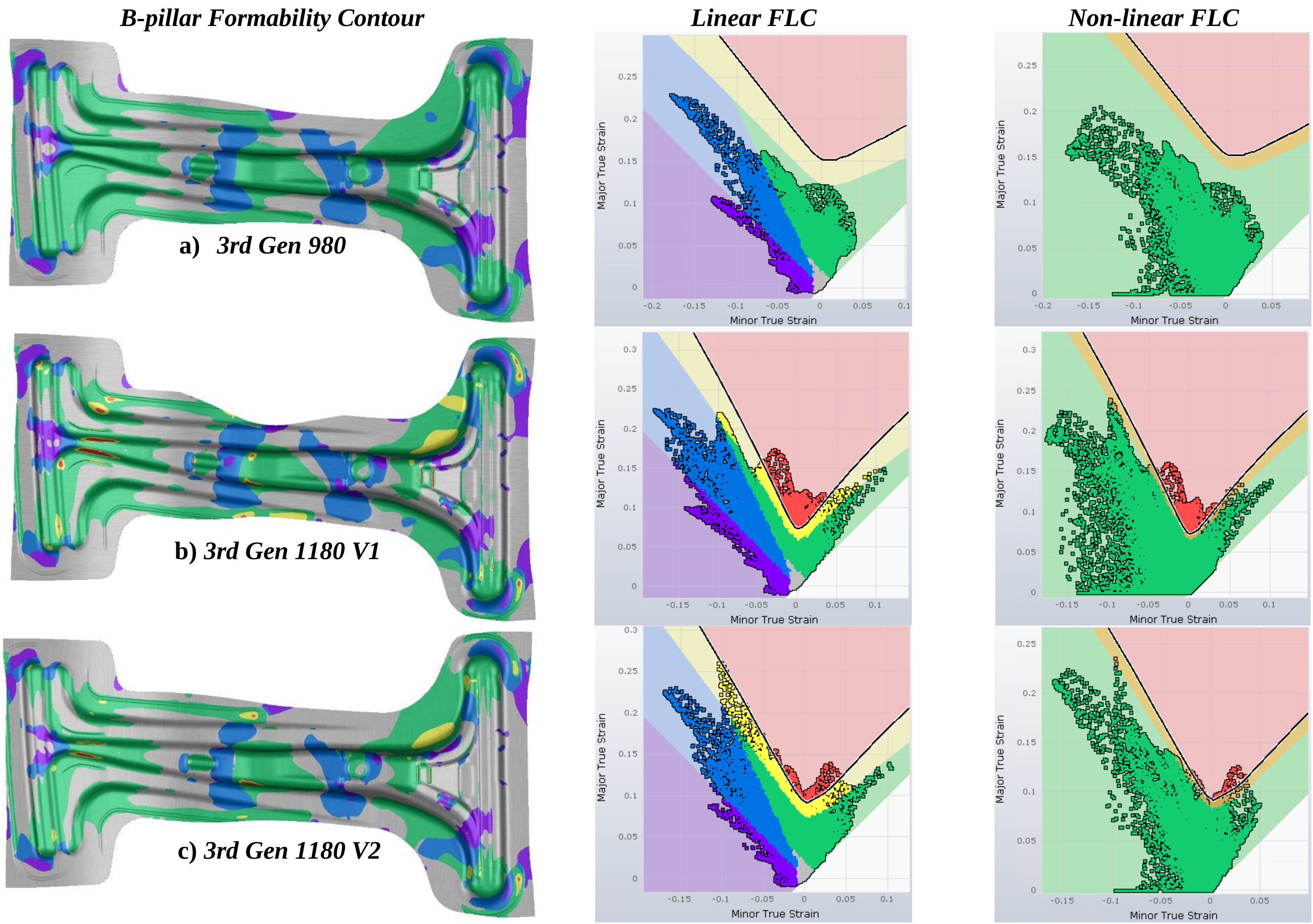

Figure 75: Formability contours of a) 3rd Gen 980, b) 3rd Gen 1180 V1, and c) 3rd Gen 1180 V2 along withs its FLC showing linear and non-linear strain paths

4.3 Correlation of AutoForm R8 Simulations with Forming Trials

The 3rd Gen 980 AutoForm R8 forming simulations predicted no splitting would occur which was confirmed in the forming trials. The formed part is shown in Figure 76. The forming simulation predicted multiple splits in the 3rd Gen 1180 V1 although only one location resulted in a fracture in 7 of 10 B-pillars and shown in Figure 77.

Figure 76: A successful forming trial of the 3rd Gen 980 B-pillar

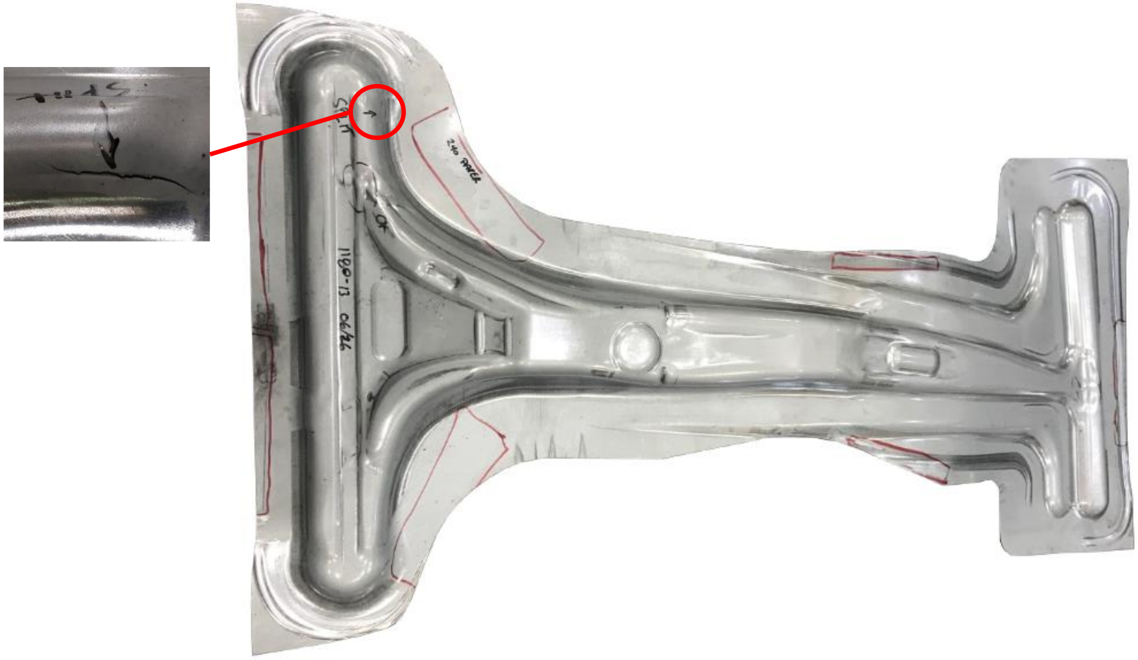

Figure 77: Split on located at the forming trial of the 3rd Gen 1180 V1 B-pillar

The occurrence of splitting is not unexpected since the strain path seen in Figure 78 indicates a risk of splitting when using the non-linear FLC option. The other locations predicted in regions around plane strain tension shown in Figure 79 were anticipated to be “false positives” due the FLC not accounting for the bending and tool contact. Highlighted in Figure 79 are the strain paths of the elements of the B-pillar that are reported to split. These elements that are predicted to split are primarily located in the middle of the B-pillar. A comparison of the Marciniak and Nakazima FLC$_0$ strains of 0.09 and 0.13, respectively, demonstrate that tool contact, and mild bending can have a marked improvement on the limit strains of the 3rd Gen 1180 V1 steel. The influence of bending in plane strain on the forming limits for both steels is shown in Figure 80.

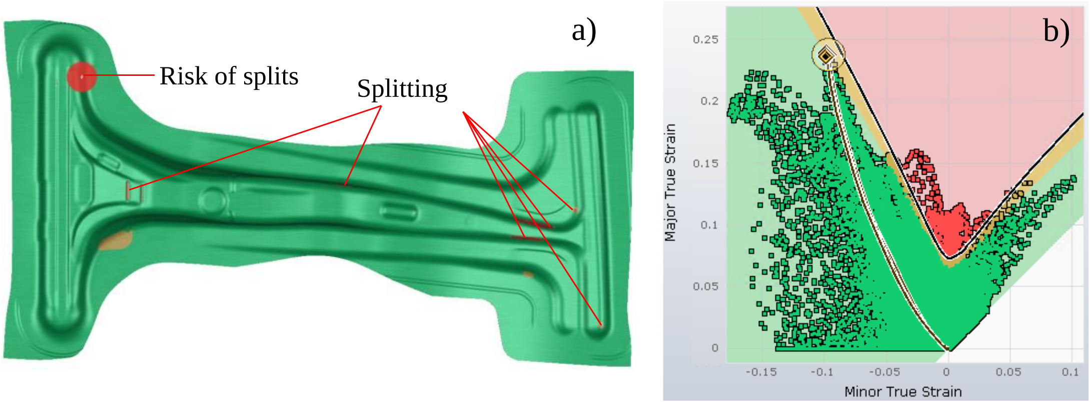

Figure 78: Formability contour a) of 3rd Gen 1180 V1 B-pillar using AutoForm R8 with the activation on the NLSP option b) using the BWx model as the FLC

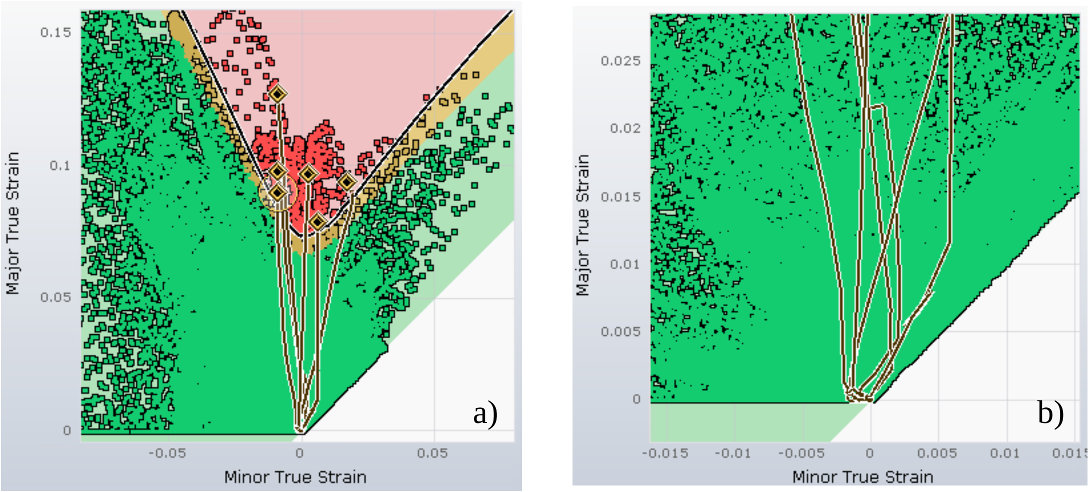

Figure 79: The strain paths of the splitting elements located at bending regions on the 3rd Gen 1180 V1 B-pillar after being formed. The alternate picture shows a zoomed in strain path highlighting non-linearity where the BWx model is used as the FLC

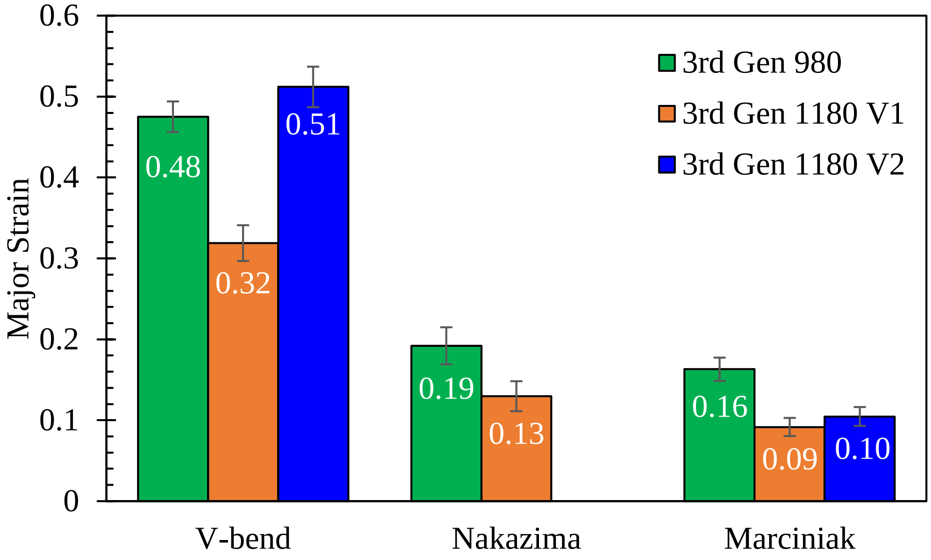

Figure 80: Major strain of 3rd Gen AHSS grades undergoing v-bending, Nakazima testing, and Marciniak testing. Note that no Nakazima tests were performed for 3rd Gen 1180 V2

4.4 Discussion, Conclusions, and Recommendations on AutoForm Forming Simulations

It is emphasized that the problematic failure predictions using the FLC is not a shortcoming of AutoForm software but a consequence of using the FLC in stamping design. The strain path by itself cannot distinguish whether the region is experiencing strain in bending or in-plane stretching. Alternate metrics of evaluating limit strains exist to account for certain process effects albeit to a limited degree. Common practice in stamping simulations is to use the so-called mid-plane rule (MPR) to evaluate the forming limits since this corresponds to the approximate location of the neutral layer in mild-to-moderate bending so that any strain present is assumed to be due to stretching. Tharrett and Stoughton (2003) proposed using the material on the inner layer in contact with the punch as the so-called concave side rule (CSR). Future work is required to account for the influence of contact stress and bending on the forming limits in stamping simulations of 3rd Gen AHSS.

5 B-pillar Forming Simulations and Correlation using LS-DYNA

This chapter discusses the methodology in developing the B-pillar forming simulations in LS-DYNA which is a commercial finite-element solver used within the automotive industry for forming and crash. AutoForm software is designed specifically for forming simulations and has some simplifying assumptions in the element options and solution methodology to enable short runtimes. LS-DYNA is a powerful explicit finite-element code that enables the use of a larger range of element types and constitutive models. The use of LS-DYNA allows for the comparison of geometry after springback which is discussed in Chapter 6. Forming simulations ran in LS-DYNA also enables the mapping of the residual strains and damage from the forming model into the impact simulations in Chapter 7. AutoForm models can be exported for input into LS-DYNA for crash but there are differences in the use of the constitutive, fracture models and element types that were desired to be avoided in this thesis.

The LS-DYNA forming simulation is significantly more involved than AutoForm which streamlines much of the modelling. The LS-DYNA simulation stages involve gravity loading then forming followed by trimming and springback stages. The gravity loading assists in locating the B-pillar appropriately on the tooling. The forming simulations were run using LS-DYNA R9.3 double precision. The finalized constitutive, formability and fracture data of Chapter 2 and 3 were used in the forming simulations as the LS-DYNA modelling followed by the B-pillar design and forming trials. The springback predicted by LS-DYNA was then compared with part-scans of the B-pillars for the 3rd Gen 980 and 3rd Gen 1180 V1. Similar to Chapter 4, the objective is to assess the formability of the 3rd Gen 980 and 3rd Gen 1180 V1 B-pillars but with LS-DYNA, additional parameters are included to observe the effects of rate sensitivity and varying number of integration points. The simulations generated in this chapter are then used in Chapter 6 (springback) and Chapter 7 (crashworthiness). The B-pillar stamping trials of the 3rd Gen 1180 V2 have not been performed due to project delays related to the pandemic but forming simulations are included for future correlation.

5.1 Simulation Stages for B-pillar Forming

5.1.1 Simulation Stage – Gravity Loading

Gravity loading is required to allow the blank to naturally conform to the shape of the binder due to the large size of the B-pillar blank of approximately 1.6 m in length with respect to its thickness of 1.4 mm. Gravity loading induces the force of gravity on the blank such that it descends on the binder. With gravity loading, the blank conforms to the shape of the binder. This assists with the forming stage so that the contact between the blank, die and punch is correctly modelled. If gravity loading is excluded, the blank would form to the shape of the die as it descended downward to the binder causing a pre-form before making contact with the punch. Allowing the blank to rest on the binder via gravity loading ensures an elastic pre-form. The shapes of the blank before and after gravity loading can be observed from the side view of the binder and blank shown in Figure 81.

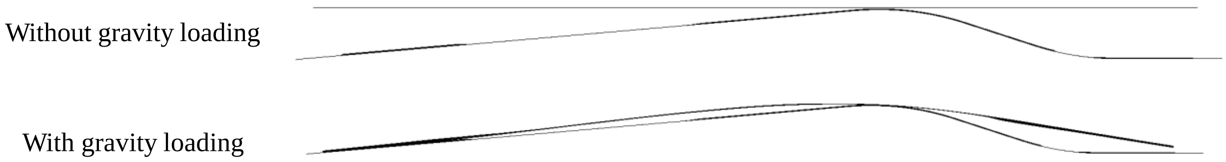

Figure 81: Side view of the binder and blank with and without gravity loading

5.1.2 Simulation Stage – Forming

The press motion, stroke rate, friction coefficient, and binder pressure are the same as described in Chapter 4.2 using AutoForm. The designation of each component of the tooling is shown in Figure 82.

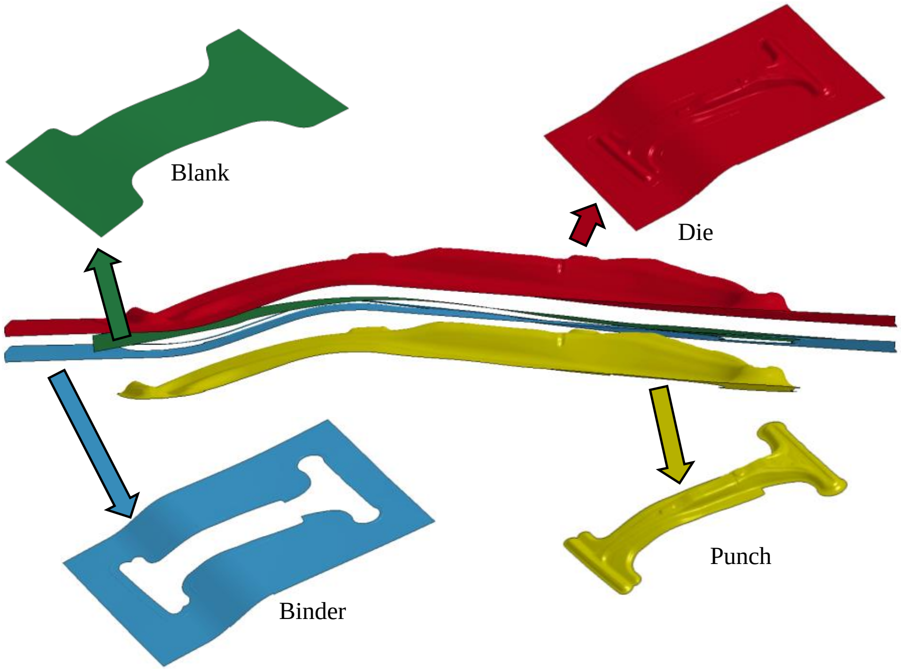

Figure 82: Tool set arrangement of the B-pillar tooling emulating the forming trials

The explicit solver within LS-DYNA is conditionally stable with the time step constrained by the Courant criterion. The time step, Δt, must not be greater than the time it takes for a sound wave to travel through the smallest element in the simulation. The Courant criterion is defined

$$\Delta t = \frac{L_{\min}}{c} = L_{\min} / \sqrt{\frac{E}{\beta}} \tag{36}$$

where c is the wave speed, β is the density and L_{min} is the minimum element characteristic length (defined as the square root of the area for shell elements or cubed root for solids).

Depending on computational resources and the size of the simulation, run times for large scale explicit simulations can take multiple days. To mitigate arduous run times, several techniques can be employed for computational efficiency. Implementing symmetry boundary conditions to reduce the model size is commonly used but is not applicable to the B-pillar. Mass scaling can be used by artificially increasing the density to relax the minimum time step. Mass scaling increases the density of certain elements consequently increasing the time step, according to Eq. 9, ultimately reducing run times. Caution must be taken when mass scaling to avoid non-physical results as it increases inertial effects that can change the deformation mode. In the present work, selective mass scaling (SMS) was invoked in LS-DYNA to only add mass to elements whose timestep fell below the specified minimum time step. A selective mass scaling factor of 10^{-6} seconds was selected after an initial parametric study. For the present study, it was not feasible to deactivate SMS due to long computational run times. The internal energy was checked against the hourglass energy where the hourglass was below 10% than the internal energy. A study done by Du Bois and Du Bois (2018) showed that mass scaling is a viable solution to reducing runtime while achieving reasonable numerical predictions.

5.2 Simulation Parameters

The tooling for the B-pillar was modelled using a rigid, non-deformable material model (*MAT_020 / *MAT_RIGID) with the standard mechanical properties of steel listed in Table 9. The tooling used tetrahedral elements with an average mesh size of 8 mm for the flat surfaces with an average mesh size of 1 mm used to describe features with a higher degree of curvature such as the drawbeads. The rigid tools such as the binder, punch, and die are shown in Figure 82. A penalty-based one-way surface-to-surface contact algorithm is defined between the blank and the tooling where the tooling is the master surface and the blank is the slave. Within LS-DYNA, the contact card used is *CONTACT_FORMING_ONE_WAY_SURFACE_TO_SURFACE.

The 1.4 mm thick blank was modelled with fully integrated (Type 16) quadrilateral shell elements with a mesh size of 3.0 mm. The number of through-thickness integration points was varied with values of 3, 7, and 11 considered. The blank deforms according to the anisotropic plane stress Yld2000 model of Barlat *et al.* (2003) (*MAT_133 / *MAT_BARLAT_YLD2000) with its parameters previously defined in Table 5.

Table 9: Mechanical properties of steel used in the rigid tooling

Property	**Value**	**Units**
Density	7890	kg/m^3
Young's Modulus	200	GPa
Poisson's Ratio	0.3	

5.3 Simulated Results – Forming

To visualize the plastic deformation of the B-pillar, the plastic strain distributions after forming for the 3rd Gen 980 and 3rd Gen 1180 V1 are shown in Figure 83. The strains are high near the drawbeads that control metal flow into the tool by bending-unbending. High strains near the drawbeads are expected and potential fracture was not a major concern. The profile of the beads can be ground down or have shims added if fracture occurs during tool try-out. No drawbead fractures occurred in the actual forming trials. The regions of concern involve moderate strains in regions of curvature due to bending and stretching in plane strain around the sidewalls. The following section will perform a deeper investigation on bend locations by looking at the strain paths, the number of integration points, and how strain rate sensitivity affects the formability and fracture predictions.

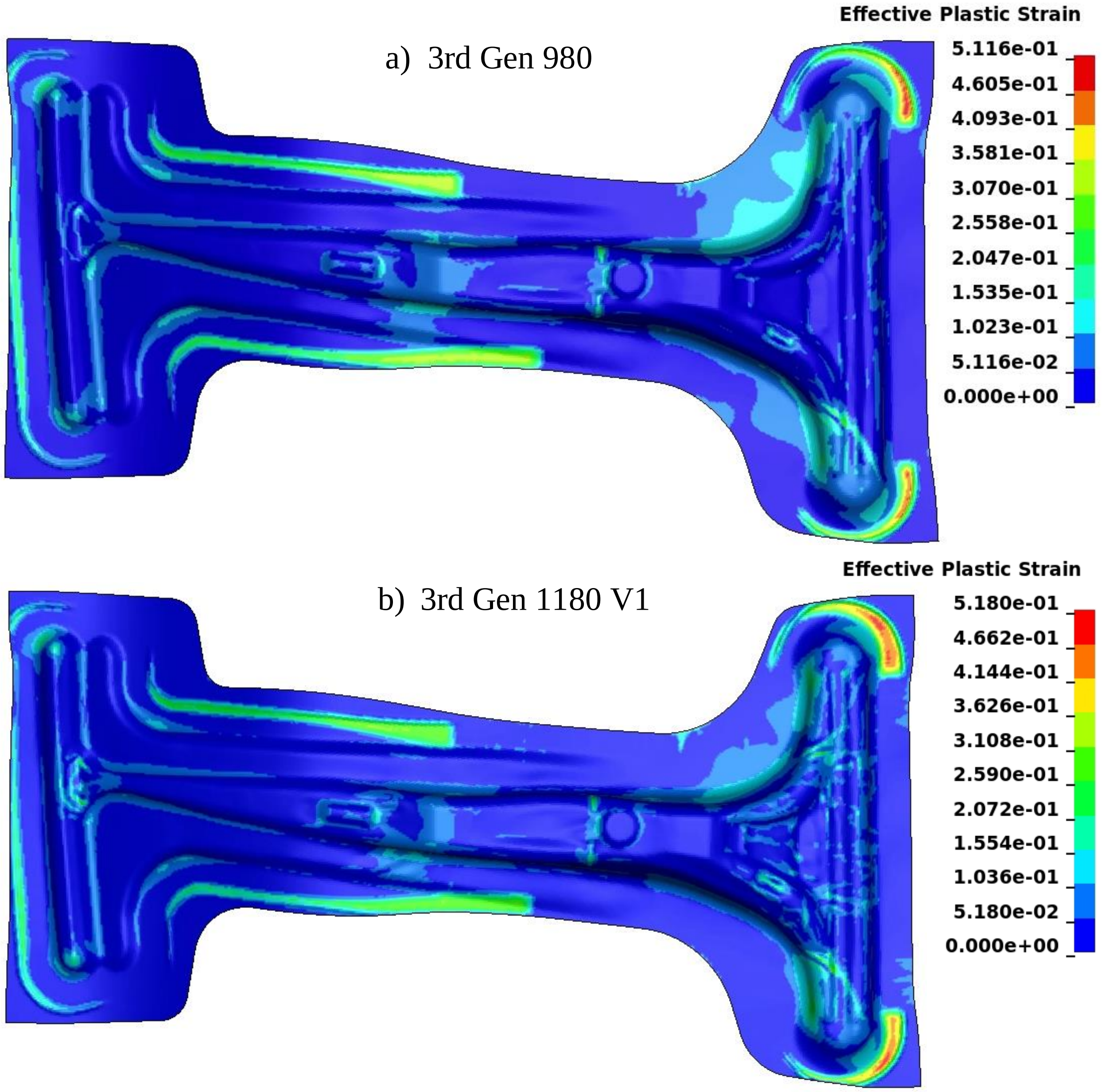

Figure 83: Strain distribution of a) 3rd Gen 980 and b) 3rd Gen 1180 V1 using 11 integration points and GISSMO disabled.

5.3.1 Influence of the Strain Rate Sensitivity and Number of Integration Points

The inclusion of strain rate on the dynamic hardening response is beneficial to accurately predict the local strains in forming operations, especially at elevated temperatures. Steels have a positive strain rate sensitivity where the hardening rate increases which serves to delay strain localization and distribute the strain in a more uniform manner. Often, only quasi-static tensile data is available due to the cost and time required for high-rate characterization so it is of interest to evaluate both cases for 3rd Gen AHSS forming along with the number of shell integration points to resolve through-thickness strain gradients in regions of stretch-bending. Fracture was turned off but was evaluated in evaluated at Appendix A.

The three different cases for the number of integration points (NIPs) of 3, 7 and 11 were selected based upon computational constraints. A preliminary case of 19 NIPs took longer than 7 days running with 32 cores and not possible to pursue due to the shared use of the cluster in the Forming and Crash research group. For each NIP case, models with quasi-static and dynamic hardening were considered for both 3rd Gen 980 and 3rd Gen 1180 V1. The forming limit index contours for 7 NIPs for 3rd Gen 980 are showcased in Figure 85 and Figure 86 with the legend for forming limit index presented in Figure 84. The forming limit curve for the BWx model from Chapter 3 was input into LS-PrePost to generate the forming limit index contour plots.

Cracks	🟥
Risk of cracks	🟨
Safe	🟩
Wrinkling tendency	🟦
Wrinkles	🟪

Figure 84: Legends from the forming simulations where each data point represents an element in the B-pillar simulation

The influence of NIP from 3 – 11 was minimal so for brevity, the case of NIP = 7, was selected as the representative case. Any notable differences for the other NIP cases are discussed within the text. The forming simulations for the 3rd Gen 980 B-pillar report forming contours where no splitting occurs with mild wrinkling in several locations as seen in Figure 85 and Figure 86. These results are consistent with the forming trials where all 3rd Gen 980 B-pillars successfully formed. The inclusion of strain rate sensitivity on the 3rd Gen 980 forming simulation did not make a significant difference on formability, especially since the part was already predicted to safe using the quasi-static data.

Two strain paths are extracted at the “Bend area” and at “Tumblehome – bottom” indicated in Figure 85 and Figure 86. The minimal effects of rate sensitivity are further substantiated by the formability strain cloud illustrated in Figure 87 for the 3rd Gen 980 with 3, 7, and 11 NIPs with and without strain-rate (SR) sensitivity. The strain paths of the lower, middle, and upper integration points are plotted. These locations were selected since splitting occurred at the tumblehome on the 3rd Gen 1180 V1 forming trials. Increasing the number of through-thickness integration points had a marginal influence upon the 3rd Gen 980 B-pillar forming simulations.

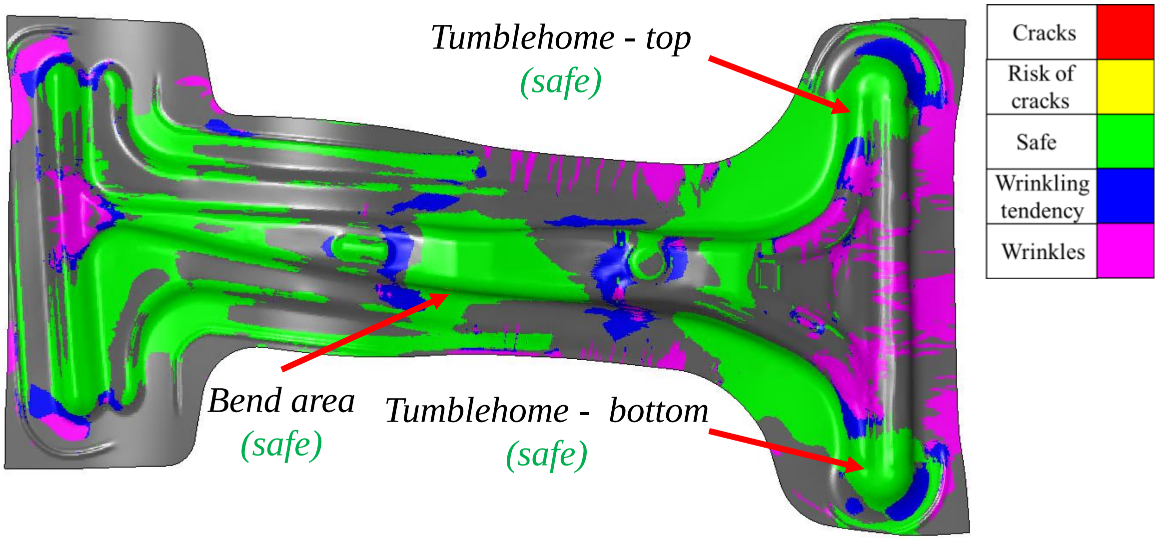

Figure 85: Strain contour of 3rd Gen 980 with 7 NIPs without strain rate effects. Strain paths extracted in Figure 86 is extracted from Tumblehome – bottom

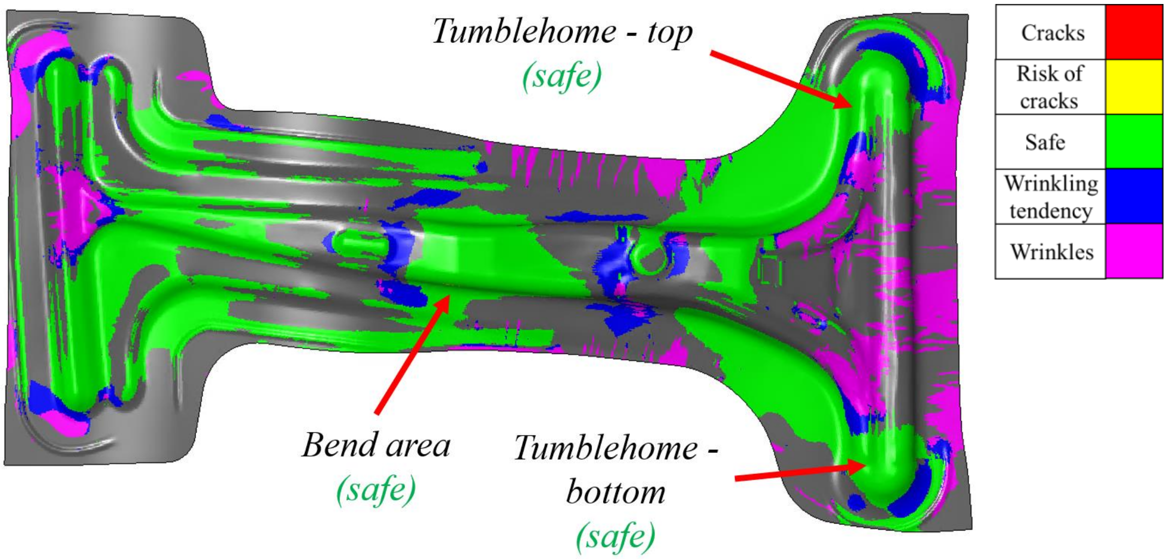

Figure 86: Strain contour of 3rd Gen 980 with 7 NIPs coupled with strain rate effects. Strain paths extracted in Figure 86 is extracted from Tumblehome – bottom

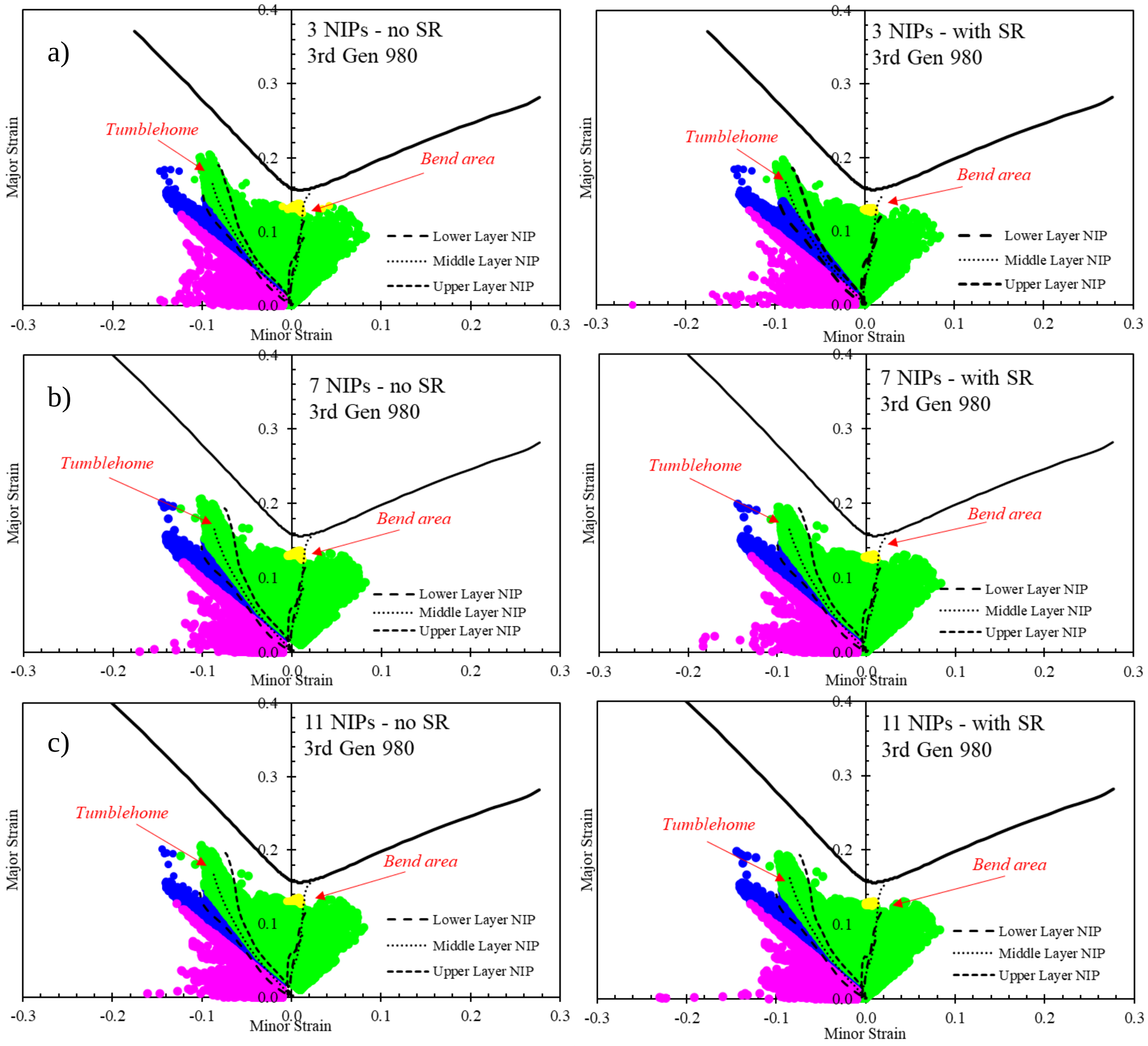

Figure 87: Formability strain cloud indicating risk of cracking, wrinkling, and the BWx model for 3rd Gen 980 using a) 3 NIPs, b) 7 NIPs, and c) 11 NIPs. The strain path from the crack location is extracted located at the tumblehome and at the bend area. Refer to Figure 83 for legend.

In contrast to the 3rd Gen 980, the 3rd Gen 1180 V1 forming simulations predict multiple splits as indicated by the red elements in Figure 88 and Figure 89 and the red data points in Figure 90. The primary locations of interest are the bend area and the tumblehome locations, both top and bottom. Strain rate effects play a significant role in the generation of strains for 3rd Gen 1180 V1 as seen in Figure 90. Without rate effects, strains accumulate to much higher values which consequently leads to the simulation reporting more elements exceeding the limit strains. As with the 3rd Gen 980, the influence of NIPs was marginal for the forming of the 3rd Gen 1180 V1 B-pillar. Overall, the fracture location at the Tumblehome in the 3rd Gen 1180 V1 is correctly predicted but as with the AutoForm simulations in Chapter 4, false positives for cracking are also reported in regions of bending due to use of the in-plane FLC.

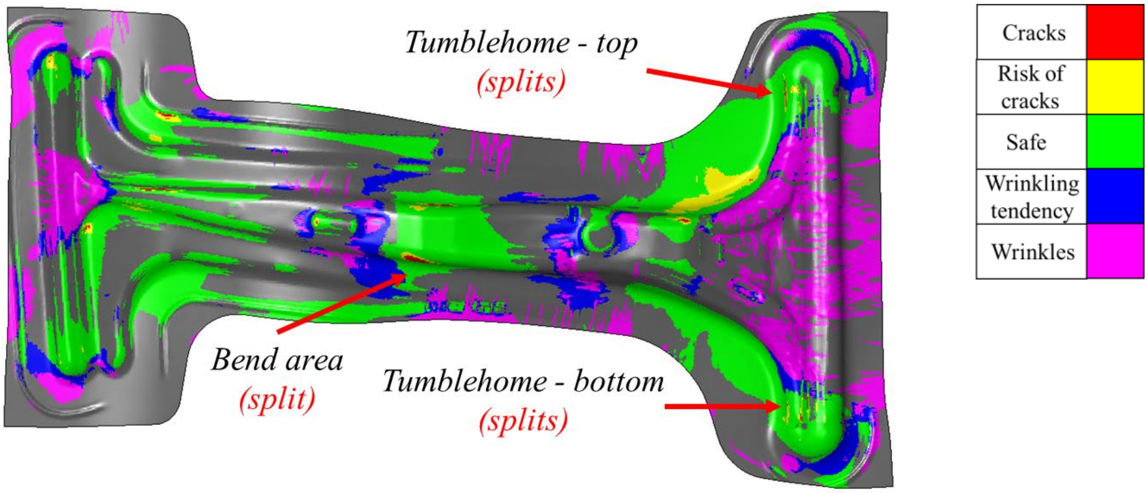

Figure 88: Strain contour of 3rd Gen 1180 V1 with 7 NIPs without strain rate effects highlighting the bend area and tumblehome. The strain path in Figure 89 is extracted from Tumblehome – bottom

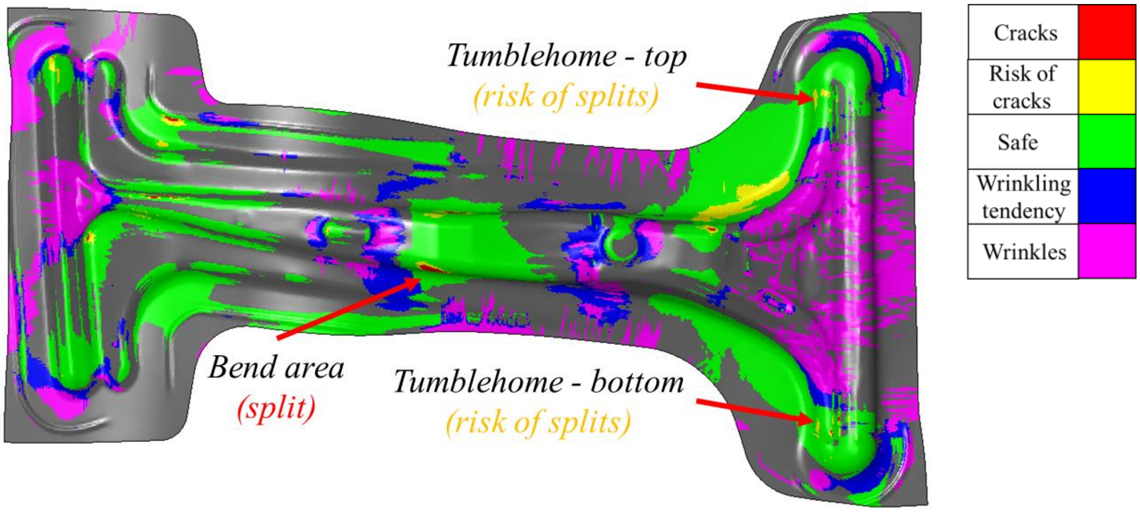

Figure 89: Strain contour of 3rd Gen 1180 V1 with 7 NIPs coupled with strain rate effects highlighting the bend area and tumblehome. The strain path in Figure 89 is extracted from Tumblehome – bottom

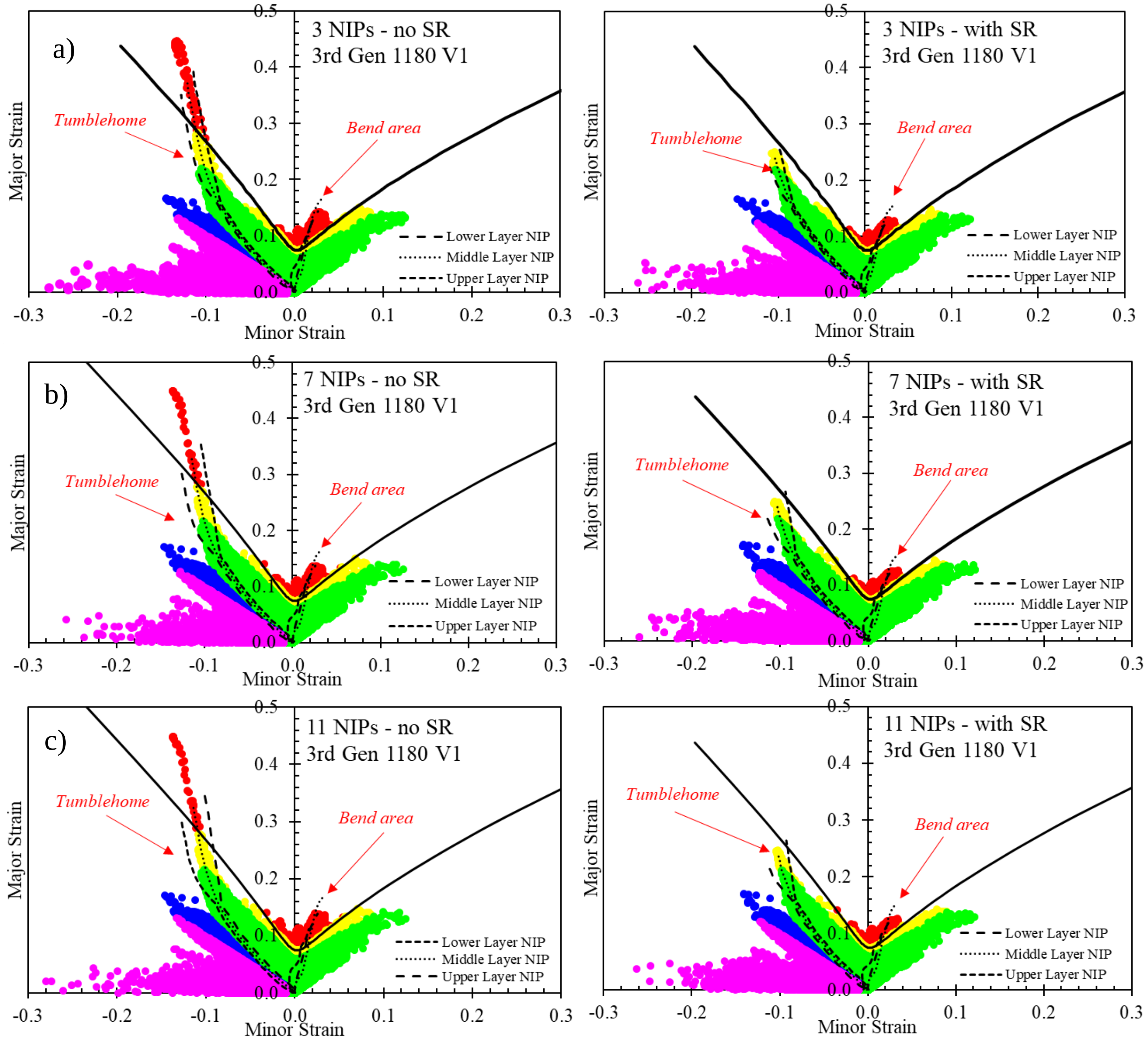

Figure 90: Formability strain cloud indicating risk of cracking, wrinkling, and the BWx model for 3rd Gen 1180 V1 using a) 3 NIPs, b) 7 NIPs, and c) 11 NIPs. The strain path from the crack location is extracted located at the tumblehome and at the bend area.

5.3.2 Study on 3rd Gen 1180 V2

No forming trials were performed for the 1180 V2 so the formability is evaluated numerically using 7 NIPs and the results shown in Figure 91. The strain paths were extracted from the lower, middle, and upper layers at the tumblehome and bend area where the side walls are formed. The inclusion of strain rate sensitivity significantly improved the predicted formability although strains in the bend area still exceed the FLC. Given the superior formability and fracture limits of the 3rd 1180 V2 compared to the V1 discussed in Chapter 2, and the fact that 3rd Gen 1180 V1 formed with minimal cracking, it is expected the V2 B-pillar would successfully form.

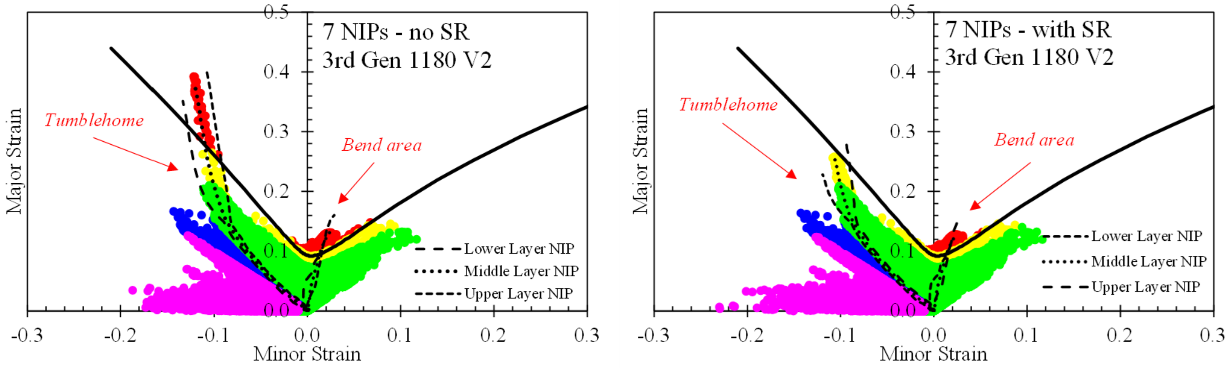

Figure 91: Formability strain cloud indicating risk of cracking, wrinkling, and the BWx model for 3rd Gen 1180 V2 using 7 NIPs. The strain path from the crack location is extracted located at the tumblehome and at the bend area.

5.4 Discussion, Conclusions and Recommendations on LS-DYNA Forming Simulations

Two deformation modes are highlighted and discussed throughout the forming of the B-pillar, in-plane stretching and stretch-bending. The FLC provided a simple overview on inspecting potential splitting based on in-plane stretching. The tumblehome of the B-pillar was a location where splitting truly occurred in the forming trials. Based on the in-plane FLC, there are two locations where splitting is predicted: the tumblehome and at the bend area where the side walls are formed located roughly in the middle of the B-pillar. Strain rate effects and number of integration points affect the final outcome of the strain cloud of the forming simulations for both variants of the higher strength 1180 MPa steels. Rate sensitivity served to reduce strain accumulation in the tumblehome region. The risk of splitting was predicted to be severe without rate sensitivity but reduced to a borderline risk when it was included. This outcome was in closer agreement with the stamping trials where splits did not occur in every panel. At the bend area, no splitting occurred in the forming trials although it was predicted in the simulations. In contrast to the 1180 MPa steels, the influence of rate effects on the 3rd Gen 980 was found to be minimal and did not show a prominent effect. This is attributed to the tooling being designed for the 3rd Gen 980 and that there were no “at risk” areas for splitting that would show a beneficial reduction in local strains by accounting for the positive rate sensitivity.

Overall, the formability predictions appear to correlate well for areas that primarily experience in-plane stretching. The false positive failure prediction is due to the assumptions made in the application of the FLC which does not consider bending or contact pressure which increases the forming limits. A method to predict limit strains that considers tool curvature can help determine the true forming limits of sheet metal with complex geometry.

6 B-pillar Springback Prediction and Correlation

This chapter details the B-pillar simulations of springback and their evaluation with part-scans using the best-fitting function within LS-PrePost software. Springback simulations of AutoForm R8 and LS-DYNA R9.3 are compared with the part scans provided by Bowman Tooling. The springback predictions using AutoForm include kinematic hardening (KH) and chord modulus degradation due to the ease of input and calibration of its internal KH model in the software. LS-DYNA requires users to calibrate the parameters in its kinematic hardening models off-line which requires the development of customized analysis scripts and calibration that were outside the scope of the thesis. Consequently, the LS-DYNA springback simulations did not consider moduli degradation or kinematic hardening but used a finer mesh of fully-integrated shell elements with isotropic hardening. Anisotropic yield criteria were used in both LS-DYNA and AutoForm. The AutoForm predictions of springback are of primary interest to forming engineers such as Bowman Precision Tooling. The objective of this chapter is to assess the current methodology in springback using AutoForm and LS-DYNA. Springback models are compared to part scans of the formed and trimmed B-pillar to observe the deviation in the models. The LS-DYNA springback predictions are more relevant for crash engineers that use the formed part geometry and residual strains as the input to crash simulations which will be performed in Chapter 7.

6.1 Simulation Stages

6.1.1 Trimming

The blank geometry from the forming simulation is subjected to a trimming stage where elements outside the trimming outline are deleted. The trimming outline was imported into LS-PrePost and the trim was performed as shown in Figure 92. Prior to trimming, the elements to be trimmed can be designated to be adaptively refined which is specified by the tolerance defined by the user. A lower tolerance further decreases the size of the original elements. As the elements being trimmed were at the edges and are not critical, a default value 0.25 of the trimming tolerance was used. This default value limits the minimum size of the newly generated element to be at a minimum of 25% of the original element size (LSTC, 1997). The effects of a smaller tolerance are visualized by Figure 93.

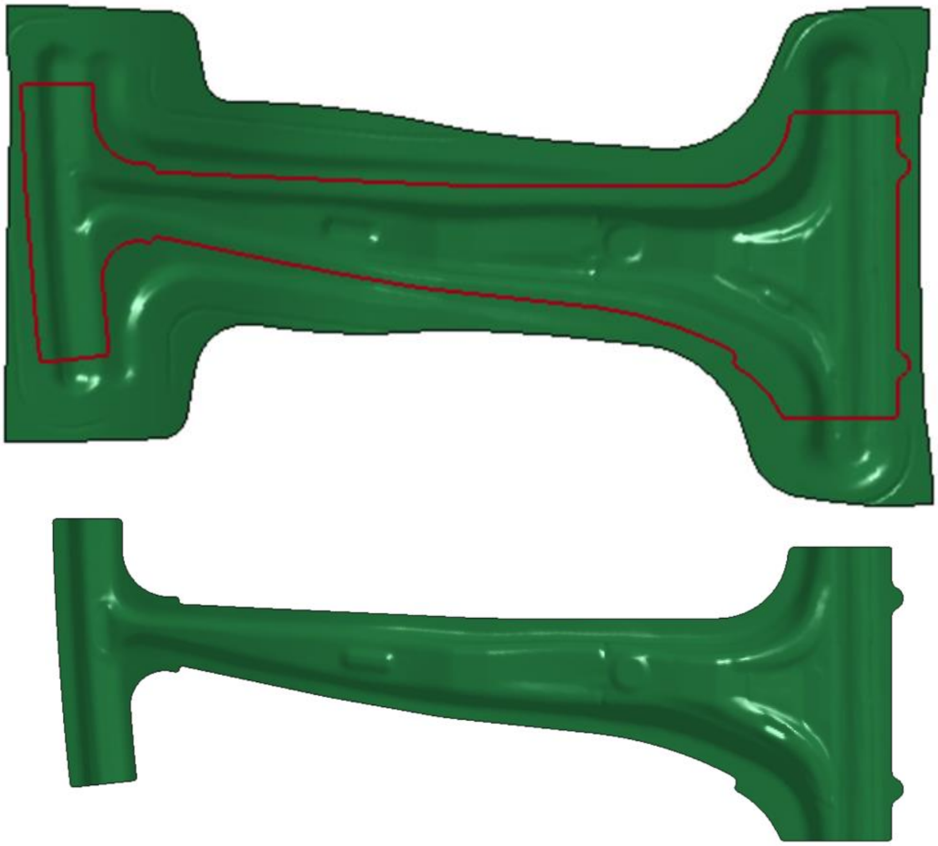

Figure 92: Visualization of a) the trimming outline used on the B-pillar and b) the trimmed B-pillar

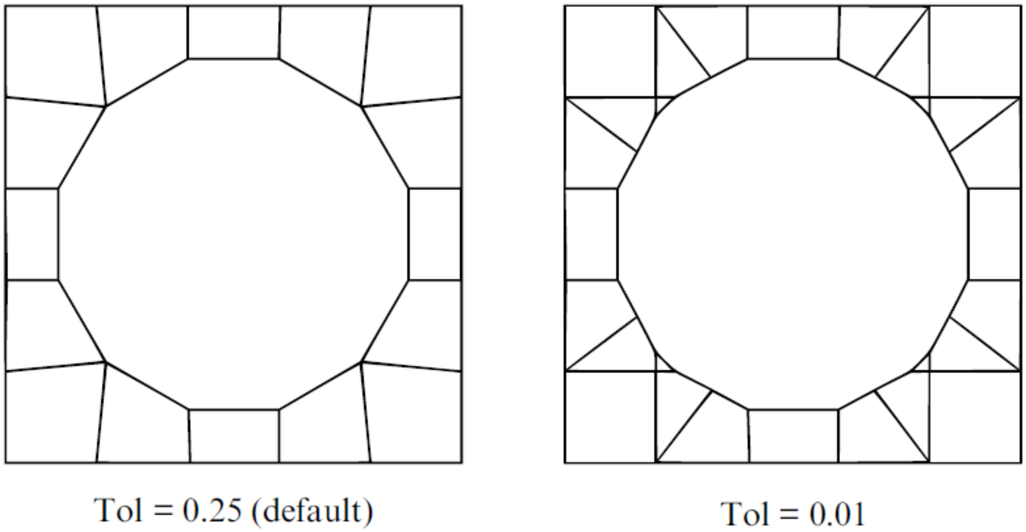

Figure 93: Effect of element tolerance on elements post-trimming

6.1.2 Springback

Due to the residual stresses induced during forming it is essential to perform a springback simulation to allow the part shape to elastically unload to its final shape and compare with the forming trial results. The output from the forming and trimming simulations of the B-pillar are used which contains the deformed geometry of the B-pillar, its residual strains, and thickness reduction. The static implicit formulation using *CONTROL_IMPLICIT_SOLVER solves for the unloaded configuration that satisfies equilibrium.

Constraints must be applied on the blank to prevent non-physical rigid body movements. In consultation with Neil Parker of Bowman, three locations were identified for constraint and is illustrated in Figure 94. This method of node constraints for springback was implemented in both LS-DYNA and AutoForm R8. Good correlation can be achieved through this constraint combination which has been used by Han (2018) and Zhou (1999).

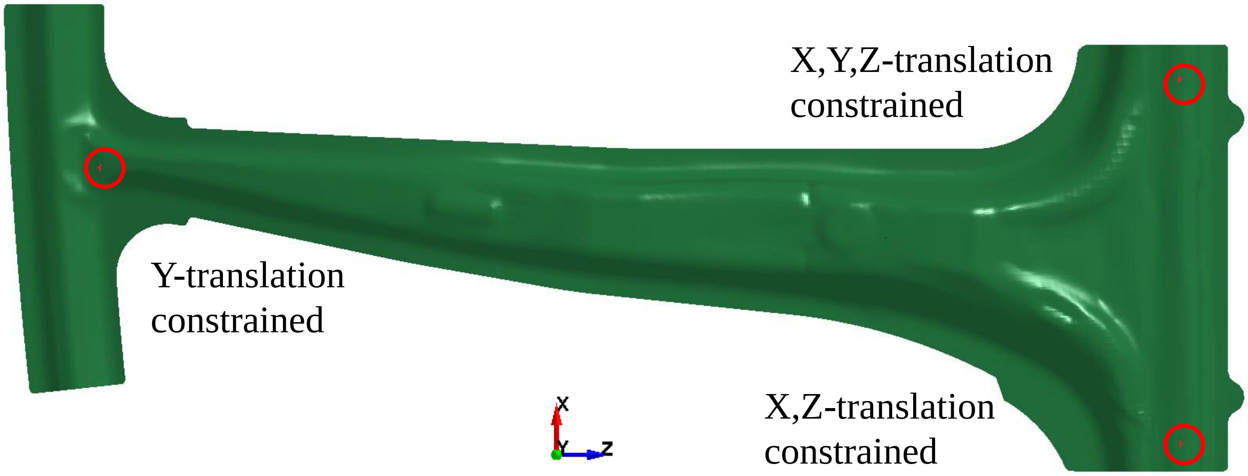

Figure 94: Constraints applied to formed and trimmed geometry of the B-pillar for its springback simulation

6.1.3 Best-fitting

Part scans of the trimmed B-pillars were provided by Bowman Precision Tooling. Using the control card *CONTROL_FORMING_BESTFIT in LS-DYNA, the final geometry predicted by the simulations is compared with the part scan with a series of rigid body rotations and translations. Three nodal control points must be defined with the locations shown in Figure 95. The selection of node pairs is based upon recommended geometry features such as tangent lines, arc centers, bosses and geometrical protrusions according to LSTC (2016).

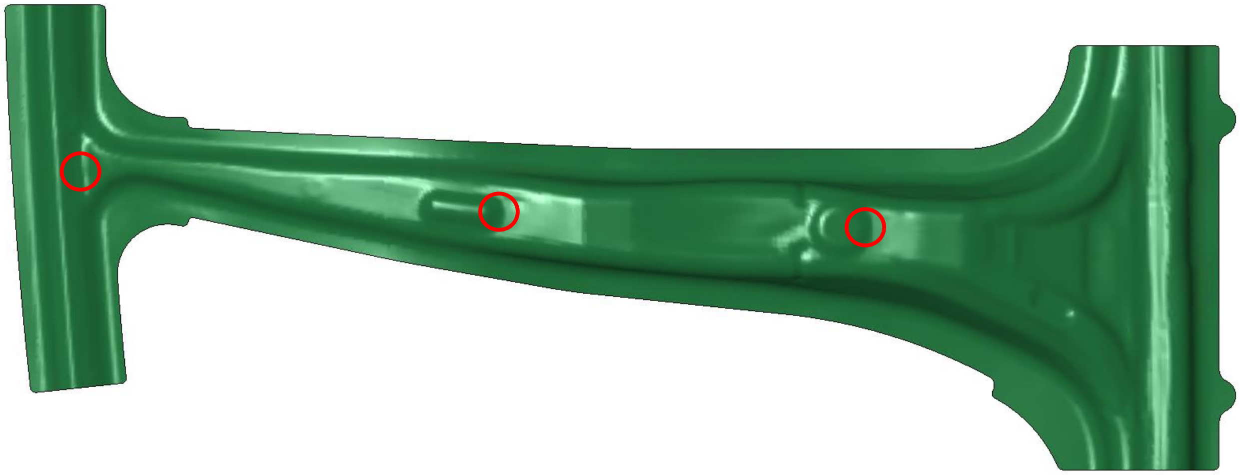

Figure 95: Location of node pairs selected for best-fitting

6.2 LS-DYNA Springback and Best-fitting Correlations

It is important to clarify the difference between springback and separation distance which are not interchangeable. Springback refers to the displacement of the geometry (nodes or elements) between the end of the forming stroke and when the blank is unloaded. The separation distance is a measure of correlation between the model and experiment which compares the final geometry of the unloaded part between the test and simulation.

6.2.1 Springback Predictions

Numerical sensitivity added to springback simulations is realized in the form of element shape, element size, and number of integration points (Mattiasson *et al.*, 1995; Lee and Yang, 1998; Wagoner et al., 1999; Li *et al.*, 2002). The choice of NIP is specific to the forming process and available computational resources to resolve the through-thickness gradients. An odd number of NIPs is often used to have an integration point at the mid-plane. An NIP of unity is moot as it cannot describe bending where 3 NIPs is considered as the minimum admissible value. In addition to describing bending, the residual stresses and strains post-forming must be modelled with sufficient accuracy to properly simulate springback. Li *et al.* (2002) and Wagoner *et al.* (1999) proposed that 51 NIPs is sufficient to achieve 1% springback accuracy. Contradicting studies have also been conducted by various researchers indicating that 3 – 10 NIP results in no differences in springback (Andersson and Holmberg, 2002), little variation between 5 NIP and 20 NIP (Bjorkhaug and Welo, 2004), and a specific NIP recommendation of 9 for accuracy (Nguyen *et al.*, 2004). For these reasons a NIP parametric study was conducted using 3 and 11 integration points with the best-fit springback methodology at 3 constrained locations. The current selection of the number of integration points were selected due to limited computational resources.

Springback can be observed on the three axes of the simulation. The relevant axes to observed are the *y*-axes which would be the vertical direction (into the page) of the B-pillar and the *x*-axes which shows how much springback has occurred on the sides of the B-pillar. The *x*- and *y*-axes are the chosen axes since the *y*-axis shows the springback at the roof rail. Similarly, it is of interest to observe the side walls which can be checked from the contour plot of *x*-displacements. Contour plots of the B-pillar are illustrated in Figure 96 and Figure 97. The simulation shows the contour plots for the 3rd Gen 980 B-pillar using 3 NIPs without any rate effects implemented. The magnitudes in *x*-displacements are more prominent on the side walls seen in Figure 96. Similarly, Figure 97 shows noticeable change in the *y*-displacement at the center of the B-pillar. Since the contour plots are rather qualitative due to the fringe levels selected, the displacements of nodes at four locations are extracted and compared and are shown in Figure 98. Locations 1 and 2 were selected closer to the roof rail for the *y*-displacement and the *x*-displacements will be extracted at the nodes from the side wall which are indicated by Locations 3 and 4.

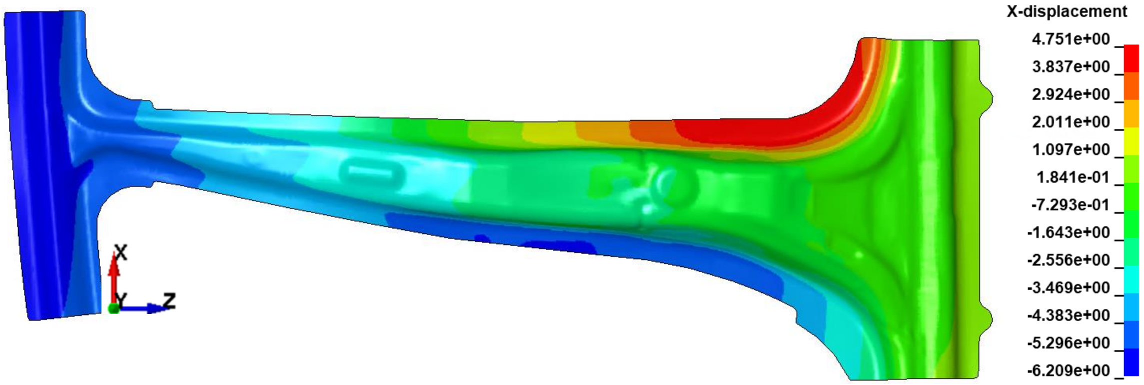

Figure 96: Contour plot of the *x*-displacement of the 3rd Gen 980 B-pillar post-springback with no rate effects with 3 NIPs

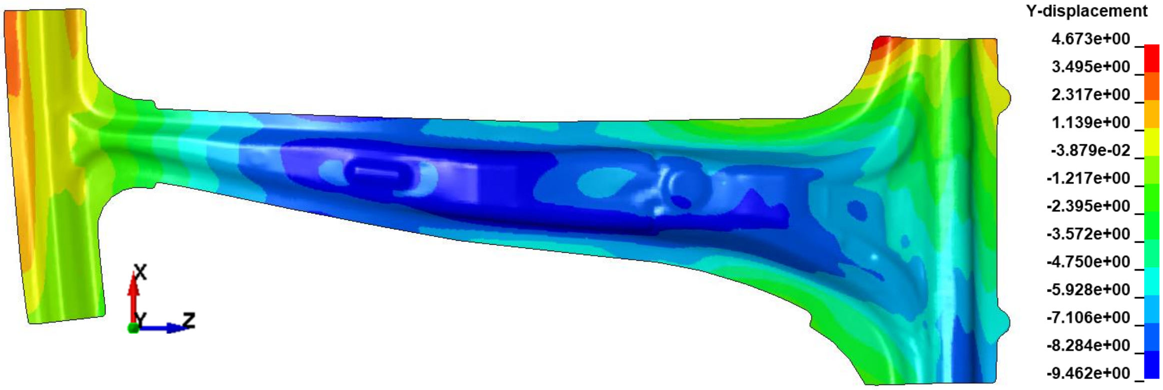

Figure 97: Contour plot of the *y*-displacement of the 3rd Gen 980 B-pillar post-springback with no rate effects with 3 NIPs

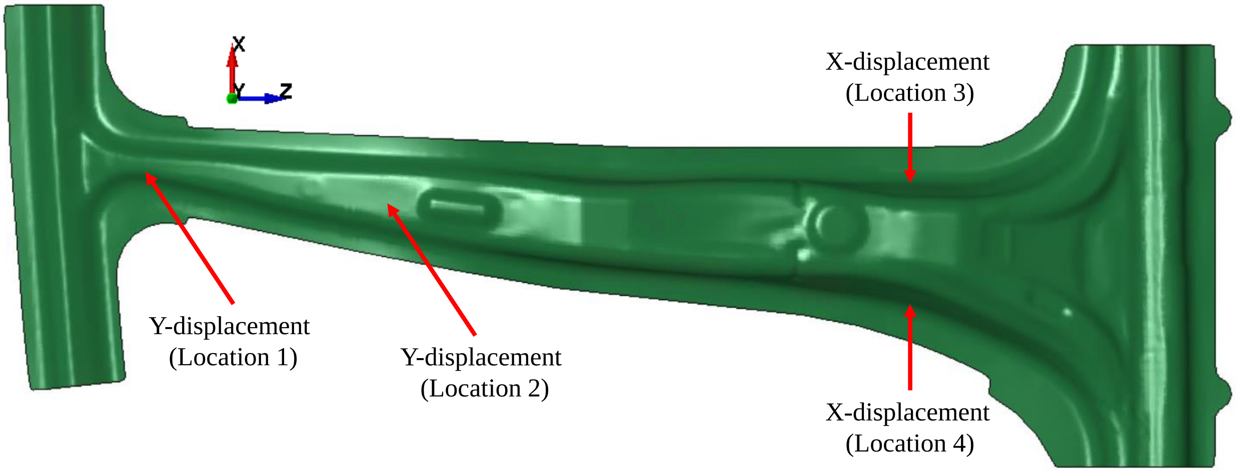

Figure 98: Selected locations for extracting nodal displacements. Each node is labelled indicating which direction the displacement is directed.

6.2.1.1 3rd Gen 980 Springback Predictions

Nodal displacements for the four locations are presented in Figure 99 for the 3rd Gen 980 which includes the influence of strain rate effects and NIPs. Overall, the springback for all 4 variations of the 3rd Gen 980 B-pillar simulation are similar.

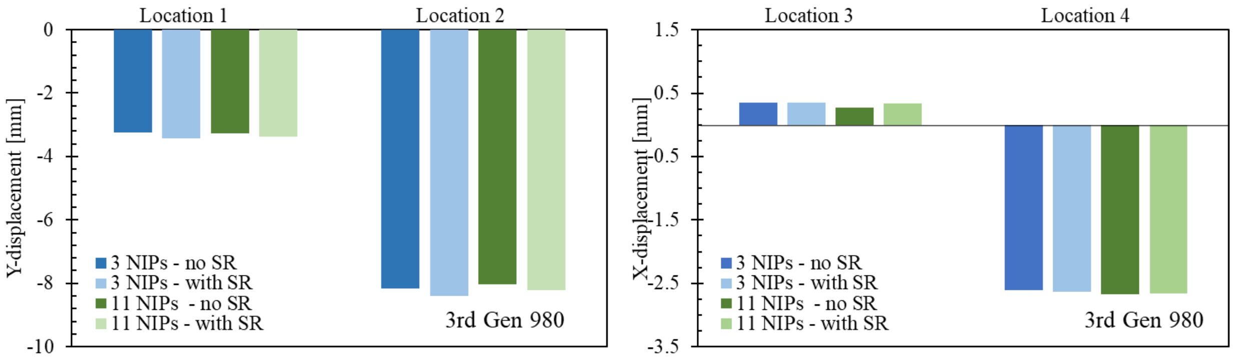

Figure 99: *Y*- and *x*-displacements extracted from the 3rd Gen 980 springback simulations. *Y*-displacements are extracted from Locations 1 and 2 while *x*-displacements are extracted from Locations 3 and 4.

6.2.1.2 3rd Gen 1180 V1 Springback Predictions

The springback predictions for 3rd Gen 1180 V1 show a similar trend as the 3rd Gen 980 but with higher magnitudes due to its higher strength. Seen in Figure 100, at Location 2 the *y*-displacements are at approximately -12 mm which is approximately 33% higher than 3rd Gen 980.

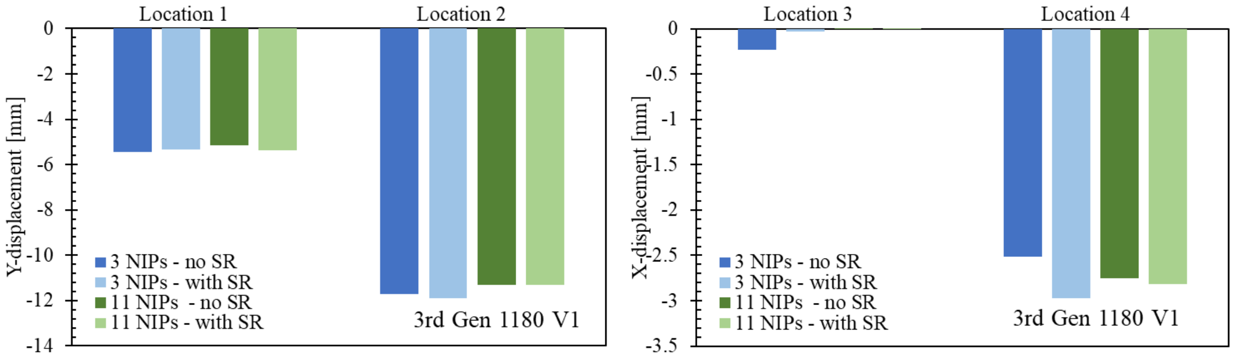

Figure 100: *Y*- and *x*-displacements extracted from the 3rd Gen 1180 V1 springback simulations. *Y*-displacements are extracted from Locations 1 and 2 while *x*-displacements are extracted from Locations 3 and 4.

6.2.2 Springback Correlation

The best-fitting simulations provide insight into correlation between the measured and predicted part shape the influence of strain rate effects and NIP. Due to the extreme values of the maximum and minimum of the contour plots shown in Figure 101 and Figure 102, the contour plots of the separation distance are washed out. The same four nodes of interest in the springback evaluation will also be considered for local evaluation of the separation distance.

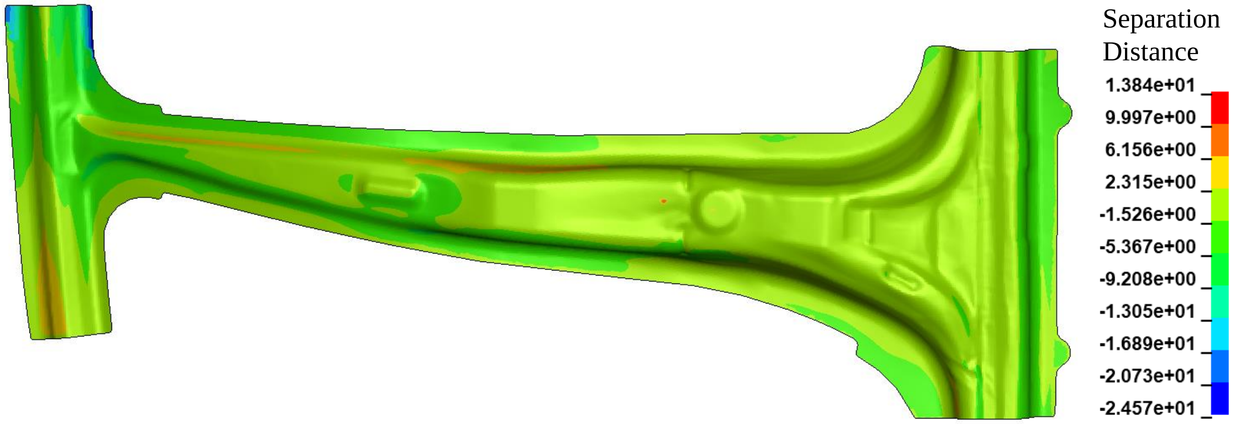

Figure 101: Contour plot of the separation distances of the 3rd Gen 980 B-pillar using 3 NIPs and no rate effects

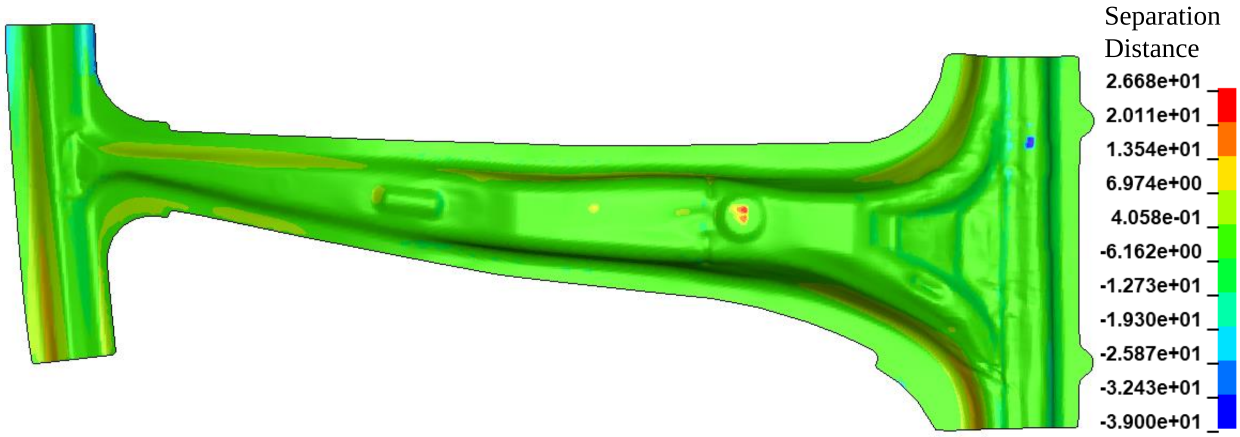

Figure 102: Contour plot of the separation distances of the 3rd Gen 1180 V1 B-pillar using 3 NIPs and no rate effects

6.2.2.1 3rd Gen 980 Separation Distances

As observed in Figure 103, the magnitude of separation distances at Locations 1 and 2 are similar and not significantly influenced by the NIP. The highest separation distance was around 1.9 mm for these locations. The inclusion of strain rate sensitivity has a more noticeable effect on separation distance at Locations 1 and 2, and especially at Location 4. Location 4, notably, has a separation distance of -1.1 mm without rate effects which is effectively reduced to zero when rate effects are included. The separation distances for Location 3 are inconclusive.

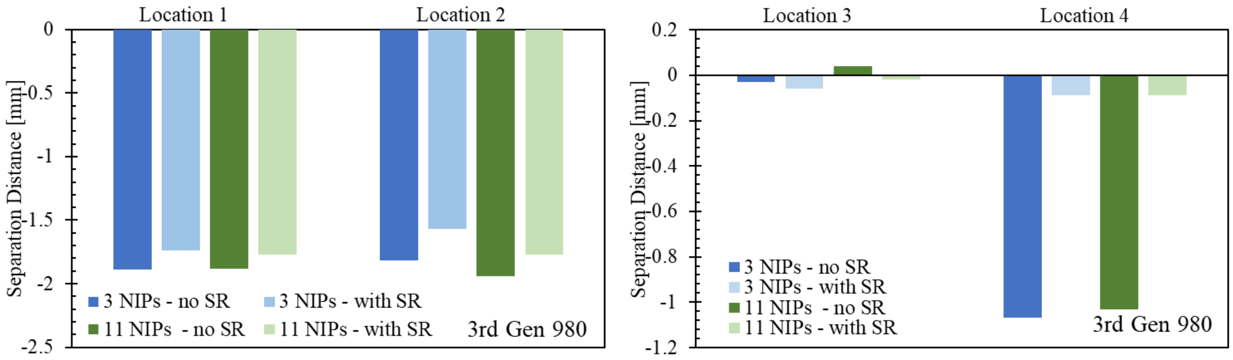

Figure 103: Separation distances between the scanned part and simulation model from the springback model of the 3rd Gen 980 B-pillar at Locations 1 to 4 using LS-DYNA

6.2.2.2 3rd Gen 1180 V1 Separation Distances

Separation distances for 3rd Gen 1180 V1 are notably higher at Locations 2, 3, and 4 seen in Figure 104 while no clear trend with NIP or rate sensitivity is observed at Location 1. In contrast with the 3rd Gen 980 B-pillar, the influence of rate sensitivity was less noticeable in the 3rd Gen 1180 V1.

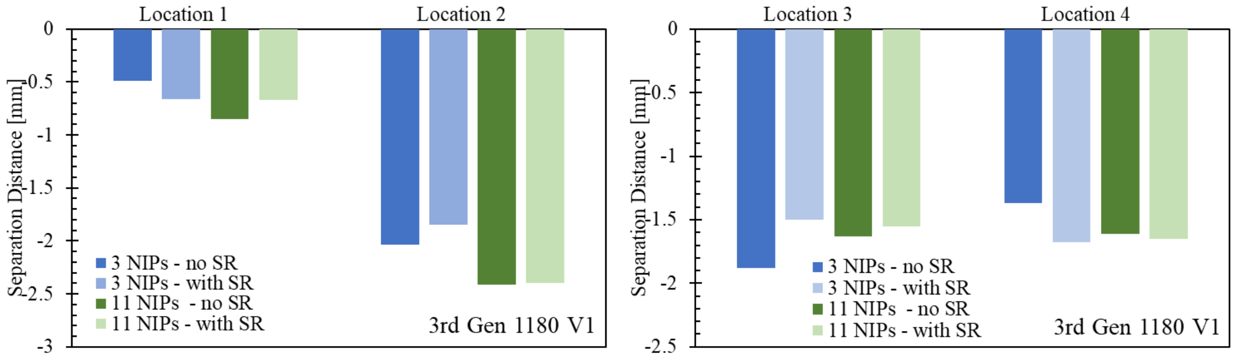

Figure 104: Separation distances between the scanned part and simulation model from the springback model of the 3rd Gen 1180 V1 B-pillar at Locations 1 to 4 using LS-DYNA

Overall, the reduced influence of the NIP and rate sensitivity on separation distance of the 3rd Gen 1180 V1 B-pillar provides insight into what may be lacking in the material model. It appears the assumption of isotropic hardening is less acceptable for the 3rd Gen 1180 V1 and kinematic effects are more pronounced. It is also important to recall that the tooling and springback compensation of the tool was based upon the 980 MPa steel and not the 1180 MPa.

6.3 AutoForm Springback Predictions and Evaluation of Separation Distance

Springback simulations were also performed using AutoForm R8 software with the same boundary conditions described in Section 6.1.2. The application of AutoForm R8 does not serve as an analogous comparison with LS-DYNA due to the different element formulations, solvers, and multiple varying simulation parameters between the two FE codes. A clear advantage of AutoForm software is that it is used by Bowman and it has a user-friendly approach to including kinematic hardening data. Within AutoForm R8, the parameters κ and ξ, control the transient softening during reverse loading such that κ controls early re-yielding. A value of 0 ensures that no early re-yielding occurs with a maximum value of 0.1. The stagnation ratio, ξ, affects the softening rate of the reverse loading where a maximum value of 1 can be assigned to ξ. The higher the softening rate results in a lower slope on the stress-strain curve during reverse loading. Elastic modulus degradation is assumed to follow the exponential relation

$$E_l\left(\bar{\varepsilon}_p\right)=E_o\left(1-\gamma\left(1-e^{-\chi\bar{\varepsilon}_p}\right)\right) \tag{37}$$

where E_0 is the initial modulus, γ and χ are dimensionless parameters.

For the current simulations, cyclic tension-compression tests from experiments, seen in Figure 105, are input into the springback simulations. AutoForm R8 can calibrate to only one load reversal with the strains enforced to be positive by mirroring as shown in Figure 105. Upon receiving the reversal strain, AutoForm R8 automatically generates the parameters forb κ, ξ, γ, and χ.

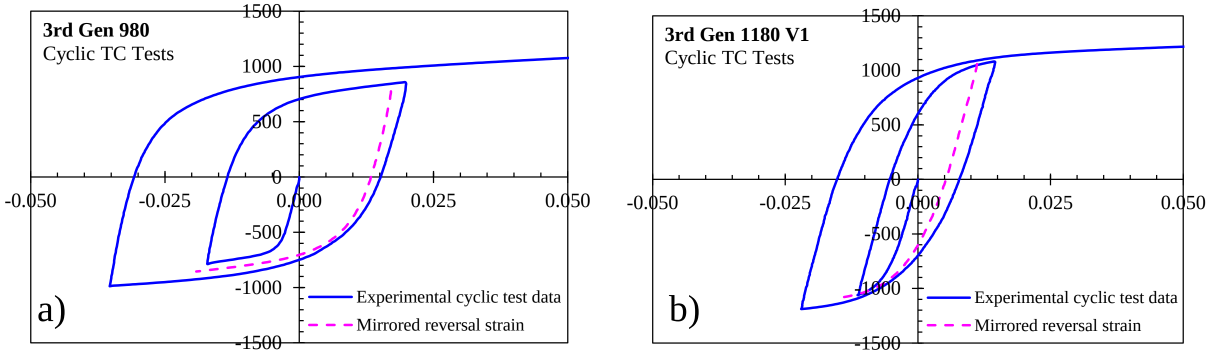

Figure 105: Cyclic tension compression tests of a) 3rd Gen 980 and b) 3rd Gen 1180 V1

To evaluate the springback simulations generated by AutoForm R8, the results are compared with the part scans. The part geometry after springback was exported from AutoForm R8 and then imported into LS-DYNA to compare with the part scans using the best-fitting analysis tool. To visualize and compare the importance of applying the appropriate material description for the Bauschinger effect, three sets of different parameters were used to perform the springback calculation: isotropic hardening, kinematic hardening data acquired from the university, and literature data on kinematic hardening obtained from Aryanpour (2011) and Seo *et al.* (2017). Each case is explained below.

Isotropic hardening was performed by disabling kinematic hardening consequently removing transient softening and early re-yielding in the material description. During the early stages of the project, test equipment to perform cyclic tension-compression tests was not yet available at the University of Waterloo. To approximate the kinematic hardening behavior of the two steels at the time, literature data obtained from Aryanpour (2011) and Seo *et al.* (2017) were digitized. Aryanpour (2011) performed cyclic tension-compression tests for a DP980 steel and Seo *et al.* (2017) for TRIP1180 steel. These initial approximations from literature data were used to account for the springback compensation of the tool based on AutoForm R7 simulations, which was the version used during the early stages of the project. Contour plots from all three cases are visualized in Figure 106 and Figure 107 illustrating 3rd Gen 980 and 3rd Gen 1180 V1, respectively.

Similar to the LS-DYNA simulations, the same four locations are used to quantify springback and the separation distance for 3rd Gen 980 and 3rd Gen 1180 V1. It is observed that activation of kinematic hardening exacerbates separation distances. No clear trends are observed for any of the locations seen in Figure 108 and Figure 109.

a) No KH

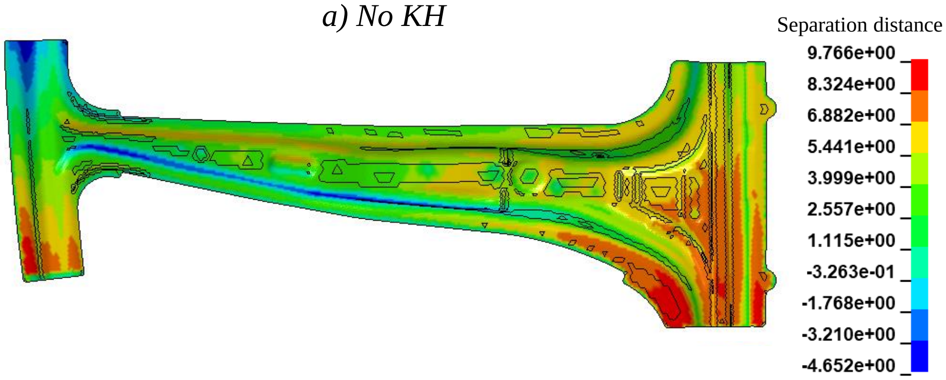

b) UWaterloo KH

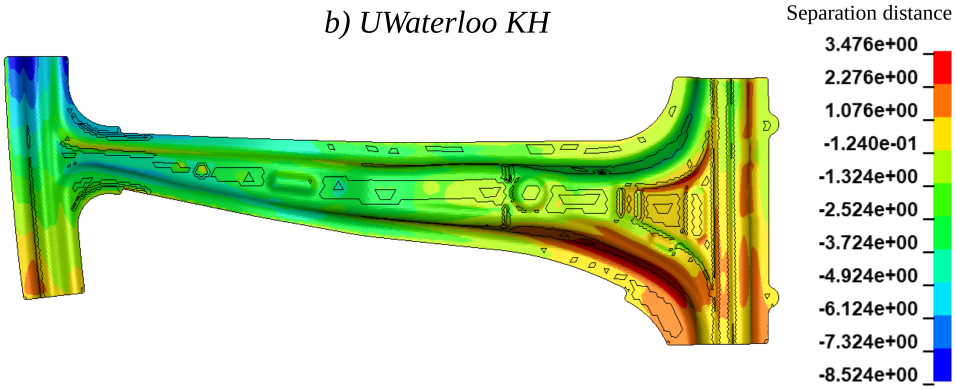

c) Literature

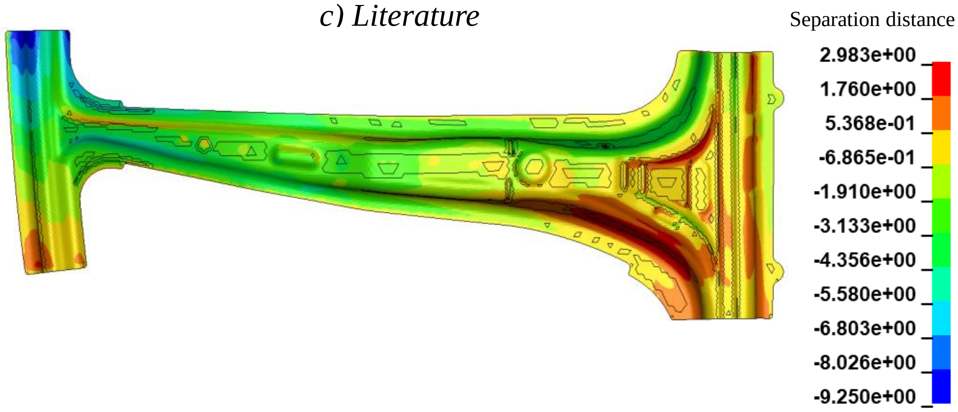

Figure 106: Best-fitting of 3rd Gen 980 springback simulations exported from AutoForm R8 showcasing results using a) isotropic hardening, b) kinematic hardening (KH) obtained from experimental cyclic tests and c) kinematic hardening parameters obtained from literature data (Aryanpour, 2011 and Seo *et al.*, 2017)

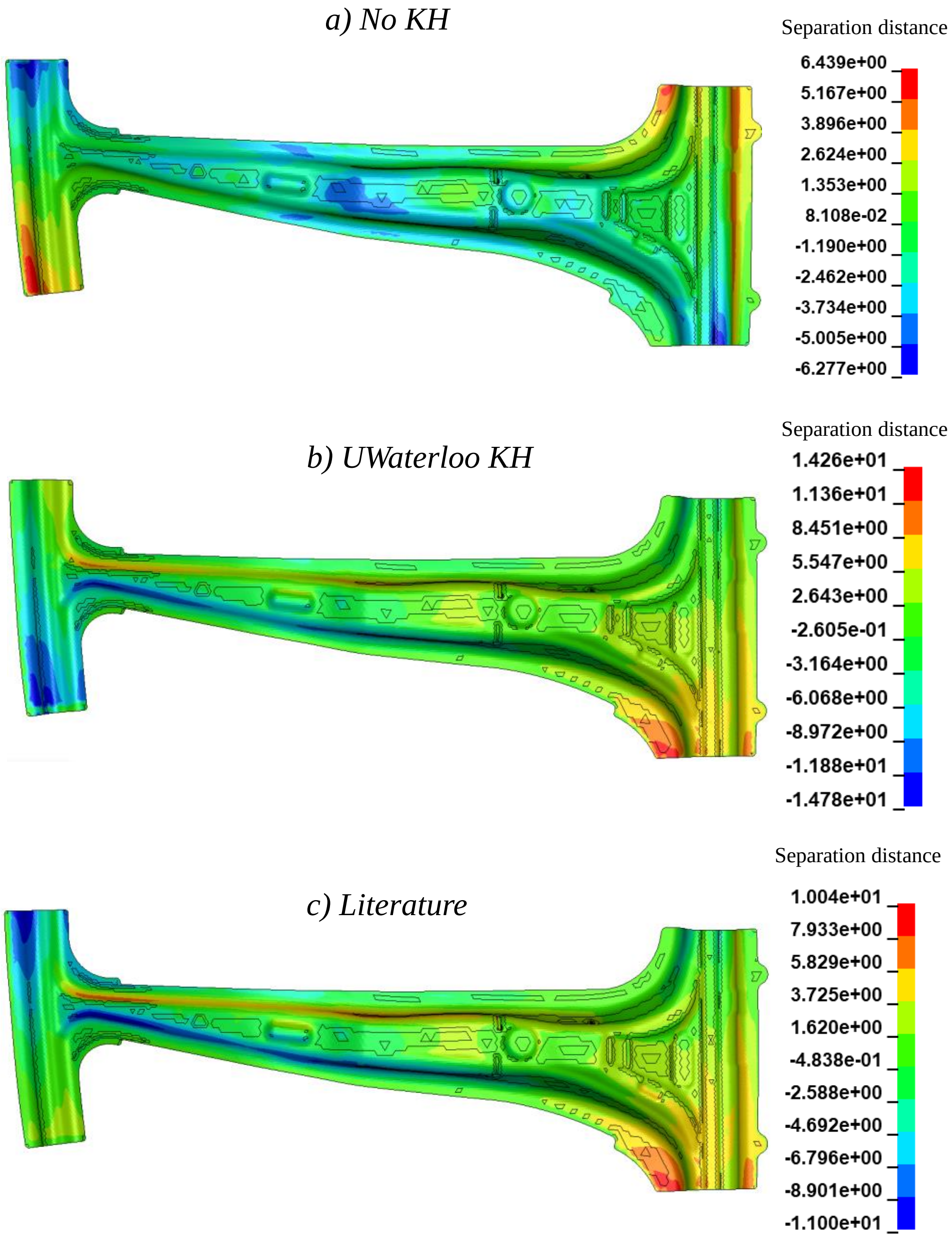

Figure 107: Best-fitting of 3rd Gen 1180 V1 springback simulations exported from AutoForm R8 showcasing results using a) isotropic hardening, b) kinematic hardening (KH) obtained from experimental cyclic tests and c) kinematic hardening parameters obtained from literature data (Aryanpour, 2011 and Seo *et al.*, 2017)

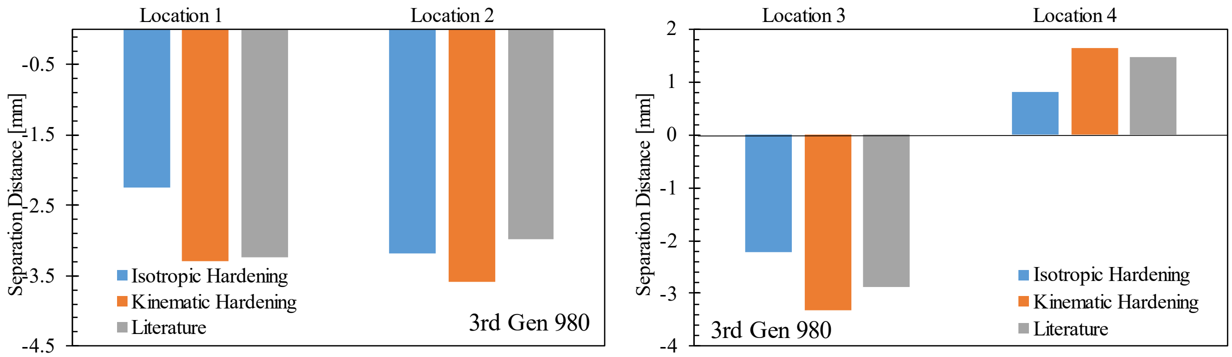

Figure 108: Separation distances between the scanned part and simulation model from the springback model of the 3rd Gen 980 B-pillar at Locations 1 to 4 using AutoForm R8

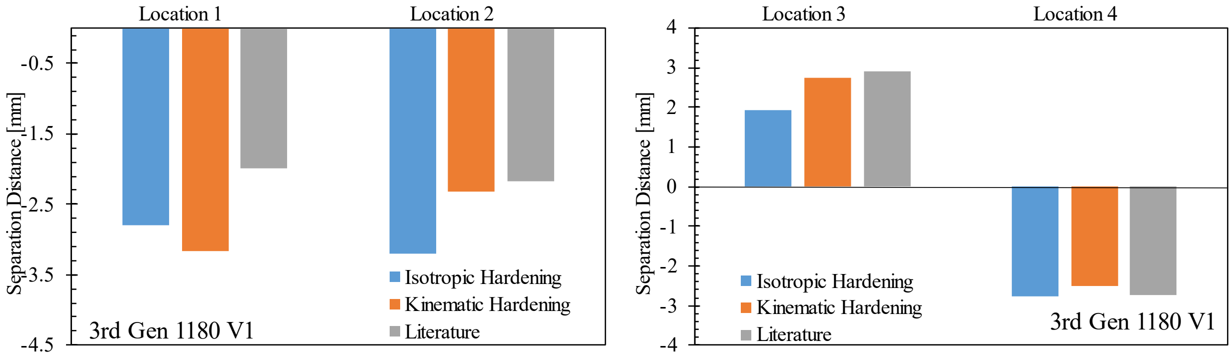

Figure 109: Separation distances between the scanned part and simulation model from the springback model of the 3rd Gen 1180 V1 B-pillar at Locations 1 to 4 using AutoForm R8

Future work should consider the Yoshida-Uemori (2001) kinematic hardening model that can better describe early re-yielding, transient Bauschinger effects, work-hardening stagnation, and permanent softening. The restriction of AutoForm to only consider a single cycle is also expected to be a source of error and hopefully will be considered in future releases of the software.

6.4 Discussion and Recommendations on Springback Methodology

The predicted springback and separation distance were evaluated with part scans of the B-pillars for 3rd Gen 980 and 1180 AHSS steels using LS-DYNA and AutoForm. Overall, the number of integration points and rate sensitivity were observed to be relatively minor but more pronounced for the 3rd Gen 1180 V1 steel. The influence of kinematic hardening was evaluated using AutoForm R8 software. Unfortunately, no clear improvement in the correlation with kinematic hardening was observed which is attributed to the relatively simple model available in AutoForm compared to the current state of the art used in the literature which are the Yoshida-Uemori (2002) and HAH models (Barlat *et al.*, 2011). The choice of strain levels in the cyclic tests and the constraint that only one reversal cycle could be used in the AutoForm calibration could be another source of the weak correlation. Future work should include coupon testing to asses springback such as cylindrical bending, U-bending, and V-bending mentioned in Section 1.3. This will assist verifying the simulation methodology which can be extended to larger automotive components such as the B-pillar. It is also expected that the implementation of more advanced hardening models within both AutoForm and LS-DYNA will improve the accuracy of the springback predictions. The B-pillar can then be re-visited with the updated methodology.

7 B-pillar Impact Tests and Simulation

This chapter focuses on the design of the B-pillar 3-point bend impact tests and subsequent correlation using LS-DYNA. The influence of the forming strains and damage from the LS-DYNA forming simulations described in Chapter 5 and 6 is considered to evaluate the predictive ability of the 3rd Gen AHSS material models from forming-to-crash. The objective of this chapter is to assess the crashworthiness of the formed B-pillars from Chapter 5. Residual strains due to forming are considered to observe its effect on crash performance compared to idealizing the component as a virgin material. Multiple variations of the boundary conditions are considered to mimic the fixture design as closely as possible. High and low friction conditions are applied to the impactor to observe changes in the mode of deformation and force response of the impact test. High-speed impact tests and crash simulations are then correlated with the test results.

7.1 Experimental Setup

7.1.1 B-pillar Fixture

To mimic a side impact scenario, the B-pillar test conditions were idealized as a three-point bend. U-channels made from A356 hot rolled steel were used to mimic the boundary conditions as if the side sill of the B-pillar was attached to the BIW. The U-channels act as a torsion bar to provide some resistance to twisting while allowing the B-pillar to rotate about the side sill as seen in a side-impact scenario. The opposite end of the B-pillar, the roof rail, simply lies on a rigid post that acts as a roller. The modelled assembly is illustrated in Figure 110. The remainder of the labelled parts such as the honeycomb, U-channels, and slotted inserts will be discussed throughout the chapter.

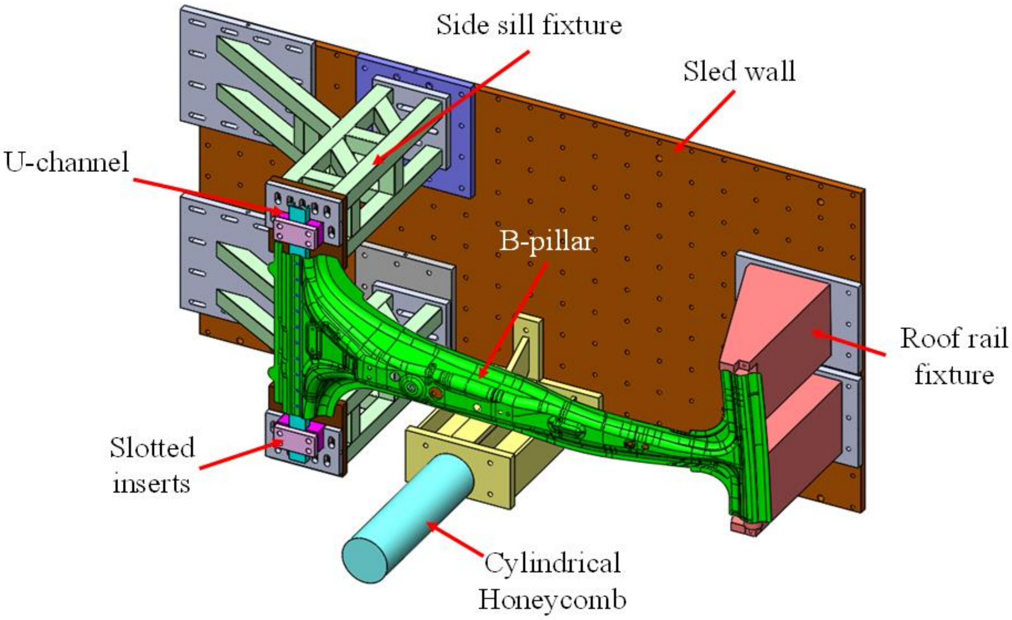

Figure 110: Assembly of the B-pillar Fixture generated using CAD software

A steel wire is tied over the roof rail side of the B-pillar to ensure contact between the roof rail and the roof rail fixture, visualized in Figure 111, is maximized. This also constrains the roof rail such that it is not loose prior to the test. This constraint does not add unwarranted loads into the test as once the B-pillar is struck by the impactor, the wire tie becomes slack. No particular analysis was performed on the roof rail fixture as the deformation it experienced was elastic since this portion of the B-pillar was not rigidly connected to the roller.

The side sill is responsible for suspending the B-pillar and must withstand the majority of the impact force of the sled. The primary body of the fixture for the side sill uses 6.35 mm thick, steel square tubes with side lengths of 50.4 mm. The feet of the fixture were MIG welded on 25.4 mm thick base plates with horizontal slots for adjustment during mounting. At the top of the fixtures, 25.4 mm thick base plates were also welded where the slotted inserts are bolted on top. The top slots are oriented perpendicular to the bottom slots for adjustability in both the horizontal and vertical directions seen in Figure 112. The slots cut on the U-channel fit into the slotted inserts and are secured on the fixture with a rectangular cap via M14 bolts illustrated in Figure 113. Above the U-channel, the B-pillar is bolted using M10 bolts. All remaining bolts used for securing the B-pillar in vertical and horizontal directions used M16 bolts. The grade of all bolts was Class 10.9.

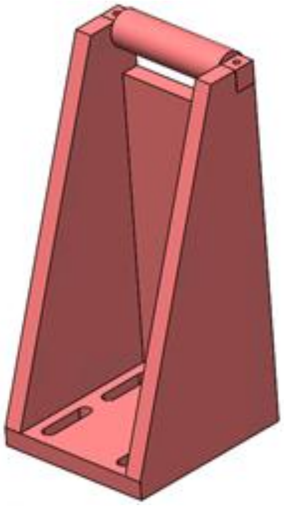

Figure 111: Roof rail fixture used for impact testing of the B-pillar

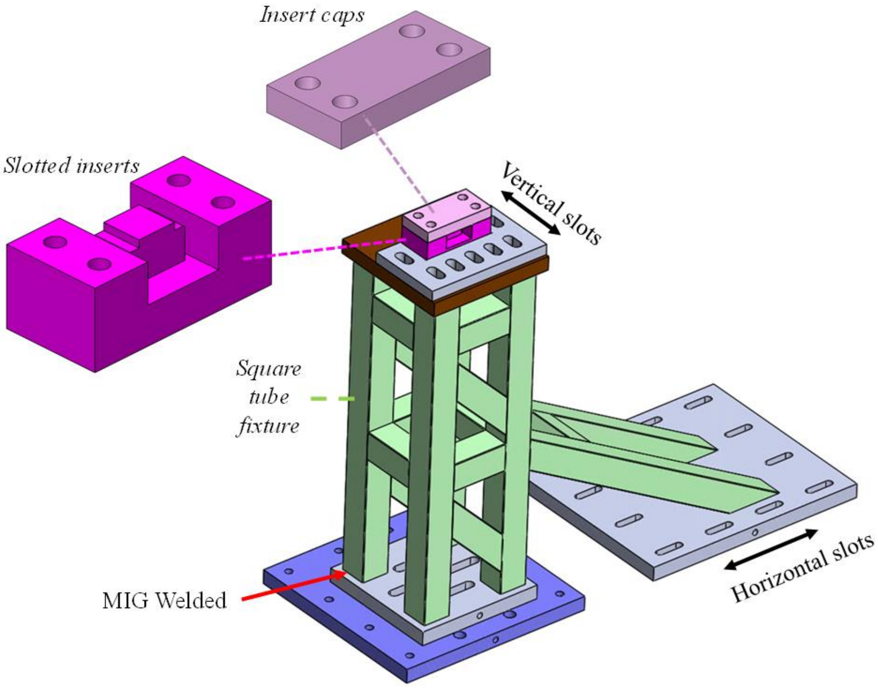

Figure 112: Side sill fixture that suspends the B-pillar used in impact testing

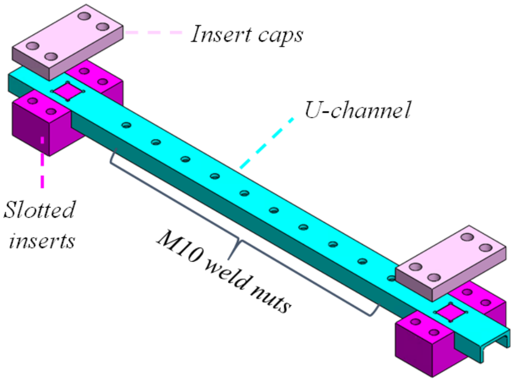

Figure 113: Placement of the U-channel on the slotted inserts. The U-channel is secured in the slotted inserts with the insert caps using M14 bolts. Underneath the U-channel, M10 nuts were welded where the B-pillar is bolted on top of the U-channel.

Cylindrical aluminum honeycomb was used to safely absorb the kinetic energy of the sled once the target impact distance of 100 mm was achieved. The honeycomb prevents the sled, its instrumentation and the crash wall from being damaged. The fully assembled apparatus for impact testing is visualized in Figure 114.

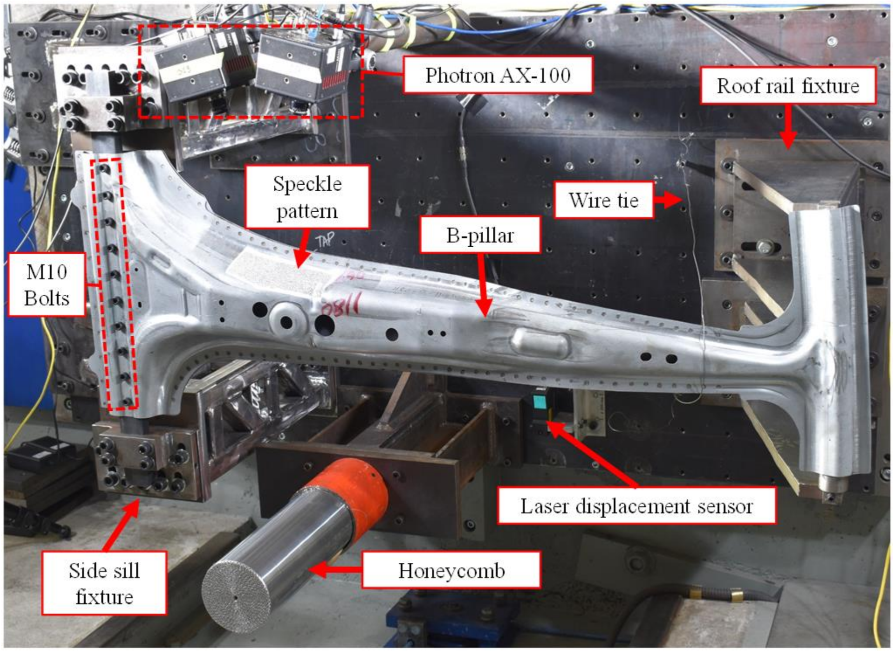

Figure 114: Fully assembled fixture with the B-pillar attached for impact testing

7.1.2 B-pillar Attachment (U-channel, Backing Plate, M10 Bolts)

The following attachments in the crash fixture are discussed separately as these are not rigid in the simulation. The following attachments to be discussed are the U-channel, the backing plate, and the M10 bolts. The U-channel is made from hot-rolled ASTM A36 steel and has the dimensions of 50.4 mm in the width direction, 25.4 mm for the height, and a thickness of 4.875 mm. The shape and dimensions of the U-channel is visualized in Figure 115. Despite its relatively low yield strength of 250 MPa, the thickness of the U-channel provides the required stiffness with no significant deformation observed in the impact tests.

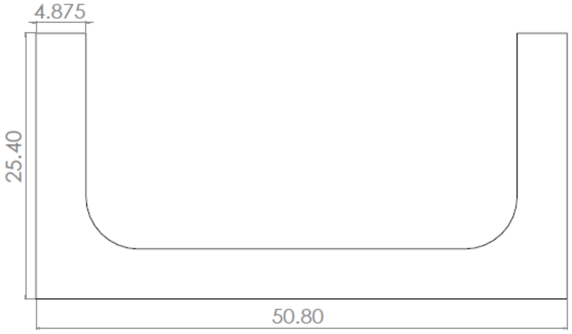

Figure 115: Dimensions of the U-channel. All dimensions are in mm.

Attached underneath to the U-channels are weld nuts. These weld nuts are used to secure the B-pillar via M10 bolts with a grade of Class 10.9. Preliminary FEA of the bolts during the crash event led to peak axial and resultant shear forces on the bots of approximately 9 kN and 14 kN which were far below the EuroCode (2021) failure thresholds for Class 10.9 bolts. The hardening for the M10 bolts and the U-channel is illustrated in Figure 116 which is also used in the simulation with a von Mises yield function. A total of 10 bolts were used to attach the U-channel.

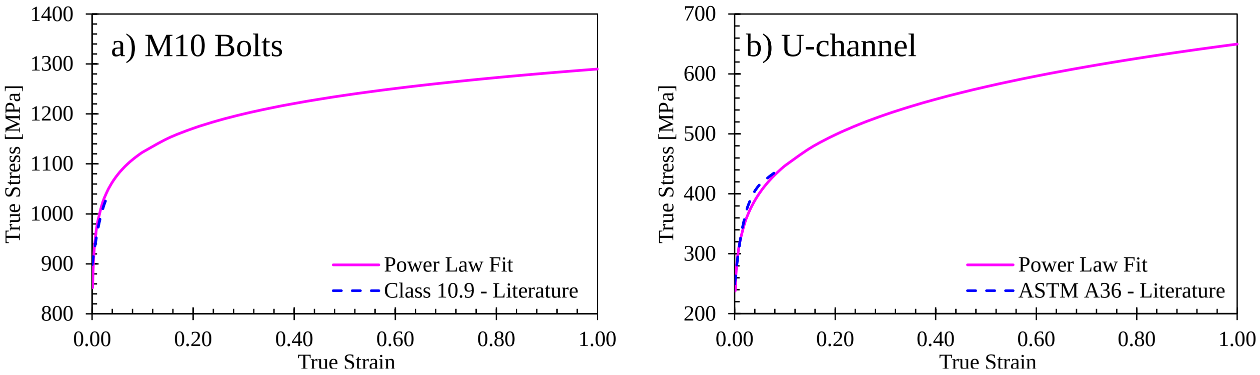

Figure 116: Power law approximations for the hardening response of a) Class 10.9, M10 bolts and b) ASTM 36 U-channels obtained from FEMA (2002) and Noury (2014), respectively

A backing plate for the B-pillar is required to constrain the cross-section from opening and flattening during the impact. The backing plate is attached via spotwelding. All spotwelds span across the flanges of the B-pillar around its edges. A total of 101 spotwelds were created to ensure attachment of the B-pillar to the backing plate after impact testing where the general locations are visualized by the yellow dashed lines seen in Figure 117. The spotwelds are 25 mm apart and 7 mm away from the edge of the B-pillar.

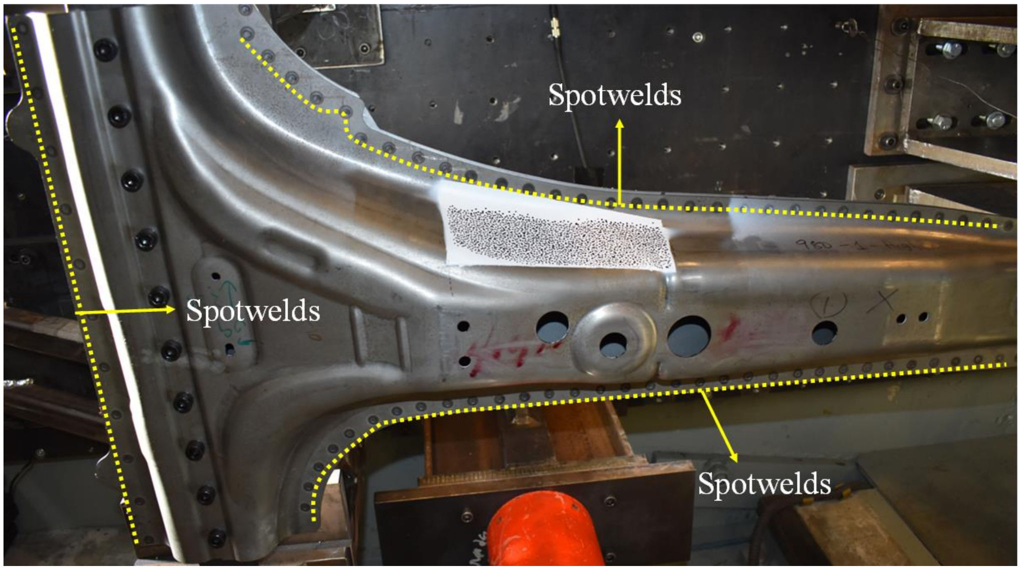

Figure 117: Locations of spotwelds on the B-pillar outlined by the yellow dashed line

Spot weld failure of 3rd Gen AHSS is a concern due to LME which can compromise weld integrity, leading to weld failures at lower forces than found in conventional AHSS such as the dual-phase class. Cross-tension tests were performed to ascertain the strength of the spotwelds. Cross-tension tests provided confidence in the strength of the welds to ensure the B-pillar and the backing plate can withstand the impact test. Cross-tension specimens were fabricated with the assistance of Postdoctoral Fellow, Dr. Abdelbaset Midawi, where a welded cross-tension test is shown in Figure 118. The weld nugget size is approximately 6.1 mm which is close to the same size as the electrode face diameter of 6 mm. An amperage and clamping force performed in spotwelding are summarized in Table 10 (Midawi, 2021) where 3rd Gen 980 and 3rd Gen 1180 V1 steels were welded with 590R as its interface. The hardening for the backing plate is shown in Figure 119.

Table 10: Weld parameters used for cross-tension tests specimens

590R Interfaced with	**Clamping Force [kN]**	**Amperage [kA]**
3rd Gen 980	3	8
3rd Gen 1180 V1	3.5	8.3

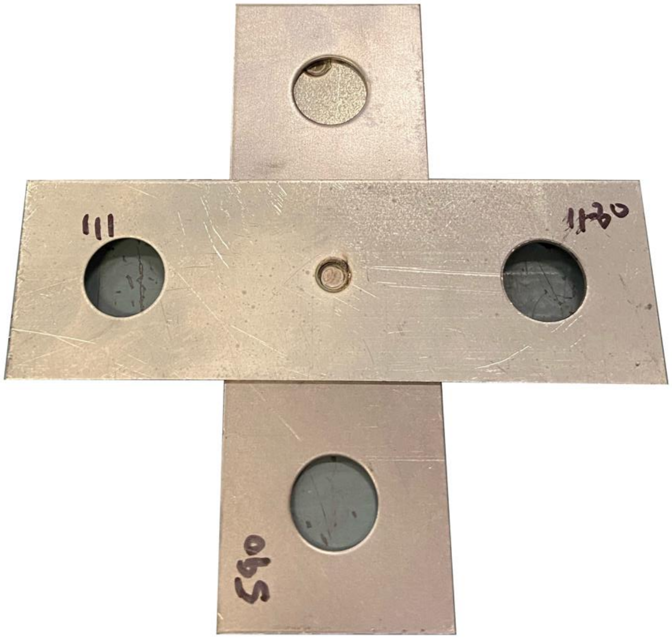

Figure 118: Cross-tension test specimen of 3rd Gen 1180 V1 spotwelded with 590R

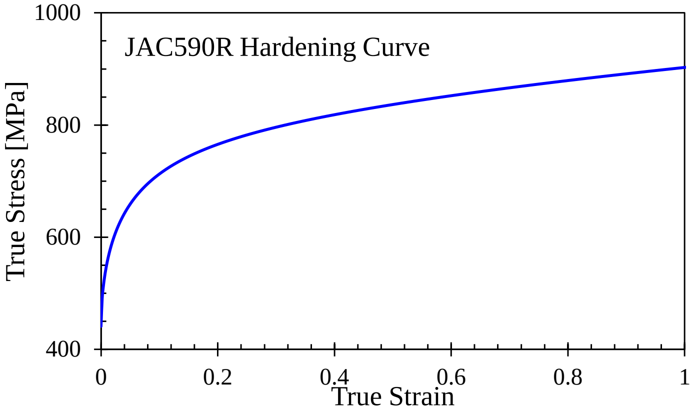

Figure 119 : Hardening response for JAC590R which uses the MHS model

Cross-tension testing followed the methodology of Shojaee *et al.* (2021). The cross-tension tests reported an average max peak force of 8.7 kN and 6 kN upon failure for 3rd Gen 980 and 3rd Gen 1180 V1, respectively. The load-displacement of the cross-tension tests are seen in Figure 120. Initial simulations of the backing plate welds reported axial forces of 3 kN and shear forces of 6 kN, suggesting the spotweld strengths are sufficient for the B-pillar impact tests. No lap shear tests were performed to confirm the shear strength of the spotwelds since the primary loading mode was closest to the cross-tension test and due to time constraints on the project. Fortunately, no spot weld failures were observed in the impact tests.

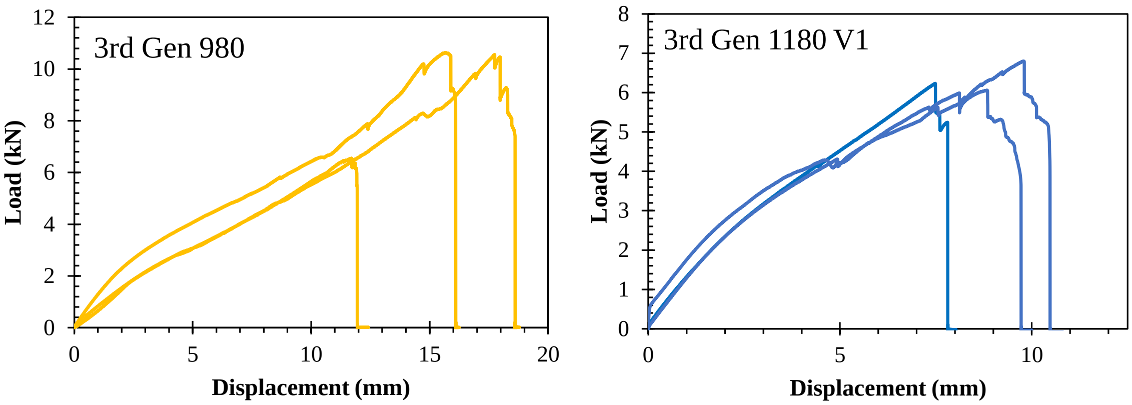

Figure 120: Force-displacement graph for 3rd Gen 980 and 3rd Gen 1180 V1 extracted from cross-tension tests. The abrupt drop in loads indicate the end of the test.

7.1.3 Crash Sled and Impactor Friction

The B-pillars were struck with a Seattle Safety D780-3.7 crash sled seen in Figure 121. Due to the configuration of the fixture, the only feasible option to mount the honeycomb was to use a fixed length as opposed to stacking it done in previous projects (Tummers 2019; Tolton 2021). The honeycomb cylinder uses a 510 mm length and is made from PlasCore AlTuCore™ (Plascore, 2021) with a nominal crush load of 772 MPa. The length of 510 mm for the honeycomb cylinder was selected to ensure 100 mm of free crush distance is achieved while having sufficient honeycomb length to decelerate the sled in a controlled manner. The length of 510 mm is the full-length of the honeycomb cylinder which provided 100 mm of free crush and uses 200 mm of engaged honeycomb being compressed to stop a moving object with a kinetic energy of 100 kJ which was more than sufficient to stop the sled with a mass of 1000 kg and a velocity of 50 km/h. It was also preferred to keep the honeycomb at its original length as surface imperfections produced from cutting the honeycomb cylinder can likely add unwanted reaction forces to an already high-energy impact test.

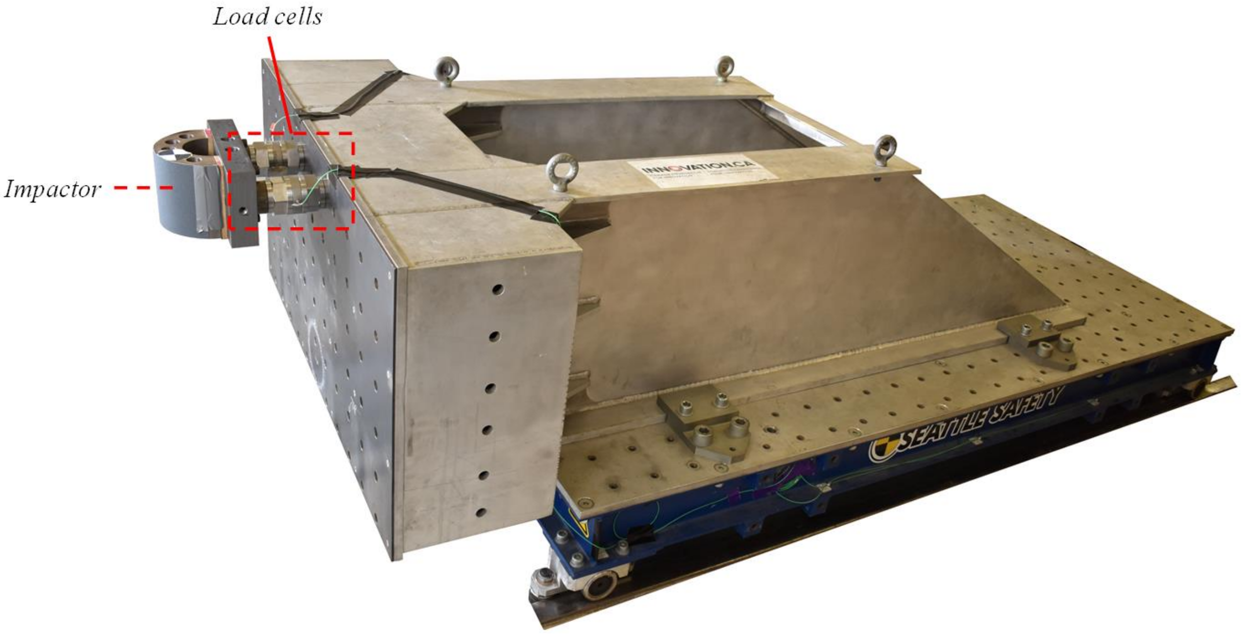

Figure 121: Crash sled experimental setup for B-pillar impact testing

The crash sled is equipped with accelerometers and uses two 120 kN Kistler 9731B piezoelectric load cells, seen in Figure 122, mounted in between the sled face and impactor plate where the half-cylindrical impactor is attached. Placed in between the impactor and the sled face is plywood to prevent damage between the impactor and sled interface. Data recorded from the load cells are totaled to measure the force from the impactor striking the B-pillar. To measure the position of the sled during the impact test, a Keyence LK507 laser displacement sensor mounted at the sled was used. This laser sensor can measure distances from 250 mm to 1000 mm away from the sensor. During the test, the sled passes through a laser trigger which signals the data acquisition (DAQ) system to start recording force and acceleration data. The frequency for recording the force, acceleration, and displacement record at a frequency of 10000 Hz for a total time of 1 second from when the laser trigger is tripped.

The crash event is recorded at 10000 frames per second using multiple high-speed cameras. Configurations of the cameras are all the same throughout all tests where the cameras are focused on areas of interest such as the area of impact, locations of high likelihood of spotweld failure, and perspective of the overall deformation of the B-pillar. The cameras used for the apparatus consist of Phtoron SA-4, Photron SA-5, Photron SA-Z, and Photron AX-100.

A total of six B-pillars were tested for this project with two different friction conditions which is summarized in Table 11. The friction coefficients stated in Table 11 are also the coefficients used in the crash simulations. Three tests were performed for both 3rd Gen 980 and 3rd Gen 1180 V1 where two tests use high friction using 120 grit sandpaper and the last test use Teflon® to reduce the coefficient of friction seen in Figure 122.

Table 11: Test matrix for B-pillar crash testing

Grade	***Low Friction (COF - 0.2)***	***High Friction (COF - 0.4)***
3rd Gen 980	1 tested	2 tested
3rd Gen 1180 V1	1 tested	2 tested

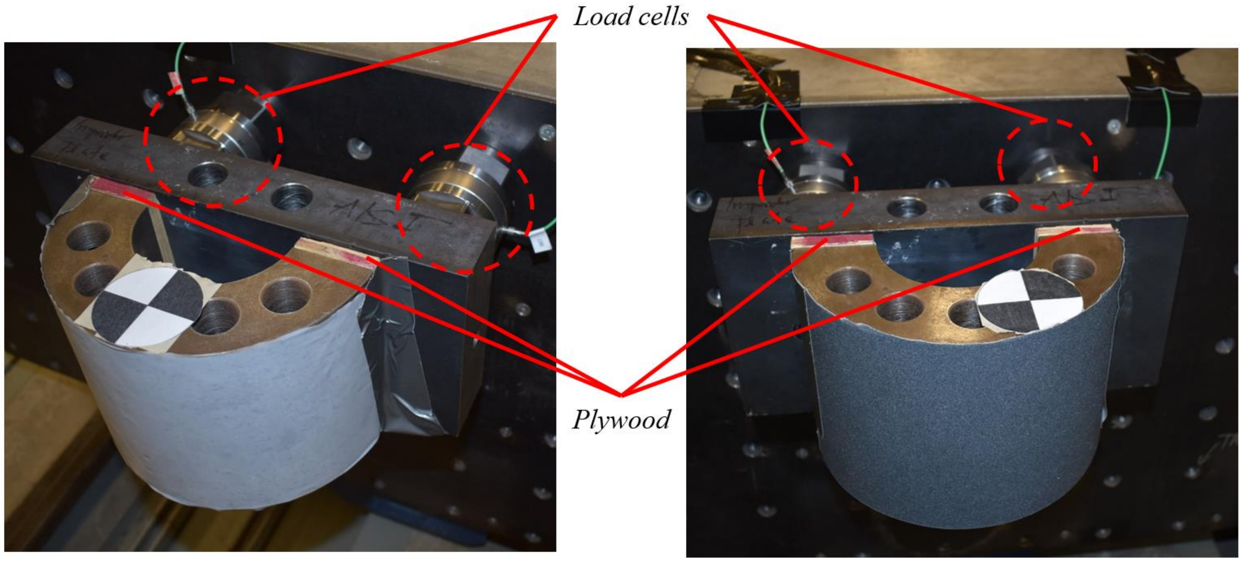

a) Teflon® - 0.1 mm thickness

b) Sandpaper – 120 grit

Figure 122: Setup of piezoelectric load cells attached to the sled face and impactor plate. Impactor surface conditions are varied with the use of a) Teflon ® and b) 120 grit sandpaper

7.1.4 Lighting and camera placements

The nature of dynamic tests requires high-speed cameras to capture the crash event that occurs in a matter of milliseconds along with significant lighting to ensure consistent illumination even as the structure deforms. The camera positions are shown in Figure 123 with multiple viewing angles to observe the test. The speckled area used for DIC analysis needed cameras to be focused directly on top such that 3D analysis could be performed, similar to how the DIC cameras are arranged for Nakazima and Marciniak tests on the dome tester. A consequence of having the DIC cameras positioned on the crash wall, they obscure the top view captured by the Photron SA-5. To compensate for the obscured view of the top camera, an isometric view of the entire apparatus is captured through another Photron SA-Z that is placed on the side. The top and isometric views on the B-pillar can be seen in Figure 124.

There was uncertainty whether or not the spotwelds would fail during the entire duration of the crash test and if so, would they fail during the free crush stage or after. To detect spotweld failure, cameras were focused on the back of the B-pillar to view the spotwelds on the backing plate near the impactor as shown in Figure 125.

Lastly, the placement of the Photron AX-100 cameras, hereinafter referred to as DIC cameras, were assigned to capture the location of highest deformation which was at the location of impact. The captured images from the DIC cameras are seen in Figure 126. It should be noted that the speckle pattern in Figure 126 eventually goes out-of-frame therefore only a partial analysis was performed. The honeycomb before and after the impact test is seen in Figure 127.

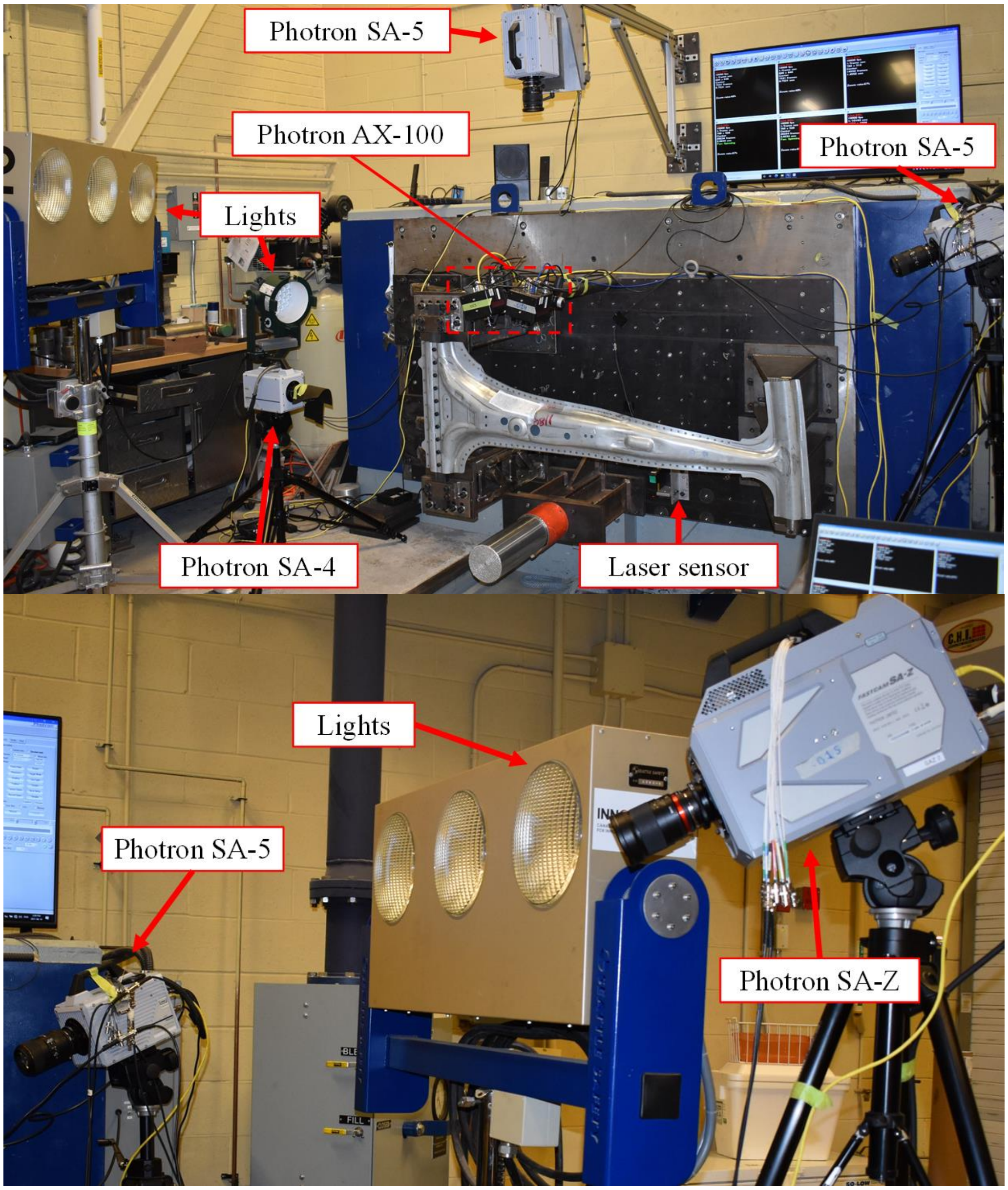

Figure 123: Camera and lighting configurations used on the B-pillar impact tests

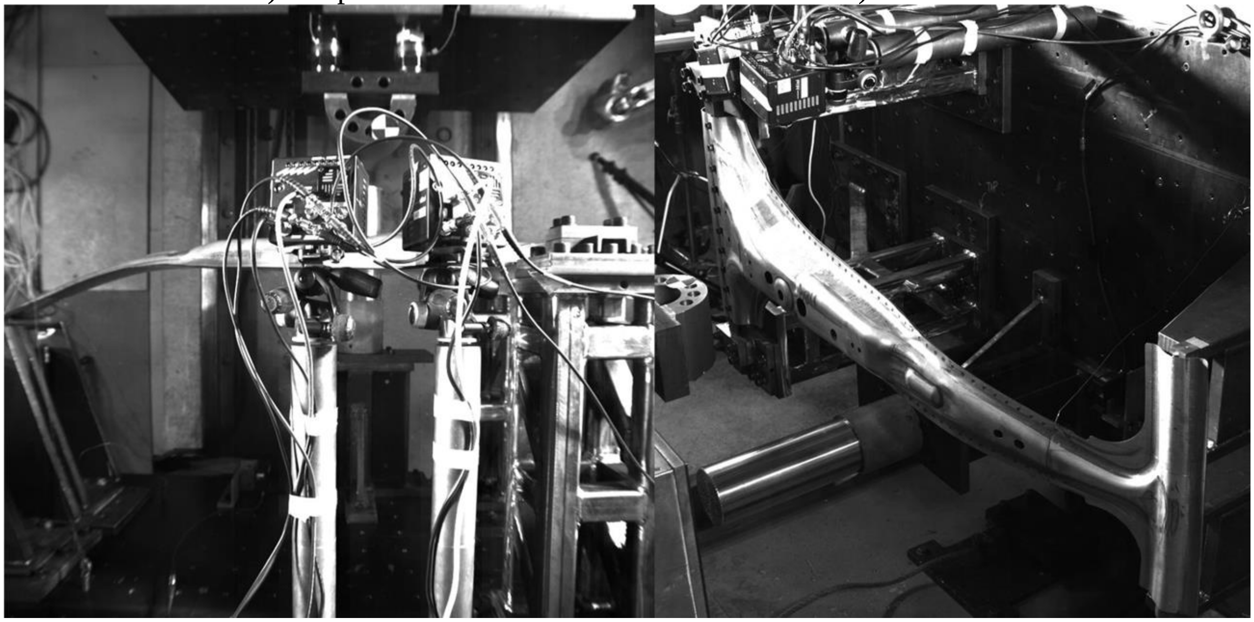

a) Top view b) Isometric view

Figure 124: Top a) and isometric b) view of the B-pillar crash test using the Photron SA-5 and SA-Z respectively

a) Back view b) Side view

Figure 125: Back a) and side b) view of the B-pillar crash test using the Photron SA-4 and SA-5 respectively

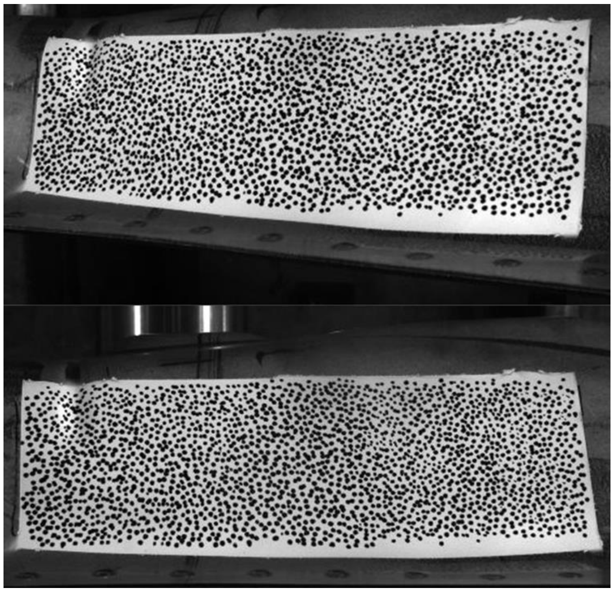

Figure 126: Speckle images captured by the Photron AX-100 cameras used for DIC analysis

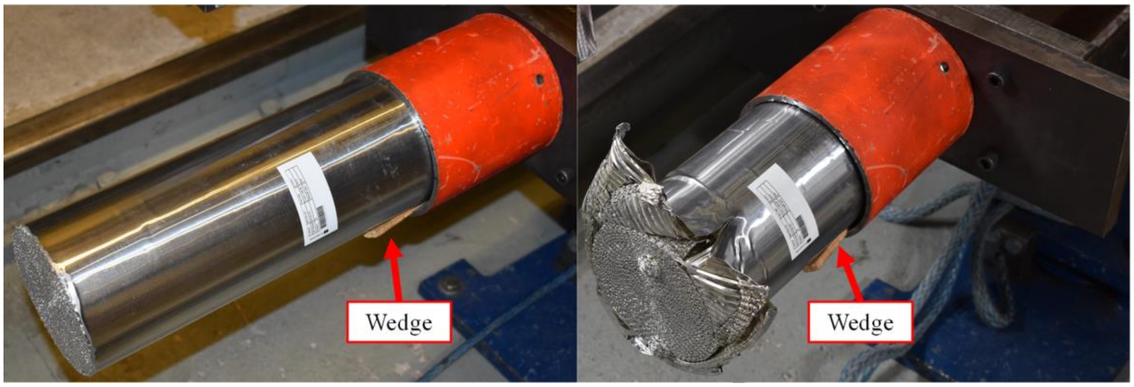

a) Full-length honeycomb b) Crushed honeycomb

Figure 127: Honeycomb showcasing its a) full-length and its b) crushed form post-test

7.2 Impact Testing

Initial designs for the impactor configurations that first arose for crash testing used the simplest design of the single impactor where the centerline of the impactor was aligned with the fold initiators. This ensures folding is engaged on the B-pillar and avoids buckling. Buckling was a concern during the early phase of generating concepts for the impact test. Another criteria that was considered was that a sufficient amount of strain would be distributed across the B-pillar which conceived the idea of a double impactor. Multiple configurations were considered to achieve the best possible deformation to extract data yet the final selection opted for the single impactor to achieve the safest testing apparatus. The analysis of the double impactor can be found in the

Appendix B as the main focus of the thesis centers on the impact testing done on the single impactor.

The high and low friction conditions were performed to observe how the impactor would bend or wrap around the B-pillar. The observable camera angles from the high-speed cameras indicating the time after impact are seen Figure 128. A top-down angle of the B-pillar was chosen so that the deformation of the B-pillar in the finite element models could be compared against the angles captured by the DIC cameras. At the last frame (67 ms), 100 mm free crush ends and the cylindrical honeycomb is engaged. Data recorded post-free crush is invalid as honeycomb is not simulated in the numerical models. The three frames show the evolution of deformation as indicated by the red dashed lines. From the second frame, the impactor initially wraps on the B-pillar at the area of impact. The impactor then releases from wrapping and proceeds to bend the B-pillar creating a v-shape typically seen on three-point bend tests. Similarly, the deformation observed on the 3rd Gen 1180 V1 exhibits comparable behavior seen in the 3rd Gen 980 seen in Figure 129.

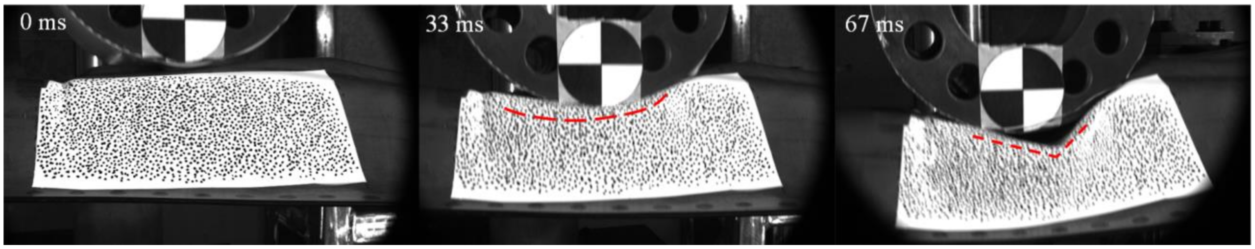

Figure 128: Synchronized frames of the B-pillar crash test and simulation highlighting the modes of deformation for the low friction condition for 3rd Gen 980

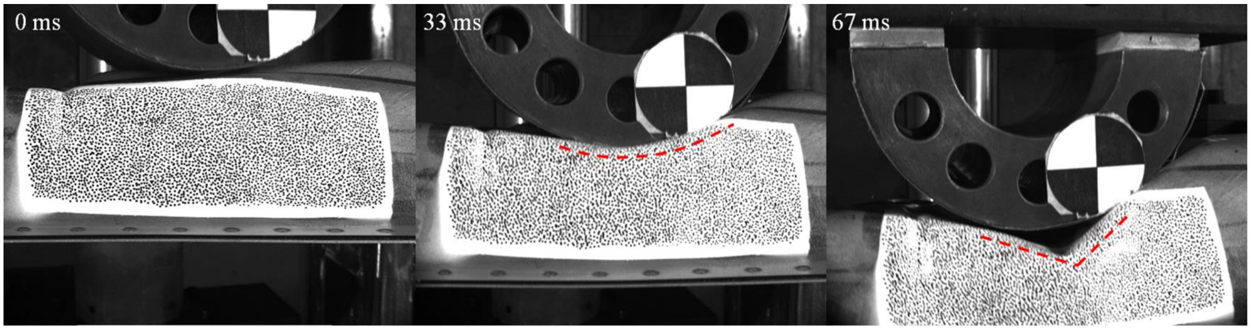

Figure 129: Synchronized frames of the B-pillar crash test and simulation highlighting the modes of deformation for the low friction condition for 3rd Gen 1180 V1

A remarkable observation on the B-pillar deformation with low friction is the obvious non-engagement of the fold initiators seen in Figure 130. The v-shape, as the B-pillar deforms, is further exacerbated past free crush which then acts as an artificial fold initiator. This non-engagement of the fold initiators is directly caused by the slippage of the impactor due to the low coefficient of friction induced by the Teflon®. The folding caused by the low friction condition is also seen in the 3rd Gen 1180 V1 steel illustrated in Figure 130. This behavior contrasts the deformation mode caused by the high friction conditions which will be discussed in the upcoming section.

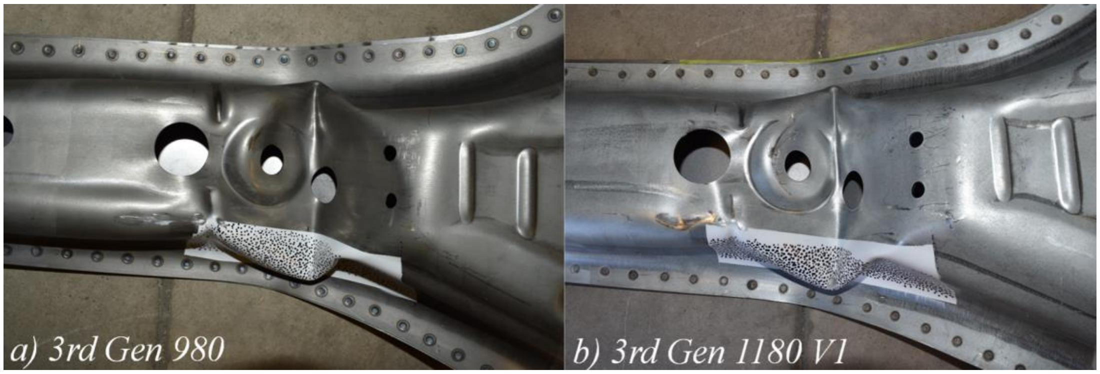

Figure 130: Folding caused by low friction conditions on the B-pillar crash tests for a) 3rd Gen 980 and b) 3rd Gen 1180 V1

7.2.1 DIC Strain Measurement

Stereoscopic DIC strain measurement was attempted on all crash tests to aid in the FE model evaluation. Various combinations of settings were tested to determine which parameters would best analyze the impact test. Step size, subset size, incremental analysis, and VSGL were among the parameters that were modified. The best combination of parameters that was used for DIC analysis that gave discernible results were a step size of 3, a larger subset of 43, and a strain filter of 2 all the while using incremental analysis. The captured images were reported to have a pixel size of 0.36 mm/pixel which gives an approximate VSGL of 2. The typical area of interest can be seen in Figure 131.

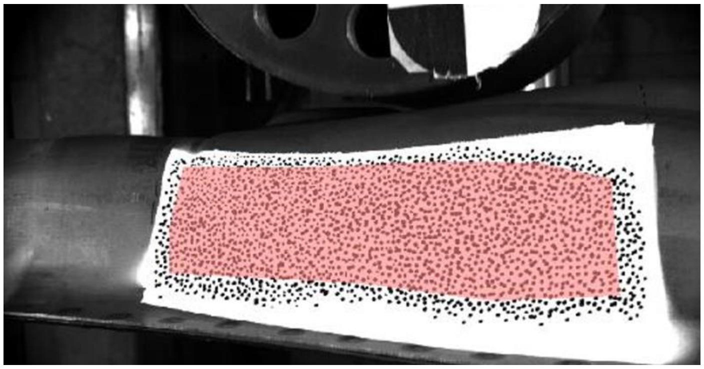

Figure 131: Typical area of interest for DIC analysis for impact tests

Unfortunately, due to minimal to no fracture observed in the B-pillar tests and the shadows induced, the DIC analysis was of limited value as deformation proceeded mostly out-of-view without any failure. An image of the major principal strains at a crush distance of 100 mm is shown in Figure 132 to highlight the measured strain field.

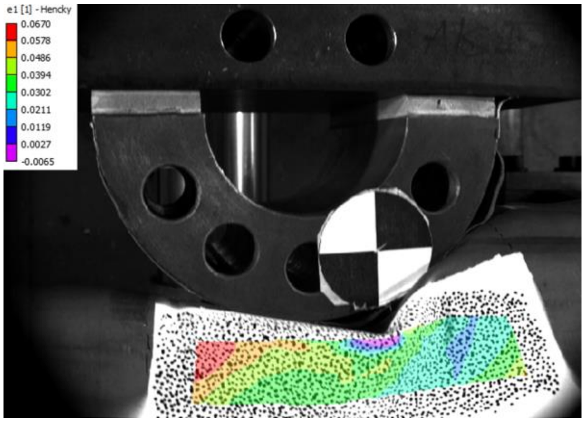

Figure 132: Major principal strain contour of 3rd Gen 980 under high friction case

7.3 FE Model Development of the B-Pillar Impact Tests

7.3.1 Modelling of Boundary Conditions

Single point constraints were used to suspend the B-pillar assembly and the alternative method physically models the slotted inserts. The B-pilar assembly and the corresponding SPCs on the assembly are illustrated in Figure 133 and Figure 134. Two configurations were used for single point constraints with the so-called ‘loose’ and ‘secured’ configurations. The loose configuration allows for some deflection and twisting of the U-channel which was present in the tests The secured configuration constrains movement in all degrees of freedom for the selected area of nodes.

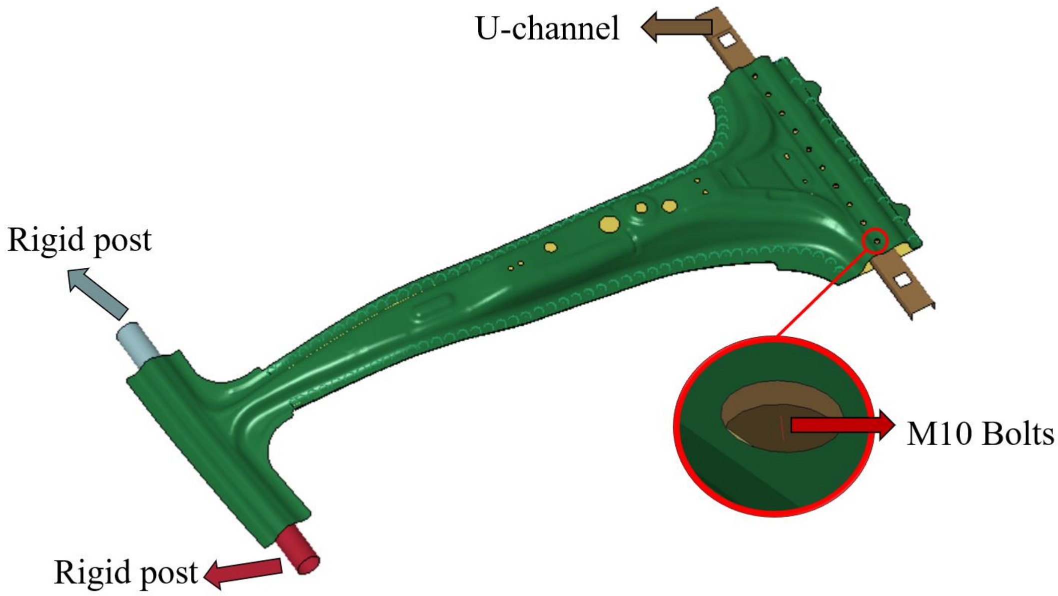

Figure 133: Boundary conditions prescribed on the B-pillar. The side sill is secured by bolting the U-channel underneath the B-pillar. The side sill lays above the rigid posts that act as rollers.

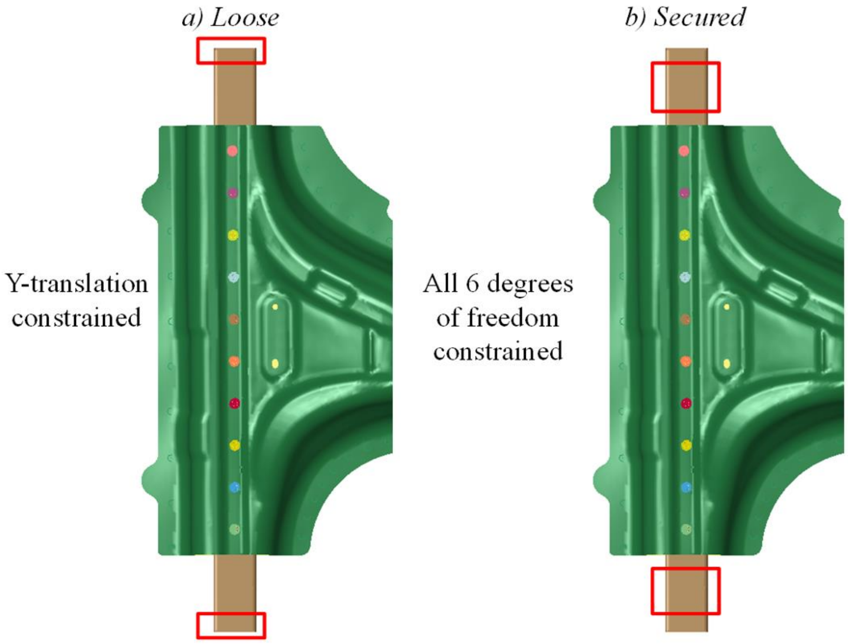

Figure 134: Locations of SPCs and the degrees of freedom constrained for the a) loose configuration and the b) secured configuration.

The next pair of configurations physically models the slotted inserts. The configurations differ by modelling them as a rigid part or an elastic part with steel properties. Physical modelling of the inserts, seen in Figure 135, gave the most representative boundary conditions of the B-pillar assembly. The rigid slotted inserts fit into the square slots on the U-channel. Securing of inserts was done by constraining the rigid parts (insert caps and slotted insert) in all degrees of freedom. A slightly more detailed modelling approach was used for the elastic inserts. Illustrated in Figure 135b, the U-channel is secured by the insert caps bolted into the slotted inserts with M14 bolts. To prevent the inserts from moving freely, the nodes on the bottom face of the inserts are constrained in all degrees of freedom.

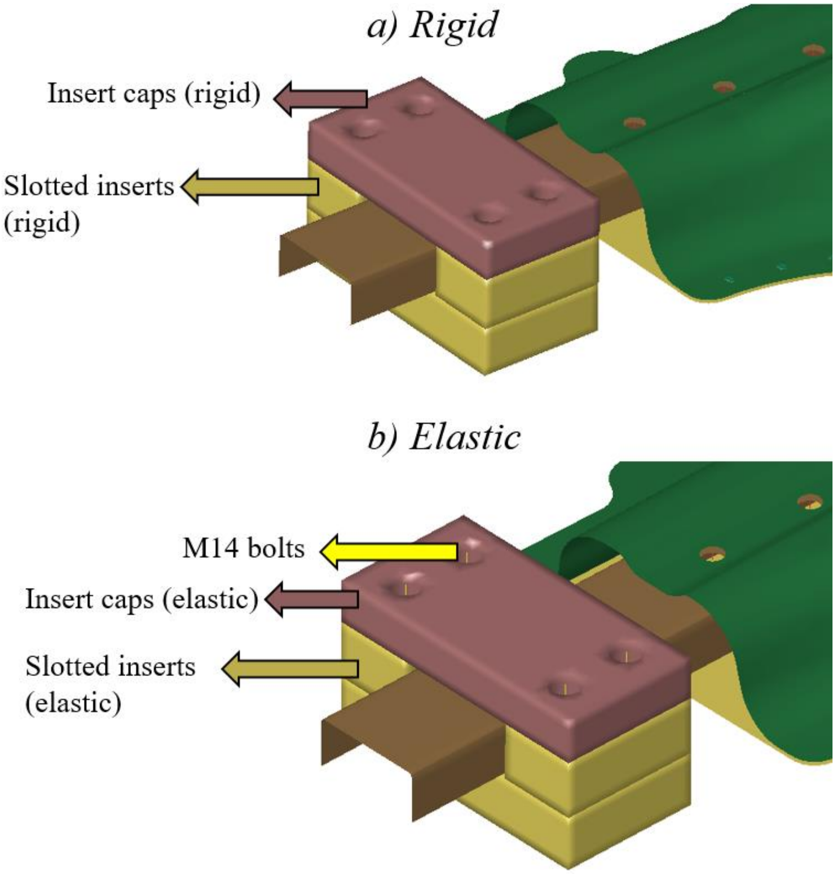

Figure 135: Physical modelling of the inserts in the crash simulation where the inserts and caps are modelled as a) rigid material and all degrees of freedom are constrained. Elastic inserts are modelled in b) where the caps are secured to the inserts with M14 bolts. The nodes of the bottom face of the inserts are constrained in all degrees of freedom to secure the assembly.

7.3.2 B-pillar Attachments

7.3.2.1 U-channel and M10 Bolts

Modelling of the U-channel follows the dimensions specified in Figure 115 where quadrilateral shell elements are used. The von Mises yield function with power law plasticity is used as the material description. The material description of the M10, Class 10.9 bolts was obtained from

FEMA (2002) where a power law fit was utilized to extend the hardening obtained from literature previously shown in Figure 116a.

The bolts were modelled used Hughes-Liu (type 1) beam elements. Beam elements are used to model the bolt shank where the beam elements are attached to the nodes around the bolt hole using nodal rigid body connections. This method of modelling bolts generates a spider mesh, seen in Figure 136, which emulates a bolt and nut. A pre-tension of 47 kN was applied to the bolts by imposing an initial axial force on the beam element in LS-DYNA.

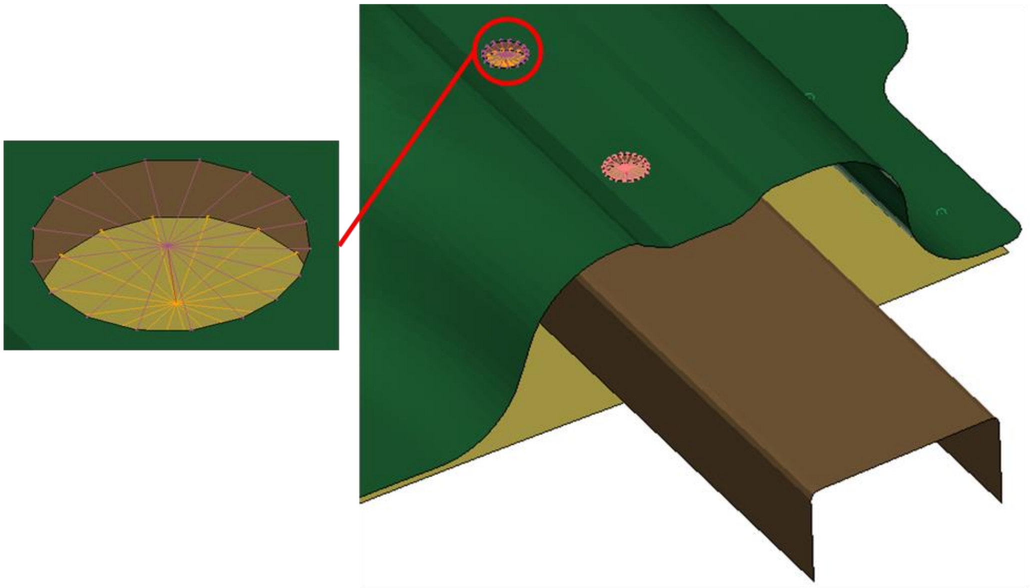

Figure 136: Spider mesh applied on the U-channel and B-pillar modelling nuts and bolts

7.3.2.2 Backing Plate and Spotweld Modelling

The backing plate was a JAC590R AHSS sheet of 1.4 mm thickness that was spotwelded on the flanges of the B-pillar. The material description for the backing plate uses a von Mises yield function. The hardening curve for JAC590R is plotted in Figure 119 and the locations of the spotwelds are seen in Figure 137.

The spot welds were modelled using the MAT_100 material card specific to beam elements that uses Hughes-Liu beam formulation (type 9) (LSTC, 2014). The beam elements representing the spotwelds uses a tied contact algorithm which attaches the B-pillar and the backing plate. The spotwelds are located 12 mm away from the edge of the flange and has a distance of 25 mm from each spotweld which comes to a total of 101 spotwelds throughout the assembly.

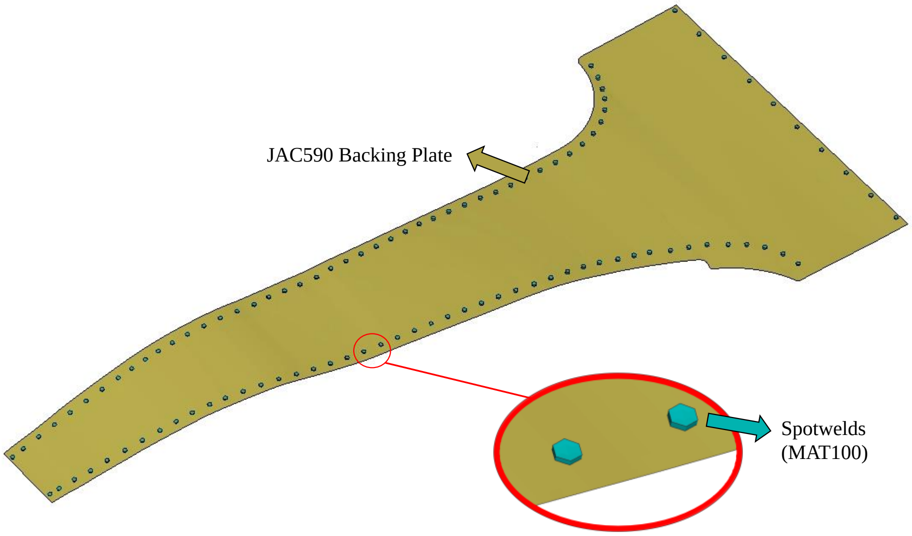

Figure 137: Location of spotwelds on the backing plate

The method employed to model the spotwelds uses solid hexahedral elements with the 8-hex configuration. Multiple variations of the hexahedral weld models exist such as the single-hex, 4-hex, and 16-hex configuration seen in Figure 138. The single-hex weld configuration can be an inadequate representation as it may not conform to the mesh if it is finer than the weld itself and can be overly stiff. The 4-hex configuration produces more reasonable results as it can conform to the mesh of the master segment better. The difference in forces and mesh conformance is minimal between the 8-hex and 16-hex configuration therefore further mesh refinement above the 8-hex mesh can be unnecessary (Malcolm and Nutwell, 2007). The weld model considers the forces and moments in the R, S, and T axes which is relative to the spotweld which can be defined in each spotweld with three nodes as shown in Figure 139. The weld model uses isotropic plasticity where a failure model can be used to delete the elements for the weld model. No failure model is applied to the spotwelds as no failure was observed during the crash experiments.

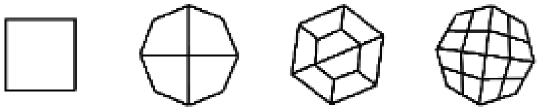

Figure 138: Hex weld configurations from 1-hex to 16-hex configurations

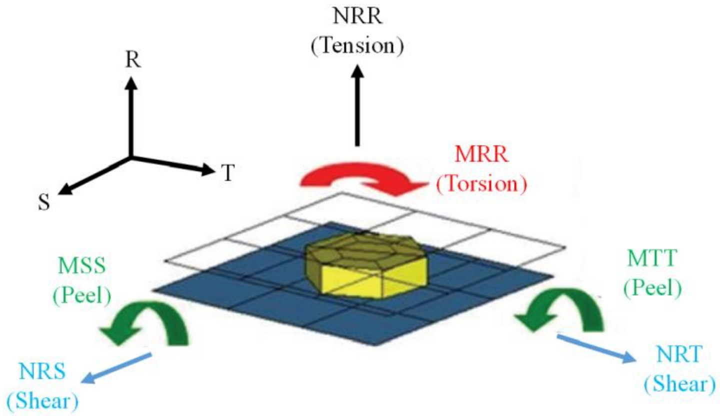

Figure 139: A 8-hex weld configuration indicating the directions of the forces and moments experienced by the weld (Malcolm and Nutwell, 2007)

7.3.3 Modelling of the crash event

The modelling of the sled models the impactor as an elastic material using the mechanical properties of steel. The impactor is cylindrical with a radius of 101.6 mm and modeled using solid elements. To mimic the mass of the sled, a defined mass of 1000 kg using *PART_INERTIA is implemented into the impactor. The initial velocity of the impactor emulates the velocity of the sled of 50 km/hr. The deceleration of the sled and load response after the sled hits the honeycomb are excluded from the correlation with the test data. Only the 100 mm of free crush is considered.

To measure the forces experienced by the impactor, a contact definition using force transducers is generated. The prescribed contact definition using force transducers requires a slave and master surface. In the simulation, the impactor is the master surface and B-pillar is the slave surface. The arrangement of the crash simulation is illustrated in Figure 140.

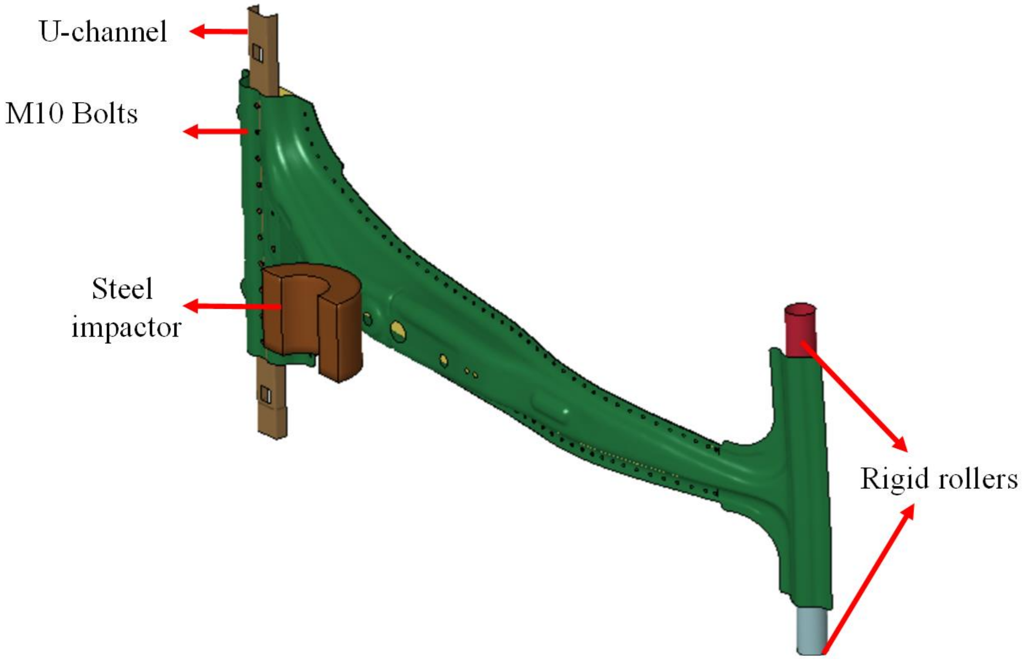

Figure 140: Crash sled modelling method

Contact definition between all metal surfaces is defined by using an automatic single surface algorithm which seeks contact between different parts defined in the slave set (LSTC, 2014). Among the relevant parameters needed to be defined include the following: the static coefficient of friction, the dynamic coefficient of friction, the coefficient of viscous friction, and the viscous damping coefficient which are provided in Table 12 for all AHSS.

Table 12: Coefficients used to define the contact between metal interfaces used in the crash simulation

μ_s	μ_d	**$V_{c\text{-}980}$ [MPa]**	**$V_{c\text{-}1180\ V1}$ [MPa]**	**$V_{c\text{-}1180\ V2}$ [MPa]**	**V_{DC}**
0.40	0.20	597	702	602	20

Prior to running the crash simulation, residual strains from the forming and springback simulations were re-mapped to a new mesh. The changing geometry due to springback affects placements of spotwelds and will misalign if, for example, the spotwelds generated for the 3rd Gen 980 B-pillar are used for the 3rd Gen 1180 V1 B-pillar and vice-versa. Although generating new spotwelds for each steel is also an option, generation of spotwelds is a time-consuming process and a slight change in simulation parameters such as NIPs or friction coefficient from either the forming or springback stages can alter the shape of the B-pillar such that spotwelds completely misalign. Instead of generating new spotwelds for each AHSS, residual strains are remapped on to a clean mesh and only the material description of the B-pillar was changed.

7.4 Impact Test Correlations

7.4.1 Force and Energy Comparisons

This section entails all simulation results extracted from the different modelling methods, friction conditions, and mapping of residual forming strains. Additionally, the crash response of 3rd Gen 1180 V2 and 590R AHSS were studied to compare with the tested 3rd Gen AHSS.

7.1.4.1 Filtered and unfiltered force responses

Force data extracted from the impact tests on the sled wall was plotted against time where the unfiltered and filtered results are illustrated in Figure 141a and b, respectively. The load cells have a capacity of 120 kN. Although the load drop in the filtered results was still distinguishable from the noise, the change in the shape of the trend and peak loads are significantly different. Peak loads from the force data dropped from 36 kN (unfiltered) to 21 kN (filtered) for 3rd Gen 980. Similarly, the force data for 3rd Gen 1180 V1 dropped from 44 kN (unfiltered) to 28 kN (filtered). After honeycomb impact, an abrupt load drop is observed from the unfiltered results. This load drop is not evident in the filtered results. Other information such as the sustained drop in forces by approximately 50% of the peak load at 0.06 seconds is also filtered to the point that it is indistinguishable. Due to much information being washed out from the filtering, the unfiltered force response is used to compare with simulation results.

The filter used and recommended by the Society of Automotive Engineers (SAE) is prescribed by SAE J211. Filtering of data acquired from the accelerometer uses a low pass filter with a channel frequency class of 60 Hz. The primary filtering process was governed by the Butterworth filter and is commonly used for impact testing (SAE, 1995). It has been recommended by Grenke (2002) that an alternative filtering method be considered using fast Fourier transforms (FFT). According to Grenke, the use of FFT can prevent distortions that are caused by Butterworth filtering.

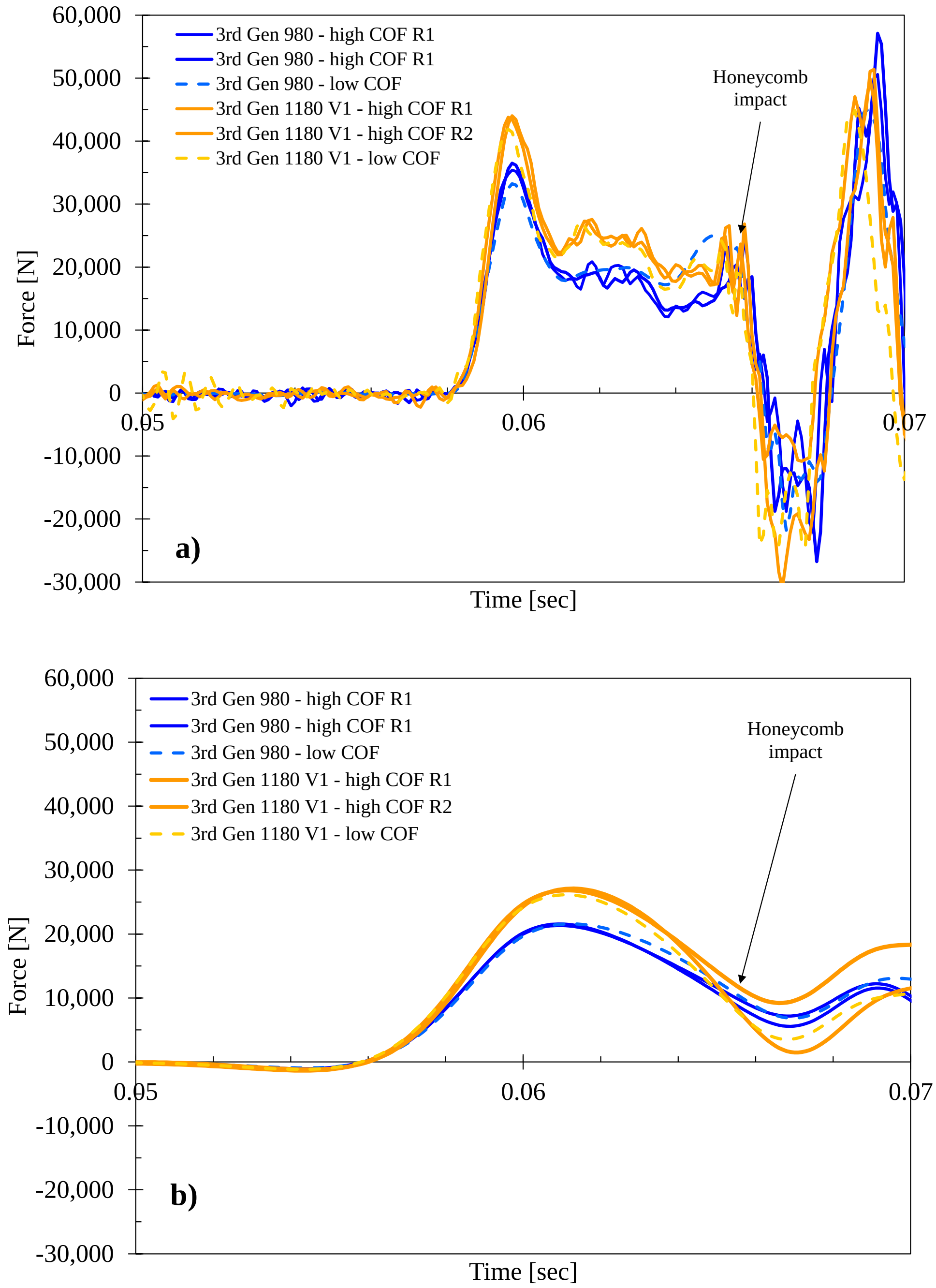

Figure 141: Force response of 3rd Gen 980 and 3rd Gen 1180 V1 showing a) unfiltered and b) filtered results

A snapshot of the crash simulation and impact test of 3rd Gen 980 under high friction at 40 mm crush distance is illustrated in Figure 142. It is evident in Figure 142a the simulation shows that the side wall is markedly collapsed compared to the experiment in Figure 142b. It is believed that due to the B-pillar side wall collapsing much earlier in the simulation, peak forces are not attained that are consistent with the experiments. The same trend is exhibited by the 3rd Gen 1180 V1 crash simulation. Correlation of the forces are discussed in the upcoming sections.

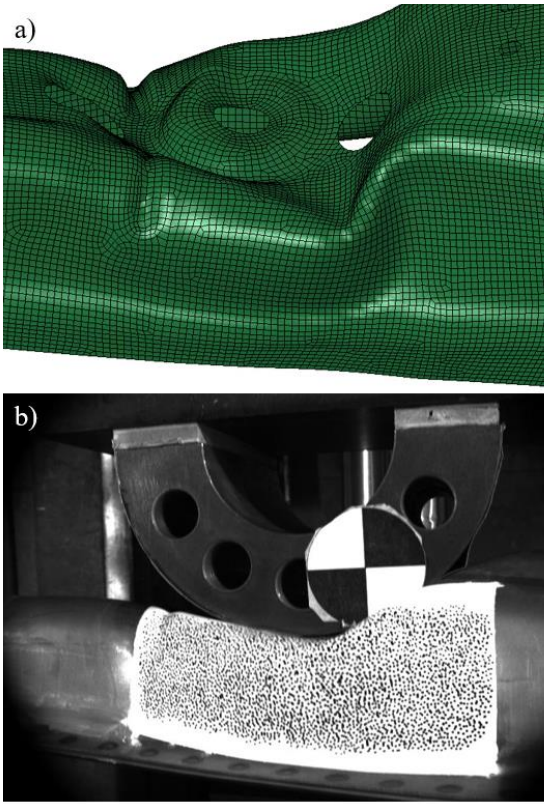

Figure 142: Impact test of 3rd Gen 980 under high COF at 40 mm crush distance showing that the side walls from the simulation model collapses much earlier than the experiment.

7.1.4.2 Friction conditions and BC configurations

The force response for all modelling methods and friction conditions for 3rd Gen 980 and 3rd Gen 1180 V1 are illustrated in Figure 143. As expected, the high friction test cases provide the highest peak forces by several kN. The low friction cases are represented by the dashed line. Repeatability in the experiments is adequate as both 3rd Gen 980 and 3rd Gen 1180 V1 exhibit a similar force evolution. Differences between the high and low friction cases, besides from the slightly lower peak forces, are subtle. The experimental force response exhibits a sudden drop in load to about 50% of its peak value at approximately 20 mm crush distance that is associated with collapse of the sidewall for both steels. Forces after free crush (100 mm) is not reported as the honeycomb has engaged to decelerate the sled.

Overall, the correlation of the force-displacement histories is underwhelming with the peak loads underestimated and the forces after sidewall collapse to be overestimated. After evaluating the influence of filtering, different modelling methods of the slotted inserts were considered such as modelling them as rigid materials and as elastically deformable material with steel properties. None of the modelling methods did not significantly affect the force response nor a change in COF. The choice of slotted inserts and high COF was then selected for the remaining simulations in this chapter.

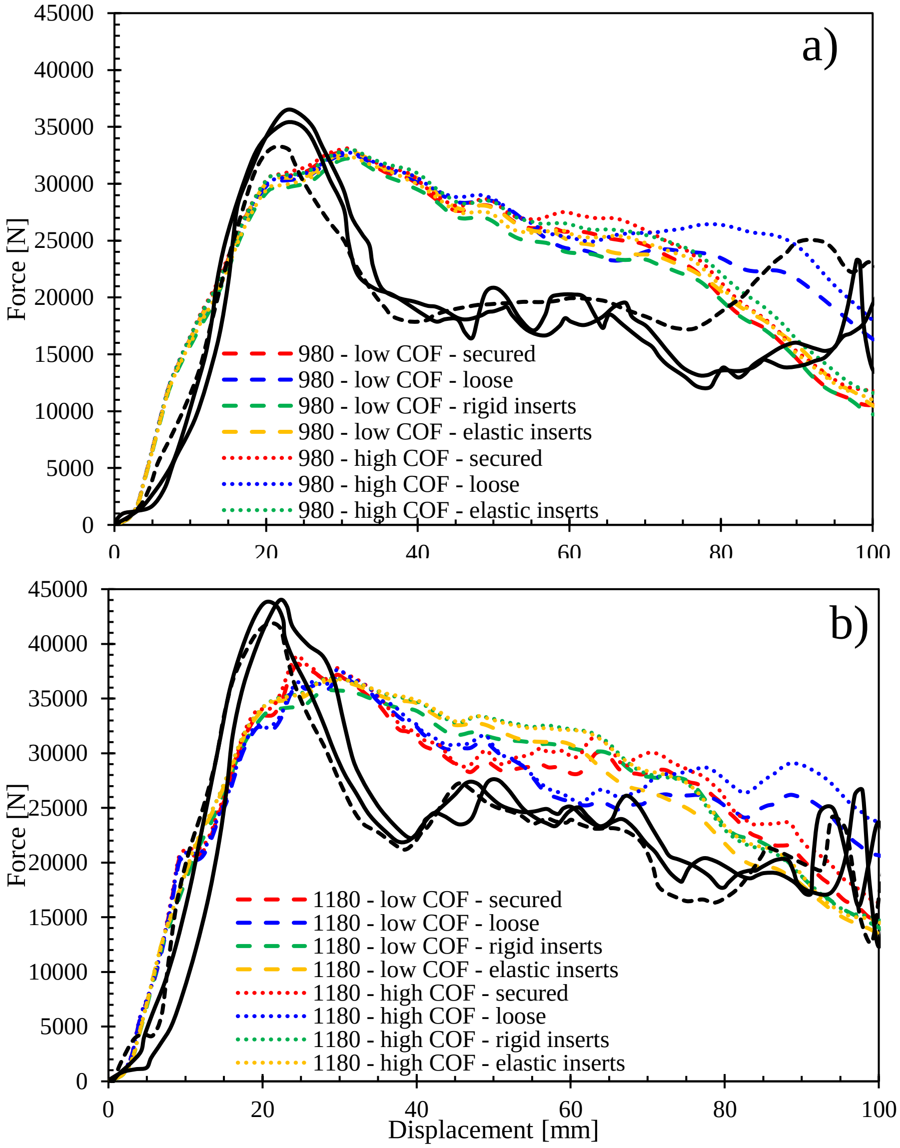

Figure 143: Force response of the crash simulation overlaid with the experimental results showing all modelling methods and friction conditions for the a) 3rd Gen 980 and b) 3rd Gen 1180 V1. Note that the black solid lines represent the experiments with high COF and the black dashed lines represent the experiments with low COF.

7.1.4.3 Residual strains and energy

To evaluate the influence of the forming history the residual strain and accumulated damage were compared with the impact forming simulations that idealize the B-pillar as a virgin material. The predicted forces are shown in Figure 144 and are more similar than first expected. The forces are slightly higher when the forming history is considered but since large regions of the B-pillar have low forming strains, the global force response was relatively close to that of the virgin material.

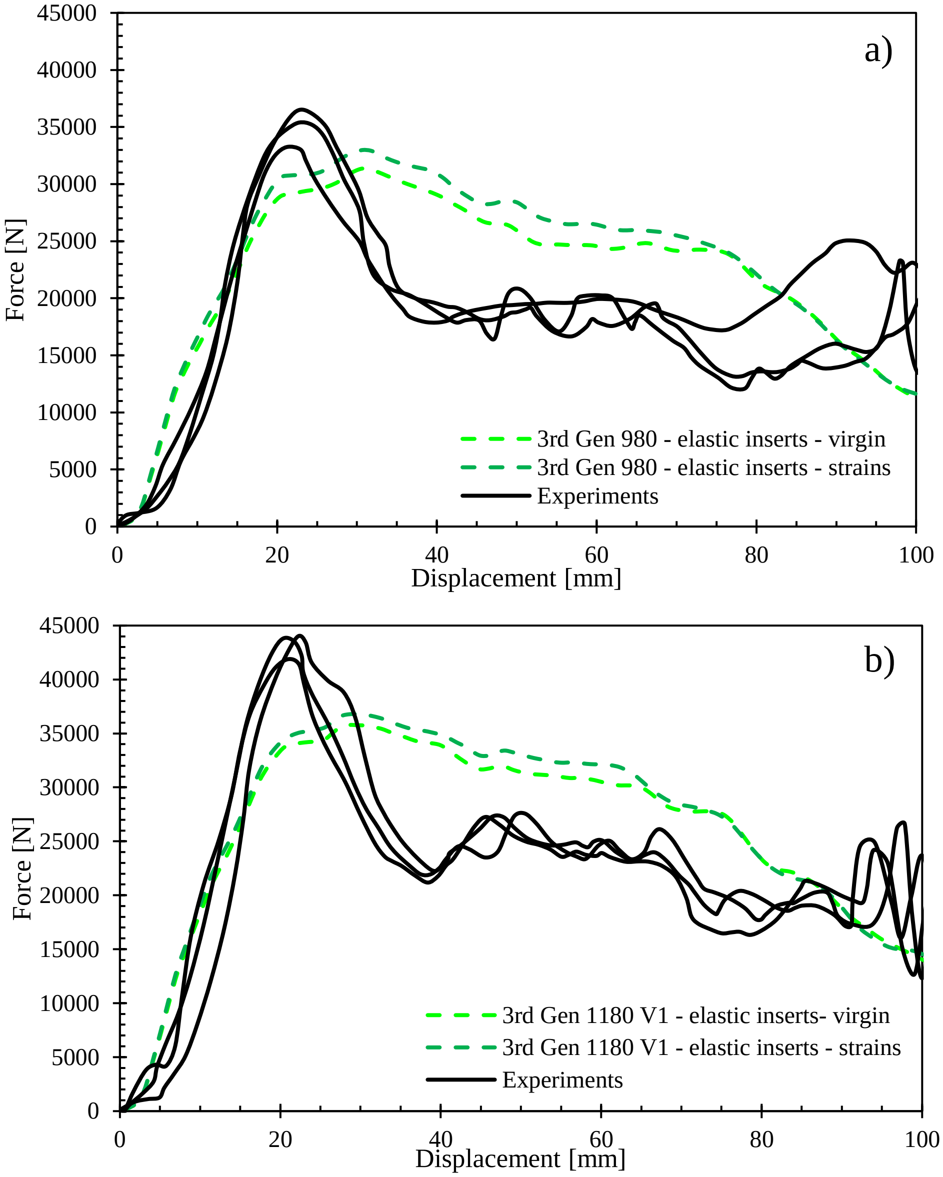

Figure 144: Force response of the B-pillar crash simulation with virgin steel and strain mapping for a) 3rd Gen 980 and b) 3rd Gen 1180 V1

Aside from the force-displacement history the amount of energy absorption is important for crash engineers to evaluate the performance of a structural component. The integrated energy with crush distance for the models and tests are shown in Figure 145. The simulations report a higher energy response due to the simulation not capturing the drop in the peak force. The simulations overestimate the energy by approximately 27% and 14% for 3rd Gen 980 and 3rd Gen 1180 V1, respectively, at the end of free crush.

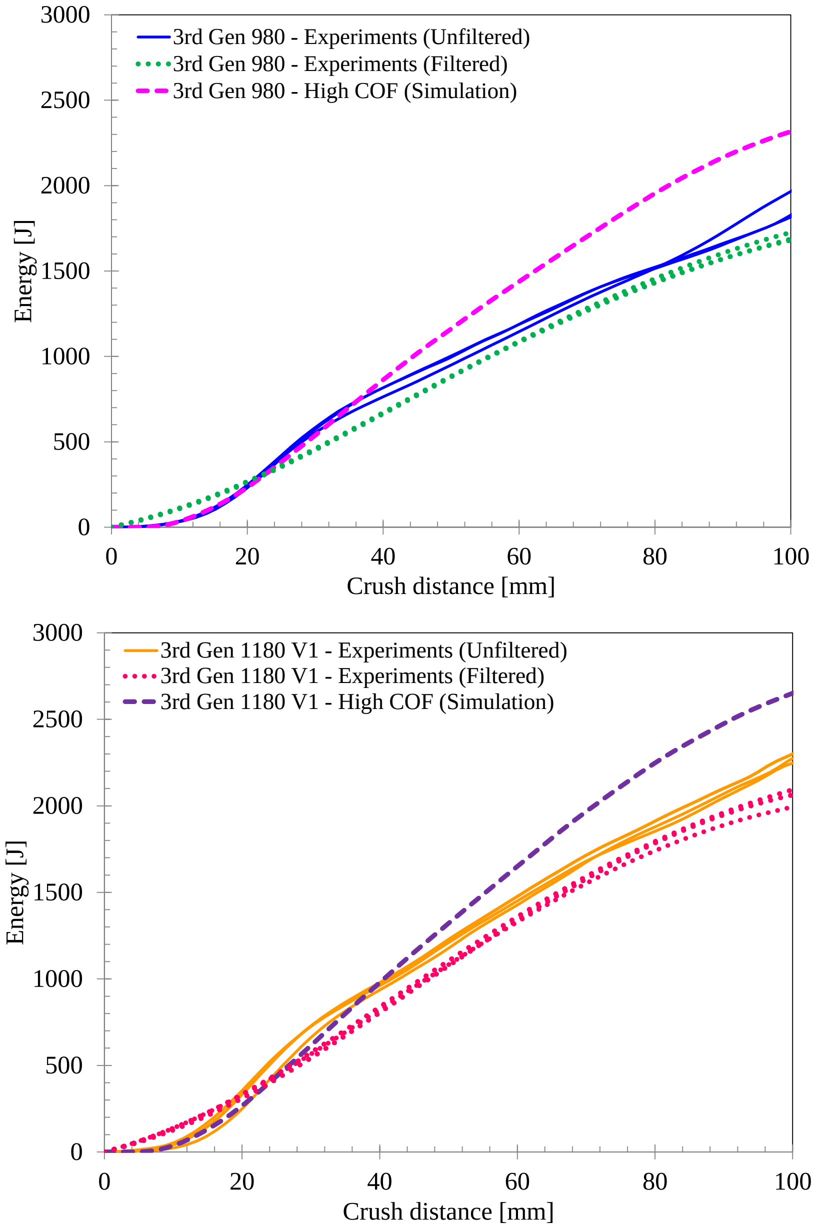

Figure 145: Energy reported by the experiments overlaid with the energy of the simulations for both a) 3rd Gen 980 and b) 3rd Gen 1180 V1.

Impact tests of the 590R AHSS and 3rd Gen 1180 V2 were not performed but are evaluated numerically. The 590R AHSS and 3rd Gen 1180 V2 were intended to be used as comparators for 3rd Gen 980 and 3rd Gen 1180 V1, respectively, to gage the difference in formability. The force and energy response of the four steels are shown in Figure 146 and Figure 147, respectively and follow the strength of each material in terms of the peak force with 590R 3rd Gen 980, 3rd Gen 1180 V2, and 3rd Gen 1180 V1.

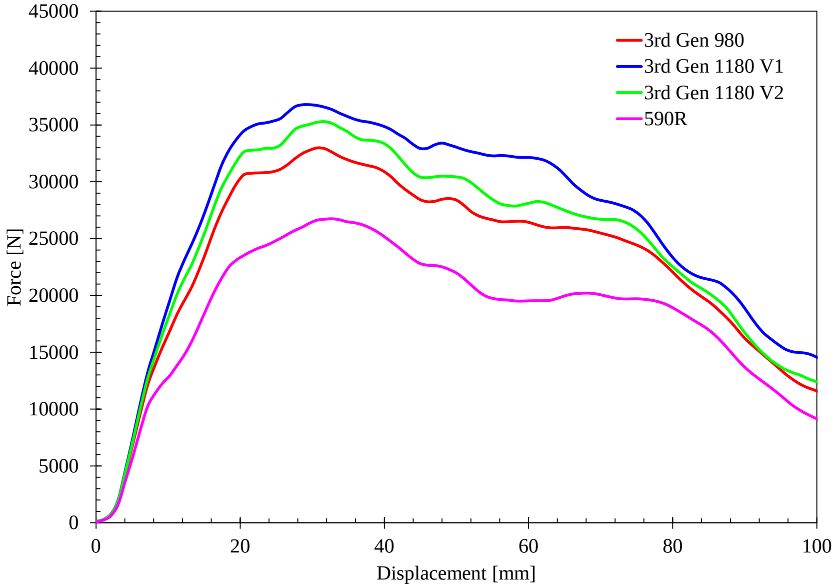

Figure 146: Force readings of all 3rd Gen AHSS impact simulations

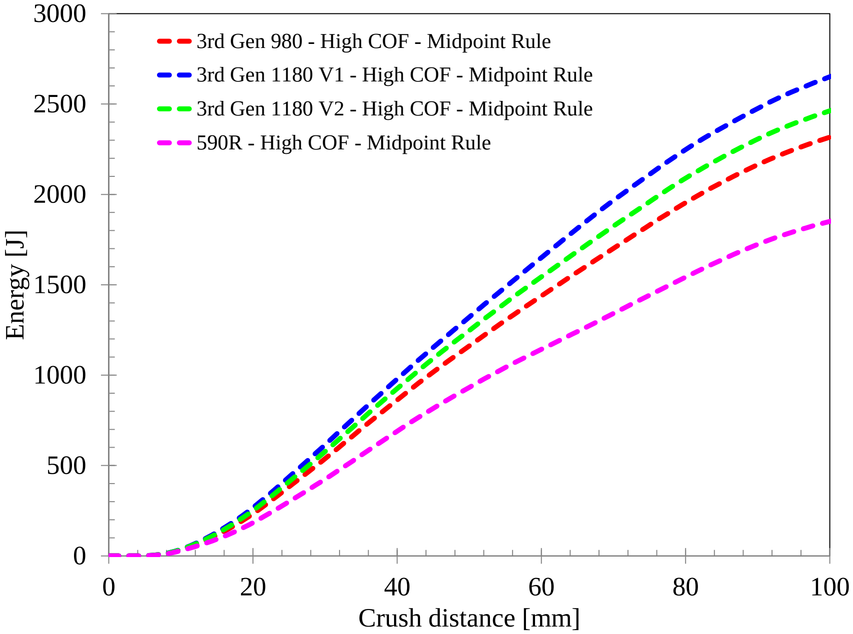

Figure 147: Energy response of all 3rd Gen AHSS integrated from the force response

7.1.4.4 Fracture prediction

Plane strain and biaxial regularization of the fracture loci were applied to the damage model to predict the splitting in the B-pillar. Although no splitting occurred during the duration of free crush for the impact tests, the GISSMO fracture model was still included in the simulations to determine if fracture would be overpredicted and provide insight on which regularization strategy for the mesh size was most effective. No fracture was predicted in the 3rd Gen 980 B-pillar simulations under either regularization condition as seen in Figure 148. No fracture in the 3rd Gen 1180 V1 B-pillar although minor local cracking was observed after the test. It is believed the minor local cracks occurred after the free crush as shown in Figure 149. High and low friction reported consistent predictions where no element deletion occurred during free crush.

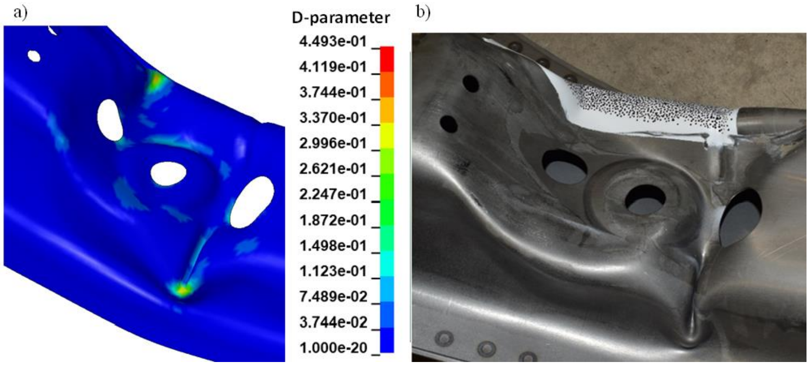

Figure 148: Contour plot of the D-parameter for the middle integration point using biaxial regularization factors for a) 3rd Gen 980 B-pillar a) and b) the crash tested 3rd Gen 980 B-pillar where no splits occur in the simulation using plane strain or biaxial regularization.

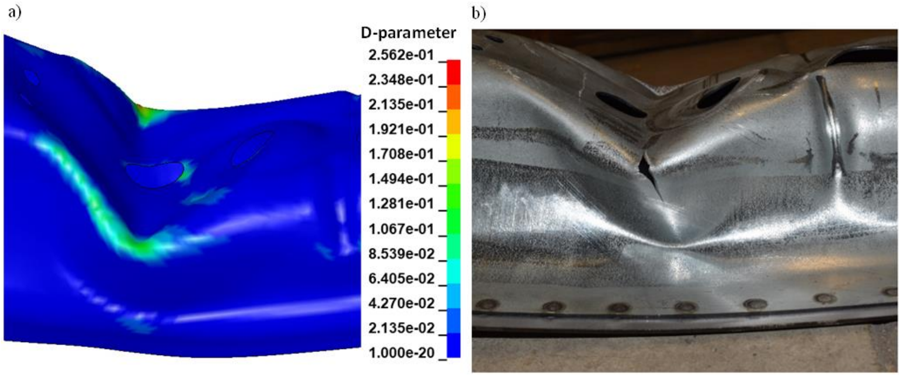

Figure 149: Contour plot of the D-parameter parameter for the middle integration point using biaxial regularization factors for a) 3rd Gen 1180 V1 B-pillar b) and the crash tested 3rd Gen 1180 V1 B-pillar showing splitting. It should be noted that splitting in the impact test occurred past free crush.

7.4.2 Deformation modes – low COF

The deformation modes from the simulations and impact tests for both steels are shown in Figure 150 and Figure 151 at crush distances of 0, 50, and 100 mm. The deformation on both steels show same trends where the simulation is consistent with the impact tests at all specified crush distances. The v-shape that is generated at 100 mm crush distance is worth noting due to how much it abruptly changes the geometry of the B-pillar. This sudden change in geometry is discussed further in the DIC analysis.

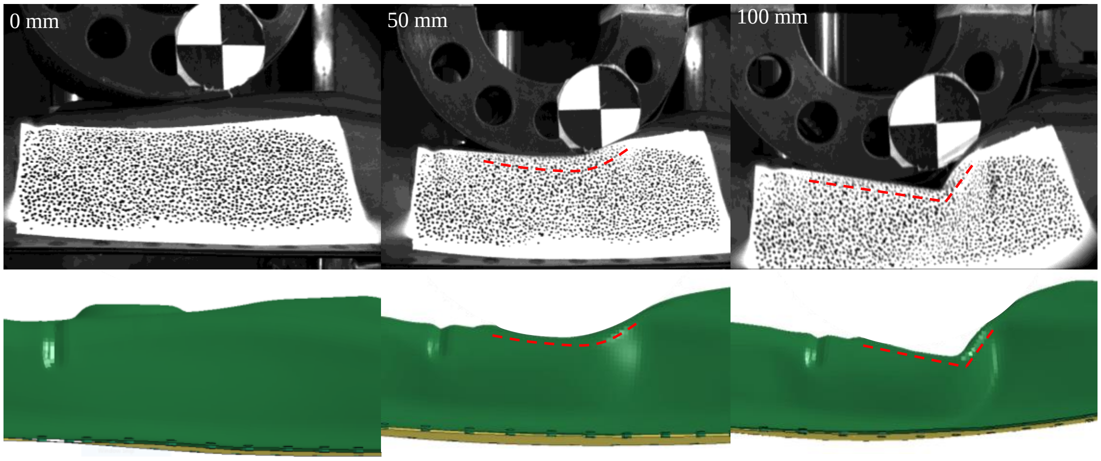

Figure 150: Synchronized frames of the B-pillar crash test and simulation highlighting the modes of deformation for the low friction condition for 3rd Gen 980

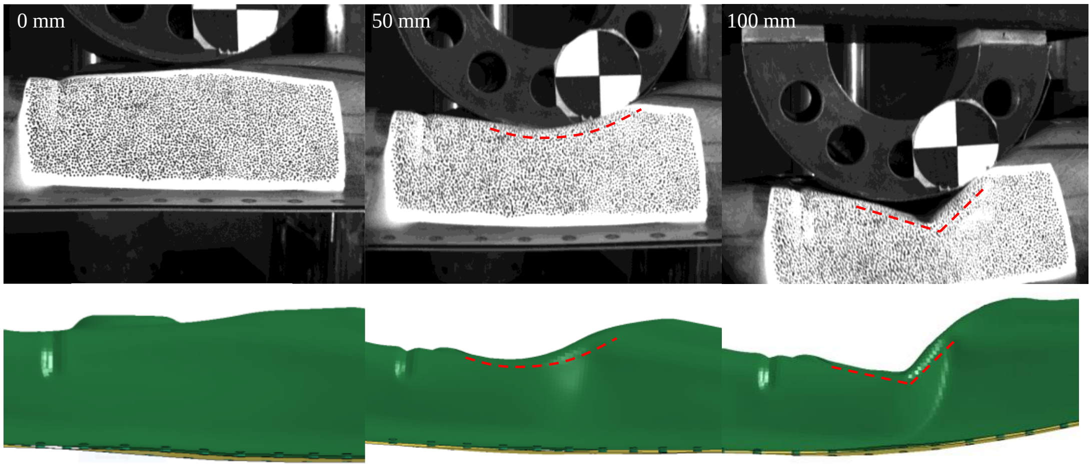

Figure 151: Synchronized frames of the B-pillar crash test and simulation highlighting the modes of deformation for the low friction condition for 3rd Gen 1180 V1

7.4.3 Deformation modes – high COF

Similarly to the low COF case, the deformations exhibited at the speckle area exhibit the same behavior of initial wrapping at 50 mm and the abrupt v-bending at 100 mm crush distance for the high friction case seen in Figure 152 and Figure 153. Using a higher COF promotes additional wrapping around the punch before the side wall collapses to form a v-shape. The wrapping is pronounced for the 3rd Gen 980 seen in Figure 154. For the 3rd Gen 1180 V1 shown in Figure 155, the influence of the COF was smaller with less wrapping around the punch which is attributed to the higher surface hardness of the 3rd Gen 1180 V1.

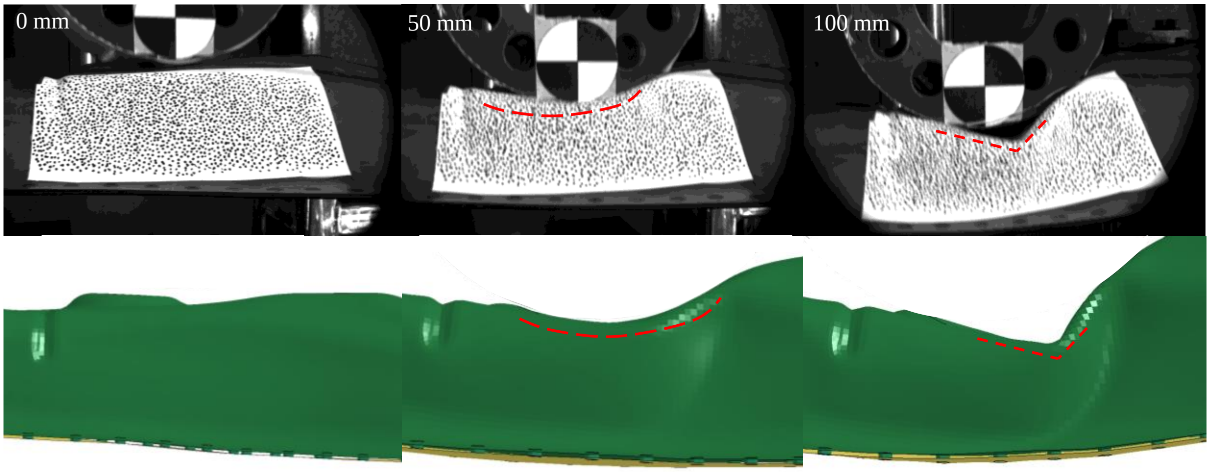

Figure 152: Synchronized frames of the B-pillar crash test and simulation highlighting the modes of deformation for the high friction condition for 3rd Gen 980

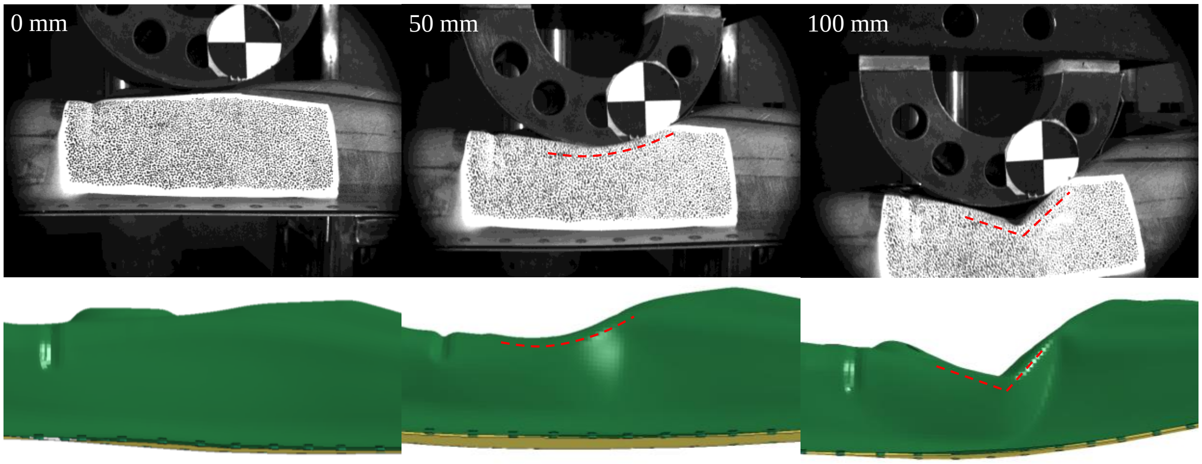

Figure 153: Synchronized frames of the B-pillar crash test and simulation highlighting the modes of deformation for the high friction condition for 3rd Gen 1180 V1

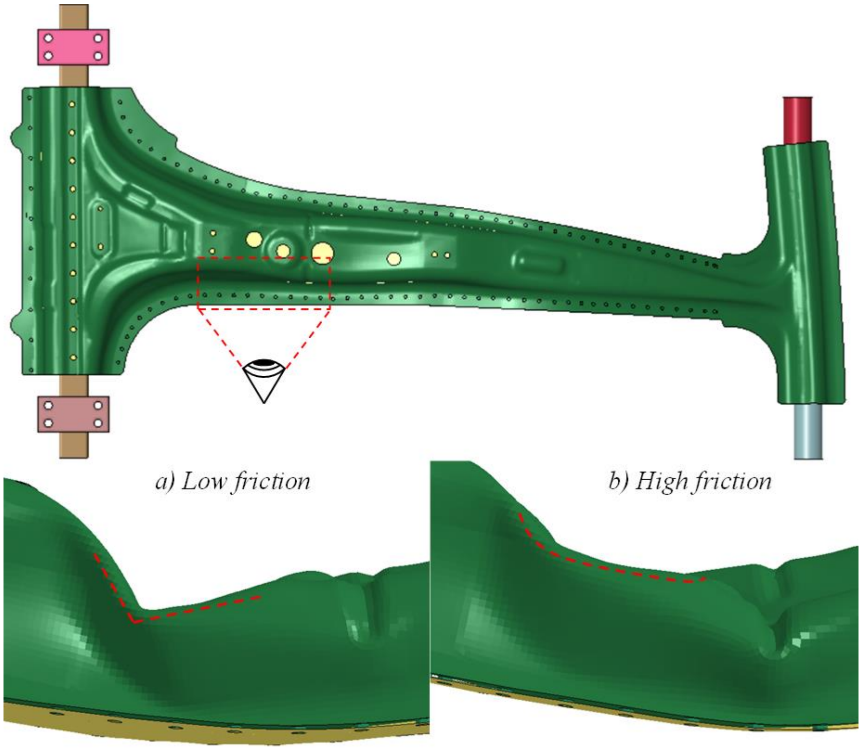

a) Low friction

b) High friction

Figure 154: Crash simulations of 3rd Gen 980 showcasing the bending and wrapping mode utilizing a) low and b) high friction, respectively. The bottom images highlight the deformation at 100 mm crush distance below where its perspective is shown by the lateral eye symbol.

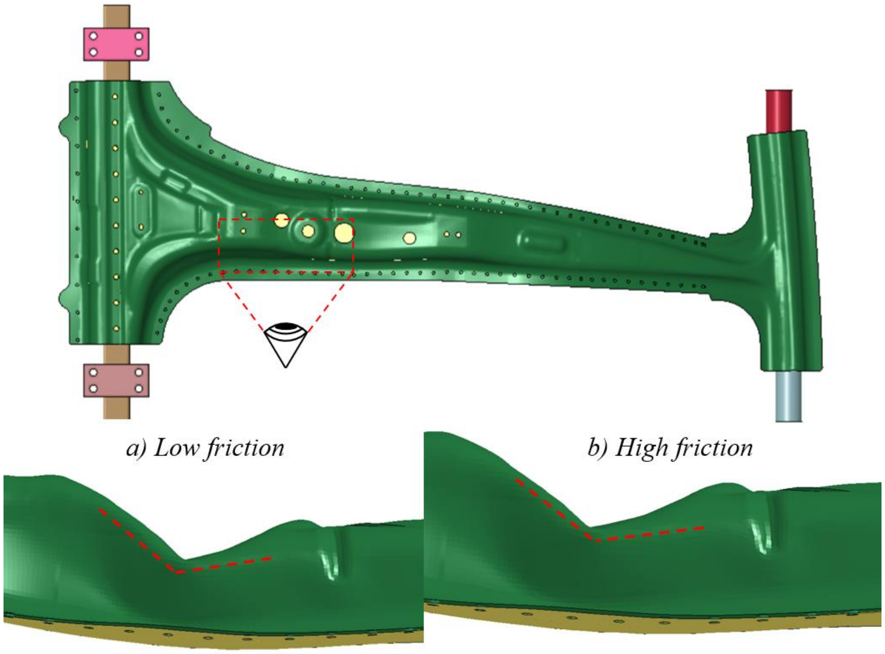

a) Low friction

b) High friction

Figure 155: Crash simulations of 3rd Gen 1180 V1 showcasing the bending mode utilizing a) low and b) high friction, respectively. The bottom images highlight the deformation at 100 mm crush distance below where its perspective is shown by the lateral eye symbol.

7.4.4 Surface strain measurement

The surface strains measured using DIC at an impactor distance of 50 and 100 mm and its corresponding simulation is shown in Figure 156. The abrupt collapse of the side wall is seen in Figure 157. Unfortunately, the DIC was not able to resolve the strains close to the impactor under bending where the strains were highest. Little information can be gleaned from the DIC for correlation beyond the general strain contours with the DIC analysis breaking down due to collapse of the sidewall and losing correlation visualized in Figure 157. Future work should consider the use of ARGUS® strain measurement where an optical system is used to measure the strains after deformation that is akin to an automated version of CGA. The DIC was not successful but the ARGUS system could provide a scan of the part with the final strains computed based upon the assumption of linear strain paths.

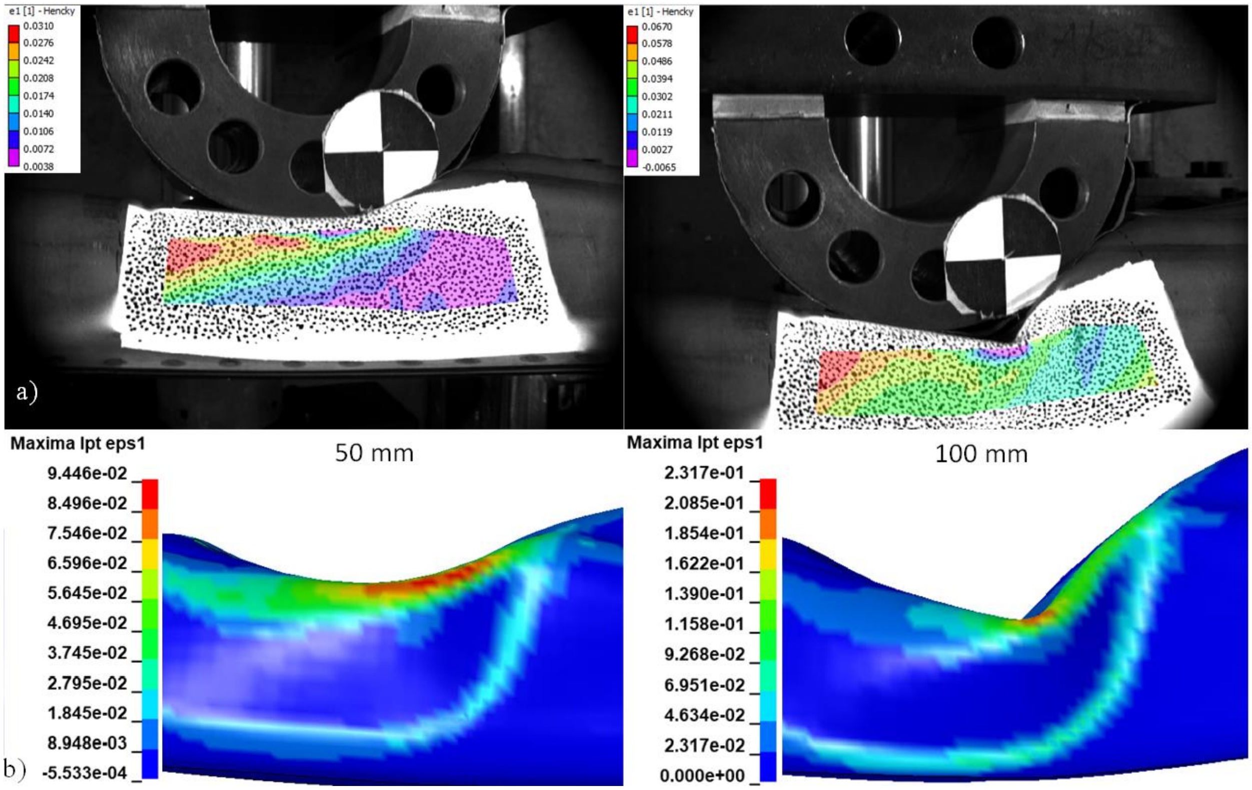

Figure 156: Comparison of crash experiments with DIC analysis and crash simulations showing its strain contour plot at 50 mm and 100 mm for 3rd Gen 980 low COF highlighting the a) DIC strain analysis synchronized with b) the crash simulations

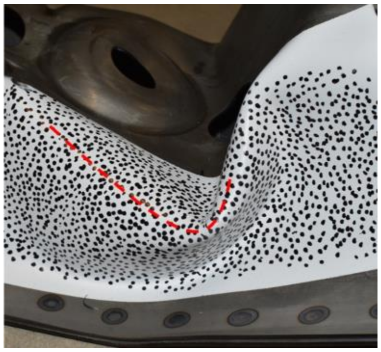

Figure 157: Bending caused by the impactor on the 3rd Gen 980 B-pillar with low COF where the dashed lines highlight the bending

7.5 Discussion of Force Correlations

The deformation of the simulation and experiments look similar, but the deformation history of the numerical model differs from the experiment. Three speculations are made that gives insight on the inconsistency in correlations. Firstly, the side walls in the simulation collapses earlier than the experiment. Once forces reaches their peak, the side walls do not collapse much further and it appears that the impactor is merely pushing on the B-pillar without further deformation of the side walls. Because of this early deformation without further collapsing the side walls, more plastic deformation is necessary to engage a full collapse. Due to the impactor not fully collapsing the side walls and only pushes on the B-pillar, the force response does not drop abruptly as it did on the experiments. Rather than the forces immediately dropping, it gradually declines after reaching its peak.

The inconsistency could also be caused by a phenomenon not captured within the simulation. High-speed impact testing results in deformation that occurs at a fraction of a second. This deformation occurring at high-speeds can induce adiabatic heating at very local regions in the B-pillar. Adiabatic heating may be enabling a deeper collapse in the experiments that is not captured in the simulation. This adiabatic heating may further promote the TRIP effect inherent in AHSS which increases the hardening within the material further increasing the peak loads in the impact test.

Lastly, which is the most probable cause of the inconsistency in force correlations, are the loose boundary conditions on the roof rail of the B-pillar. From the high-speed imaging, having the side sill just lay on the roller fixtures causes an uncontrolled mode of deformation. The side sill vigorously flaps and is very difficult to capture within the simulation. Constraining the side sill to some degree could mitigate the inconsistency in forces within the impact simulations.

Certain snapshots in time of the impact tests appear similar but the subsequent deformation behavior between simulations and experiments are dissimilar. This inconsistency makes a difficult one-to-one comparison. It would be of interest to observe the microstructure of the AHSS after forming and impact testing to confirm if TRIP effects were present and further activated after crash testing. Implementation of thermal cameras would also aid in confirming the occurrence adiabatic heating.

7.6 Discussion, Conclusions, and Recommendations of Impact Tests and Simulations

Predictions from the simulations were evaluated with the impact tests of the B-pillar for 3rd Gen 980 and 1180 V1 using LS-DYNA. Multiple modelling variations were considered in LS-DYNA to correlate with the experiments. Although deformation modes are similar, simulations did not provide a representative correlation of the force response. It is speculated that although snapshots for deformation mode looks similar, the deformation history are not the same which in turn results in different force responses. To aid in achieving a consistent deformation history with the impact test, fixing the tumblehome would prevent it to undergo such rigid movement as it mostly slid down the support. Such constraints would aid in initiating the desired collapse in the side walls. Element deletion was not present in either 3rd Gen 980 or 3rd Gen 1180 V1. Impact tests did not report fracture that occurred during free crush. It is recommended that future projects involving AHSS which have a prominent TRIP effect have their microstructure evaluated after forming and crash to quantify how much martensite is formed after subsequent deformation. Implementation of a thermal camera can also aid in which areas to study. Refinement of DIC methods is also necessary to capture strain measurements to enable correlations with simulations.

8 Summary

The work of this thesis aimed to assess the feasibility of 3rd Gen AHSS in forming, springback, and crash applications. The following conclusions and recommendations are discussed.

8.1 Conclusions

8.1.1 Forming

- Material descriptions using the Barlat Yld2000 yield function, Modified Hockett-Sherby hardening characterized by tensile and simple shear tests appropriately captured the hardening and the anisotropy of 3rd Gen 980 and 3rd Gen 1180 V1.
- Forming trials of the 3rd Gen 980 B-pillar exhibited superior formability forming without concern of splitting. Its higher strength 3rd Gen 1180 V1 counterpart exhibited splitting at the tumblehome.
- Forming simulations using AutoForm R8 reported an overestimation of the calculation of strains predicting splitting at the bend area where the side walls are formed. A similar prediction is reported by the LS-DYNA simulations.
- Numerical simulations of the forming of the B-pillar using LS-DYNA and AutoForm R8 correctly predicted splitting at the tumblehome. Strain paths illustrated that strains at the tumblehome were experiencing in-plane uniaxial stretch which was accurately captured by the BWx FLC.
- Implementation of strain rates had a prominent effect in the generation of forming strains in the B-pillar forming simulations of 3rd Gen 1180 V1. High-rate effects on forming strains of the 3rd Gen 1180 V1 B-pillar noticeably improved predictions by reporting lowered strains particularly at uniaxial tension. Rate effects did not have much of an effect on the forming of the 3rd Gen 980 B-pillar.

8.1.2 Springback

- Using LS-DYNA, increasing the number of through-thickness integration points did not have a noticeable effect on separation distances for 3rd Gen 980 and 3rd Gen 1180 V1.
- Rate sensitivity clearly reduced the separation distances for 3rd Gen 980 but did not significantly improve the predictions for the 3rd Gen 1180 V1.

- Springback simulations were also performed with AutoForm R8 using isotropic hardening and kinematic hardening. The overall results were comparable with those using LS-DYNA and the influence of kinematic hardening did not show clear improvements as expected.

8.1.3 Crashworthiness

- Two friction conditions were considered using Teflon® sheets for low friction and 120 grit sandpaper for high friction. Wrapping of the impactor was observed from the 3rd Gen 980 B-pillar impact test as well as engagement of the fold initiator under high friction conditions. Wrapping was less pronounced for the 3rd Gen 1180 V1.
- High speed DIC strain measurement was not successful due to out-of-plane deformation, the region of interest moving out of frame and the viewing window being obscured by the folding and shadows caused as the sidewall collapsed.
- The predicted force and energy histories of the B-pillar were reasonable but not as close as expected to the test results. The boundary conditions were varied, and filtering of the load response was considered but did not bring the results into closer agreement. It is believed that the sidewall collapse was not properly captured within the model due to the use of shell elements and/or other boundary conditions not properly captured in the model such as the plywood used for damping between the impactor and sled which may have influenced the force measurement.
- No fracture was observed on the B-pillar during free crush and is reflected in the simulations where no elements were deleted. Spotweld failure did not occur for any of the crash experiments.

8.2 Recommendations

8.2.1 Forming

- The FLC serves is a powerful tool in determining the formability of a material. Complex forming geometries benefit from the FLC but can also be misinterpreted as FLCs only consider in-plane deformation. It is recommended that locations with out-of-plane deformation be carefully scrutinized and the forming limit curve obtained using stretch bending (or Nakazima test data if not available) to reduce “false positives” for fracture.
- Implementation of rate effects have had an overall positive effect on the forming strains as they improved the formability predictions of the B-pillars by reducing the local strains in regions

of bending or high deformation. Strain-rate sensitivity of 3rd Gen AHSS should be considered in forming simulations.

8.2.2 Springback

- Advanced kinematic hardening models are recommended to include multiple cycles of tension-compression data and to better capture transient Baushinger effects. It is believed a more sophisticated modelling of kinematic hardening would improve the springback predictions but was outside the scope of work for this thesis.
- Coupon-level springback characterization tests should be performed to first evaluate the accuracy of the plasticity models such as U-bending and/or v-bending with different levels of uniaxial pre-strain. Simulations can then be performed to evaluate the predicted bend angles after springback to establish confidence in the plasticity models. The large-scale B-pillar is industrially representative but proved difficult to interpret the influence of the kinematic hardening models on springback.

8.2.3 Crashworthiness

- Accurate modelling of boundary conditions reflects the outcome of the force evolution in the simulation. Complete modelling of boundary conditions is recommended to prevent possible oversights that may lead to inconsistencies between the model and experiments.
- Adjustments to the test fixture by fixing the roof rail is recommended to prevent the sliding down of the B-pillar down the support. It is believed that this additional constraint will aid the simulations in achieving a more consistent deformation history with the impact tests.
- The 100 mm crush distance was not sufficient to produce fracture. This lack of fracture in the crash tests does not enable comparisons between the simulations in terms of element deletion in the simulation. Implementation of GISSMO is not needed and does not validate the correctness of the fracture loci or regularization factors. To increase the probability of fracture, it is recommended that free crush is increased to its maximum given the allowable geometry of the experimental setup.
- Implementation of DIC for dynamic crash events require multiple iterations and refinement to obtain satisfactory correlations between simulations and experimental data.

References

Abspoel, M., Scholting, M.E., Lansbergen, M., An, Y., Vegter, H. (2017). *A new method of predicting advanced yield criteria input parameters from mechanical properties.* Journal of Materials Processing Tech. 248 (2017) 161 – 177.

Alsos, H.S., Hopperstad, O.S., Törnqvist, R., Jørgen, A. (2008). *Analytical and numerical analysis of sheet metal instability using a stress-based criterion.* Int. J. Solids. Struct. 2008, 45, 2042 – 2055.

Aryanpour, A. (2011). *Experimental & Numerical Study of Sidewall Curl in Advanced High Strength Steels.* Master of Applied Science Thesis. University of Windsor, Mechanical, Automotive and Materials Engineering Department.

American Honda Motor Co. (2019), *2016 Pilot: Body Repair Information* [Online]. Available: https://techinfo.honda.com/rjanisis/pubs/web/ABN01970.PDF. [Accessed November 23, 2020].

Andresson, A., Holmberg, S. (2002). *Simulation and verification of different parameters effect on springback results.* NUMISHEET 2002, Jeju Island, Korea, pp. 201 – 206.

Arrieux, R., Bedrin, C., Boivin, M. (1982). *Determination of an intrinsic forming limit stress diagram for isotropic sheets*. In Proceedings of the 12th IDDRG Congress, vol. 2, pp. 61-71.

Bai, Y., Wierzbicki, T. (2008). *A New Model of Metal Plasticity and Fracture with Pressure and Lode Dependence*. International Journal of Plasticity, vol. 24, pp. 1071 – 1096, 2008.

Barratt, C. (Producer), Wate, J. (Director). (2006). *Samurai Sword: The Making of a Legend.* Retrieved from https://www.amazon.com/Samurai-Sword-Making-John-Wate/dp/B078G244CP. [Accessed November 23, 2020].

Barlat, F., Jalinier, J.M. (1985). *Formability of sheet metal with heterogeneous damage.* J. Mater. Sci. 1985, 20, 3385 – 3399.

Barlat, F., Brem, J.C., Yoon, J.W., Chung, K., Dick, R.E., Lege, D.J., Pourboghrat, F., Choi, S.-H., Chu, E. (2003). *Plane stress yield function for aluminum alloy sheets—part 1: Theory*. Int. J. Plast. 2003, 19, 1297–1319.

Barlat, F., Gracio, J.J., Lee, M.G., Rauch, E.F., Vincze, G. (2011). *An alternative to kinematic hardening in classical plasticity.* International Journal of Plasticity, 27 (2011) 1309 – 1327.

Bauschinger, J. (1886). *Mechanisch-Technischen Laboratorium.* Materials Forum, 1886.

Basaran, M., Wolkerlin, S.D., Feucht, M., Neukamm, F., Weichert, D. *An Extension of the GISSMO Damage Model Based on Lode Angle Dependence*, in LS-DYNA Awenderfoum, Bamberg, 2010.

Billur, E., (2010). *Die materials and wear in stamping, Part I: Die wear and die coatings*. Stamp. J., January/February 2010. Available online:

https://ercnsm.osu.edu/sites/ercnsm.osu.edu/files/uploads/S_fric/628-9.pdf. [Accessed November 23, 2020].

Billur, E., Altan, T. (2013). *Three generations of advanced high-strength steels for automotive applications, Part I*. Stamp. J., November/December 2013. Available online: https://ercnsm.osu.edu/sites/ercnsm.osu.edu/files/uploads/S_FormingAHSS/664-1.pdf. [Accessed November 23, 2020].

Billur, E., Dykeman, J, Altan, T. (2014). *Three generations of advanced high-strength steels for automotive applications, Part II*. Stamp. J., January/February 2014. Available online: https://ercnsm.osu.edu/sites/ercnsm.osu.edu/files/uploads/S_FormingAHSS/664-2.pdf [Accessed on 29 June 2020].

Billur, E., Teague, R., Barış Çetin (2019). *Hot Stamping of Ultra High-Strength Steels, From a Technological Perspective*. pp. 225 – 245. Springer International Publishing.

Billur, E.; Altan, T. (2014). *Three generations of advanced high-strength steels for automotive applications, Part III*. Stamp. J., March/April 2014. Available online: https://ercnsm.osu.edu/sites/ercnsm.osu.edu/files/uploads/S_FormingAHSS/664-3.pdf [Accessed on 29 June 2020].

Bjorkhaug, L., Welo, T. (2004). *Local calibration of aluminum profiles in rotary stretch bending* – Anisotropy effects. Materials Processes and Desgin: Modeling, Simulation and Applications – NUMIFORM 2004. In: Proceedings of AIP Conference 712, Columbus. OH, USA, American Institute of Physics. Pp. 749 -754. ```

Burchitz I. (2005). *Springback: improvement of its predictability: Literature study report*. NIMR project MC1.02121: Netherlands Institute for Metals Research; 2005. Available online: https://research.utwente.nl/en/publications/springback-improvement-of-its-predictability-literature-study-rep

Butuc, M.C. (2004). *Forming Limit Diagrams: Definition of Plastic Instability Criteria.* Ph.D. Thesis, Engineering Faculty of Porto Univeristy, Porto, Portugal, March 2004.

Carbrain. (2021). *What is Frame Damage? Cost to Repair vs Selling Your Car.* Online blog. Accessed: September 15, 2021. Available online: https://carbrain.com/blog/what-is-frame-damage

Chaboche, J.L. (1986). *Time-independent constitutive theories for cyclic plasticity.* International Journal of Plasticity 2, 149 – 188.

Chaboche, J.L. (2008). *A review of some plasticity and viscoplasticity constitutive theories.* International Journal of Plasticity 24 (2008) pp. 1642 – 1693.

Chan, K.S., Koss, D.A., Ghosh, A.K. (1984). *Localized Necking of Sheet at Negative Minor Strains.* Metall. Trans. A. 1984, 15, 323 – 329.

Chen, X., Niu, C., Lian, C., Lin, J. (2017). *The Evaluation of Formability of 3rd Generation Advanced High Strength Steels QP980 based on Digital Image Correlation Method.* Procedia Engineering 207 (2017) pp. 556 – 561.

Cheong, D.K. (2019). *On the Influence of the Through-Thickness Strain Gradients for Characterization of Formability and Fracture of Sheet Metal Alloys.* MASc. Thesis. Department of Mechanical and Mechatronics Engineering, University of Waterloo, 2016.

Chou, I.N., Hung, C., (1999). *Finite element analysis and optimization on springback reduction.* International Journal of Machine Tools & Manufacture, 39 (1999) pp. 517 – 536.

Cleveland, R.M., Ghosh, A.K. (2002). *Inelastic effects on springback in metals.* International Journal of Plasticity. 2002, 18, 769 – 785. doi:10.1016/S0749-6419(01)00054-7.

Considère, A. Mémoire sur L'Emploi du Fer et de L'Acier dans les Constructions. In Annales de Ponts et Chaussées; Commission des Annales des Ponts: Paris, French, 1885; Volume 9, pp. 574–775.

Davenport, M.D. (2017). *Third Generation Advanced High-Strength Steel Emerges*. Stamp. J. 2017, 22–28. Available online: https://www.thefabricator.com/stampingjournal/article/stamping/third-generationadvanced-high-strength-steel-emerges [Accessed on November 23, 2020].

Dorn, J.E., Thomsen, E.G. (1947). *The ductility of metals under general conditions of stress and strain.* Trans. Am. Soc. Met. 39, 741 – 772.

Du Bois, J.H., Du Bois, P. (2018). *A study in Mass Scaling for Sheet Metal Forming with LS-DYNA®*. 15th International LS-DYNA® Users Conference. June 10 – 12, 2018.

Eller, T.K., Greve, L., Andres, M.T., Medricky, M., Hatscher, A., Meinders, V.T., van der Boogaard, A.H. (2014). *Plasticity and Fracture Modelling of Quench-Hardenable Boron Steel with Tailored Properties*. Journal of Materials Processing Technology, vol. 214, pp. 1211 – 1227, 2014.

Eggersten, P.A., Mattiasson, K. (2010). *On the Modeling of the Unloading Modulus for Metal Sheets.* Internation Journal of Material Forming, 3, pp. 127 – 130, 2010.

Eggersten, P.A., MAttiasson, K. (2010a). *On Constitutive modeling for springback analysis*. International Journal of Mechanical Sciences. 2010, 52, 804 – 818.

Eurocode Applied (2021) *Table of design properties for metric hexagonal bolts M5 to M39 (stress area, shear strength, tensile strength, bearing strength.*

Eyckens, P., Van Bael, A., Van Houtte, P. (2009). *Marciniak-Kuckzynski type modeling of the effect of through-thickness shear on the forming limits of sheet metal.* Int. J. Plasticity, 2009; 25 (12): 2249 – 68.

Fan, D.W., De Cooman, B.C. (2012). *State-of-the-Knowledge on Coating Systems for Hot Stamped Parts*. Steel Research International. 83 (2012) No. 5, pp. 412 - 433.

Goodwin, G.M. (1968). *Application of strain analysis to sheet metal forming in the press shop.* In SAE Paper 680093.

Ghosh, A., Hecker, S. (1974). *Stretching Limits in Sheet Metals: In-Plane Versus Out-of-Plane Deformation*. Metall. Trans. 1974, 5, 2161–2164.

Ghosh, A., Hecker, S. (1975). *Failure in Thin Sheets Stretched Over Rigid Punches*. Metall. Trans. A 1975, 6, 1065–1074.

Govik, A., Rentmeester, R., Nilsson, L. (2014). *A study of the unloading behaviour of dual-phase steels.* International Journal of Plasticity, 45, 174 – 187. Doi: https://doi.org/10.1016/j.jmatprotec.2015.08.024

Gutierrez, J.E., Noder, J., Butcher, C. (2020). *Experimental Characterization and Deterministic Prediction of In-Plane Formability of 3rd Generation Advanced high Strength Steels.* Metals 2020, 10, 902, doi:10.3390/met10070902.

Grenke, B.D. (2002). *Digital Filtering for J211 Requirements using a Fast Fourier Transform Based Filter.* SAE Technical Paper. 2002-01-0796.

Han S.S., Park, K.C. (1999). *An investigation of the factors influencing springback by empirical and simulative techniques*. In NUMISHEET '99. The 4th International Conference and Workshop on Numerical Simulation of 3D Sheet Forming Processes, Besancon, France, 1999, pp. 53 – 58.

Hall, A. (2020). *Vehicle Safety Insight: Side Impact – IIHS Concepts*. Article. Available online: https://www.linkedin.com/pulse/vehicle-safety-insight-side-impact-concepts-andrew-hall/

Heyn, E. (1918). *Theory of the cancelled elastic stresses.* Metall und Erz, Zeischrift, 15, pp. 411 – 422, November 1918.

Hill, R. (1952). *On discontinuous plastic states, with special reference to localized necking in thin sheets.* J. Mech. Phys. Solids. 1952, 1, 19 – 30.

Hora, P.; Tong, L.; Berisha, B. (2013). *Modified maximum force criterion, a model for the theoretical prediction of forming limit curves*. Int. J. Mater. Form. 2013, 6, 267–279.

Hovorun, T.P., Berladir, K.V., Pervera, V.I., Rudenko, S.G., Martynov A.I. (2017). *Modern Materials for Automotive Industry, Journal of Engineering Sciences*, vol. 4, no. 2, pp. F8-F18, 2017.

Huh, H., Kim, K.P., Kim, S.H., Song, J.H., Kim, H.S., Hong, S.K. (2003). *Crashworthiness Assessment of Front Side Members in an Auto-Body Considering the Fabrication Histories*. International Journal of Mechanical Sciences, vol. 45, pp. 1645 – 1660, 2003.

Ibrahim, H.K. (2009). *Design Optimization of Vehicle Structures for Crashworthiness Improvement*. Doctoral Thesis. Department of Mechanical and Industrial Engineering, Concordia University, Montreal, 2009.

International Organization for Standardization. *Metallic Materials Sheet and Strip—Determination of Forming Limit Curves—Part 2: Determination of Forming Limit Curves in the*

Laboratory; ISO/DIC 12004-2:2008. International Organization for Standardization: Geneva, Switzerland, 2008.

FEMA. (2002). *World Trade Center Performance Study: Data Collection Preliminary Observations, and Recommendations.* Federal Emergency Management Agency.

Insurance Institute for Highway Safety. (2020). *Side Impact Crashworthiness Evaluation 2.0 Crash Test Protocol (Version I).* Available online: https://www.iihs.org/media/0027a26d-8dd2-4de4-affc-0eb98338c6ba/cLjh9w/Ratings/Protocols/current/test_protocol_side-2.0.pdf

Jain, E. (2016). *Investigation of Effect of Temperature and Forming Speed on the Formability of AA3003 Brazing Sheets.* MASc. Thesis. Department of Mechanical and Mechatronics Engineering, University of Waterloo, 2016.

Kaller, 2021. *Gas spring calculators and configurators.* Force and Temperature Calculator. Accessed October 17, 2021. Website: https://www.kaller.com/en-us/support/user-tools/

Keeler, S.P. and Backofen, W.A., 1963. *Plastic instability and fracture in sheets stretched over rigid punches*. Asm Trans Q, 56(1), pp.25-48.

Keeler, S., Ulnitz, P. (2009). Forming Higher-Strength Steels. *Metalforming Magazine*, April 2009, pp 18-25.

Konieczny, A. (2003). *Advanced High Strength Steels Formability.* Presented at Great Designs in Steel 2003. Accessed: September 14, 2021. http://worldautosteel.wpengine.com/wp-content/uploads/GDIS-Prez/K-1_03%20-%20AHSS%20Formability_2003.pdf

Kuwabara, T., Nakajima, T. (2011). *Material modeling of 980 MPa Dual Phase Steel Sheet Based on Biaxial Tensile Test and In-plane Stress Reversal Test*. J. Solid Mech. Mater. Eng. 2011, 5, 709–720.

Kubli, W., Krasovskyy, A., Sester, M. (2008a). *Advanced modelling of reverse loading effects for sheet metal forming processes.* In Proceedings of NUMISHEET 2008, 479 – 484.

Kubli, W., Krasovskyy, A., Sester, M. (2008b). *Modelling of reverse loading effects including work hardening stagnation and early re-plastification.* In Proceedings of ESAFORM 2008.

Kupke, A. (2017). *Effect of the microstructure on the unloading characteristics of DP steel.* Doctoral thesis. Institute for Frontier Materials, Deakin University. Available online: http://hdl.handle.net/10536/DRO/DU:30103707.

Lehmann, H. (2011) Developments in the Field of Schwartz Heat Treatment Furnaces for Press Hardening Industry. *Proceedings of 3rd International Conference on Hot Sheet Metal Forming of High-Performance Steel,* Kassel, 171–180.

Lems, W. (1963). *The change of Young's Modulus After Deformation at Low Temperature and its Recovery.* Doctoral Thesis. Delft University of Technology, Faculty of Applied Sciences, 1963.

Available online: https://repository.tudelft.nl/islandora/object/uuid%3Adcd1ba54-e207-42d0-a1af-e3a3e6979ddc

Li, K.P., Carden, W.P., Wagoner, R.H. (2002). *Simulation of springback.* International Journal of Mechanical Sciences 44 (1), 103 – 122.

Livermore Software Technology Corporation (LSTC). (1997). *User's Guide to Adaptive Mesh Trimming in LS-DYNA.* Technical Document. Accessed online: https://lost-contact.mit.edu/afs/nada.kth.se/misc/pdc/j90/ls-dyna/manuals/950/trim_users_guide.pdf

Livermore Software Technology Corporation (LSTC). (2014a). *LS-DYNA® KEYWORD USER'S Manual Volume I.* Livermore Software Technology (LSTC).

Livermore Software Technology Corporation (LSTC). (2014b). *LS-DYNA® KEYWORD USER'S Manual Volume II – Material Models.* Livermore Software Technology (LSTC).

Livermore Software Technology Corporation (LSTC). (2016). *New Features in Current LS-PrePost® and its Future Development.* Presentation. Accessed online: https://www.lstc.com/lspp/content/pages/7/bestfit/bestfit.shtml

Malcolm, S., Nutwell, E. (2007). *Spotweld Failure and Prediction using Solid Element Assemblies.* In Proceedings of 6th LS-DYNA Users Conference, Gothenburg, Sweden, 2007.

Marciniak, Z.; Kuczynski, K. (1967). *Limit Strains in the Process of Stretch-Forming Sheet Metal*. Int. J. Mech. Sci. 1967, 9, 609–620.

Marciniak, Z., Kuczyński, K. and Pokora, T., (1973). *Influence of the plastic properties of a material on the forming limit diagram for sheet metal in tension*. International Journal of Mechanical Sciences, 15(10), pp.789-800.

Masing, G. (1923). Zur Heynschen Theorie der Verfestigung der Metalle durch verborgene elastische Spannungen, Mittl. aus dem Forschungslaboratorium Siemensstadt 3 (1923) 231 – 239

Matin, P.H., Smith, L.M. (2005). *Practical limitations to the influence of through-thickness normal stress on sheet metal formability.* International Journal of Plasticity, 21, 671 – 690.

Meinders, T., Konter, A.W.A., Meijers, S.E., Aztema, E.H., Kappert, H. (2006). *A Sensitivity Analysis on the Springback Behavior of the Unconstrained Bending Problem.* International Journal of Forming Processes, vol. 9, no. 3, 2006, pp. 365 – 402.

Merklein, M., Wieland, M., Lechner M., Bruschi, S., Ghiotti, A. (2016). *Hot stamping of boron steel sheets with tailored properties: A review*. Journal of Materials Processing Technology, vol. 228, pp. 11-24, 2016.

Midawi, A. (2021). Private communications.

Min, J., Stoughton, T.B., Carsley, J., Lin, J. (2016). *Compensation for process-dependent effects in the determination of localized necking limits*. Int. J. Mech. Sci. 2016, 117, 115–134.

Mohammadi, M., Brahme, A.P., Mishra, R.K., Inal, K. (2014). *Effects of post-necking hardening behavior and equivalent stress-strain curves on the accuracy of M-K based forming limit diagrams*. Comput. Mater. Sci. 2014, 85, 316–323.

Mompiou, F., Caillard, D., Legros, M., Mughrabi, H. (2012). *In situ TEM observations of reverse dislocation motion upon unloading in tensile-deformed UFG aluminum.* Acta Mater. 2012, 60, 3402 – 3414, doi: 10.1016/j.actamat.2012.02.049

Morestin, F., Boivin, M. (1996). *On the necessity of taking into account the variation in the Young Modulus with plastic strain in elastic-plastic software.* Nuclear Engineering and Design. Vol 162, 1, March 1996, pp. 107 – 116

Mroz, Z. (1967). *On description of anisotropic workhardening.* Journal of the Mechanics and Physics of Solids 15, 163.

Mukai, Y. (2005). The Development of New High-strength Steel Sheets for Automobiles. KOBELCO Technology Review, No. 26, Dec 2005, p. 26. Accessed: September 16, 2021. https://www.kobelco.co.jp/english/ktr/pdf/ktr_26/026-031.pdf

Müschenborn, W., Sonne, H.M. (1975). *Einfluß des Formänderungsweges auf die Grenzformänderungen des Feinbleches,* Arch Eisenhüttenwes 46 (1975) 597–602.

Nakazima, K., *Kikuma T., Hasuka K. (1968). Study* on the *Formability* of *Steel Sheets* Yamata *Technical* Report, No. *264*, *1968*, pp. *8517-8530*.

National Highway Traffic Safety Administration. (2011). *NHTSA and EPA Set Standards to Improve Fuel Economy and Reduce Greenhouse Gases for Passenger Cars and Light Trucks for Model Years 2017 and Beyond*.

National Highway Traffic Safety Administration. (2020). *The Safer Affordable Fuel-Efficient (SAFE) Vehicles Rule for Model Year 2021 – 2026 Passenger Cars and Light Trucks.*

Nguyen, V.T., Chen, Z., Thomson, P.F. (2004). *Prediction of spring-back in anisotropic sheet metals.* Journal of Mechanical Sciences 44 (1), 103 – 122.

Noder, J. (2017). *Characterization and Simulation of Warm Forming of 6xxx and 7xxx Series Aluminum Alloys*, MASc. Thesis. Department of Mechanical and Mechatronics Engineering, University of Waterloo, 2017.

Noder, J., Gutierrez, J.E., Zhumagulov, A., Dykeman, J., Ezzat, H., Butcher, C. (2021). *A Comparative Evaluation of Third-Generation Advanced High-Strength Steels for Automotive Forming and Crash Applications.* Materials, 2021, 14, 4970/ doi: https://www.mdpi.com/1996-1944/14/17/4970

Noder, J. (2021). Private communications.

Noury, P. (2014). *Fracture Mechanics in Design and Assessment of Existing Structures: Two Case Studies.* Licentiate Thesis. Luleå University of Technology, Department of Civil. Environmental and Natural Resources Engineering, November 2014.

National Highway Traffic Safety Administration. (2020). *The Safer Affordable Fuel-Efficient (SAFE) Vehicles Rule for Model Year 2021 – 2026 Passenger Cars and Light Trucks.*

Oakley, D. (2015). *2015 Nissan Murano*. Presented at Great Designs in Steel 2015. Accessed September 16, 2021. http://worldautosteel.wpengine.com/wp-content/uploads/GDIS-Prez/C-32_Track%202%20-%20Coakley%20Murano_2015.pdf

Oakley, D., Zischke, J. (2015). *The 2016 Nissan Maxima.* Presented at Great Designs in Steel 2015. Accessed September 16, 2021. http://worldautosteel.wpengine.com/wp-content/uploads/GDIS-Prez/C-33_Track%202%20-%20Coakley%20Maxima_2015.pdf

Oliveira, D.A., Worswick, M.J., Grantab, R., Williams, B.W., Mayer, R. (2006). *Effect of Forming Process Variables on the Crashworthiness of Aluminum Alloy Tubes*. International Journal of Impact Engineering, vol. 32, pp. 826 – 846, 2006.

Ormaetxea A., Aramburu A., Belategi, I. (2013) *Improved Productivity and Energy Consumption on Press Hardening by Means of Mechanical Servo Press Technology*. Proceedings of 4th International Conference on Hot Sheet Metal Forming of High-Performance Steel, Luleå, 185–190.

Parker, N (2020). Private communications.

Paul, S.K. (2021). *Controlling factors of forming limit curve: A review.* Advances in Industrial and Manufacturing Engineering 2 (2021) 100033.

Peirs, J. Verleysen, P., Degrieck, J. (2012). *Novel Technique for Static and Dynamic Shear Testing of Ti6Al4V Sheet.* Exp. Mech. 2012, 52, 729 – 741.

Peister, C., O'Keeffe, C., Imbert, J., Butcher, C., Worswick, M., Malcolm, S., Dykeman, J., Yau, C., Soldaat, R., Bernert, W. (2018). *Dynamic and Quasi-Static Testing and Modeling of Hot Stamped Tailor-Welded Axial Crush Rails*. Conference Paper. Presented at the 18th International Conference on Experimental Mechanics (ICEM18), Brussels, Belgium, 1–5 July 2018.

Peister, C. (2019). *Axial Crush Performance of Hot Stamped Tailor Welded Blanks, Experiments and Numerical Simulations.* MASc. Thesis. Department of Mechanical and Mechatronics Engineering, University of Waterloo, 2019.

Plascore. (2021). *Plascore AltuCore*. Product data sheet. Accessed: October 13, 2021. https://www.plascore.com/download/datasheets/energy_absorption_documentation/Plascore_Altucore-2021.pdf

Rahmaan, T., Abedini, A., Butcher, C., Pathak, N., Worswick, M.J. (2017). *Investigation into the shear stress, localization and fracture behaviour of DP600 and AA5182-O sheet metal alloys under elevated strain rates*. Int. J. Impact Eng. 2017, 108, 303–321.

Rahmaan, T. *Constitutive and Fracture Characterization of High Strength Aluminum Alloys at Elevated Strain Rates.* (2018). Ph. D. Thesis, University of Waterloo, ON, Canada, 2018.

Shojaee, M., Midawi, A.R.H., Ghassemi-Armaki, H. (2021). *Mechanical properties and failure behavior of resistance spot welded third-generation advanced high strength steels.* Journal of Manufacturing Processes 65(1): 364 – 372. Doi: 10.1016/j.jmapro.2021.03.047

Ratchev, P., Van Houtte, P., Verlinden, B., De Smet, P., Neutjens, P., Baartman, R., Drent, P. (1994). *Prediction of forming limit diagrams of Al-Mg rolled sheets taking texture into account.* Textures Microstruct. 1994, 22, 219 – 231.

Seo, K.Y., Kim, J.H., Lee, H.S., Kim, J.H., Kim, B.M. (2018). *Effect of Constitutive Equations on Springback Prediction Accuracy in the TRIP1180 Cold Stamping.* Metals 2018, 8, 18. doi: https://doi.org/10.3390/met8010018

Smerd, R.; Winkler, S.; Salisbury, C.; Worswick, M.; Lloyd, D.; Finn, M. (2005). *High strain rate tensile testing of automotive aluminum alloy sheet.* Int. J. Impact Eng. 2005, 32, 541–560, doi:10.1016/j.ijimpeng.2005.04.013.

Society of Mechanical Engineers. (1995). *SAE J211-1 (1995): Instrumentation for Impact Test, Part 1, Electronic Instrumentation.* 72 FR 25514, May 4, 2007.

Stoughton, T.B., Yoon, J.W. (2012). *Path independent forming limit in strain and stress spaces*. International Journal of Solids and Structures. 49 (2012) 3616 – 3625.

Sun. L., Wagoner, R.H. (2011). *Complex unloading behavior: Nature of the deformation and its consistent constitutive representation.* International Journal of Plasticity 27 (2011) 1126 – 1144.

Sun, L., Wagoner, R.H. (2013). *Proportional and non-proportional behavior of dual-phase steels.* Int. J. Plast. 2013, 45, 174 – 187.

Teoh, E.R., Lund, A.K. (2011). *IIHS Side Crash Test Ratings and Occupant Death Risk in Real-World Crashes*. Traffic Injury Prevention 12 (5): 500 – 507. doi: 0.1080/15389588.2011.585671

Tisza, M., Czinege, I. (2018). *Comparative Study of the Application of Steels and Aluminum in Lightweight Production of Automotive Parts.* International Journal of Lightweight Materials and Manufacture, vol. 1, no. 1, pp. 229-238, 2018.

Tharrett, M.R., Stoughton, T.B. (2003) *Stretch-bend forming limits of 1008 AK steel*, SAE Technical Paper, 2003-01-1157, 2003.

Tummers, M. (2019) *Development of a Tailor-Welded Hot Stamped Side Frame Member*. MASc. Thesis. Department of Mechanical and Mechatronics Engineering, University of Waterloo, 2019.

VDA 238-100. *Test Specification: Plate Bending Test for Metallic Materials*. VDA: Berlin, Germany 2017.

Vegter, H., van den Boogaard, A.H. (2006). *A Plane Stress Yield Function for Anisotropic Sheet Material by Interpolation of Biaxial Stress States.* International Journal of Plasticity, 22, 557 – 580, 2006.

Wagoner, R.H., Geng, L.M., Li, K.P. (199). *Simulation of springback with the draw/bend test.* In Proceedings of IPMM '99: The Second International Conference on Intelligent Processing and Manufacturing of Materials, HI, USA. Pp. 91 – 104.

Wagoner, R.H., Li, M. (2006). *Simulation of springback: Through-thickness integration.* International Journal of Plasticity, 23 (2007) 345 – 350.

World Auto Steel. (2019) *Advanced High Strength Steel (AHSS) Application Guidelines Version 6*.0, April 2017. https://www.worldautosteel.org/downloads/599700/

World Auto Steel. (2020). *3rd Generation Steels.* Accessed September 16, 2021. https://ahssinsights.org/metallurgy/steel-grades/3rd-generation-steels/

World Auto Steel. (2021). *Battery Electric Vehicles – Boom or Bust for AHSS?* Accessed September 15, 2021. https://ahssinsights.org/main-blog/battery-electric-vehicles-boom-or-bust-for-ahss/

Worswick, M. (2019). *ME725 Simulation of Forming and Impact, Chapter 8: Planning the Simulation – Simulation Methodology.* ME 725 Course Notes.

Xu, L., Barlat, F., Ahn, D.C., Bressan, J.D. (2011). *Forming limit and fracture mechanism of ferritic stain steel sheets.* Materials Science and Engineering, A 528 (2011) 3113 – 3121.

Yun, J. (1998) *Study of Basuchinger Effect in Various Spring Steels*. MASc. Thesis. Graduate Department of Metallurgy & Materials Science, University of Toronto, 1998.

Yoshida, F., Uemori, T. (2002). *A model of large-strain cyclic plasticity describing the Bauschinger effect and workhardening stagnation*. International Journal of Plasticity, 18 (2002) pp. 661 – 686.

Yoshida, F., Uemori, T., Fujiwara, K. (2002). *Elastic-plastic behavior of steels under in-plane cyclic tension-compression at large strain*. International Journal of Plasticity, 18, 5 – 6, October 2002, pp. 633 - 659

Zhang, L.C., Lu, G., Leong, S.C. (1997). *V-shaped sheet forming by deformable punches.* Journal of Materials Processing Technology, 63 (1 – 3): pp. 134 – 139, 1997.

Zhang, C., Leotoing, L., Guines, D., Ragneau, E. (2009). *Theoretical and numerical study of strain rate influence on AA5083 formability.* J. Mater. Process. Technol. 2009, 209, 3849 – 3958.

Zhou, J., Wang, B.-y., Huang, M.-d., Cui, D. (2014) *Effect of Hot Stamping Parameters on the Mechanical Properties and Microstructure of Cold-Rolled 22MnB5 Steel Strips*. International Journal of Minerals, Metallurgy and Materials, vol. 21, no. 6, pp. 545 - 555, 2014.

Zhao, X. (1999). *Numerical Prediction of Springback in U-channel Forming of Aluminum Tailor Welded Blanks.* Master of Engineering Thesis. Carleton University, Department of Mechanical and Aerospace Engineering. 1125 Colonel By Drive, Ottawa, ON.

Zhu, X., Zhang, L. (2018). *Advance in Sheet Metal Forming – One-step Solution, Multi-Beads, Gravity Prebending, Auto Nets, and Local Compensation.* 12th Internaltional LS-DYNA ® Users Conference. June 2018.

Appendices

Appendix A: Mesh Regularization

Mesh Regularization using Nakazima Hemispherical Dome Tests

The prediction of fracture is strongly related to the element size to capture strain localization. The fracture locus, implemented into the GISSMO fracture model in LS-DYNA, requires scaling based upon the element size and stress state. Nakazima hemispherical dome tests in the equal-biaxial stretching and plane strain conditions were selected since these geometries are amenable to the use of shell elements with sizes up to 5.0 mm. A quarter symmetry model is used for computational efficiency where a penalty-based surface-to-surface contact definition *CONTACT_FORMING_ONE_WAY_SURFACE_TO_SURFACE used. The friction coefficient of the blank and punch interface has a value of 0.04 which accounts for the Teflon lubrication. A friction coefficient of 0.4 was used for all other contacts between the blank, die and binder. No lockbead was incorporated in the dome simulations to maintain a consistent mesh size on the blank. Instead of the lockbead, a clamping load of 640 kN sufficiently provided enough force to prevent draw-in of the blank. Four different mesh sizes (see Figure 158) were used with the fracture locus scaled such that fracture (element deletion) would occur at the experimental dome height. The facture loci for both 3rd Gen 980, 3rd Gen 1180 V1, and 3rd Gen 1180 V2 are shown in Figure 159 along with its regularization factors as a function of element size in summarized in Figure 160. Overall, the predicted force-displacement curves are in good agreement with the test data as shown in Figure 160 and Figure 161. In the plane strain simulations, the mesh size of 5 mm was rather coarse to properly reflect the deformation of the blank as it bends and stretches over the punch, leading to an overestimation of the force. Regularization factors of each steel and mesh size are summarized in Table 13.

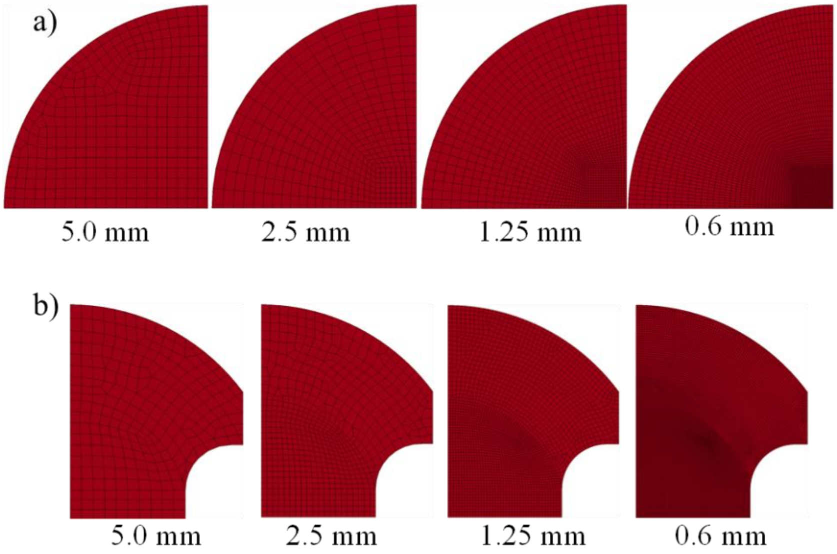

Figure 158: Average mesh size used in mesh regularization for a) equi-biaxial and b) plane strain Nakazima dome test simulations

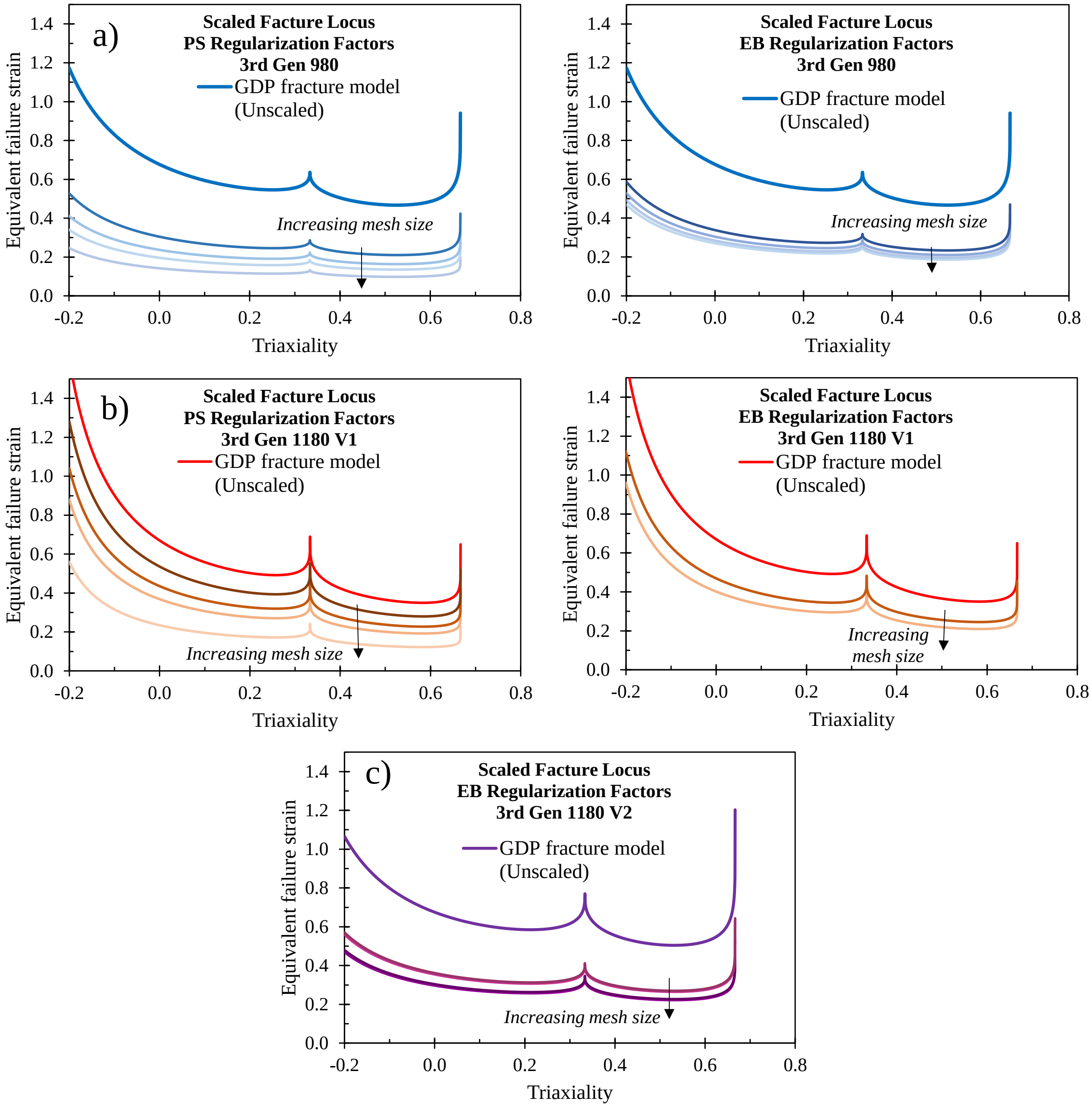

Figure 159: Experimental damage curve for a) 3rd Gen 980, b) 3rd Gen 1180 V1, and c) 3rd Gen 1180 V2. No plane strain dome simulations were performed. Unscaled fracture loci provided by Dr. Jacqueline Noder

Table 13: Regularization factors for 3rd Gen 980 and 3rd Gen 1180 V1 utilizing plane strain (PS) and equibiaxial (EB) dome tests. Only equi-biaxial dome experiments for 3rd Gen 1180 V2.

Mesh Size [mm]	**3rd Gen 980**		**3rd Gen 1180 V1**		**3rd Gen 1180 V2**
	PS	**EB**	**PS**	**EB**	**EB**
5.00	0.21	0.40	0.35	0.60	0.440
2.50	0.29	0.42	0.55	0.60	0.450
1.25	0.35	0.45	0.65	0.70	0.525
0.60	0.45	0.50	0.80	0.70	0.535

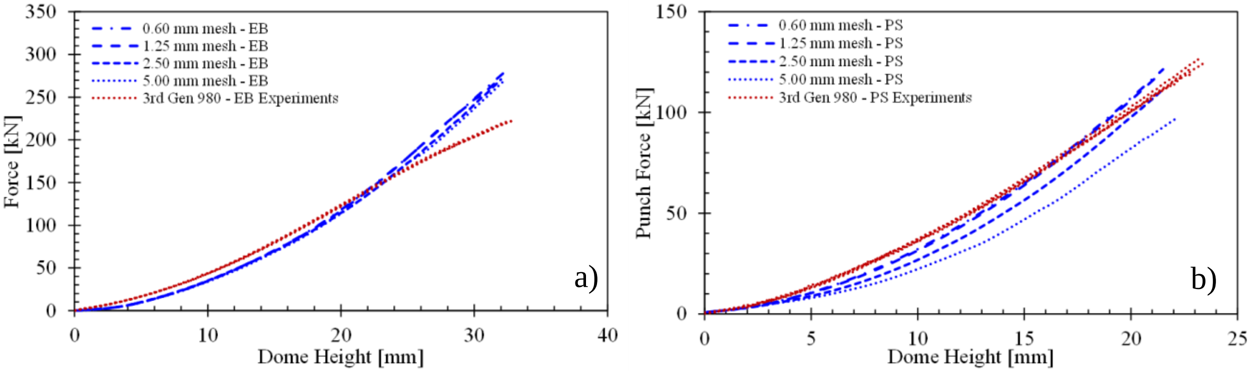

Figure 160: Force-displacement curves of the Nakazima dome tests for 3rd Gen 980 undergoing a) equi-biaxial stretch and b) plane strain tension and overlaying the experimental results against the simulations ran with 0.6 mm mesh size. No experimental Nakazima dome tests were performed for 3rd Gen 1180 V2.

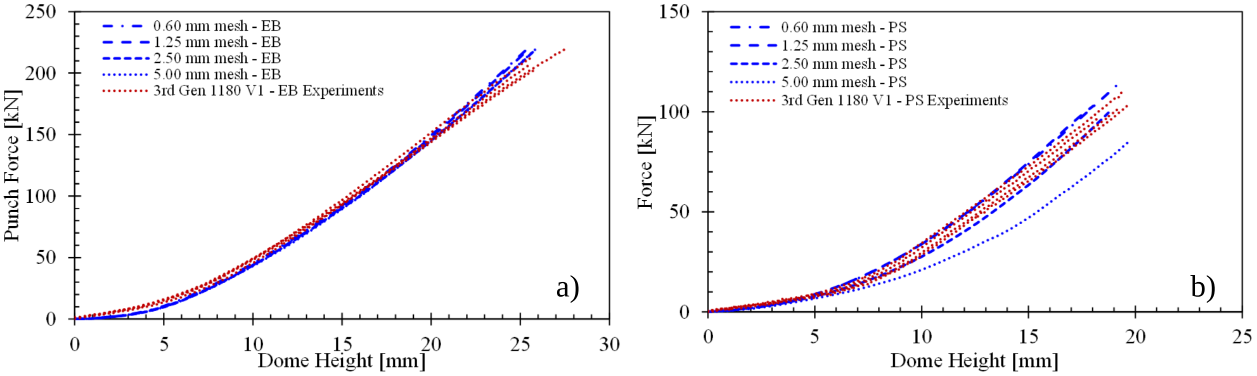

Figure 161: Force-displacement curves of the Nakazima dome tests for 3rd Gen 1180 V1 undergoing a) equi-biaxial stretch and b) plane strain tension and overlaying the experimental results against the simulations ran with all mesh sizes. No experimental Nakazima dome tests were performed for 3rd Gen 1180 V2.

Mesh Regularization and Fracture Prediction of the B-pillar

In addition to the in-plane FLC, implementation of GISSMO also assists in identifying splits in forming simulations. With GISSMO, it can aid in bending related fractures and can help dispel misreported splitting by the in-plane FLC. The stress-state dependent fracture behavior can be included within the LS-DYNA model to give more insight into the forming process. The FLC can more accurately predict in-plane necking failures while GISSMO can assist in predicting fracture at locations where process effects are induced such as bend-dominated areas. The use of GISSMO also aids in determining which regularization factors to use in crash, if necessary. Regularization factors used for the forming operation utilizes equi-biaxial regularization (EB reg.) and plane strain regularization (PS reg.). The following section looks at the effects of equi-biaxial regularization and plane strain regularization separately. Within LS-DYNA, the number of integration points to failure can be set such that a percentage of integration points must reach a D-parameter of 1 before the element is deleted. The current percentage is set at 70% for all simulations as per the recommendation of HRA. For 3 NIPs, all 3 integration points must reach the threshold whereas 11 NIPs only require 8 out of 11 layers to reach a D-parameter of unity in order for elements to be deleted.

Equi-biaxial regularization – Comparison of 3 NIPs vs. 11 NIPs

The effect of integration points on equi-biaxial regularization is first observed. Both steels are illustrated to see the effects of regularization using 3 NIPs in Figure 162 and 11 NIPs in Figure 163. Only 3 and 11 NIPs are selected to observe the changes in element deletion with the least number of integration points and how element deletion changes when bending is more representative with increased NIPs.

Observation of 3 NIPs for both 3rd Gen 980 and 3rd Gen 1180 V1 using biaxial regularization are illustrated in Figure 162. Element deletion is observed at the drawbead locations of the B-pillar for both steels where it is primarily bending. It should be noted that at the tumblehome locations, the D-parameter contours show no indication that the elements are going to be deleted as it shows that the elements only attain a D-parameter that ranges from 0.5 to 0.7.

Similar results are seen for forming simulations with 11 NIPs using equi-biaxial regularization for both steels visualized in Figure 163. With a higher number of integration points, the splitting is milder for both steels but are still located at the drawbeads. One split is located closer to the roof rail of the B-pillar. Overall, equi-biaxial regularization appears quite liberal for 3rd Gen 1180 V1 as no element deletion occurs right at the tumblehome locations and due to the inherently higher formability of 3rd Gen 980, minimal amount of element deletion is being predicted. The elements deleted at the drawbead locations can be dismissed upon observing the Nakazima and Marciniak tests that have a more aggressive lockbead radius than that of the B-pillar tooling.

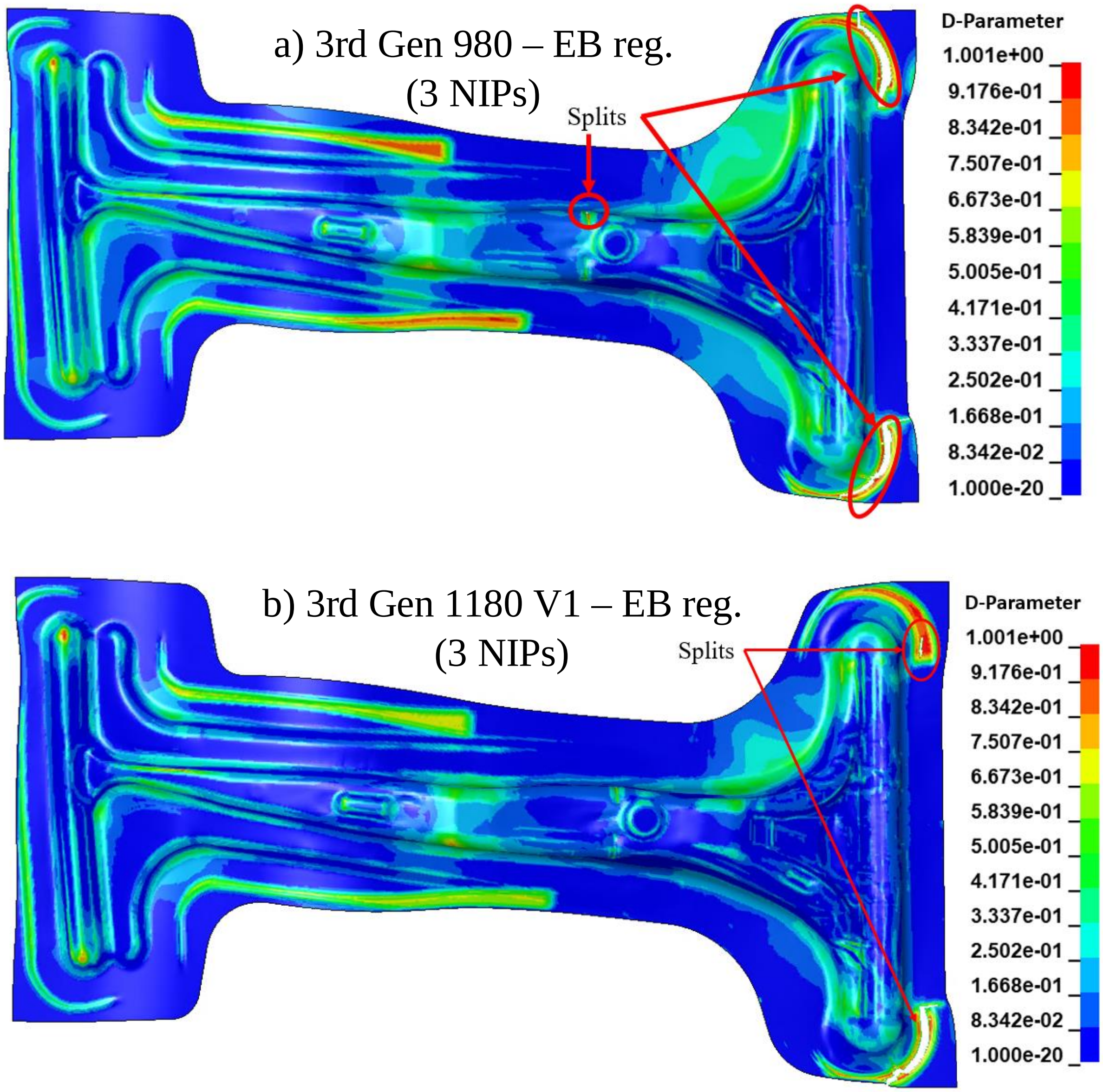

Figure 162: B-pillar forming simulations of a) 3rd Gen 980 and b) 3rd Gen 1180 V1 with 3 NIPs using equi-biaxial regularization factors showing the D-parameter for the upper integration point

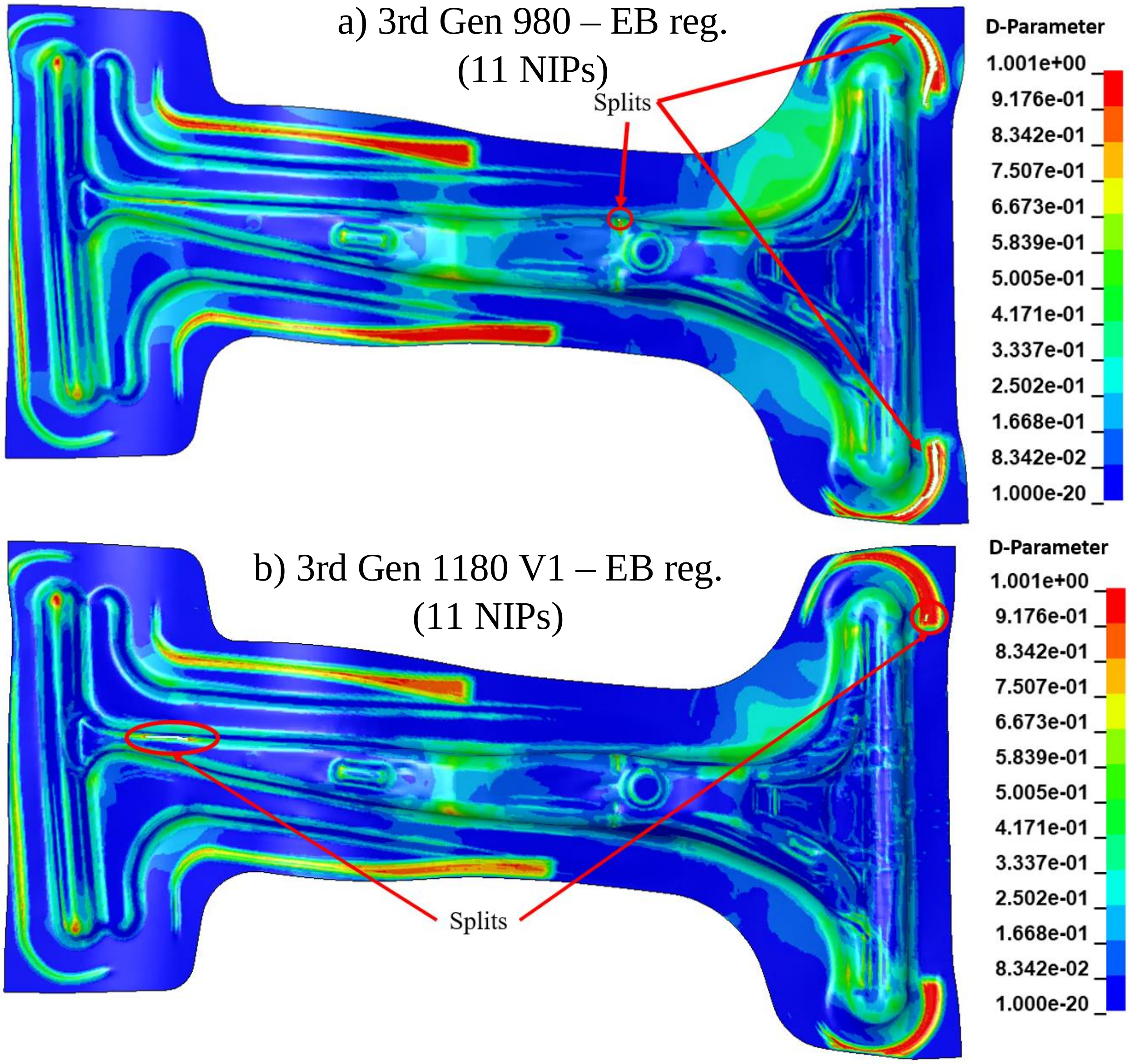

Figure 163: B-pillar forming simulations of a) 3rd Gen 980 and b) 3rd Gen 1180 V1 with 11 NIPs using equi-biaxial regularization factors showing the D-parameter for the upper integration point

Plane strain regularization – Comparison of 3 NIPs vs. 11 NIPs

Plane strain regularization factors implemented in GISSMO yield vastly different results from equi-biaxial regularization for both steels using 3 NIPs and 11 NIPs. For the 3rd Gen 980 B-pillar simulation using plane strain regularization that only uses 3 NIPs, seen in Figure 163a, it exhibits a similar pattern of element deletion with equi-biaxial regularization using 3 NIPs. Splits are located at the drawbeads. Element deletion using plane strain regularization for 3rd Gen 1180 V1 using 3 NIPs, however, shows excessive splitting on various locations of the B-pillar seen in Figure 163b. Even at bend areas, splitting occurs which is contrary to the forming trials. With an increase in integration points of 11, 3rd Gen 980 shows considerably more splitting that are located at drawbead areas and at the roof rail. The increase in elements being deleted are the number of integration points reaching the threshold sooner for element deletion. For 3 NIPs, it effectively requires all integration points to reach a D-parameter of 1. What has occurred in the simulation for 3 NIPs is that only 2 of the 3 integration points failed which amounts to just 67% of integration points failing. For the higher number NIPs of 11, once 8 integration points reach a D-parameter of 1, the element is deleted. For 3 NIPs, it effectively requires 100% of NIPs to be deleted but for 11 NIPs, once it passes 72%, elements are deleted. For plane strain regularization, it is evident that it is excessively conservative from the numerous splitting at multiple locations of the B-pillar where no splitting occurred at most locations of the B-pillar. Splitting under plane strain regularization (seen in Figure 164) is exacerbated under higher integration points which holds true for both 3rd Gen 980 and 3rd Gen 1180 V1 since more integration points attain a D-parameter of unity reaching the threshold of 70% for number of integration points to fail.

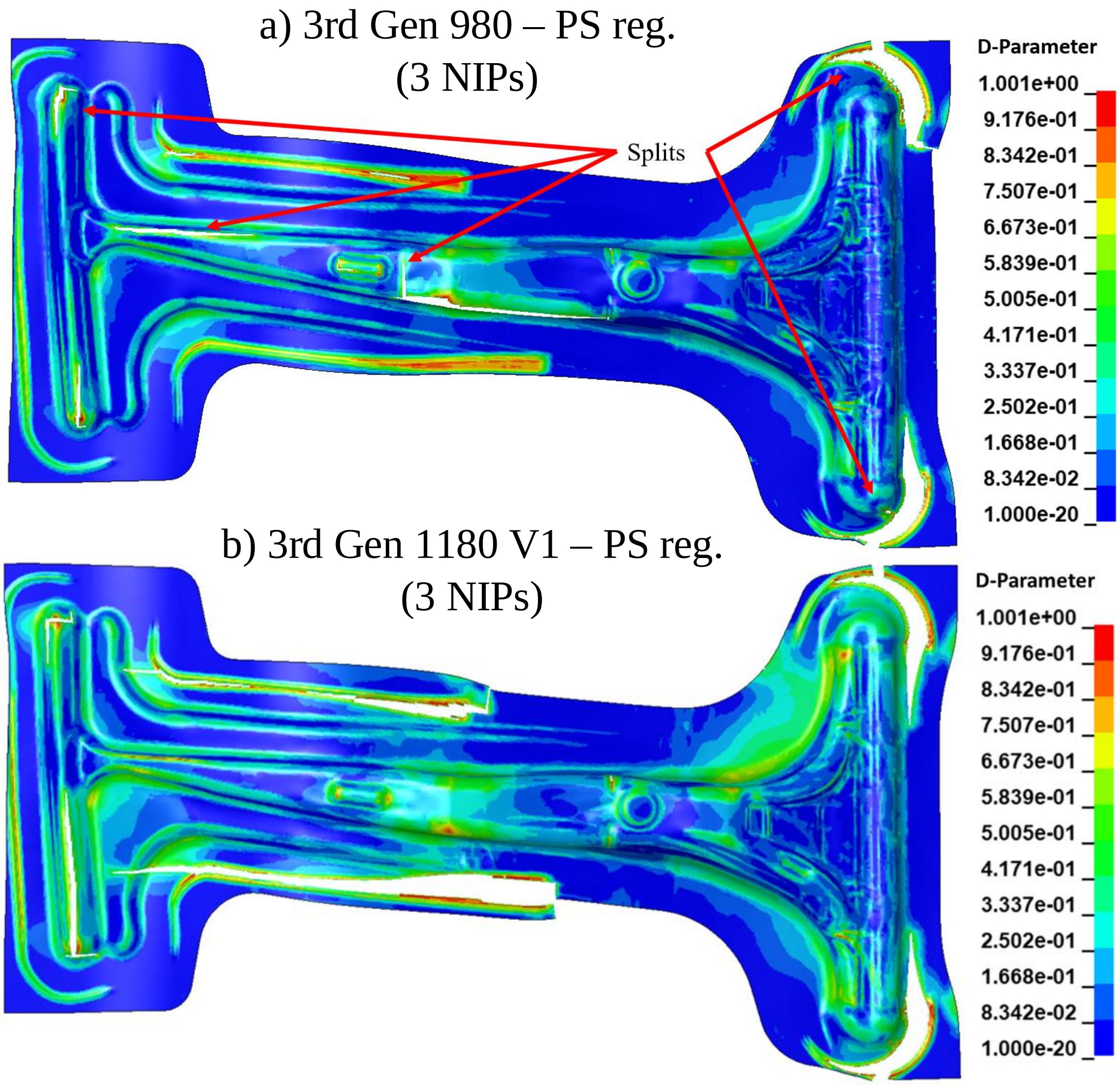

Figure 164: B-pillar forming simulations of a) 3rd Gen 980 and b) 3rd Gen 1180 V1 with 3 NIPs using plane strain regularization showing the D-parameter for the upper integration point

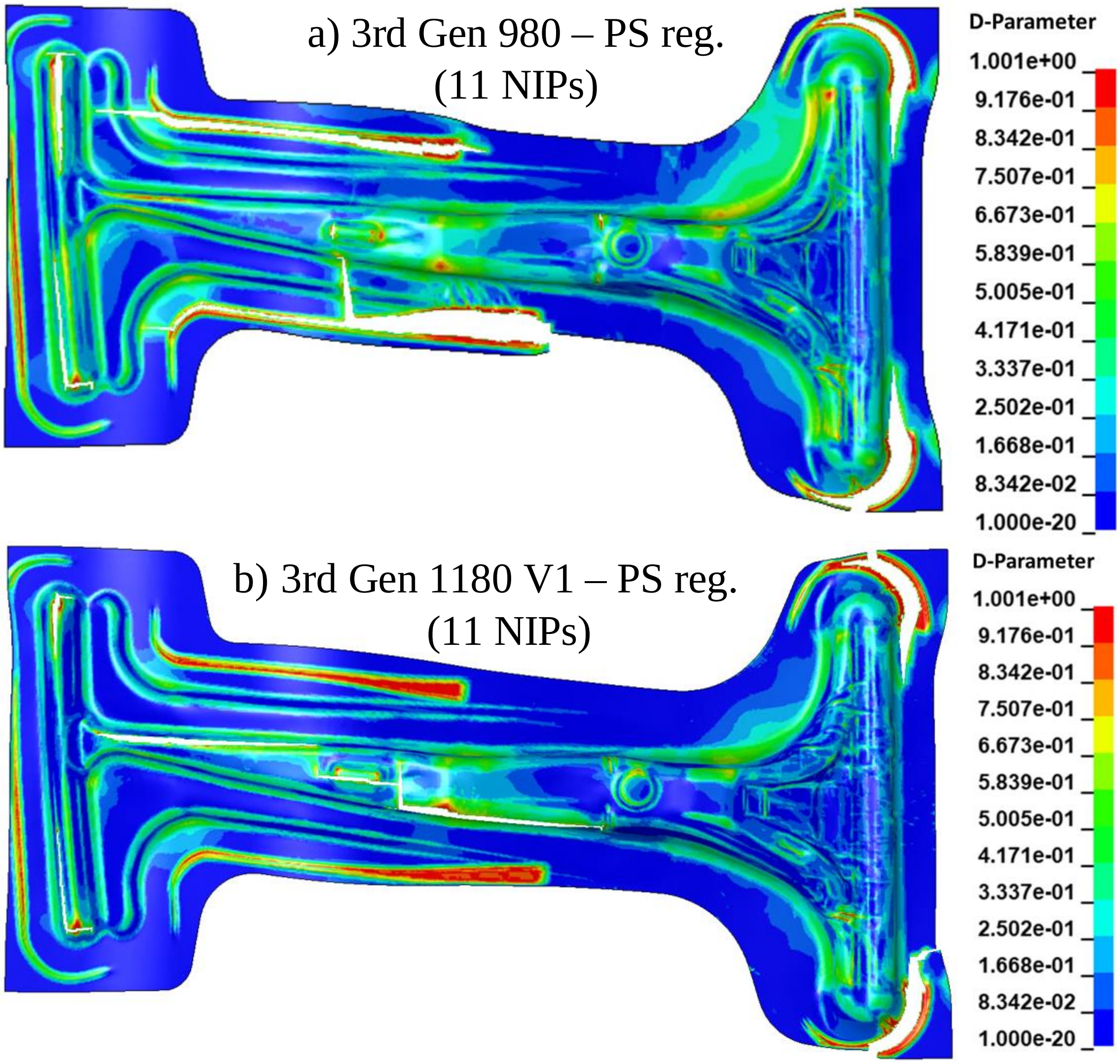

Figure 165: B-pillar forming simulations of a) 3rd Gen 980 and b) 3rd Gen 1180 V1 with 11 NIPs using plane strain regularization showing the D-parameter for the upper integration point

Appendix B: Double Impactor

Single impactor vs. double impactor

The primary configurations initially proposed for the impactors were to use single or double impactors. It is typical of standardized side impact tests such as the SICE50 (IIHS, 2020) to use a moving deformable barrier (MDB) seen in Figure 166. The lower portion of deformable barrier acts as a single impactor which mimics the bumper of a life-sized vehicle. The concept of the double impactor was then proposed to generate more strains at the B-pillar to mimic a full-sized deformable barrier where the second impactor would emulate the upper portion of the MDB. The intended outcome with the double impactor was to create a more even distribution of strains such that if DIC was implemented on the impact tests, there exists a metric to compare simulations and impact testing. This method of analysis also presented a unique analysis that is not typically carried out in impact tests.

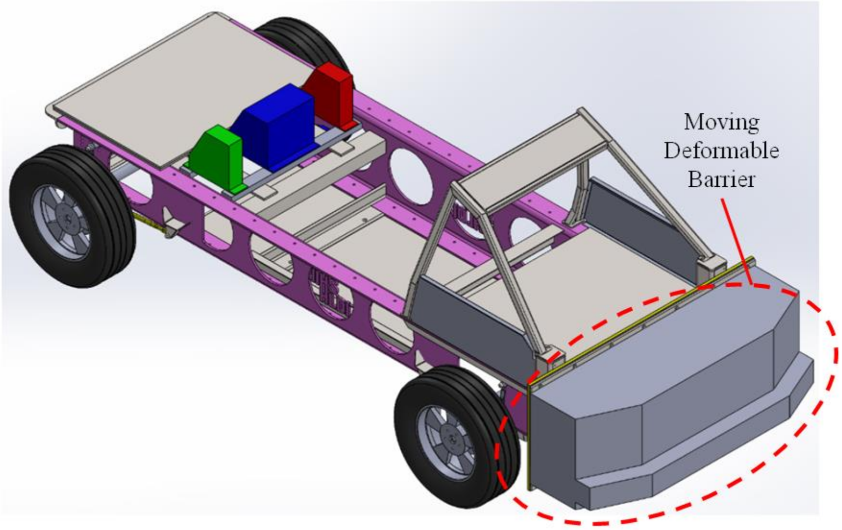

Figure 166: Model of the IIHS test cart highlighting the moving deformable barrier (MDB) (IIHS, 2020)

The first proposed placement of the impactor was to have it in-line at the fold initiator. This results in high deformation at the fold initiators however it reports very low strains in every other location of the B-pillar as seen in Figure 167. The contour plot of the B-pillar reports overall near-zero strains which makes deformation of the impact simulation non-discernible. To assist in generating an even distribution of strains on the B-pillar, it was proposed to use two impactors displaced some distance from each other. The impactors were located at the side sill and the other placed closer to the roof rail which can be seen in Figure 168. From this double impactor configuration, strains are less localized in the fold initiators and the location of impact is more evident. Although the strains are more distributed throughout the locations of impact, numerous disadvantages arise. Clearly evident from Figure 168, buckling at one location occurs which is undesirable in the experiment.

Consequently, due to an additional impactor being added to the assembly, an increase in reaction forces are compounded in the simulation. This ultimately leads to a less feasible design due to the questioned integrity of the bolts and spotwelds along with an increased probability of derailing the sled due to the asymmetric forces experienced by the sled.

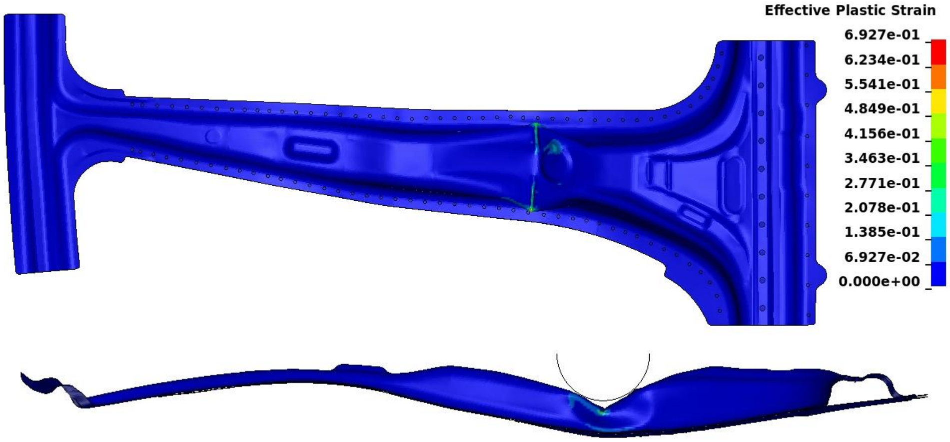

Figure 167: Crash simulation of the 3rd Gen 980 B-pillar where the impactor is centered at the fold initiators at approximately 150 mm crush distance

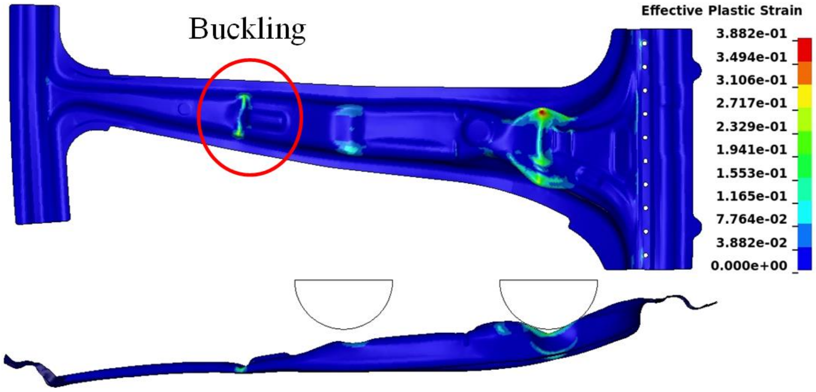

Figure 168: Crash simulation of the 3rd Gen 980 B-pillar where double impactors are used at approximately 150 mm crush distance

The reaction forces on the bolts, in particular the axial and shear forces, were within specification of withstanding both the single and double impactor configurations. Due to the remarkably high strength of the Class 10.9 M10 bolts, failure was not a concern. A maximum of approximately 9 kN and 14 kN were reported for the axial and resultant shear forces, respectively, for the M10 bolts with the double impactor configuration. These forces are below the threshold for axial and shear forces for Class 10.9 bolts (EuroCode Applied, 2021) which are deemed safe in the simulation and subsequently, impact testing. Bolt forces in the single impactor report slightly lower forces but are nonetheless sufficiently safe in the impact tests.

Spotweld forces pose more of a concern than bolts in the selection of the impactor configuration. The axial and shear forces reported in the simulation of the double impactor would reach force magnitudes close to the forces achieved by cross-tension tests. Spotweld failure can be problematic as multiple spotwelds failing can result in inconsistent correlations between the simulation and experiments. A certain axial force and shear force can be specified such that when the accumulated forces in the weld is achieved, failure is reached. To justify the implementation of a weld failure model, cross-tension tests were performed to observe the axial forces in the weld.

Another concern with the double impactor configuration are the moments imposed on the crash sled. Typical applications of impact tests performed in the UW crash lab uses a single impactor that strikes the sample at its center ensuring symmetric reaction forces on the sled. The B-pillar is a non-symmetric part that is being struck at locations close to the side sill and roof rail when using the double impactor configuration. Although the B-pillar has non-symmetric geometry, having one impactor ensures symmetry in the reaction force because it is placed in the middle of the crash sled as seen in Figure 169a. The double impactor configuration seen in Figure 169b differs in reaction forces caused by the non-symmetric shape of the B-pillar. This imbalance of reaction forces may derail the sled and cause further damages in the impact tests.

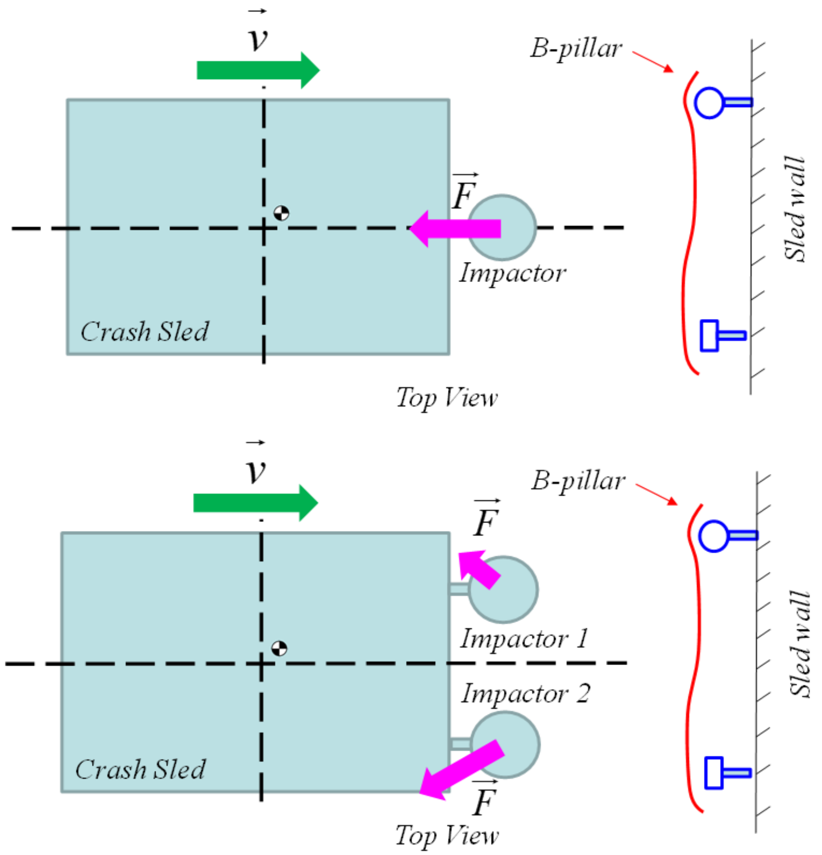

Figure 169: Top view schematic of the crash sled assembly with the B-pillar showing a) single and b) double impactor configurations indicating the direction of reaction forces. Not to scale.

After much consideration of the previously mentioned factors, the influence of the second impactor causes multitudes of concerns that could lead to a failed experiment or damage to the testing equipment. It was concluded that the double impactor, although it provided numerically discernable results, was ruled out as an impactor configuration for crash testing. The originally proposed single impactor was selected as the configuration for the impact test.

Single impactor placement: centered / right offset/ / left offset

The placement of the impactor relative to the fold initiators is a significant design consideration as it affects the way the B-pillar deforms. It has been previously discussed when the center of the impactor is aligned at the fold initiators, buckling is imminent and strains are too heavily localized at the fold initiators that strains at other locations seem imperceptible. It is also desirable to completely avoid the severe buckling mode while generating perceptible strains from the impact test. The centered configuration is forgone and two other placements of the single impactor were studied to justify its location; one location offset from the right of the fold initiator and the other offset from the left where the reference can be seen from Figure 170.

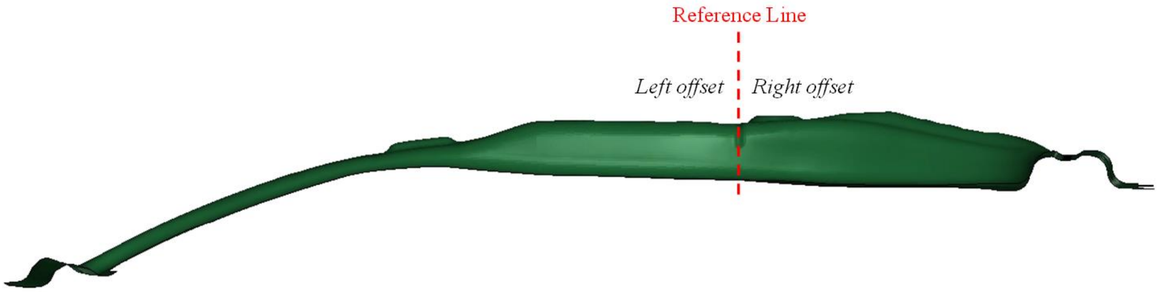

Figure 170: Indicator of left and right offsets locations relative to the fold initiator

Simulations performed with each configuration (seen in Figure 170) provided noticeably varying results. The offset distance was set to 50 mm from the reference line. Simulations created where the impactor was placed 50 mm to the left of the reference line, referred to as the left offset, produced similar deformation to the centered configuration where the impactor is directly aligned with the fold initiators. Buckling also remains a concern for the left offset configuration. At the right offset, there is more material contact between the impactor and the B-pillar. Due to that, strains for the right offset configuration are more distributed at the region of impact and buckling is less exacerbated than that of the left offset. This configuration also assists in lowering the moment arm in the test by having the impactor be moved closer to where the nodes of the U-channel are constrained. Because the right offset configuration creates more discernible strains and lowers overall forces in the test, the right offset configuration of the single impactor is selected.

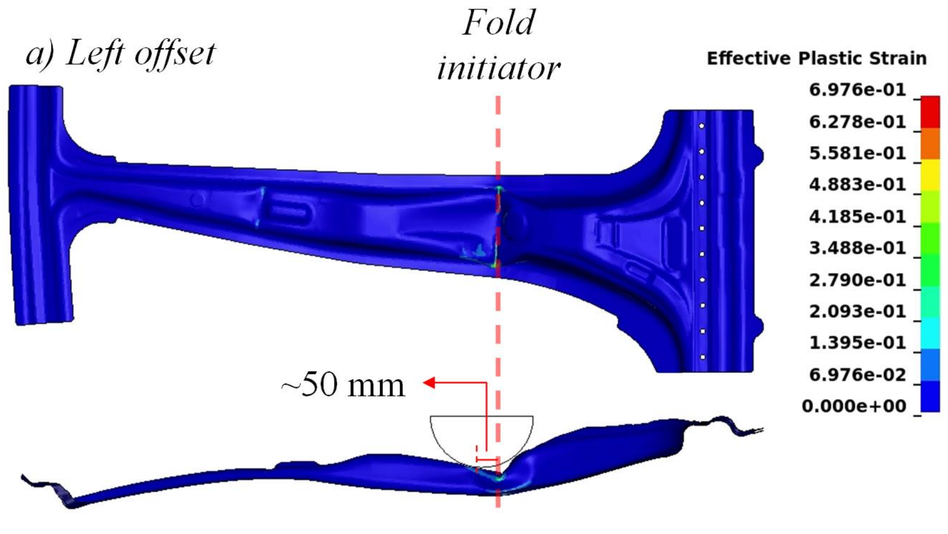

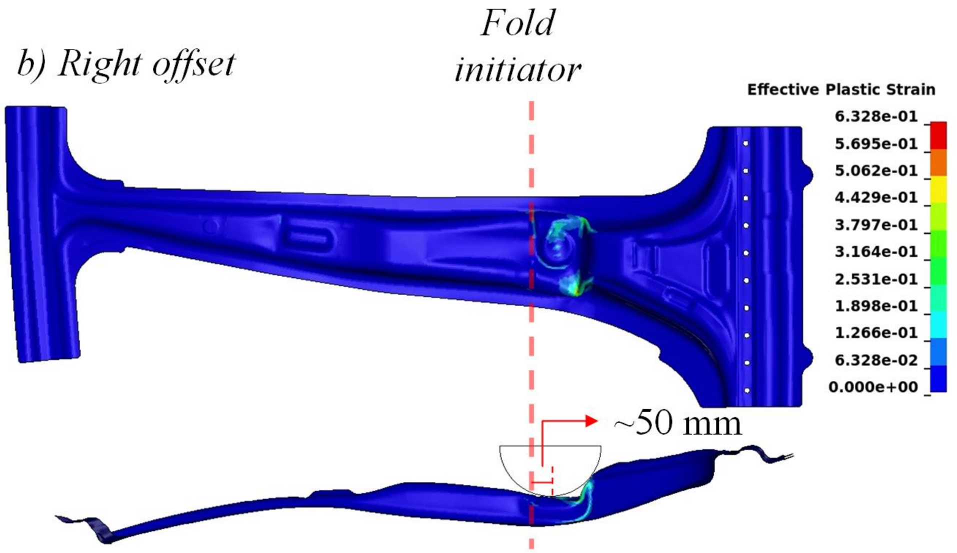

Figure 171: Deformation of the 3rd Gen 980 B-pillar using the a) left offset configuration and b) right offset configuration